Analysis of the physical and chemical properties of atmospheric aerosol at the Puy de Dôme station

Antoine Farah

Université Clermont-Auvergne
Clermont-Ferrand

Graduate School of Fundamental Sciences

PhD. Thesis

in partial fulfillment of the requirements for the degree of

Doctor of Philosophy

of the Université Clermont-Auvergne

Specialty

Physique-chimie de l'atmosphère et climat

Submitted and presented by
Antoine FARAH

Analysis of the physical and chemical properties of atmospheric aerosol at the Puy de Dome station

Defended the 19th of December 2018

PhD. Committee:

PhD. Reviewers: *Paolo LAJ, IGE CNRS, Grenoble, France*
John WENGER, University College Cork, Ireland

PhD. Supervisors: *Karine SELLEGRI, LaMP CNRS, Clermont-Ferrand, France*
Evelyn FRENEY, LaMP CNRS, Clermont-Ferrand, France

Remerciements

Eh bien ça y est !!! Apres avoir effectué quelques dizaines de routines au Puy de Dôme, analysé des milliers de lignes de données et parcouru le Monde…. L'heure est à la rédaction de la partie la plus lue d'une thèse.

Les premiers remerciements vont à Joël Van Baelen, qui m'a ouvert les portes du Labo, dès la première année de mon Master à l'université Clermont-Auvergne, ce qui m'a permis de réaliser ma thèse dans les meilleures conditions.

Je voudrais ensuite remercier tout particulièrement mes encadrantes, Karine et Evelyn, et mes encadrants, Wehbeh et Maher, qui ont su être complémentaires tout au long de ma thèse et ainsi m'apporter des conseils pour construire cette étude. Vous m'avez fait confiance en m'accordant une certaine liberté dans mes différents travaux et, de ce fait, me permettez d'apprécier de les partager et de les transmettre.

Je remercie bien entendu les membres du jury, Paolo Laj et John Wenger, qui ont bien voulu prendre de leur temps pour lire soigneusement les pages de ce manuscrit, de m'avoir rejoint pour la soutenance en terre auvergnate et de m'avoir conseillé sur chaque détaille de mes travaux.

Je pense également à tous les gens du Labo avec qui j'ai travaillé et qui m'ont permis de passer trois années dans une ambiance conviviale. Je remercierai tout particulièrement Laëtitia, Mickaël R., Jean-Marc, David et Joël B. (le brésilien et italien qui parle français anglais et allemand) pour leurs disponibilités à chaque question technique sur tous ces instruments mystérieux et capricieux, et pour tous les d'agréables moments sur notre cher Puy de Dome. Je n'oublierai pas non plus les aides de Sandra et Edouard lors de mes nombreux soucis informatiques.

Ces trois années de thèse n'auraient pas pu mieux se passer sans le soutien de « la Team 8220 ». Je pense alors aux premiers qui m'ont accepté dans ce bureau comme Clémence, Aurelien my BRO (merci d'ailleurs pour ton bureau 😁), mais aussi à Kévinou le glaçon, Brice le malice, Pierro Fréro, Paolo mio, Allessia mia, Maher (I agree with you), Miao, Maia et Manon qui ont su apporter une ambiance unique durant ces trois années. En espérant que nous resterons en contact malgré les diverses voies prises par chacun… Sans oublier bien entendu « les expats du batiment 5 », je pense alors à Thibault, Dany, Alaa, Christina, Hélène, Ibrahim, Angelica, Pamela, et Alexis qui ont également énormément compté dans le bon déroulement de cette thèse.

Le basket étant mon sport préférer, Je tiens à remercier « la team basket », je pense alors a Nicoletta, Arthur, Pierre B., Alex et j'en oublie certainement.

Le mot de la fin est bien sûr destiné à ma famille, qui m'a permis d'arriver là où je suis et m'a supportée au quotidien: ce diplôme de doc, il est pour vous.

Contents

Contents

Contents

Chapter 1: General introduction and aims of this doctoral thesis

1.1. General Introduction

Climate science is currently found in the heart of the political, national and international issues whether with the European elections or the Copenhagen summit. Since the IPCC (Intergovernmental Panel on Climate Change) report in 2007 (IPCC, 2007), it is known to all that our planet is getting warmer, there is already rising sea levels, widespread melting of snow and glaciers. This report shows an increase in global surface temperature of + 0.74 ° C between 1906 and 2005, of which 0.65 ° C only between 1956 and 2005. Since the 1950s, this warming is mainly a result of the increase in anthropogenic greenhouse gas (GHG) emissions (IPCC, 2007, 2013). The EEA (European Environment Agency) reports that in Europe, the decade 2002-2011 was the hottest since meteorological data were available, with + 1.3 ° C compared to the pre-industrial average, and predicts that in 2050 temperatures will have increased from +2.5°C to + 4°C.

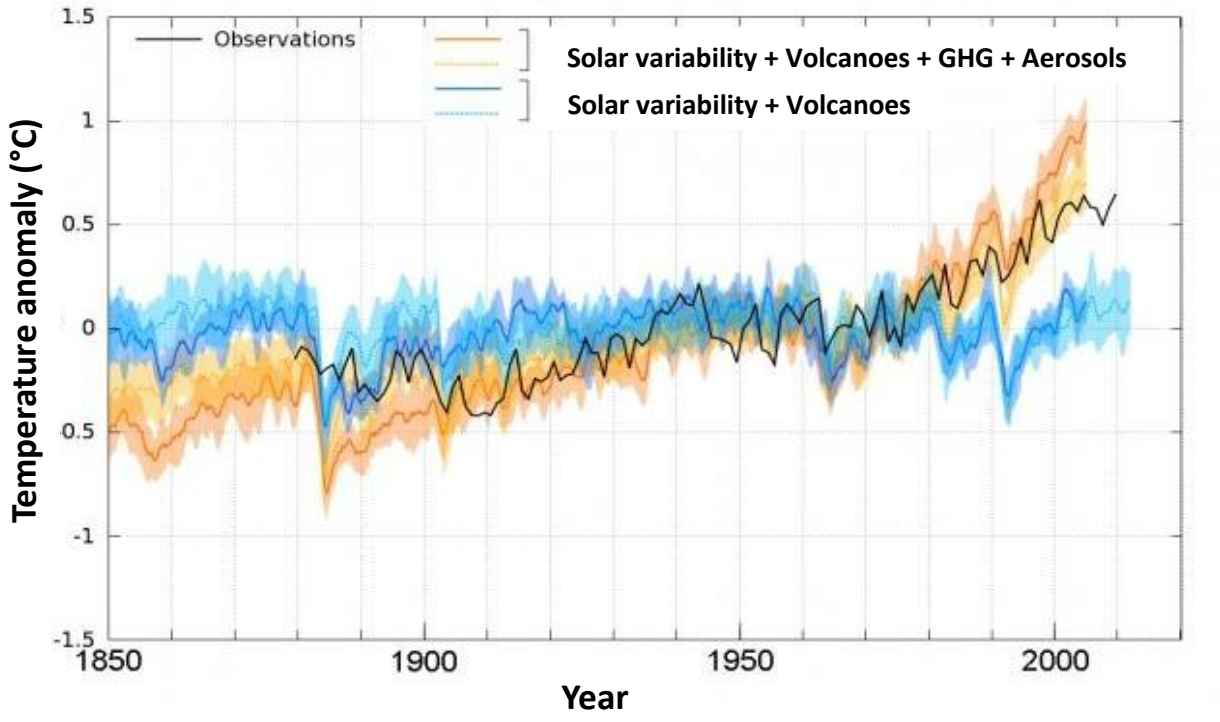

Figure 1. 1. Evolution of the mean annual temperature at the Earth's surface from 1850 to 2000 relative to the average temperature for the period 1901-2000 taken as a reference, measured (black curve) and calculated by CNRM-CERFACS models (dashed lines) and IPSL (solid lines). The blue curves only take into account natural forcing (solar variability and volcanoes) whereas the orange curves take into

account natural and anthropogenic forcing (greenhouse gases and aerosols). For each of the curves, the results were obtained from a dozen simulations whose average corresponds to the curve and the variation around this average to the colored envelope. The reference period 1901-2000 serves as a zero crossing for the different curves. Reference: "http://www.insu.cnrs.fr/environnement/climat-changement-climatique/les-resultats-les-temperatures.".

In order to better control this climate change and try to limit its consequences, it seems particularly necessary to know all the actors involved in climate regulation. In addition to GHGs, aerosol particles emitted directly (primary aerosols) by anthropogenic or natural sources, or indirectly formed by physicochemical processes (secondary aerosols), are likely playing a role in climate change. These particles, whose size can vary from a few nanometers to 100 microns, can be classified according to their aerodynamic diameter (da). PM_{10} (da <10 μm), $PM_{2.5}$ (da <2.5 μm) and PM_1 (da <1 μm) are distinguished. The impact of these compounds on the climate is illustrated in figure I.1. This figure shows that the models taking into account the natural forcing (solar energy and volcanoes) and anthropogenic, including the GHGs and aerosols, result in a better estimation of the measured temperatures in comparison with the modeling made from only natural forcing. Their varied and unevenly distributed emissions not only have an impact on climate through their radiative forcing but also an impact on our health.

Aerosol particles have the most detectable and rapid health effects. The study of air quality in urban environments, initiated in the 1950s as a result of pollution episodes, clearly documented the link between aerosols and mortality. The PM_{10} in urban areas is estimated to lead to 800 000 premature deaths worldwide each year, including 100 000 in Europe (Cohen et al., 2005). The impact of aerosols on health is also dependent on their concentration, size and composition. The submicron aerosols produced by combustion would be more harmful than the larger natural aerosols, because of the facility they have to penetrate deeper into the respiratory tract and their toxicity related to the presence of metals and polycyclic aromatic hydrocarbons (PAHs) considered carcinogenic (Curtis et al., 2006; Knibbs et al., 2011).

As previously mentioned, aerosol particles also have an impact on the climate by their radiative forcing. These particles have a direct effect: they interact with solar and telluric radiation, leading, according to their chemical composition, to the warming or cooling of the atmosphere (Charlson et al. , 1991, 1992). On a global scale, it seems that cooling is predominant, but the intensity associated with it remains uncertain (-0.27 Wm-2 [-0.77 0.23], IPCC, 2013). On the other hand, aerosol particles have an indirect effects, which concern the particles likely to serve as a condensation nucleus for the formation of cloud droplets (CCN) (Albrecht, 1989; Twomey, 1977). This effect, just

like the direct effect, seems to lead to a phenomenon of cooling of the atmosphere, but the uncertainty associated with it is even greater than that observed for the direct effect (-0.55 Wm-2 [-1.33 -0.06], IPCC (2013)). Numerous studies have investigated the direct and indirect radiative effects of aerosols in different regions of the world and by different types of sources (Charlson et al., 1992; Coakley et al., 1983; Mishra et al., 2014; Penner et al., 1992; Satheesh and Krishna Moorthy, 2005) and according to their nature (Satheesh and Krishna Moorthy, 2005). By the diversity of their nature and the processes of interaction with their environment, the taking into account of these particles remain a major source of uncertainties in climate models. Because the radiative impacts of aerosols depends on the size and nature of the aerosols, it is essential to obtain information on the spatial and temporal variability of the microphysical and chemical characteristics of aerosols. In particular, the peculiarities of the atmospheric circulation cause significant vertical and horizontal heterogeneities of the aerosol concentration in the atmosphere and cause difficulties in estimating the global impact of aerosol particles on climate and health (Ginoux et al., 2001; Luo et al., 2003; Ramanathan et al., 2001).

Aerosol particles emitted from the ground are mostly concentrated in the atmospheric Boundary Layer (BL) which is the layer that ranges from 500 m (over the sea) to 2 km above land. These particles can be transported to higher altitudes, and into the free troposphere (FT), during important convective events or orographic lifting of air masses. Depending on the altitude where aerosol particles lay, their residence time and thus their impact on the climate are different. Atmospheric dynamics in the FT, which can range between about 2 and 10 km, allows for long range transport of these particles and can influence the physical, chemical and optical properties of the atmosphere on a global scale.

An essential step to understand atmospheric transport between the different layers of the atmosphere is to determine the boundary layer height (BLH). BLH can be determined in several ways including radio sounding system (Seibert et al., 2000), active remote sensing of meteorological parameters (ceilometer, sodar and LIDAR) (Emeis et al., 2004; Wiegner et al., 2006), trace gases, and aerosol particles concentrations, or wind sensors from high altitude sites (Chambers et al., 2016; Griffiths et al., 2014; Herrmann et al., 2015; Zellweger et al., 2003). However, it was highlighted that the major difficulties in these studies is providing a robust selection of FT air masses (for ground-based studies) or providing statistically representative properties (for airborne studies).

1.2. Aims of this doctoral thesis and organization of the manuscript

The first general objective of this thesis is to provide a robust selection of FT air masses at the PUY station using a combination different criteria. These criteria are based on LIDAR measurements using the wavelet covariance transform (WCT), BLH simulations using the European Center for Medium –Range Weather Forecasts (ECMWF) model, and in-situ measurements of BL tracers (NOx/CO and radon-222 (^{222}Rn)).

This segregation of air masses in FT/BL will enable the realization of the second objective of this thesis, which is to establish the seasonal variation of aerosol size distribution and non-refractory-PM1 (NR-PM1) data at the PUY station with emphasis on the boundary layer/ free troposphere segregation.

For this I will use a long time series of in-situ measurement of physical (size distribution), and chemical (NR-PM1) properties which operate continuously at the PUY station over a 12-month period, during 2015-2016.

To answer these objectives, this thesis is based on the measurements that have been deployed at multiple sites including the Cézeaux, and the PUY in Clermont-Ferrand, as well as measurements made in the city of Clermont-Ferrand. In chapter 2 we have presented the main concepts that define aerosols, their properties and their characteristics, as well as their impacts. I will present in Chapter 3 the instrumentation put in place for the chemical and physical characterization of aerosols, and the methods used and / or developed to interpret these measurements and to answer the objectives of the thesis.

The rest of the manuscript will be devoted to the results, which will be articulated around three chapters. Chapters 4.1 and 4.2 present a detailed analysis of the physical and chemical composition of aerosol sources over 12 months period during 2015-2016. Chapter 4.3 will be dedicated to the study of the links between the chemical composition of PM1 at the high altitude PUY station and measurements made simultaneously in the city of Clermont-Ferrand.

Chapter 2: State of the art

Aerosol particles are an atmospheric component characterized by large diversity. In this part of the manuscript, we describe the properties of atmospheric aerosol. In particular, the focus will be on their microphysical and chemical properties, as well as describing how these properties can vary depending on their sources photochemical processing and evolution as they are transported through the atmosphere.

2.1. Aerosol particles

Aerosol particles are, by definition, all the liquid and / or solid particles suspended in the atmosphere. In general aerosol refers to a group of particles in either liquid or solid form and the term particle refers to an individual particulate species. In the thesis, these terms particle and aerosol will be used together to describe all suspended solid matter.

2.1.1. Sources

In order to distinguish the aerosol particles from the point of view of their source, there are two main classifications. The first proposes to classify the particles according to their origin, anthropogenic or natural/biogenic, whereas the second proposes to differentiate the particles from their mode of emission in the atmosphere, primary or secondary. It is finally possible to combine the two classifications for a more complete description, the primary and secondary particles being able to be of natural/biogenic or anthropogenic origin.

At a global scale, natural emissions account for between 70 and 90% of mass emitted particle fluxes (Delmas et al., 2005). Significant natural sources of particles include soil and rock debris (terrestrial dust), volcanic action, sea spray, biomass burning, and reactions between natural gaseous emissions. Table 2.1 presents a range of emission estimates of particles generated from natural and anthropogenic sources, on a global basis. Emissions of particulate matter attributable to the activities of humans arise primarily from four source categories: fuel combustion, industrial processes, nonindustrial fugitive sources (roadway dust from paved and unpaved roads, wind erosion of cropland, construction, etc.), and transportation sources (automobiles, etc.).

The following paragraphs will first describe the main natural and anthropogenic sources of aerosols, considering successively their primary and their precursor's emissions.

Dust source in the atmosphere consist of two major sources – **mineral** and **volcanic**.

- M**ineral** sources arises from wind acting on soil particles. The major dust sources are located in arid and semiarid regions of the world, which cover about one-third of the global land area. The largest global source is the Sahara-Sahel region of northern Africa; central Asia is the second largest dust source. Estimates of global dust emissions are uncertain. Published global dust emission estimates since 2001 range from 1000 to 3000 Tg/yr (Table 2.1), and atmospheric burden estimates range from 8 to 36 Tg (Zender et al., 2004). The large uncertainty range of dust emission estimates is mainly a result of the complexity of the processes that raise dust into the atmosphere. The emission of dust is controlled by both the wind speed and the nature of the surface itself. In addition, the size range of the dust particles is a crucial factor in emissions estimates. It is generally thought that a threshold wind speed as a function of particle size is required to mobilize dust particles into the atmosphere. The average lifetime of dust particles in the atmosphere is about 2 weeks, during which dust can be transported thousands of kilometers. Saharan dust plumes frequently reach the Caribbean and Europe, and plumes of dust from Asia are detected on the west coast of North America.

- **Volcanic** sources have much more variable emissions. They depend on the frequency of direct volcanic eruptions in the atmosphere of volcanic ash, which consist mainly of pulverized rocks and minerals. These primary volcanic aerosols, usually greater than one micron in diameter, will have a short lifetime in the atmosphere, unless the ejection velocity allows them to reach the free troposphere and above. On the other hand, these eruptions are accompanied by gaseous releases rich in sulfur compounds such as SO_2 and H_2S, whose annual emissions range from 6 to 20 Tg of sulfur per year (Table 2.1). The oxidation in the atmosphere of these precursor gases leads to the formation of sulfate aerosols, which depend on the altitude at which they are emitted and therefore will have a lifetime of a few weeks (troposphere) to several months or even years (stratosphere).

Marine source is the most important natural source of aerosols, emitting between 1000 and 6000 Tg of sea spray per year (Table 2.1). These marine aerosols, of primary types, are produced by the mechanical action of the wind on the surface of the oceans (Woodcock et al., 1953). The emission of these aerosols thus depends mainly on the wind speeds, which above a certain threshold allow the tearing and suspension in the atmosphere of seawater droplets drying out to particles. The diameter of this marine spray can vary from a twenty nanometers to about ten micrometers. Marine sprays may contain a part of biological material and inorganic salts, more generally called sea salts (SS for sea salt). In terms of mass flux, most of the emissions of these marine salts are in the supermicron fraction (da> 1µm) (O'Dowd et al., 1997).

Biogenic sources are emissions that come from natural sources of particles, including pollens which correspond to coarse aerosols, with sizes range from 1 to 100 µm and spores which are emitted up to 30 Tg/yr (Table 2.1). Bacteria and viruses are also considered as biogenic particles, their diameter varying from a few nanometers to several microns for the largest bacteria (Jaenicke and Mathias-Maser, 1992). Marine sea-level emissions can also result in the suspension of organic material associated with marine biological activities, resulting in primary submicron organic aerosol emissions (Leck and Keith Bigg, 2008). Also a significant fraction of biogenic particles in forested areas are the source of precursor gas emissions such as volatile organic compounds (VOCs) as well as more moderate amounts of nitrogen oxides (NOx). The most Known VOC is the dimethyl sulfide (DMS) who's mainly emitted by phytoplankton.

Natural Biomass Burning (BB) sources are resulting from the intentional burning of land which is the major source of combustion products to the atmosphere. Most of this burning occurs in the tropics, leading to emissions of gas precursors including VOC, NOx, SO2, and NH3 and primary aerosols including organic carbon compounds, mainly consisting of oxygen and hydrogen atoms, and black carbon (BC), mainly composed of carbon atoms. The quantity and type of emissions from a biomass fire depend not only on the type of vegetation but also on its moisture content, ambient temperature, humidity, and local wind speed. Seinfeld and Pandis, (2006) show an estimation of global emissions of trace gases from BB. They show that CH4 contribute 40 Tg/yr out of a total flux of 598 Tg/yr, CO contribute 700 Tg/yr out of a total source of 2780 Tg/yr. For NOx, biomass burning is estimated to contribute globally 7.1 Tg/yr, as compared to 33 Tg/yr from fossil-fuel burning.

Anthropogenic Biomass Burning sources such as wood-burning, represent emissions of 50 to 90 Tg/yr on a global scale (Table 2.1). In terms of primary aerosol emissions, the anthropogenic BB source appears to be superior to the natural source. In addition, these primary aerosols have predominantly submicron diameters (Rau, 1989) and a supermicron fraction (Park and Lee, 2003).

Table 2. 1. Estimated emissions flux of the main types of primary and secondary aerosols en Tg=10^{12} g. (Boucher, 2015)

Source	Estimated flux (per year)
Natural	
Primary	
Mineral dust	1000-3000 Tg
Seasalt	1000-6000 Tg
Biomass burning aerosols	20-35 Tg
Biogenic aerosols	Order of 1000 Tg
Including bacteria	0.04-1.8 Tg
Including spores	30 Tg
Secondary	
Dimethylsulphide (DMS)	20-40 Tg S
Volcanic SO_2	6-20 Tg S
Terpenes	40-400 Tg
Anthropogenic	
Primary	
Industrial dust	40-130 Tg
Biomass Burning	50-90 Tg
Black carbon (from fossil fuel)	6-10 Tg
Organic carbon (from fossil fuel)	20-30 Tg
Secondary	
SO_2	70-90 Tg S
Volatile Organic compounds (VOCs)	100-560 Tg C
NOx	20-50 Tg N
NH_3	30-40 Tg N

C carbon, S sulfur, N nitrogen

2.1.2. Chemical composition

The chemical components present in particulate form in the atmosphere are extremely numerous and varied. These components are specific to the particles origin and formation process and, can evolve rapidly during atmospheric transport during condensation, coagulation, and photochemical processes. Understanding the chemical composition of aerosol particles is important since it can influence the optical

properties of the particles (Maring et al., 2000; Pilinis et al., 1995), their health impact and their ability to form a cloud droplets. The most important chemical species in the submicron atmospheric aerosols are: ammonium, sulphates, nitrates, chlorides and organic matter (OM). Despite the challenges associated with in-situ aerosol chemical characterization, analytical techniques available today allow complex insights into the main particulate components properties (Putaud et al., 2010).

An example of this characterization is presented in Figure 2.1 This figure shows the annual average chemical composition from off-line filter measurements at 39 sites across Europe across different size ranges: $PM_{2.5}$ and those associated with coarse particles (PMcoarse; $PM_{2.5-10}$) (Putaud et al., 2010). The significant portion of unaccounted mass, referred as unacc, evidences the complexity of a total chemical characterization in Figure 2.1 (obtained as the difference between the gravimetrically measured aerosol mass concentration and the sum of the aerosol component concentrations) which is found in $PM_{2.5-10}$ and $PM_{2.5}$ fractions for most sites. This unacc mass fraction can result from analytical errors, a possibly systematic underestimation of the PM constituents whose concentrations are calculated from measured data (e.g. OM, carbonaceous matter (CM), and mineral dust (MD)), and aerosol-bound water (especially if mass concentrations are determined at RH >30%). Furthermore, these chemical compositions show significant variability according to the types of sites (urban, peri-urban, rural, regional background, etc.). These results also show differences in chemical composition according to the fractions in particle sizes. In Europe, $PM_{2.5}$ is dominated by OM, with a significant fraction due to elemental carbon (EC) and by non-marine sulphate (nss-SO4). Nitrates (NO_3) are species whose contributions appear to be roughly equivalent in $PM_{2.5-10}$, $PM_{2.5}$ and PM_{10}, whereas MD and SS influence the $PM_{2.5-10}$ and PM_{10}, and are higher depending on their location (proximity to the Sahara or littorals, respectively).

There are, however, disadvantages in off-line filter measurements of aerosol chemistry: large uncertainties on the measurements and low time resolution.

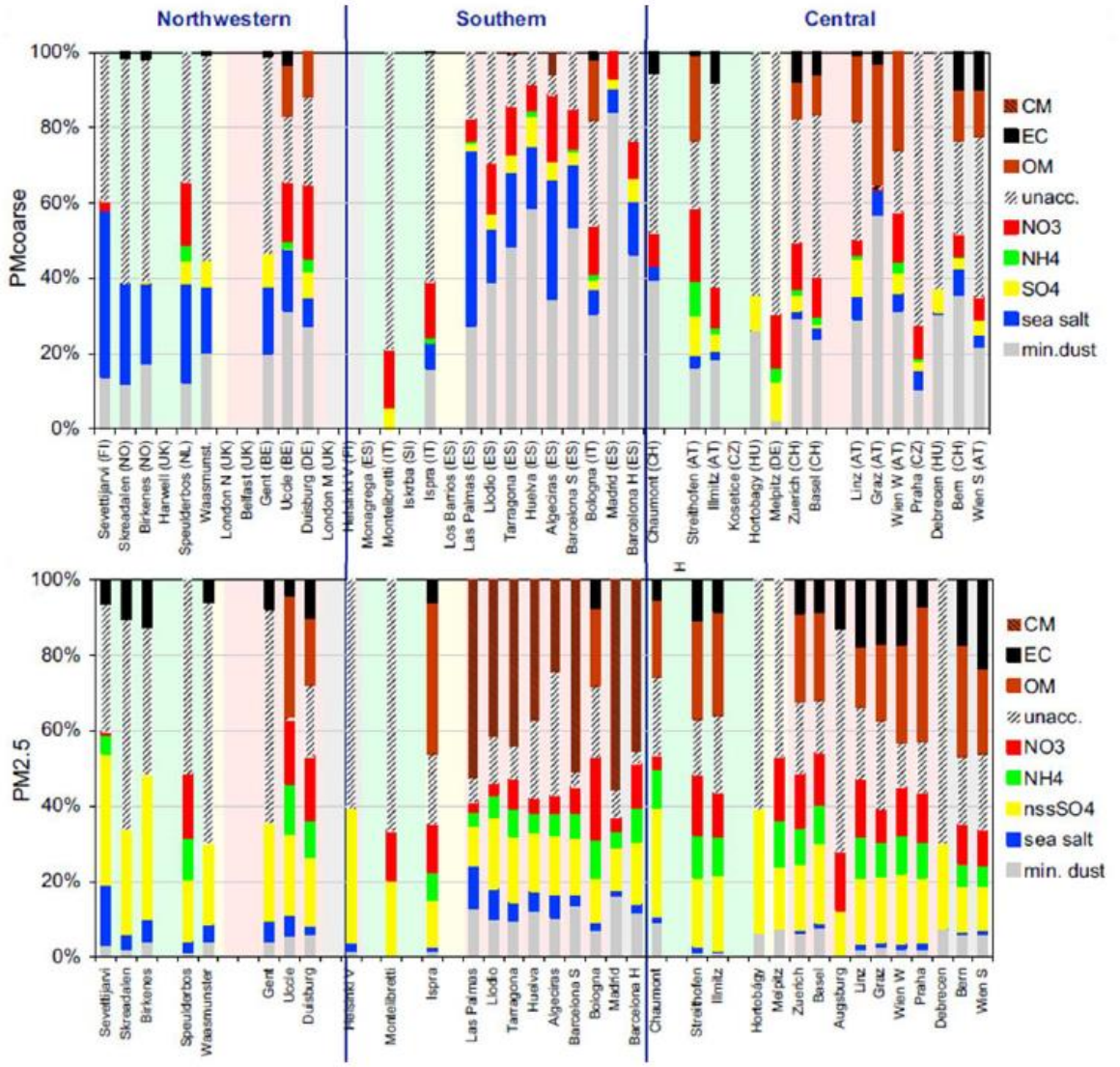

Figure 2. 1. PM2.5 and PMcoarse (PM2.5-10) annual mean chemical composition in the 39 European sites of different typologies (Adapted from Putaud et al., (2010)). The sites are classified according to their geographical position (from left to right: north-west, south and central Europe). Pastel background colors indicate the site types (green: rural background, yellow: near-city, rose: urban background, grey: kerbside).

In recent years, instrumental advances in aerosol mass spectrometry (AMS) have allowed on-line and high-resolution temporal characterization of chemical composition and size distribution of non-refractory submicron aerosols (NR-PM1), which corresponds to species vaporizable at temperatures below 600 °C. This measurement technique therefore excludes MD, SS and EC, but on the other hand makes it possible to quantify the PM_1 concentrations of ammonium, sulphates, nitrates, chlorides and organic matter. Furthermore, spectral analysis of different

species allows insights into their origin, particularly primary or secondary organic aerosol. Although most AMSs do not measure refractory PM1 (or R-PM1), it should be noted that some versions of AMS make possible the more specific characterization of BC, SS or MD (Cross et al., 2009; Onasch et al., 2012). Several short term studies of AMS in the Northern Hemisphere (Jimenez et al., 2009; Ng et al., 2010; Zhang et al., 2005), shows that submicron particle mass is largely dominated by aged organic compounds. Petit et al., (2017) in urban sites in France, shows that all sites are characterized by a strong predominance of secondary pollution, and more particularly of ammonium nitrate, which accounted for more than 50% of submicron aerosols. Lanz et al., (2010) at an alpine region, show that the NR-PM1 aerosol particles are dominated by organics (36% to 81%). Other main constituents comprised ammonium (5–15%), nitrate (8–36%), sulfate (3– 26%), and chloride (0–5%). Freney et al., (2011) at PUY site, show highest nitrate and ammonium mass concentrations were measured during the winter and during periods when marine modified air masses were arriving at the site, whereas highest concentrations of organic particles were measured during the summer and during periods when continental air masses arrived at the site. Kiendler-Scharr et al., (2016) at urban and rural sites in Europe, show that organic nitrates contribute substantially to particulate nitrate and organic mass, and represent 34% to 44% of measured submicron aerosol nitrate and are found at all urban and rural site. Also, Zhang et al., (2007) identified chemical compositions and mean concentrations of NR-PM1 measured at 37 sites all over the world. These results show that, despite a certain variability in the chemical composition, the NR-PM1s are globally dominated by organic and sulphates species, with respective fractions of 45 and 32% on average over all 37 sites. The ACSM (Aerosol Chemical Speciation Monitor, (Ng et al., 2011)), recently developed for the routine and long-term chemical characterization of NR-PM1, is based on the same principle as AMS, but does not provide access to the size distribution. This instrument, deployed in our study for the chemical characterization of aerosols, will be described in more detail in chapter 3 of this manuscript.

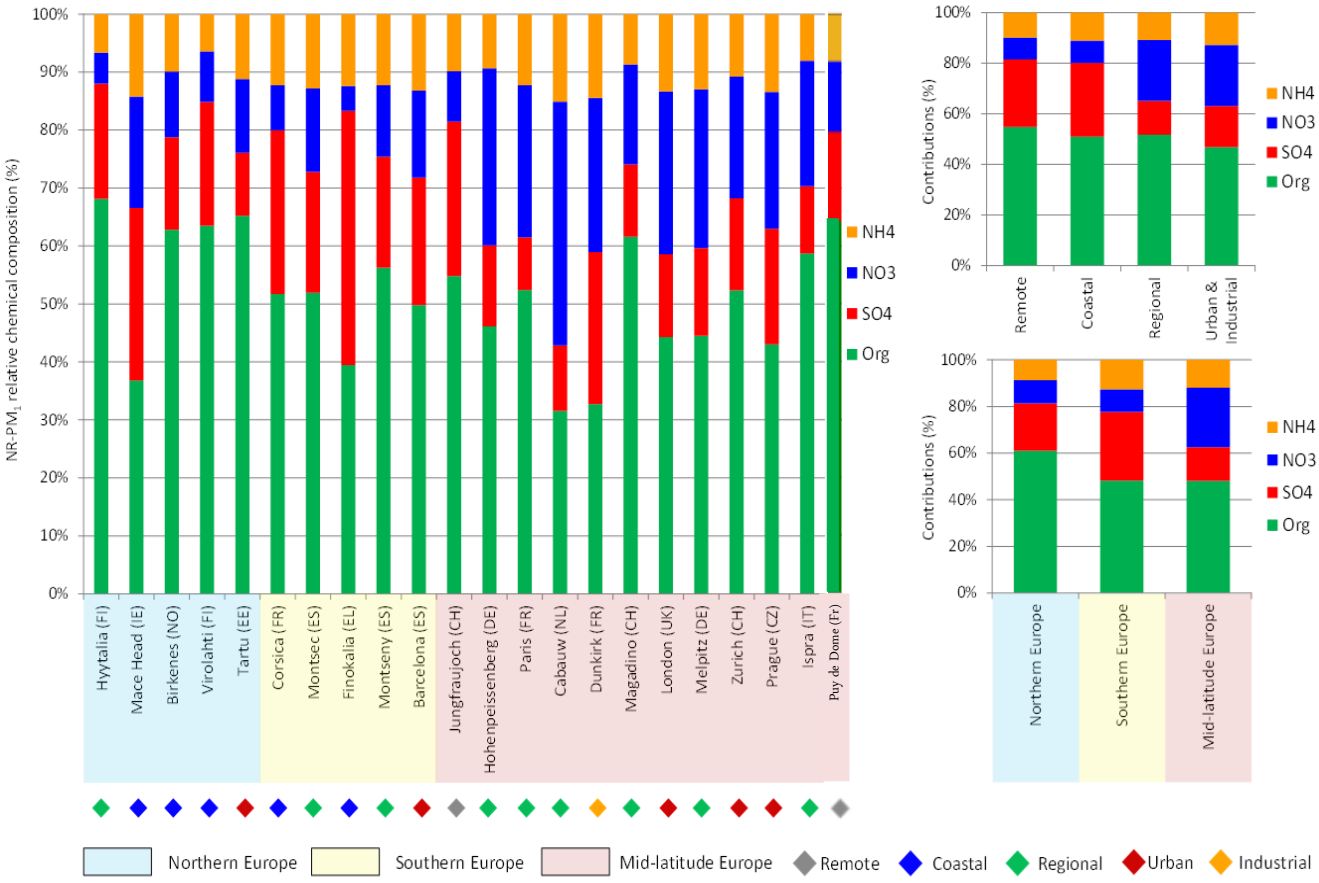

Figure 2. 2. Annual average NR-PM_1 relative chemical composition across Europe. Geographical locations are shown by coloured background panels. The type of site is indicated by coloured diamonds (Bressi et al., 2018).

In recent years, the deployment of mass spectrometers dedicated to aerosols during field campaigns conducted on different continents has made it possible to highlight geographical and seasonal trends in the chemical composition of NR-PM1. Long term measurements are important to facilitate continuous control of air quality, monitoring of climate changes, to study the seasonal variation, for long range transport and to increase statistics on the measurements. Long-term ACSM data sets have recently been presented in the literature almost all over the world such as: 2 years near Paris (France) (Petit et al., 2015), 1.5 years in central Oklahoma (Parworth et al., 2015), 1 year in Zurich (Switzerland) (Canonaco et al., 2013, 2015), near Johannesburg (South Africa) (Tiitta et al., 2014; Vakkari et al., 2014), near Barcelona (Spain) (María Cruz Minguillón et al., 2015; Anna Ripoll et al., 2015), and in the Southeastern United States (Budisulistiorini et al., 2016). Also, Bressi et al., (2018) identified the relative chemical compositions of NR-PM1 measured at 21 sites across Europe, where the ACSM (19 sites) and AMS (2 sites) were implemented. These results, presented in Figure 2.2,

show that, despite a certain variability in the chemical composition, the NR-PM1s are globally dominated by organic aerosol (OA) over all 21 sites. It is also observed that the OA contributions are similar at remote, coastal, regional, urban or industrial areas (between 50% and 56%). Slightly higher OA contributions are found in Northern Europe compared to Southern Europe or Mid-Latitude Europe. Sulphate and nitrate contributions largely differs on the European site (9-44% and 4-42%, respectively). On average, higher sulphate and nitrate contributions are found remote/coastal areas and urban/regional areas, respectively. Higher sulphate contributions can be associated with shipping emissions of SO_2 influencing coastal sites (Viana et al., 2014) and relatively long (days) lifetime and in-cloud formation kinetics of sulphate (Stein and Lamb, 2002 and references therein). Higher nitrate contributions can be associated with Local anthropogenic emissions of NOx - mostly from road and non-road transport, energy transformation and industrial combustion in Europe (Pay et al., 2012).

These high-time resolution measurements of aerosol chemistry performed across Europe can help assess the efficiency of abatement policies implemented on short- and long-term durations (e.g. traffic rationing and sulphur emission reductions, respectively), and at the local and European-wide scales.

2.1.3. Microphysical properties

The diversity of aerosol particles sources, the physical, and chemical mechanisms of aerosol formation leads to a large variation in the aerosol size distributions and morphologies. Diameters of aerosol particles are distributed over several orders of magnitudes from a few nanometers up to tens of microns. The particle size distribution (PSD) can be expressed in number or mass concentration, as well as a function of surface of volume. The measurement and characterization of the PSD is essential in order to understand aerosol particles sources and to determine the impact of different atmospheric physical, chemical and radiative processes.

Figure 2.3, displays an example of different size modes (expressed as volume distributions) that can be observed in the atmosphere as well as the processes at the origin of their formations and their deposits. Diameters corresponding to PM_1, $PM_{2.5}$ and PM_{10} as well as those of ultrafine, fine and coarse particles have also been reported for comparison. This figure shows in particular that the total suspended particles is distributed around three modes.

The ultrafine particles, corresponding to all particles with diameters less than 0.1 µm, are mainly composed of secondary aerosols. These ultrafine particles are divided into two distinct modes: the nucleation mode and Aitken mode. These particles are produced by homogeneous and heterogeneous nucleation processes (Kulmala and Kerminen, 2008). They can form during natural gas-to particle condensation or during condensation of hot vapor in combustion processes. Nucleation mode particle diameters are less than 0.02 µm whereas, in the Aitken mode particles are defined within a diameter range between 0.02 and 0.1 µm.

The fine particles covers all particles with diameters less than 2.5 µm, indicating that it comprises all the ultrafine particles, those resulting from the condensation of gases on these ultrafine particles or their coagulation, as well as some primary particles that are directly formed in the submicron sizes. These phenomena lead to the formation of particles with diameters greater than 0.1 microns, which consequently belong to the accumulation mode. The upper limit of the accumulation mode is generally considered to be 1 µm (Oberdörster et al., 2005; J. H. Seinfeld and Pandis, 2006; Whitby et al., 1978) although other studies reported the value of 2 µm (Jacobson, 2005; Nazaroff, 2004).

Aerosols with larger diameters belong to the coarse mode, mainly consisting of primary particles of natural origin such as mineral dust (MD), pollen or sea salts (SS).

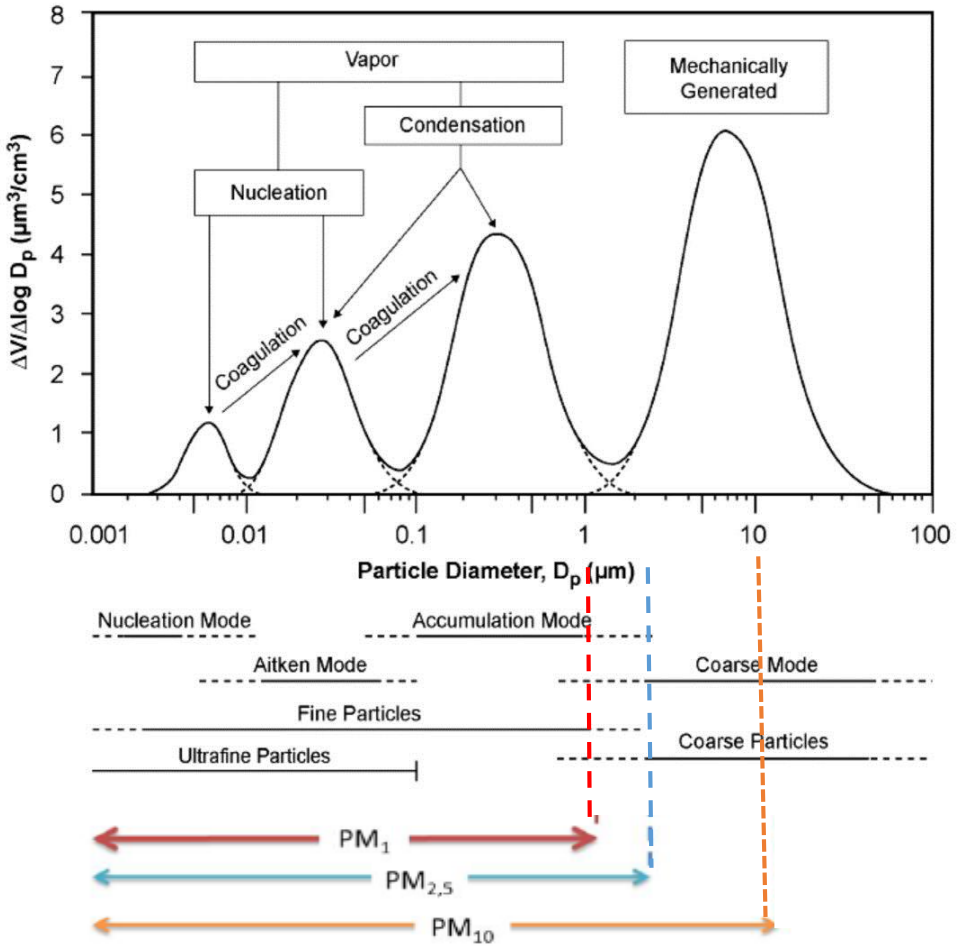

Figure 2. 3. Example of different particle size modes expressed as volume distribution (adapted from Oberdörster et al., (2005)).

During transport in the atmosphere, aerosol particles can be modified and transferred from one mode to another according to physicochemical processes and meteorological conditions. The gases available in the environment can be absorbed by the aerosol particles and thus increase their size, this is referred to as condensation. Particles can also grow in size from coagulation processes, where two or more particles come in contact and aggregate together. Inverse processes can in turn cause a decrease in particle size such as abrasion, or evaporation (transition from liquid to gaseous state, e.g NH_4NO_3). Finally, depending on their chemical composition and under certain meteorological conditions, certain aerosol particles can be activated in cloud droplets or ice crystals. These particles are then defined as cloud condensation nuclei (CCN) and ice nuclei (IN). The representation of the most widespread PSD is described by the log-normal statistical distribution. The variation of the number of particles as a

function of the logarithm of the diameter is given according to Seinfeld and Pandis, (2006) as:

$$\frac{dN}{dlogD} = \sum_i \frac{N_i}{\log\sigma \,.\, \sqrt{2\pi}} \,.\, exp\left(\frac{(\log D_i - \log \bar{D})^2}{2 \,.\, \log\sigma}\right) \quad (1.1)$$

PSDs are increasingly being measured in the context of air quality at multiple locations. For example, at the European level, the EUSAAR (European Supersites for Atmospheric Aerosol Research) project of the Sixth Framework Programme of the European Commission contributed to the development of a harmonised and quality-controlled network of measurements (Asmi et al., 2011; Beddows et al., 2014; Philippin et al., 2009). The EUSAAR project coordinated 24 European sites measuring aerosol chemical, physical and optical properties following a standardised protocol of instrument maintenance, measurement procedures and data delivery using a common format to a single database (Wiedensohler et al., 2012). Recently, the EUSAAR project activities continued within the ACTRIS project (Philippin et al., 2009) then progressed to ACTRIS 2 and now efforts are being concentrated into making this a permanent research infrastructure. Asmi et al., (2011) and Beddows et al., (2014) presented a detailed overview of the sites and seasonally disaggregated size distributions collected at the EUSAAR and the German Ultrafine Aerosol Network (GUAN) stations for the dry diameters between 30 and 500 nm for the years 2008 and 2009 (Table 2.2, referred to Asmi et al., (2011)). Asmi et al., (2011) shows that the aerosol concentrations in Europe are highly variable spatially:

- The "Central European Aerosol" (BOE, WAL, MPZ, OBK and KPO (table 2.2)), observed at low-land stations showed low seasonal changes, high particles concentrations, almost unimodal median distributions and relatively low variability.
- The "Northern European Aerosol" (BIR, VHL, ASP and SMR), has clearly lower concentrations, with decreasing concentrations at higher latitudes. The seasonal cycle has a strong effect on the particles in this region, and the overall variation is relatively large.
- The "Mountain aerosol" (JFJ, BEO, ZSF and CMN) is characterized by episodes of extremely clean air, most probably from the free troposphere, mixed by episodes of relatively polluted air masses, especially during daytime in summer.

- The "Arctic aerosol" shows a very low concentrations and evidence of Arctic haze events during winter season.
- The "North Italian aerosol" shows very high number concentrations, especially during winter in accumulation mode and with a unimodal median particle number size distribution;
- The "Mediterranean aerosol" also shows maximum number concentrations during summer and spring.
- The "Western European aerosol" shows clear influence of multiple sources of aerosol (clean and polluted), and with a high seasonal cycle for smaller particle sizes.

It is important to note that all these sites are considered as remote or rural regional monitoring sites. Data were collected using either Differential Mobility Particle Sizer (DMPS) or Scanning Mobility Particle Sizer (SMPS) instruments and then harmonised into a single data set.

Having a large scale monitoring network such as ACTRIS and GUAN, is important to enable the community to efficiently characterize the aerosol number distribution, and thus improve the potential of characterizing the climate impacts of the aerosols in different atmospheric layers. These datasets are available for the modelers in easy-to-use format for particle sizes which have potential for climate relevance. This dataset is a valuable comparison toolbox for the use of the global and regional modelling communities.

Table 2. 2. Locations and names of stations used in the data analysis. The site altitudes are given in reference to standard sea level. The areas indicated are grouped by European sub-divisions using definitions from Central Intelligence Agency (2009). Country codes are given in ISO 3166 standard. (Asmi et al., 2011)

Station name	Station code	Country	Coordinates, altitude	Category[a]	Instrument	Reference
			Low altitude sites (less than 1000 m a.s.l.)			
Nordic and Baltic						
Aspvreten	ASP	SE	58° 48′ N, 17° 23′ E, 30 m		DMPS	Tunved et al. (2004)
Birkenes[b]	BIR	NO	58° 23′ N, 8° 15′ E, 190 m	2	DMPS	Amunsen et al. (1992)
Pallas	PAL	FI	67° 58′ N, 24° 7′ E, 560 m		DMPS	Lihavainen et al. (2008)
Preila	PLA	LT	55° 55′ N, 21° 0′ E, 5 m	6	SMPS	Ulevicius et al. (2010)
SMEAR II	SMR	FI	61° 51′ N, 24° 17′ E, 181 m		DMPS	Hari and Kulmala (2005)
Vavihill	VHL	SE	56° 1′ N, 13° 9′ E, 172 m		DMPS	Kristensson et al. (2008)
Central Europe						
Bösel	BOE	DE	53° N, 7° 57′ E, 16 m		SMPS	Birmili et al. (2009a)
K-Puszta	KPO	HU	46° 58′ N, 19° 33′ E, 125 m	1	DMPS	Kiss et al. (2002)
Melpitz	MPZ	DE	51° 32′ N, 12° 54′ E, 87 m		DMPS	Engler et al. (2007)
Kosetice	OBK	CZ	49° 35′ N, 15° 5′ E, 534 m	1	SMPS	Červenková and Váňa (2010)
Hohenpeissenberg	HPB	DE	47° 48′ N, 11° E, 988 m	1	SMPS	Birmili et al. (2003)
Waldhof	WAL	DE	52° 31′ N, 10° 46′ E, 70 m		SMPS	Birmili et al. (2009a)
Western Europe						
Cabauw	CBW	NL	51° 18′ N, 4° 55′ E, 60 m	3	SMPS	Russchenberg et al. (2005)
Harwell	HWL	UK	51° 34′ N, 1° 19′ W, 60 m	3	SMPS	Charron et al. (2007)
Mace Head	MHD	IE	53° 19′ N, 9° 53′ W, 5 m	5	SMPS	Jennings et al. (1991)
Mediterranean						
Finokalia	FKL	GR	35° 20′ N, 25° 40′ E, 250 m	2	SMPS	Mihalopoulos et al. (1997)
JRC-Ispra	ISP	IT	45° 49′ N, 8° 38′ E, 209 m	3	DMPS	Gruening et al. (2009)
Arctic						
Zeppelin	ZEP	NO	78° 55′ N, 11° 54′ E, 474 m		DMPS	Ström et al. (2003)
			High altitude sites (over 1000 m a.s.l.)			
Western Europe						
Puy de Dôme	PDD	FR	45° 46′ N, 2° 57′ E, 1465 m	4	SMPS	Venzac et al. (2009)
Central Europe						
Schauinsland	SCH	DE	47° 55′ N, 7° 55′ E, 1210 m	1	SMPS	Birmili et al. (2009a)
Zugspitze	ZSF	DE	47° 25′ N, 10° 59′ E, 2650 m	4	SMPS	Birmili et al. (2009a)
Jungfraujoch	JFJ	CH	46° 32′ N, 7° 59′ E, 3580 m	2	SMPS	Jurányi et al. (2011)
Balkans						
BEO Moussala	BEO	BG	42° 10′ N, 23° 35′ E, 2971 m		SMPS	Nojarov et al. (2009)
Mediterranean						
Monte Cimone	CMN	IT	44° 11′ N, 10° 41′ E, 2165 m	4	DMPS	Marinoni et al. (2008)

[a] Station representativeness classification from Henne et al., (2010) (if available):
(1) Rural; (2) Mostly remote; (3) Agglomeration; (4) Weakly influenced; (5) Generally remote; (6) Weakly influenced, generally remote

[b] Station was moved in summer 2009 to location 58 ◦230 N 8◦150 E, 219 m a.s.l.

2.2. *Spatial distribution*

Physical and chemical properties of aerosol particles can change according to their vertical and horizontal variations. The horizontal variability is high because of the relatively various lifetime of the aerosol (of the order of a few days to about a few weeks) in the lower layers of the atmosphere. Indeed, the sources are unequally distributed on the globe and different atmospheric processes lead to a transport to more or less long distances from the source. Thus, the aerosol particles are subjected, depending on their size and weight, to deposition by sedimentation or diffusion (dry deposit) or, during a precipitation phenomenon, to leaching (wet deposition). The vertical variability of the aerosol are also important, and determined by the thermodynamic structure of the atmosphere.

The atmosphere can be divided into different layers according to changes in flow regime or temperature. Thus, we distinguish the troposphere (from 0 to 15 km approximately), the stratosphere (from 15 to 50 km), the mesosphere (from 50 to 85 km), the thermosphere (from 80 to 500 km) and the exosphere beyond these layers. 80% of the mass of the atmosphere is found in the troposphere thus containing the majority of aerosol particles (J. H. Seinfeld and Pandis, 2006). This latter is divided into two distinct sub-layers: the Boundary Layer (BL), which is close to the ground and therefore directly influenced by the Earth's surface, and responds to surface forcing within a timescale of an hour or less (Stull, 1988), and the free troposphere (FT) above. The BL develops during daytime in response to convection, and is therefore usually referred to as a convective mixed layer. Slightly before sunset, when turbulence decreases, the formerly mixed layer is replaced by the so-called residual layer (RL), which initial properties (in terms of both mean state variables and concentrations) are similar to those of the mixed layer. As the night advances, the lower part of the residual layer which is in contact with the ground is progressively transformed into a stable BL (Figure 2.4).

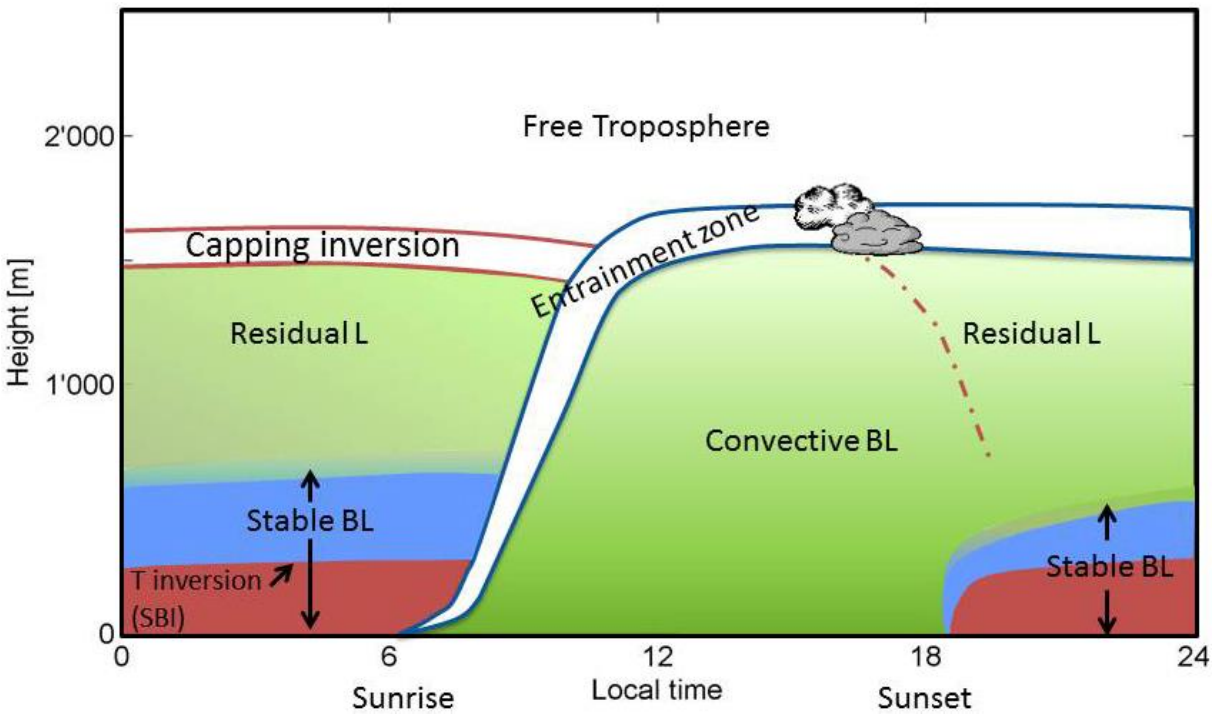

Figure 2. 4. Schematization of the atmospheric mixing layer throughout the day (adapted from Stull, (1988)).

BL aerosols can be transported into the FT when they cross the temperature inversion at the top of the BL, either due to turbulences in the inversion layer, strong thermal convection or cold fronts over polluted areas (Hov and Flatøy, 1997). Other sources of particles in the FT can be nucleation of low-volatility gas-phase components into new particle clusters and their growth to new particles of larger sizes. As evidenced in earlier studies (Moorthy et al., 2011; Rose et al., 2013; Kompalli et al., 2014) new particle formation (NPF) may have specific characteristics at high altitudes. Once in the FT, aerosol particles have a longer residence time due to the lower frequency at which they are scavenged by clouds and precipitation, allowing them to be transported in the atmosphere for several days (Freney et al., 2016) increasing their impact on the climate. Figure 2.5 shows that the lifetime of particles in the atmosphere is more or less extended depending on their involvement in different layers of the atmosphere, and it can reach several weeks in the FT. Also, aerosol particles transported into the FT or formed in the FT can be re-injected again into BL, affecting the air quality far from the source region (Mckendry et al., 2001; Timonen et al., 2013). For these reasons, it is important to characterize the properties of FT aerosols. Additionally, these measurements are needed to validate and improve numerical meso-scale or global scale transport models (Martin et al., 2004). A number of studies focused on FT conditions from ground based high altitude sites (Venzac et al., 2009;

Herrmann et al., 2015; Freney et al., 2016) and from ATR-42 aircraft (Crumeyrolle et al., 2012; Rose et al., 2015a), providing information on aerosol physical and chemical properties in this part of the atmosphere. Fröhlich et al., (2015) and Freney et al., (2016) showed that the FT air masses are strongly influenced by injections from BL, however the number of studies comparing the transport from the boundary layer to the FT over long periods of time are rare.

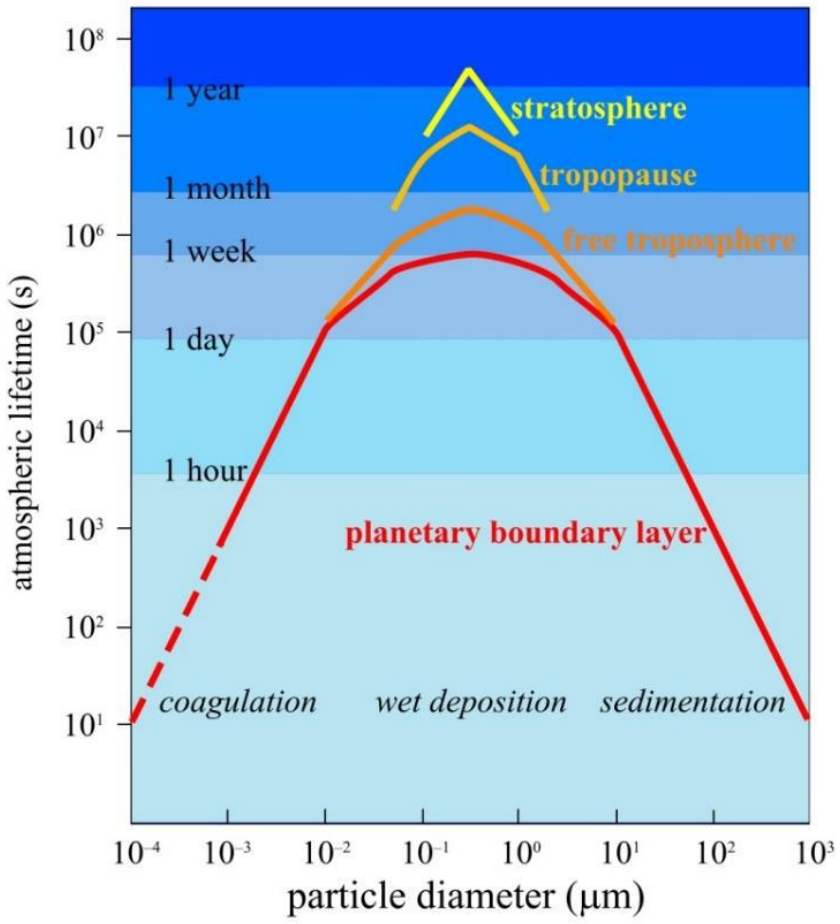

Figure 2. 5. Atmospheric lifetime of different size particles at different levels of the atmosphere (Lagzi et al., 2014).

The BL height (BLH) varies daily and seasonally according to surface energy balance, and the top of the BL is usually found between 500 m over the sea and 2 km above land. However, as illustrated by Herrmann et al., (2015), the determination of the BLH is complex due to the lack of a commonly accepted technique to measure it. This evaluation is even more challenging over complex mountainous terrain, above which the atmospheric structure becomes more complicated (De Wekker and Kossmann, 2015). For this the real forced convection from the local topography needs

to be taken into account. It is then possible to calculate the splitting height (SH) which corresponds to the height below which an air mass encountering an obstacle is going around it, and above which the air mass is overpassing it. Details of the method for calculating SH is described in Etling, (1989), (Eq. 2.1).

$$SH = H\,(1 - Fr) \tag{2.1}$$

H is the height difference between the summit and the foot of the mountain and Fr is the Froude number such as:

$$Fr = \frac{U_0}{N.H} \tag{2.2}$$

U_0 is the horizontal wind speed and N is the Brunt-Väisälä frequency such as:

$$N = \sqrt{\frac{g}{\theta_v} . \frac{\delta\theta_v}{\delta Z}} \tag{2.3}$$

θ_v is the potential virtual temperature and g is the acceleration of gravity (9.81 $m.s^{-2}$).

When BLH is higher than the altitude of summit, the station is always considered to be in the BL. This is especially the case for unstable conditions (Fr > 1), when the BLH always reaches the station after the air mass encounters the obstacle. For stable conditions (Fr < 1), two different situations are identified depending on SH. If the BLH is lower than SH, the stream will drift away from the obstacle, and the station will be in free tropospheric conditions. In contrast, for a BLH higher than SH, the air mass will be uplifted along the mountain slope, and the station will hence lay in the BL/AL (Table 2.3).

Table 2. 3. Classification of the air mass type (BL or FT) sampled at the station as a function of BLH and Splitting Height (SH).

	Comparison of station altitude, BLH and SH	**station conditions**
Unstable Conditions	BLH > station	BL
Stable Conditions	BLH > station	BL
	BLH < station & BLH > SH	BL
	BLH < station & BLH < SH	FT

In addition to pioneer methods based on vertical temperature profiles (Holzworth, 1964; Holtslag et al., 1990), several techniques have been developed to determine the BLH. Those include radio sounding system (Seibert et al., 2000), active remote sensing such as ceilometer, sodar and LIDAR (Emeis et al., 2004; Wiegner et al., 2006), in-situ measurements of trace gases, aerosol particles concentrations and wind direction from high altitude sites (Zellweger et al., 2003; Griffiths et al., 2014; Herrmann et al., 2015; Chambers et al., 2016 ; Moreno et al., 2017) as well as atmospheric models (Baars et al., 2008; Venzac et al., 2009). However, the majority of the abovementioned methods retrieve the height of the so-called aerosol layer (AL, also referred to as aerosol mixing layer in the literature), whose behavior with respect to the underlying topography can occasionally differ from the BLH (De Wekker and Kossmann, 2015 and references therein). Mostly during daytime, the AL can be assimilated to the BL, when aerosol particles are homogeneously mixed within the BL (De Wekker and Kossmann, 2015). Herrmann et al., (2015) compared three criteria for selecting free tropospheric conditions at the Jungfraujoch (JFJ) research station (Swiss Alps, 3580 m a.s.l.), and found that FT conditions prevail for 39% of the time (over 60% during winter and below 20% during summer). However, it was highlighted that the major difficulties in these studies is providing a robust selection of FT air masses.

Chapter 3: Sampling sites and analytical tools

3.1. Sampling sites

The atmospheric site of the Puy-de-Dôme (PUY) is located in the center of France (45°77 N; 2°96 E) and comprises two instrumented stations (Figure 3.1). The Puy-de-Dôme high altitude station (PUY, 1465 m), labeled Global Atmospheric Watch (GAW) station in 2015 and included in the European program ACTRIS2 (Aerosol, Cloud and Trace gases Research Infrastructure Network), allows a complete and continuous analysis of atmospheric constituents with climatic relevance (reactive trace gases and particulate phase). The PUY station is located on the first mountain range encountered by a dominant west wind and is one of the highest peaks of the Chaîne des Puy extending over 45 km north-south and only 3 to 4 Km of width. About 16 km east of the PUY station, a second site is located at the university campus Cézeaux (CZ, 420 m) mainly consists of remote sensing instruments. This site is aslo included as part of ACTRIS network.

The topography around the PUY station allows a virtual absence of valley wind unlike other stations located on larger mountain ranges. Due to the smaller deformations of the structure of the atmosphere at the approach of the PUY site, it is possible to study phenomena representative of the boundary layer (BL) and the free troposphere (FT). Studies have also shown that the Puy de Dôme station is generally representative of regional atmospheric conditions (Asmi et al., 2011; Henne et al., 2010), thus allowing the characterization of oceanic, Mediterranean, and continental air masses.

The station hosts a wide variety of instruments to characterize the aerosols, gas, and cloud properties. For instance, the long-term variation of the particle size distribution has been studied by Venzac et al., (2009), and the occurrence of the new particle formation (NPF) process was specifically investigated in several dedicated studies (Venzac et al., 2007; Boulon et al., 2011; Rose et al., 2015a). Filter measurements as well as online mass spectrometry analysis have been used to document the particles chemical composition (Freney et al., 2011; Bourcier et al., 2012; Freney et al., 2016) and aerosol-cloud interactions were also investigated from this station which offers favorable conditions for such analysis (Sellegri et al., 2003; Asmi et al., 2012; Guyot et al., 2015). The second site, Cézeaux, hereafter referred as CZ, is located on the University campus in Clermont-Ferrand (420 m a.s.l.), 16 km west from PUY.

Continuous measurement of routine meteorological parameters, as well as a Rayleigh-Mie-Raman Raymetrics LIDAR system are operated at CZ.

Figure 3. 1. **(Top)** The regional map of Clermont-Ferrand; **(bottom)** Zoom on Clermont-Ferrand city. The green house represents the CZ station, and the orange volcano represents the PUY station. (Adapted from Google Earth).

In addition to continuous long-term measurements at PUY site, a measurement campaign (winter and spring 2018) was carried out at Atmo Auvergne-Rhône-Alpes (AtmoAura's) station in Montferrand (urban site at Clermont-Ferrand).

In order to better analyse each of the properties defining the aerosol, numerous instruments are used at the PUY and AtmoAura's stations. In this PhD thesis (Chapter 3), we focus on: Scanning Mobility Particle Sizer (SMPS) and an GRIMM optical particle counter (OPC) (Burkart et al., 2010) for particle size distribution measurements, a Multi Angle Absorption Photometer (MAAP) and Aethalometer

(AE33) for absorption properties and aerosol equivalent black carbon (EBC) content and a time of flight aerosol chemical speciation monitor (TOF-ACSM) for aerosol particle chemical composition. Also, the LIDAR system at CZ station, is used to determine the vertical aerosol layer height (ALH).

In addition to aerosol properties, auxiliary measurements were used in the current study. Routine gas, i.e. carbon monoxide (CO), nitrogen oxides (NOx), radon-222 (^{222}Rn), and meteorological parameters, i.e. wind direction, wind speed, relatively humidity (RH), pressure (P), and temperature (T) are measured continuously throughout the year on the PUY site.

Measuring instruments dedicated to the study of aerosol particles are connected to a whole air inlet (WAI), with a 50% cut-off diameters of 30 µm. This allows the whole aerosol size distribution to be sampled, even in the presence of a cloud. Although, cloud events were excluded from our study, these inlets ensure that cloud droplets are evaporated in the WAI so that both interstitial and residual cloud residues are sampled (as if they had not been activated into cloud droplets)(Asmi et al., 2012).

3.2. Analytical tools

3.2.1 In-situ measurements

3.2.1.1 Particle size distribution

In order to cover the full range of aerosol sizes and to better define each of the modes characterizing atmospheric aerosol diversity (section 2.1.3), several instruments are used simultaneously.

3.2.1.1.1 Scanning Mobility Particle Sizer (SMPS)

Particle number size distributions in the range from 10 to 650 nm were measured using a custom-made scanning mobility particle sizer (SMPS), with a time resolution of 130 seconds. This instrument consists of a differential mobility analyser (DMA) as described by Villani et al., (2007), a CPC (TSI model 3010) for particle detection downstream of the DMA and a ^{63}Ni aerosol neutralizer, 95 MBq source. The DMA sheath flow rate is controlled using a blower in a closed-loop arrangement (Jokinen and Mäkelä, 1997). The SMPS has been intercompared with other European SMPS and DMPS systems in the framework of the European structure ACTRIS (Aerosols, Clouds and Trace gases Research Infrastructure Network) in March 2018, and satisfies all requirements for providing a reliable aerosol size distribution. In specific,

uncertainties of the measurements conducted in the frame of ACTRIS were reported to be lower than 10% for particle number size distributions in the 20 to 200 nm size range, while below and above this size range the discrepancies increase (Wiedensohler et al., 2012).

Three particle size distribution modes were previously identified by Venzac et al., (2009) using SMPS data at the PUY station. Hence, based on the aforementioned study, we define the nucleation mode concentration as the integrated concentrations of particles ranging from 10 nm to 20 nm, the Aitken mode concentration as the integrated concentrations of particles ranging from 40 nm to 80 nm and accumulation mode (100-300 nm) for aged particles. Particles having diameters from 20-40 nm and 80-100 nm are not included as they can either be nucleation or Aitken modes, and Aitken or accumulation modes, respectively.

3.2.1.1.2. Optical Particle Counter (OPC)

Particle number size distributions from 350 nm to 18 µm were measured using an optical particle counter (OPC, GRIMM 1.108) over a total of 16 size channels (Grimm 1.108). Whenever a particle passes the laser, the scatter signal is transmitted to a receiving diode. The received signal is associated with a size class according to its power. This size is calculated using a Mie calculation. It assumes particle shape and refractive index. Figure 3.2 shows the merged size distribution of GRIMM OPC measurements with those obtained from the SMPS over the year 2015. Merging these measurements allowed us to cover diameters ranging from 10 nm up to 18 µm, and therefore characterizing 4 particle size distribution modes (Nucleation, Aitken, Accumulation and Coarse).

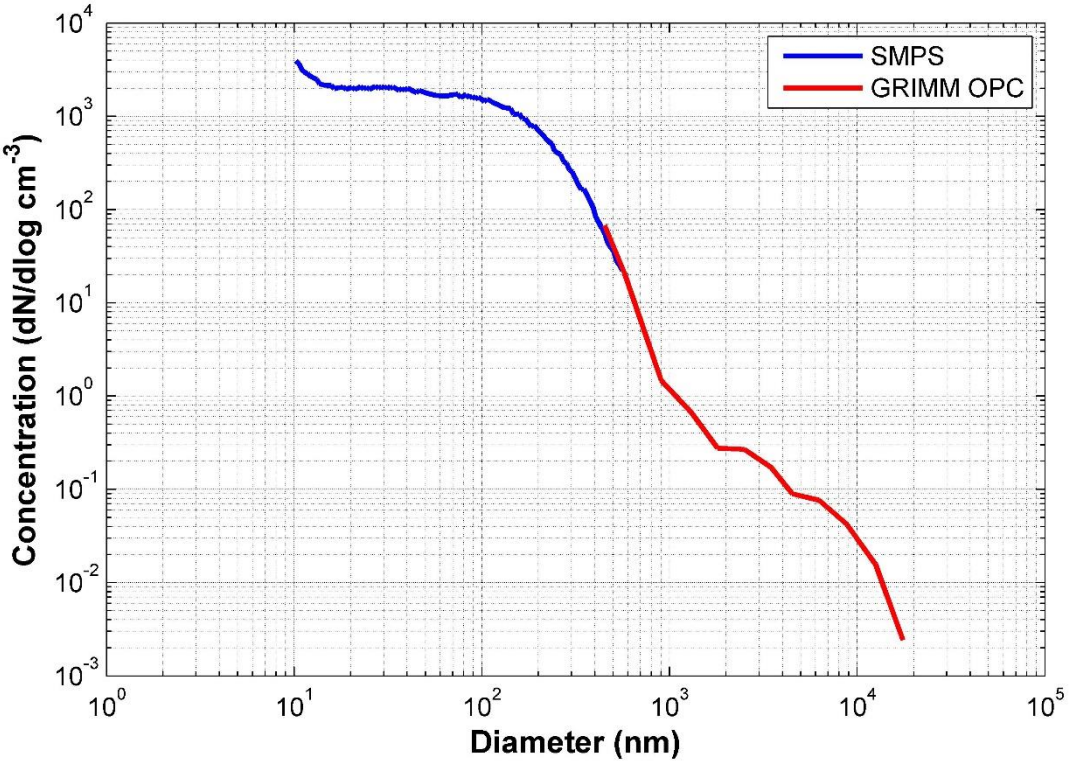

Figure 3. 2. Particle size distributions measured by the SMPS and GRIMM OPC.

3.2.1.2. Equivalent Black carbon (EBC) concentrations

Two measurement techniques were used to obtain information on Equivalent black carbon (EBC) concentrations.

3.2.1.2.1. Multi Angle Absorption Photometer (MAAP)

EBC concentrations were derived from particle absorption measurements conducted with a Multi Angle Absorption Photometer (MAAP 5012). Emitting a 670 nm laser beam, it measures the transmitted and backscattered radiation impacted by the particles on a filter that can be converted into an equivalent black carbon mass concentration (m_{EBC}). Uncertainties in the measurements were around 12% (Petzold and Schönlinner, 2004). The absorption coefficient σ_{abs} can be calculated from the m_{EBC} measured by the instrument and a specific absorption coefficient (Q_{EBC}=6.6 m^2/g) according to Eq. 3.1 (Müller et al., 2011). In addition, since the wavelength of the instrument given by the manufacturer is not exactly that emitted (637 nm instead of 670 nm), it is necessary to add a corrective factor to the measurements (1.05 according to Müller et al., (2011)).

$$\sigma_{abs} = m_{EBC} \cdot Q_{EBC} \cdot 1.05 \quad (3.1)$$

σ_{abs} is the absorption coefficient, m_{EBC} is the equivalent black carbon (EBC) mass concentration and Q_{EBC} is the specific absorption coefficient.

3.2.1.2.2. Aethalometer-33 (AE33)

Equivalent black carbon (EBC) concentrations are retrieved from real time measurements of aerosol absorption performed every minute by as seven-wavelength (370; 470; 525; 590; 660; 880 and 940 nm) Aethalometer (AE33, Magee Scientific Inc.). The instrument was equipped with a PM1 impactor inlet (BGI model SCC-0.732, Waltham, MA, USA) and sampled at 5 L/min. The AE33 principle is based on analyzing the aerosol by measuring the transmission of light through a filter tape acting as a reference area. The attenuation is then converted into an aerosol absorption coefficient σ_{aer} for each wavelength. The AE33 instrument uses two corrections in order to obtain this coefficient, the first is based on the Weingartner et al., (2003) algorithm to account for multiple scattering by the filter by applying a factor C = 1.57 (multiple scattering parameter) specific to the filter of the instrument. The second correction uses the "dual spot" technology to compensate the loading effect of the filter, all the characteristics of the instrument being developed in more detail in Drinovec et al., (2015). The EBC concentrations are then calculated by applying a specific mass absorption efficiency (MAE) on the absorption coefficient at 880 nm as follow:

$$EBC = \frac{b_{abs}}{MAE} \quad (3.2)$$

Were b_{abs} is the absorption coefficient as follow:

$$b_{abs} = \frac{b_{atn}}{C} \quad (3.3)$$

Were C is the multiple scattering parameter (C=1.57) and b_{atn} is the attenuation coefficient as follow:

$$b_{atn} = \frac{S.(\Delta ATN/100)}{F_{in}\Delta t} \quad (3.4)$$

Were S is the spot; t is the time; ATN is the optical attenuation and F_{in} is the flow as follow:

$$F_{in} = F_{out}.(1 - \xi) \quad (3.5)$$

$$ATN = -100.ln(I/I_0) \quad (3.6)$$

Were I_0 is the reference signal and I the spot signal

The MAEs for each wavelength are respectively 18.47; 14.54; 13.14; 11.58; 10.35; 7.7 and 7.19 m^2/g, from 370 to 940 nm.

Having multiple wavelengths allow for spectral analysis of the data which can be of importance for understanding the direct effect of EBC , climate forcing (IPCC, 2013) or mineral dust detection (Collaud Coen et al., 2004). This could be done through the determination of the single scattering albedo dependence on the wavelength, or source apportionment (Sandradewi et al., 2008).

3.2.1.3. Gas concentrations

3.2.1.3.1. Carbon monoxide (CO)

Carbon monoxide has been measured at PUY station using the Thermo Scientific™ Model 48i-TLE CO analyzer, which is based on the principle that CO absorbs infrared radiation at a wavelength of 4.6 microns. The infrared absorption is a nonlinear measurement technique; it is therefore required for the instrument electronics to transform the basic analyzer signal into a linear output. This instrument uses an exact calibration curve to accurately linearize the instrument output over any range up to a concentration of 1000 ppm.

3.2.1.3.2. Nitrogen oxides (NOX)

The concentration of nitrogen oxides (NOx) was measured using the NO_2 chemiluminescence technology with the Thermo Scientific™ Model 42i-TL TRACE Level NOx Analyzer. The Model 42i-TL is a unique chamber and unique

photomultiplier tube system, which alternates between the NO, NOx, and zero modes. Zero mode measurements are performed on a weekly basis to ensure the long term stability and low detection limits.

3.2.1.3.3. RADON-222

Radon-222 (^{222}Rn) has been measured at PUY station with the active deposit method (Biraud et al., 2000). The method is based on the measurement of ^{222}Rn short-lived daughters (^{218}Po, ^{214}Bi, ^{214}Po) (Polian et al., 1986) which are quickly absorbed onto aerosol particles. The accumulated aerosol particles are collected on a cellulose filter during one hour. Then the filter is automatically moved under an alpha detector coupled to a photomultiplier. Total α radioactive decay is measured every 10 min over the span of one hour. Uncertainties in the measurements can reach 10 to 20% (Polian et al., 1986). A disequilibrium factor of 1.15, like the one estimated by Schmidt, (1999) for a similar mountain station at Shauinsland, Germany, was used for correcting the data.

3.2.1.4. Non refractory - PM1 chemical concentrations

3.2.1.4.1. Time-of-Flight Aerosol Chemical Speciation Monitor (ToF- ACSM)

The ToF-ACSM (Aerodyne Inc., Billerica, MA, USA), presented in Figure 3.3 and described in detail in Fröhlich et al., (2015, 2013), is an instrument for real-time measurement of non-refractory submicron particles chemical composition. Like the Q-ACSM (N. L. A. R. Ng et al., 2010), the TOF-ACSM is based on the aerodyne AMS technology but in a compact design, relatively low cost, and (relative to the quadrupole counterpart), significantly improved mass resolution and detection limits. In comparison to the Q-ACSM, the TOF-ACSM uses a mass resolving power ($M/\Delta M$) of ≈500, and higher sensitivity by discriminating against the electronic noise, making it suitable for deployments at remote, typically cleaner, sites. Additionally, the TOF-ACSM can provide an m/z range up to 300. At the PUY station, a time resolution of 10 min was chosen.

Sampling of the ambient air is carried out through a sampling line oriented vertically on the instrument with a flow of 3 L/min. This line is equipped upstream of a $PM_{2.5}$ sampling head and a Silica gel based dryer to reduce air sampling relative humidity (RH). Particle loss in the sampling line was estimated to be less than 2% between 50 nm and 1 µm (the size range sampled by the ACSM aerodynamic lens system) through particle loss calculator developed by von der Weiden et al., (2009).

Background measurements are done every 30 seconds or depending on the switching set up, by using an automatic 3-way valve, which switches between aerosol sample and particle-free sample (using a HEPA filter). After passing through the aerodynamic lens and the PM1 critical orifice, the particles are concentrated in a beam and then introduced to chambers maintained under vacuum by 4-stage turbomolecular pump. They are then vaporized during their impact on an inverted cone-shaped surface, heated to 600 ° C, and the volatilized molecules are ionized by electronic impact (70 eV). These ions will be detected by TOF mass analyzer allowing the characterization of the different species by obtaining mass / charge spectra. The filtered air gas mass spectra are then subtracted from the unfiltered spectra in order to obtain an aerosol specific mass spectrum.

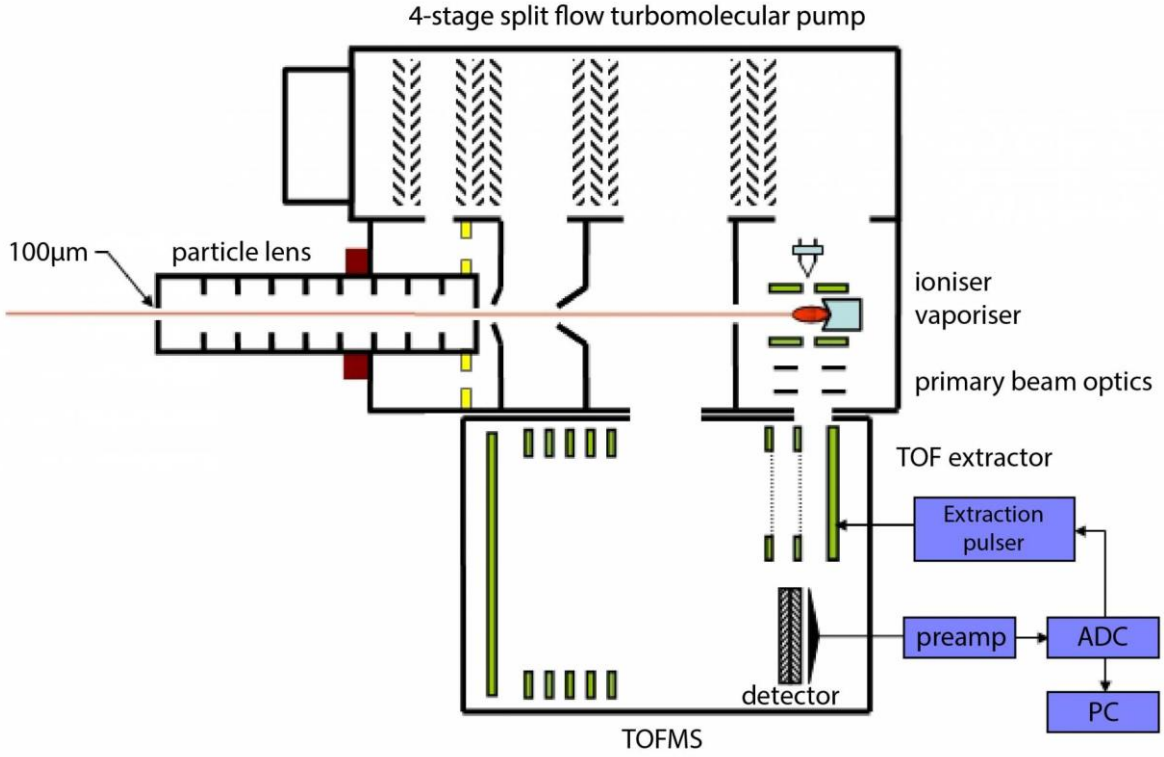

Figure 3. 3. ToF-ACSM schematic.

In order to separate the TOF-ACSM raw data into partial mass spectra for individual aerosol species, the standard assumptions was applied as described by Allan et al., (2004) and improved by Canagaratna et al., (2007). The resolved mass concentrations include organic, nitrate (NO_3), sulfate (SO_4), ammonium (NH_4) and chloride (Cl). At the PUY, Cl has low concentrations that are close to the detection limit of the instrument (max 0.07 µg/m^{-3} (Freney et al., 2011)) and hence they are omitted in

the following discussion. The allocation of these spectra provides the mass concentrations (Cs) of each species using the following equation:

$$C_s = \frac{CE}{T_{m/z}} \cdot \frac{10^{12}}{RIE_s} \cdot \frac{Q_{cal} G_{cal}}{RF_{NO3}} \cdot \frac{1}{Q.G} \sum_i IC_{s,i} \qquad (3.7)$$

where CE is the collection efficiency; $T_{m/z}$ the correction of the transmission efficiency of the TOF ions measured by monitoring the naphthalene peaks emitted continuously below the vaporization zone; RIE the relative ionization efficiency for each species compared to nitrate; RF_{NO3} the nitrate response factor; Q and G the volume flow and the gain of the multiplier during the measurement respectively, and their equivalents (Qcal and Gcal) obtained during the calibration of the RF_{NO3}; and ICs, the signal intensity of each fragment i of the species s.

RF calibrations are performed by establishing a sampling line of nitrate signal intensity measured by the ACSM in response to the injection of a known concentration of nitrate. The generation of monodisperse ammonium nitrate aerosols is by vaporization of an aqueous solution of NH_4NO_3 (Sigma-Aldrich,> 99%) at 5×10^{-3} $mol.L^{-1}$. These aerosol generated through an atomizer are then dried (desiccant consisting of silica gel) then filtered through a by-pass system used to manually regulate the concentration of aerosol, before being sent to a DMA (for differential mobility analyzer) which will allow to select particles with a diameter of 300 nm by means of their electric charge. These monodisperse aerosols are then sent in parallel to a particle counter (CPC Model 3788, TSI) and the ACSM. Particle size (300 nm) and particle number concentration (N_{CPC}) given by the CPC give access to the nitrate concentration (in $\mu g\ m^{-3}$), calculated using equation 3.8:

$$[NO_3] = N_{CPC}.S.V_{part} \cdot \rho \cdot \frac{M(NO_3)}{M(NH_4NO_3)} \qquad (3.8)$$

where S is the shape factor generally equal to 0.8; V_{part} the volume of a particle (in cm^3, considering the spherical particles); ρ the density of ammonium nitrate (1.72 $g\ cm^{-3}$); $M(NO_3)$ and $M(NH_4NO_3)$ the respective molar masses of nitrate and ammonium nitrate. The RF is then obtained by linear regression between the intensity of the NO_3 signal, which corresponds to the sum of the NO^+ (m/z 30) and $NO2^+$ (m /z 46) signals

measured by the ACSM, and the mass concentration obtained via CPC (Eq.2.2). The RIE of NH_4 is obtained in parallel, replacing in equation 3.7 the NO_3 by NH4 and dividing the slope obtained by linear regression between the intensity of the NH_4 signal (sum of m/z 15, 16 and 17) and $[NH_4]_{cpc}$ by the value of RF_{NO3}. The RIE values of SO_4 and Chl with respect to NO_3 are obtained in a manner similar to that of NH_4.

In this study two ToF-ACSM were used, the first is at PUY and the second at AtmoAura (Montferrand). The two ACSM was compared to a reference instrument of the European program ACTRIS in 2016.

The RF and RIE calibrations of the ACSM at PUY were performed on the sampling site. For the ACSM deployed in AtmoAura, calibrations could not be conducted at the sampling site, but in the laboratory, prior instrument deployment. The concentrations measured by the ACSM were determined by applying the RF and RIE values for each species reported in Table 3.1 These values correspond to all calibrations carried out until March 2018 for PUY and from January until May 2018 for AtmoAura.

Table 3. 1. RF and RIE calibration values used for PUY and AtmoAura's ACSM measurements.

	$RF(NO_3)$ $x10^{-11}$	RIE (OM)	RIE (SO_4)	RIE (NO_3)	RIE (NH_4)	RIE (chl)
PUY	2	1.4	1.2	1.1	3.5	1.3
AtmoAura	1.63	1.4	1.08	1.05	3.4	1.3

In order to correct the TOF-ACSM data for particle losses due to non-spherical particles or as a result of particle bounce off the vaporizer, we apply a composition-dependent collection efficiency (CDCE) factor to all aerosol species (Middlebrook et al., 2012). In this study, the ammonium nitrate mass fraction (ANMF) was always less than 0.4, for this a constant CDCE of 0.45 was applied to the data. Once this factor was applied, the TOF-ACSM mass concentrations were converted to volume concentrations using densities of 1.75 $g.cm^{-3}$ for inorganic species, and 1.3 $g.cm^{-3}$ for organic species. The TOF-ACSM volume concentration was compared with the volume concentration measured by the SMPS, sampling behind the same inlet (Figure 3.4).

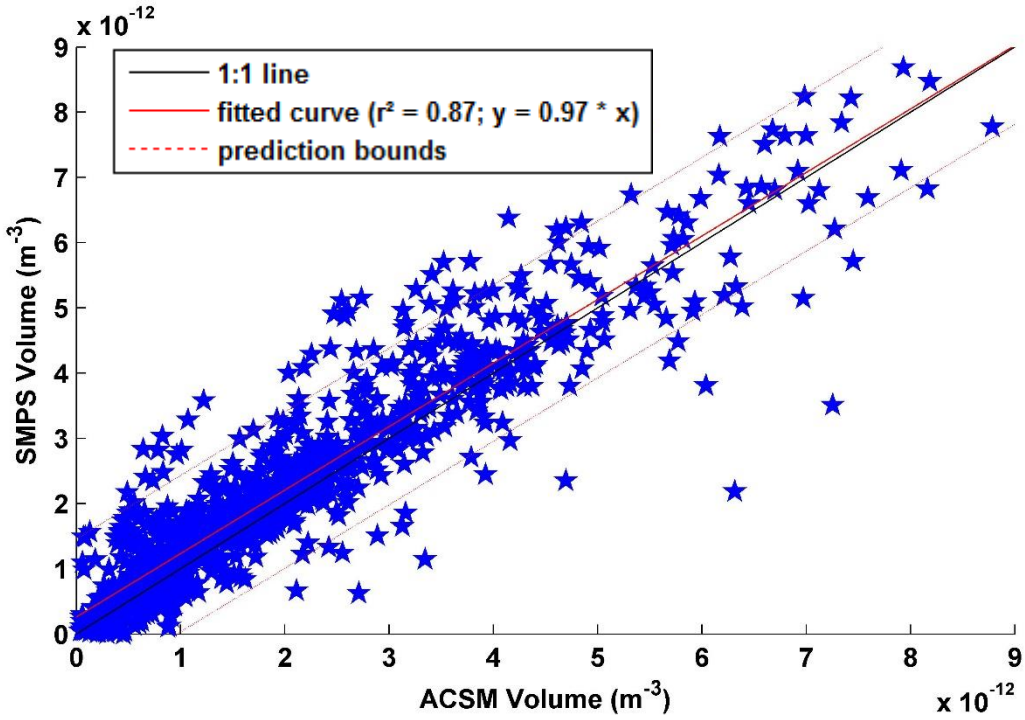

Figure 3. 4. Scatter plot between ACSM volume and SMPS volume.

3.2.1.4.2. Positive Matrix Factorization (PMF)

Positive Matrix Factorization (PMF) (Paatero, 1997; Paatero and Tapper, 1994) is a well-established program to solve receptor-only models and is used in the determination of the sources when the profile of the sources are poorly known. The fundamental principle of receptor modeling is that mass storage can be assumed and a mass balance analysis can be used to identify and allocate sources of suspended particulate matter in the atmosphere (Hopke, 2003).

PMF is a multivariate factor analysis tool that decomposes a matrix of measured data into two matrices: factor contributions (Time series) and factor profiles (Mass spectra). In PMF, the mass balance equation is as follows:

$$X = G.F + E \qquad (3.9)$$

$$x_{i,j} = \sum_{k=1}^{p} g_{i,k} \cdot f_{k,j} + e_{i,j} \qquad (3.10)$$

Where i and j refer to row and column indices in the matrix, respectively, k is the number of factors in the solution. This number is determined formally by the user (Figure 3.5). x_{ij} is an element of the *mxn* matrix X of measured data elements to be fit. In AMS data, the m rows of X are ensemble average mass spectra (MS) of typically tens of thousands of particles measured over each averaging period (typically 5 min) and the n columns of X are the time series (TS) of each m/z sampled. g_{ij} is an element of the *mxp* matrix G whose columns are the factor TS, f_{ij} is an element of the pxn matrix F whose rows are the factor profiles (MS), and e_{ij} is an element of the *mxn* matrix E of residuals not fit by the model for each experimental data point (E=X−GF). Both features lay the foundation of making the link between the mathematical solution and the processes of the real world possible. In practice, sources are better separated and positive scores and loadings are physically meaningful (Huang et al., 1999). PMF ignores negative entries throughout G and F. This constraint makes the PMF algorithm particularly suitable when mass concentrations must always be positive. The PMF can be solved by two common programs, PMF2 (Paatero, 2007) and multilinear engine-2 (ME-2; (Paatero, 1999)). In this study PMF algorithm was solved using the ME-2 and the Source Finder toolkit (SoFi v.6.395; (Canonaco et al., 2013)) was used to configure the PMF model and for post analysis. The SoFi was developed at PSI in order to facilitate the testing of different rotational techniques available within the ME-2 engine by providing a priori factor profiles for some or all of the expected factors.

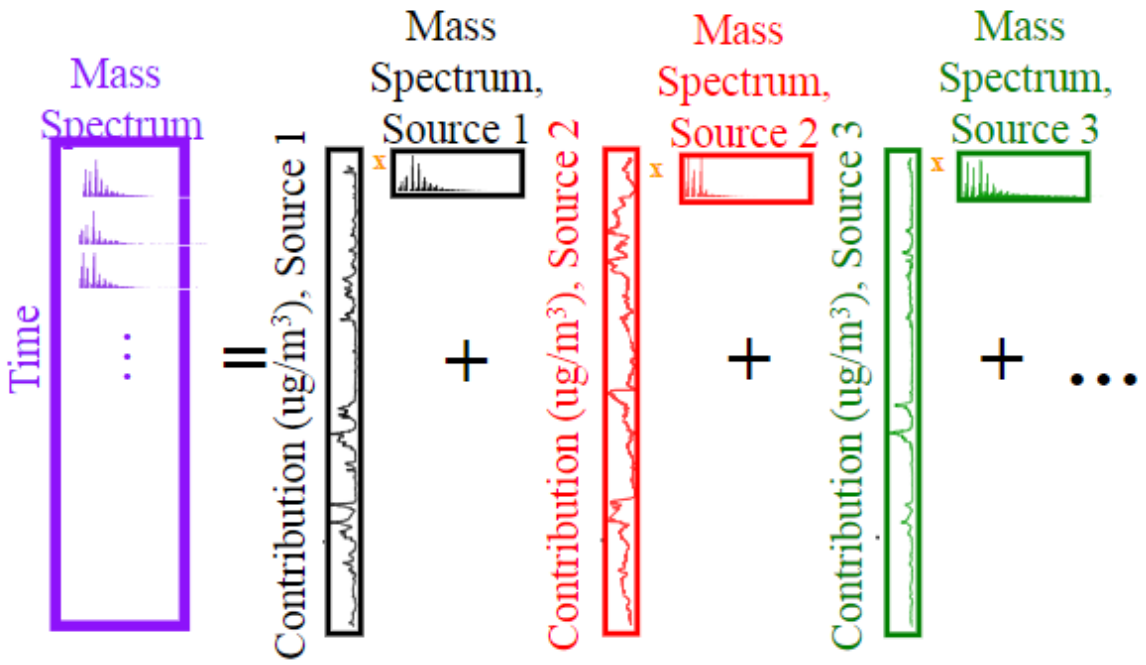

Figure 3. 5. PMF principle applied to OM (Adapted from Ulbrich et al., (2009).

However for ME-2 solver, the entries in G and F are fit using a least squares algorithm that iteratively minimizes the quantity Q^m, defined as the sum of the squared residuals weighted by their respective uncertainties, where the uncertainty may contain the measurement and model uncertainty:

$$Q^m = \sum_{i=1}^{m}\sum_{=1}^{n}\left(\frac{e_{ij}}{\sigma_{ij}}\right)^2 \qquad (3.11)$$

Where σ_{ij} are the measurement uncertainties for the input points ij. The Q^m is normalized by the degree of freedom of the model solution (Q_{exp}), then this normalization is used as an indicator for the solution reliability. Q/Q_{exp} value of 1 is expected if the model could entirely explain the variability and all uncertainties of the measured data. In case of known factors, a reference factor profiles, as a constraints, could be imposed on the factors solution as inputs. Therefore an 'a value' ranging from 0 (no degree of freedom) up to 1 (totally unconstrained) can be applied to those constraints.

3.2.2. Remote Sensing

3.2.2.1. LIDAR

The Light Detection and Ranging (LIDAR) is an active remote sensing instrument mainly composed of a transmitting part (laser) and a receiving part (telescope) (Figure 3.6). The pulsed emitted laser beam is absorbed and scattered in all directions by the molecules and particles encountered, and the backscattered signal is then received by a telescope. The time taken from transmission to reception provides the elevation of each of the backscattered signals. In the past, the first atmospheric LIDAR applications were dedicated to the detection of cloud altitude. Atmospheric LIDARs are now widely used for the detection of the vertical distribution of aerosol in the atmosphere (elastic signal), the distribution of water vapor or gaseous constituents (such as nitrogen dioxide and ozone from inelastic signals) but also wind (LIDAR Doppler) and temperature measurements.

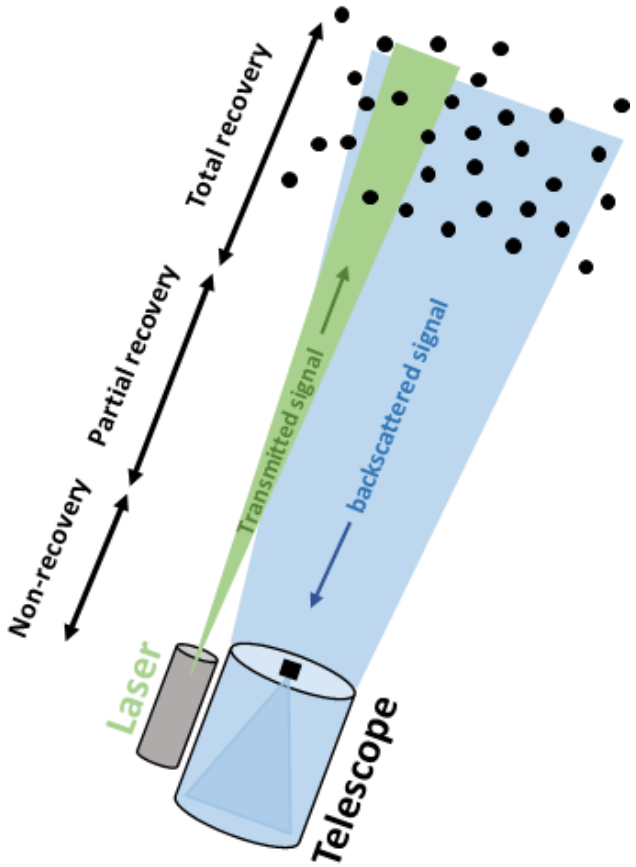

Figure 3. 6. Schematic illustration of a LIDAR

The LIDAR used in the present work is located on the roof of the OPGC (Observatoire de Physique du Globe de Clermont-Ferrand) on the Cézeaux station (Clermont-Ferrand) (Figure 3.7). It is a Rayleigh-Mie and Raman LIDAR allowing both information on aerosols (Rayleigh and Mie scattering), clouds (Mie scattering) and N2 and H2O gases (Raman scattering). The instrument includes a laser type Quantel CFR-400 emitting at 355 nm and a 400 mm Cassegrain telescope. An optical box is dedicated to the splitting of the receiving laser light in 4 different channels (2 elastic channels in parallel and cross polarization, and 2 inelastic channels for nitrogen and water vapor Raman scattering) (Papayannis et al., 2005). Vertical profiles of volume backscatter coefficients, extinction coefficients, and depolarization ratio are retrieved with a time resolution of 10 min. The system is in operation in the framework of the ACTRIS network (Aerosols, Clouds, and Trace gases Research Infrastructure Network). More details on the instrument can be found in the study reported by Freville et al., (2015).

Figure 3. 7. Optical part of the LIDAR on the roof of Clermont-Ferrand University (Freville et al., 2015).

The amount of backscattered light is described by the LIDAR equation:

$$P(R) = \frac{E_0 . C . O(R)}{R^2} \beta(R) . e^{\int_0^R -2\alpha(r)dr} \quad (3.12)$$

with P(R) the backscattered power at a distance R from the LIDAR, E_0 the transmitted laser energy, C the LIDAR constant describing the efficiency of the optical and detection system, O (R) the overlap function representing the beam portion laser in the field of view of the telescope at the distance R. β(R) and α(R) represent the coefficients of backscattering and extinction, sum of the molecular and particulate contributions, respectively.

It is also important to note that due to the biaxial configuration of the LIDAR system (the telescope optical axis and the laser beam axis are separated from 300 mm), the laser beam doesn't overlaps completely the field of view of the telescope below 1000 m (Chauvigné PhD thesis). An overlap correction must be applied to process the measurement data when the overlap is not full. Many methods exist to estimate this overlap function as ray tracing calculation or horizontal LIDAR measurements assuming that the atmosphere is homogeneous and that the alignment of the system remains the same horizontally and vertically (no deformation of the telescope).

3.2.2.2. Aerosol layer height

LIDAR profiles are specifically targeted to evaluate the aerosol layer height (ALH) (section 2.2). The ALH is essential to better understand the measurements made at Puy de Dôme. The estimation of ALH is based on the gradient in aerosol concentrations observed at the top of the AL, which coincides with a sharp change in the return signal from LIDAR. Different LIDAR techniques have been developed to identify the top of the ALH such as the gradient method (FLAMANT et al., 1997; Menut et al., 1999), the variance method (Piironen and Eloranta, 1995) and the WCT method (Wavelet Covariance Technique, (Brooks, 2003)). Following earlier work by Baars et al., (2008), we applied the Wavelet Covariance Technique (WCT) method, reported as a robust technique that can handle very different aerosol situations during all seasons of the year.

The WCT uses the covariance transform of the Haar function (Brooks, 2003) as follows:

$$WCT_f(a,b) = \frac{1}{a}\int_{z_b}^{z_t} f(z).\, h\left(\frac{z-b}{a}\right) dz \qquad (3.13)$$

With

$$h\left(\frac{z-b}{a}\right) = \begin{cases} +1, & b - \frac{a}{2} \le z \le b \\ -1, & b \le z \le b + \frac{a}{2} \\ 0, & elsewhere \end{cases} \qquad (3.14)$$

where f(z) is the LIDAR signal corrected with z^2, with z being the altitude, z_b and z_t are the lower and upper limits of the LIDAR signal, respectively, a is the extent of the step function. a was set to 12 Δz in the present work, as recommended by Baars et al., (2008), where Δz = 7.5 m is the spatial resolution of the LIDAR.

Equation (3.14) was applied to all LIDAR profiles with a time resolution of 10 minutes and the ALH was determined in clear sky conditions as the maximum of the WCT_f function. These calculations were made under the assumptions that 1) topography make a small deformation of the ALH at the location where the LIDAR measurements take place and 2) aerosol particles are homogeneously mixed within the AL. These hypothesizes had already been tested by Boulon et al., (2011). Indeed, some of the work reported in this paper was devoted to the validation of the ALH estimation at PUY derived from LIDAR measurements by equivalent potential temperature calculations (Te) conducted at the PUY and an intermediate altitude station (660 m) located near the PUY. The results of this study show that when the LIDAR indicates that the PUY is in the ALH, the Te calculated at the two sites are comparable (with computational uncertainties) and have strongly correlated evolutions, suggesting that the two sites are well located in the same atmospheric layer. On the contrary, when LIDAR indicates that the PUY is above the ALH, the calculated Te at the two sites have both different values and evolutions, suggesting in this case that the two sites are in two different atmospheric layers.

3.2.3. Models

3.2.3.1. ECMWF-ERA-Interim and LACYTRAJ

The boundary layer height (BLH_{ECMWF}) was extracted from the reanalysis ERA-Interim of the European Center for Medium –Range Weather Forecasts (ECMWF) model (Venzac et al., 2009; von Engeln and Teixeira, 2013). This technique is based on the "global method of Richardson" (Troen and Mahrt, 1986) which is used to measure the relative importance of the available convection potential energy and vertical wind shear by establishing the ratio between the atmospheric thermal turbulence produced by the vertical shear. To estimate BLH_{ECMWF} at the location of the PUY, we extracted the nearest grid point (45°75'N, 3°25'E) in a resolution of 0.25° x 0.25° grid.

However, it should be noted that the ECMWF model provides a BLH above sea level, but does not take into account the surface elevation field, therefore it is necessary to add a ground surface height above sea level to estimate a true BLH. Using the ERA interim model (https://software.ecmwf.int/wiki/display/CKB/ERA-Interim%3A+elevation+and+orography), this surface space layer height of the relevant grid square (45°75'N, 3°25'E) was calculated to be 620 ± 10m (Figure 3.8).

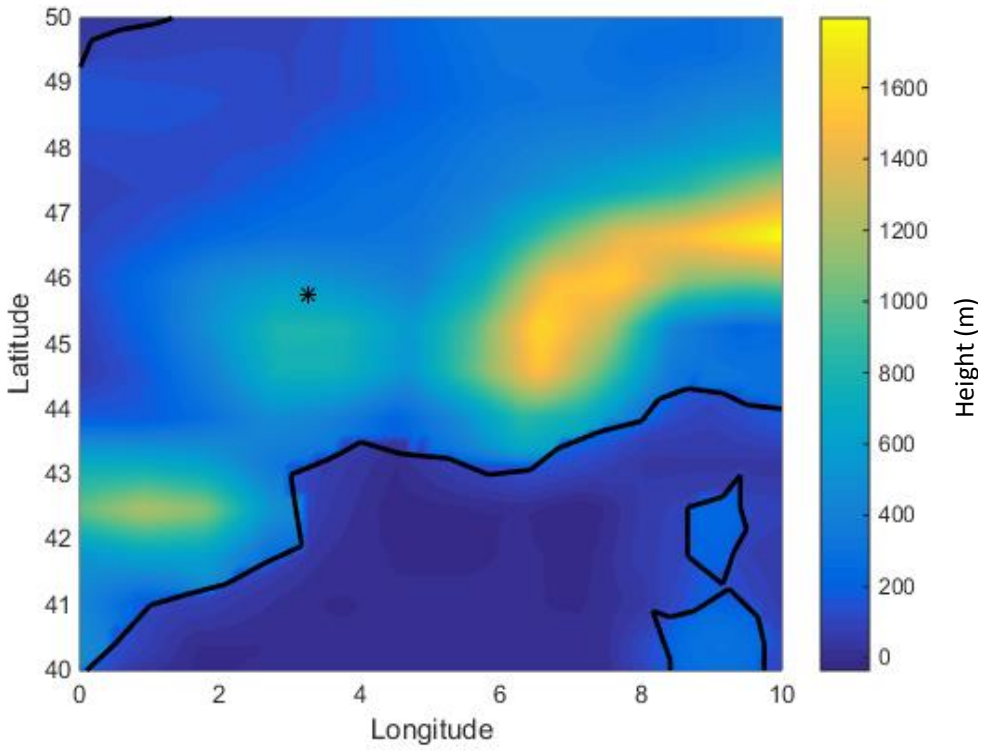

Figure 3. 8. Ground surface height of the nearest grid square to the PUY station (45°75'N, 3°25'E) (Black star) produced by the ERA-Interim reanalyses.

Back-trajectories have been computed using LACYTRAJ, a three-dimensional kinematic trajectory code (Clain et al., 2010). We use 3D wind fields produced by the ERA-Interim reanalyses with a horizontal resolution of 1° in latitude and longitude, and 37 vertical levels for the trajectory calculations. Each grid point is advected using a bilinear interpolation for horizontal wind fields and time and a log-linear interpolation on pressure level for the vertical wind field. A cluster of 100 trajectories starting from a box between 45.6 and 46°N and 2.7 and 3.1°E near 1465 m a.s.l is calculated, with a time resolution of 15 minutes, during 204 hours.

The altitude of each trajectory is compared with the calculated BLH (considering the ground surface height), interpolated in time and space from ECMWF ERA-Interim, along all trajectory points, in order to estimate the interaction of the air mass with the BL, i.e. the time spent of the sampled air mass in the FT since last contact with the BL.

3.2.3.2. HYSPLIT

The influence of air mass history on the occurrence of aerosol particles at the PUY site (1465 m), was studied using four days (96 hrs) air mass back trajectories computed with the Hybrid Single Particle Lagrangian Trajectory (HYSPLIT) model (Draxler and Rolph, 2003). Back-trajectories were calculated every three hours in 2015, 2016 and 2018. Air masses were further classified according to the maximum time spent in each sector as either continental (CONT), oceanic (OC), oceanic modified (OC_MOD), local (LOC) and Mediterranean (MED). As illustrated on Figure 3.9, the Local sector corresponds to the geographical area were most of air masses are around the PUY station (centered on the position 45°46′ N/2°57′E), while oceanic modified, oceanic, Mediterranean Sea, and continental types are related to the sectors 80 – 140°, 140 – 190°, 190 – 340° and 340 – 80°, respectively.

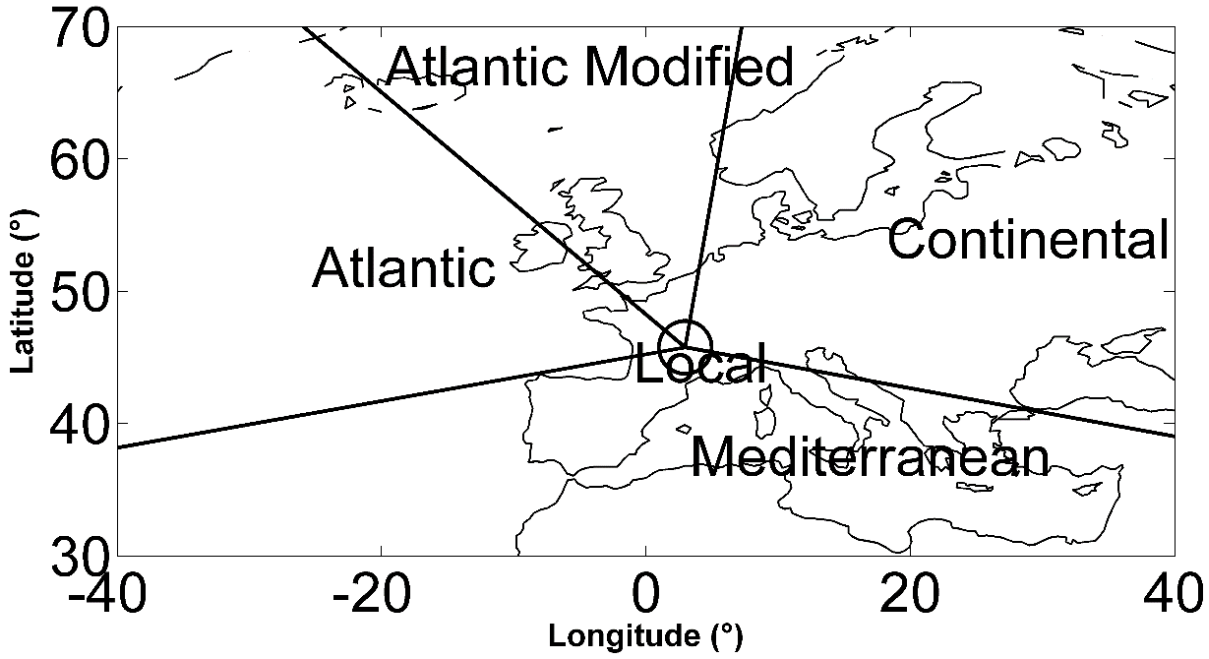

Figure 3. 9. Sector definitions for different air masses arriving at the PUY site.

Chapter 4: Results

4.1. Seasonal variation of aerosol size distribution data at the Puy de Dôme station with emphasis on the boundary layer/ free troposphere segregation (Farah et al., (2018) published in atmosphere)

In the mixing layer, aerosols are subjected to many processes that reduce their lifetime in the atmosphere such as sedimentation, coagulation or rain. Once injected into the FT, aerosol particles have a longer residence time due to the lower frequency at which they are scavenged by clouds and precipitation, allowing them to be transported in the atmosphere for several days increasing their impact on the climate. As illustrated by Herrmann et al., (2015), the determination of the BLH is complex due to the lack of a commonly accepted technique to measure it. This evaluation is even more challenging over complex mountainous terrain, above which the atmospheric structure becomes more complicated (De Wekker and Kossmann, 2015). As mentioned previously in section 2.1.3, several methods were used in the literature to segregate between BL/FT air masses. However, the major difficulties in this studies is providing a robust selection of FT air masses.

The objective of this first chapter of results is to compare four parameters for determining the BLH relatively to the high altitude Puy de Dôme station (PUY) during the year 2015. These parameters are based on LIDAR measurements using the wavelet covariance transform (WCT) method, BLH simulations from the ERA-Interim reanalysis of the European Center for Medium–Range Weather Forecasts (ECMWF) model, and in-situ measurements of BL tracers (NOx/CO and radon-222 (^{222}Rn)). Then, the four parameters are combined to reliably segregate the BL and FT air masses sampled at the PUY station. The segregation between BL and FT air masses is then used to investigate the differences in aerosol properties belonging to each of these atmospheric layers over the 12-month period.

4.1.1. Segregating between Boundary Layer (BL)/Aerosol Layer (AL) and FT air masses

Four different criteria were investigated in the present work to determine when the PUY station is sampling in the BL/AL or in the FT, including the analysis of LIDAR profiles, radon concentration, the ratio of NOx to CO concentrations and ECMWF outputs. In the present work, as in previous studies (example: (De Wekker and Kossmann, 2015)), we assimilate the ALH to the convective BLH during daytime, and to the RLH during nighttime. In order to harmonize the different data sets over the same time resolution, data were averaged over a time step of 3 hours. The data set was

further harmonized by only selecting data when all methods are available simultaneously; resulting in 1429 values (Figure 4.1.1). Specifically, this implies that only clear sky conditions will be discussed hereafter since the presence of clouds prevents the estimation of the ALH from LIDAR.

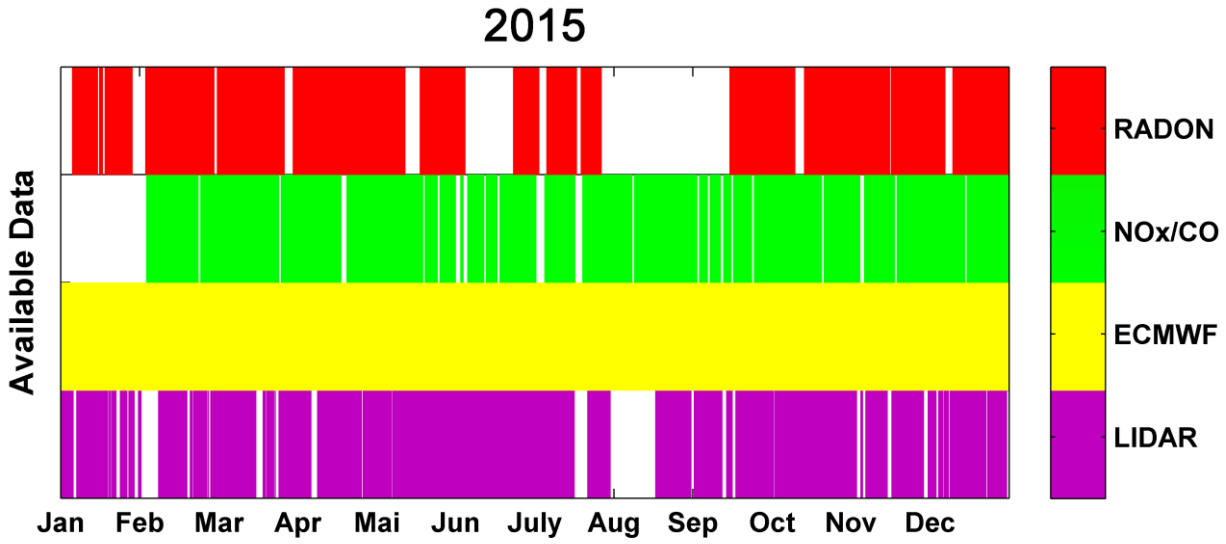

Figure 4.1. 1. Available data from the main instruments used in the determination of the boundary layer height. Red: Radon-222, Green: NOx/CO, Yellow: ECMWF, and Violet: LIDAR.

In the following sections, we will compare these four different criteria in order to segregate FT from "BL/AL" air masses.

4.1.1.1. Comparison between the Aerosol Layer Height from LIDAR Profiles and Boundary Layer Height Simulated with ECMWF

Figure 4.1.2a shows the 3h average diurnal variation of the ALH retrieved from the LIDAR profiles (ALH_{LIDAR}) for the four seasons separately (Winter: 1 January to 19 March, Spring: 20 March to 19 June, Summer: 20 June to 21 September, and Autumn: 22 September to 21 December) using data from 2015. The ALH_{LIDAR} does not show strong variations with the time of the day. The maximum of the ALH_{LIDAR} is reached during summer and spring (average 2000 m a.s.l., green and black) while in winter and autumn (red and blue), the average ALH_{LIDAR} never exceeds 1600 m. Lowest ALH_{LIDAR} are observed during night time, before 9 UTC, when the WCT most likely retrieves the height of the RL. These typical ALH diurnal and seasonal variations are similar to the ones previously reported for the PUY station (Figure 2 in Chauvigné et al., (2016)) and for the Leipzig station (Figures 7, 9 and 17 in Baars et al., (2008)). The LIDAR is located approximately 16 km to the east of the PUY station, that is, downwind of the North-

South mountain chain for the western prevailing winds. It is likely that there is a deformation of the upwind atmospheric structure due to the obstacle that the mountain chain represents and, hence, we expect that the ALH retrieved by the LIDAR is slightly increased compared to the surrounding flat and low altitude areas.

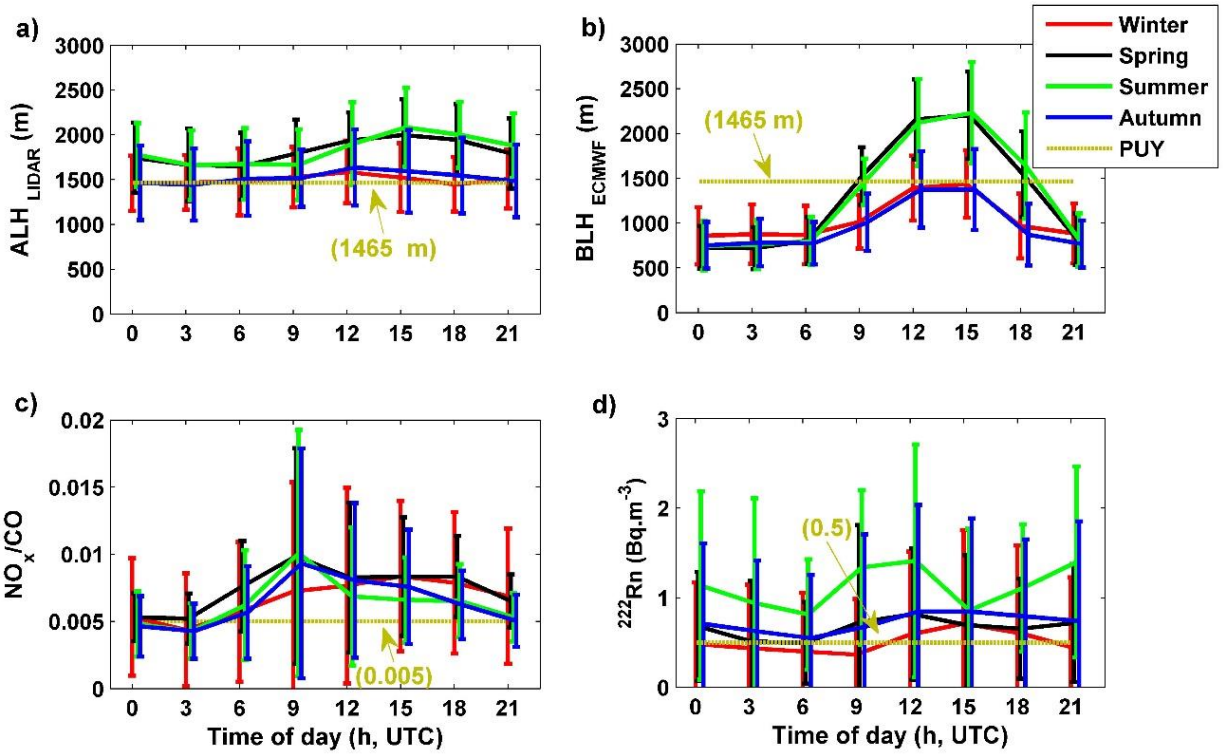

Figure 4.1. 2. The diurnal variation of the 3-h averaged parameters used to segregate between BL/AL and FT air masses as a function of the season: (a) ALH_{LIDAR}; (b) BLH_{ECMWF}; (c) NO_x/CO, and (d) ^{222}Rn. Variability within each season indicates the standard deviation.

BLH_{ECMWF} varies between 700 m a.s.l. at night in winter and 2200 m a.s.l. during the day in summer (Figure 4.1.2b). The model predicts that the PUY station is in the BL during the day (between 9 and 18 UTC) in summer and spring, with 3-h averaged BLH_{ECMWF} reaching a maximum of 2200 m a.s.l. In contrast, the model shows that the site is generally above the BL at all times during winter and autumn, and therefore considered to be in the FT. These results are in agreement with the study performed by Venzac et al., (2009) who reported that the PUY station was in the BL during the daytime during the warm seasons (spring and summer) and in the FT during nighttime during the cold seasons (autumn and winter). The ECMWF model is not taking into account the forced convection on the mountain chain. Hence, we expect that the model underpredicts the BLH above the grid square.

Significant differences are observed between ALH_{LIDAR} and BLH_{ECMWF} during nighttime (Figure 4.1.2a,b). This is related to the fact that the LIDAR retrieves RLH, while BLH_{ECMWF} instead corresponds to the height of the shallower stable nocturnal BL. On the contrary, ALH_{LIDAR} can be compared to the BLH_{ECMWF} over the daytime period (9 UTC-18 UTC), when the AL can be assimilated to the convective BL. As evidenced in Figure 4.1.3, the ALH_{LIDAR} and BLH_{ECMWF} correlate and agree well with each other (correlation coefficient Pr = 0.6 and linear regression slope 0.78). The value of the slope below 1 either indicates an overestimation of the ALH_{LIDAR} or an underestimation of the BLH_{ECMWF}. As mentioned above, the overestimation of the ALH_{LIDAR} could be due to the deformation of the upwind atmospheric structure between CZ and PUY stations. Indeed, the ECMWF model spatial resolution does not take into account local scale dynamical processes around the PUY mountain chain (due to a flattening effect over the surface mode grid).

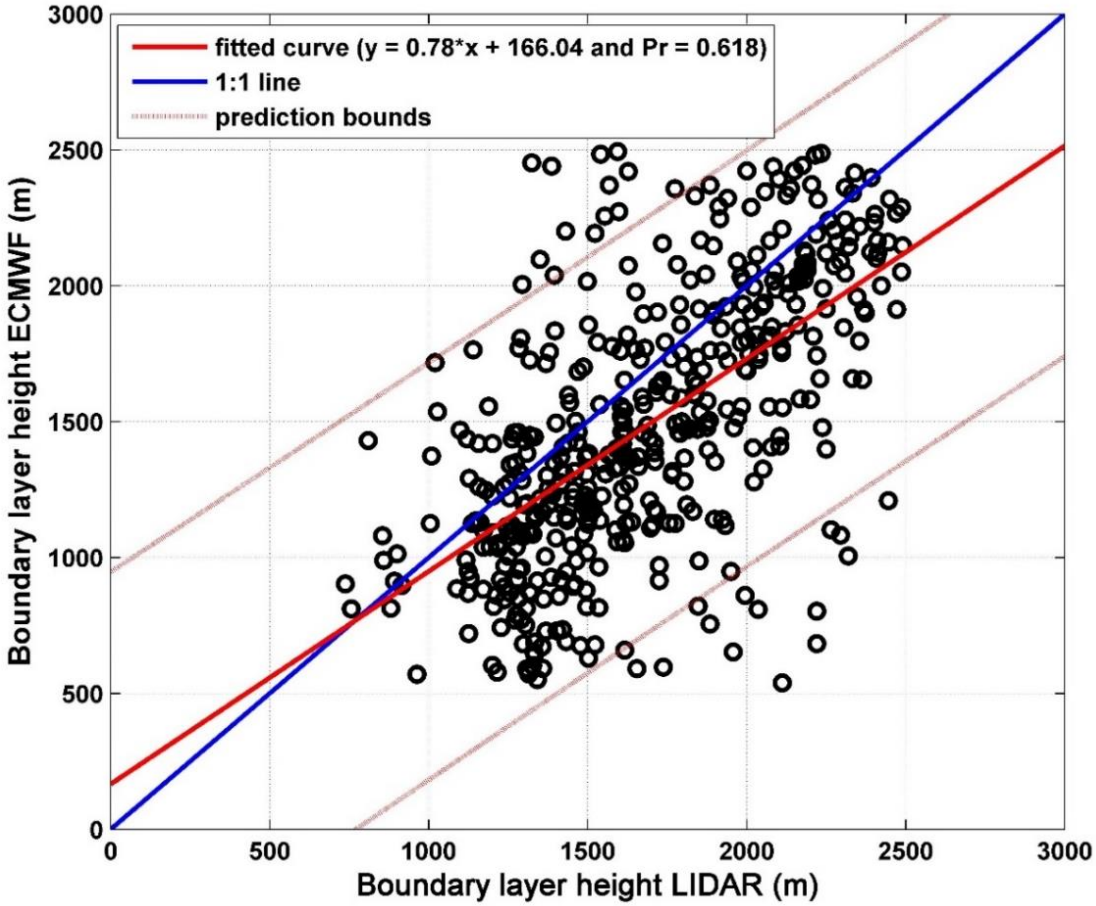

Figure 4.1. 3. The BLH from ECMWF versus LIDAR on the site 'CZ' between 9 and 18 UTC. Blue, red line, red dashed line, and Pr represent the first bisecting, the linear regression, the prediction bounds and the correlation coefficient, respectively.

In order to assess if the PUY station is within the BL/AL or in the FT, the real forced convection from the local topography needs to be taken into account. We calculate the splitting height (SH) for both WCT and ECMWF methods, which corresponds to the height below which an air mass encountering an obstacle is going around it, and above which the air mass is overpassing it. Details of the method for calculating SH is described in Etling, (1988), (Equation (4.1.1)).

$$SH = H\,(1 - Fr) \tag{4.1.1}$$

H is the height difference between the PUY station and the foot of the mountain and Fr is the Froude number (Etling, 1988; Venzac et al., 2009). When ALH/BLH are higher than the altitude of PUY, the station is always considered to be in the BL/AL. This is especially the case for unstable conditions ($Fr > 1$) when the BLH always reaches the PUY station after the air mass encounters the obstacle. For stable conditions ($Fr < 1$), two different situations are identified depending on SH. If the BLH/ALH is lower than SH, the stream will drift away from the obstacle, and the station will be in free tropospheric conditions. In contrast, for a BLH/ALH higher than SH, the air mass will be uplifted along the mountain slope, and the station will, hence, lay in the BL/AL (Table 4.1.1 SH data was calculated every three hours for 2015.

Table 4.1. 1. The classification of the air mass type (BL/AL or FT) sampled at the PUY station as a function of BLH/ALH, and Splitting Height (SH).

	Comparison of PUY Altitude, ALH/BLH and SH	PUY Conditions
Unstable Conditions	BLH/ALH > PUY	BL/AL
Stable Conditions	BLH/ALH > PUY	BL/AL
	BLH/ALH < PUY and BLH/ALH > SH	BL/AL
	BLH/ALH < PUY and BLH/ALH < SH	FT

4.1.1.2. NO_y/CO

NO_y/CO is an indicator of the "photochemical age" of an air mass that can be used to identify fresh pollution transported to high altitude sites from lower atmospheric layers (Herrmann et al., 2015; Zellweger et al., 2003). Higher values of NO_y/CO represent fresh pollution, while lower values correspond to regional air masses. Hence, this ratio usually shows lower values in the FT than in the AL (Herrmann et al., 2015). NO_y is defined as the sum of NO_x and its atmospheric oxidation products (that is, NO_z). In absence of NO_y measurements at PUY in 2015, we used NO_x data, since a good agreement between NO_y and NO_x is observed at this site based on measurements conducted in 2012 (Pr = 0.93 and slope = 1.11, Figure 4.1.4). We, therefore, consider that at the PUY, the NO_x measurements are a relatively good indicator of aged air masses. However, we are aware that NO_x measurements can often be influenced by more local emissions than NO_y, and care should be taken when interpreting these measurements.

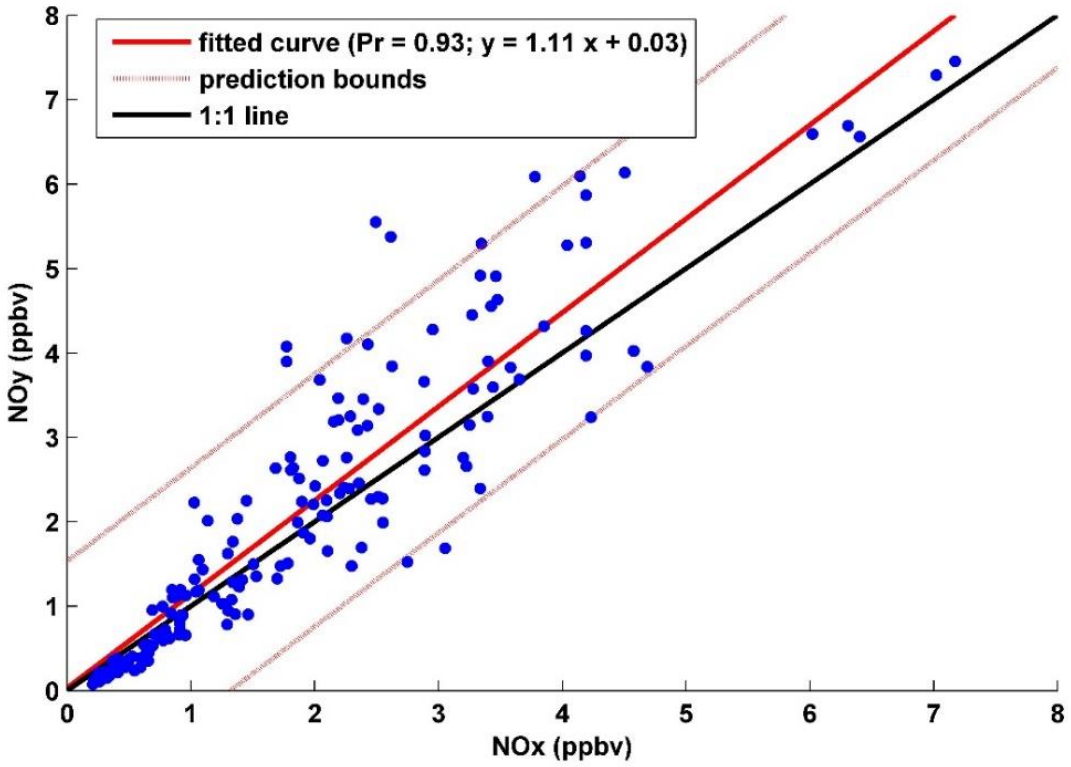

Figure 4.1. 4. Scatter plot between NOx and NOy concentrations.

For all seasons, we observe a clear diurnal variation with low values at night and high values during the day (Figure 4.1.2c). During daytime, an average NO_x/CO

maximum of 0.01 was observed for spring, summer, and autumn, at 9 UTC. For winter, a maximum of 0.08 was reported at 18 UTC.

In order to determine whether NO_x/CO is a good indicator for segregating between AL and FT conditions, we investigated the linear regression between NO_x/CO and the BLH_{ECMWF}. We found that both criteria are correlated at the 95% significance level (Pr = 0.54) with the following equation determined over the one-year dataset:

$$BLH_{ECMWF} = 1204 + 1.3 \times \left(\frac{1}{NO_x/CO}\right) \quad (4.1.2)$$

This equation allowed us to determine a threshold value of NO_x/CO = 0.005 above which the PUY station is considered to be in the FT (that is, for BLH_{ECMWF} > 1465 m).

However, we observe that the diurnal amplitude of the NO_x/CO ratio varies according to the season (Figure 4.1.2c). As a consequence, using a yearly threshold, the site is considered to be in the AL during the day (between 6 and 21 UTC) and in the FT in the night (from 21 to 6 UTC) for all seasons.

4.1.1.3. Radon-222 (^{222}Rn)

The last technique to evaluate AL/FT conditions is based on the level of ^{222}Rn measured at the PUY station. ^{222}Rn is naturally emitted from the land surface at a relatively constant rate (Szegvary et al., 2007; Zhang et al., 2011). Since ^{222}Rn is naturally emitted from land surfaces, it is often used as a mean to determine the level of contact of the air mass to the land surface. Hence, the lower the value of ^{222}Rn, the less contact the air mass has had with the AL. This criterion was recently used by Griffiths et al., (2014) and Herrmann et al., (2015) to study vertical mixing, based on sites at different altitudes (Chevillard et al., 2002) or on vertical profiles from aircraft (Guedalia et al., 1972; Lee and Larsen, 1997; Williams et al., 2010). It has also been used for the estimation of local to regional surface emissions of trace gases (van der Laan et al., 2014).

As shown in Figure 4.1.2d, the ^{222}Rn concentration does not show strong seasonal variations at PUY, with the exception for summer. As expected, the maximum values of the ^{222}Rn concentration are reached during summer (average 1.41 $Bq \cdot m^{-3}$), especially during daytime. This is likely caused by the increased vertical mixing of air masses during the summer transported to the PUY site. In winter, spring, and autumn,

the average ^{222}Rn concentrations never exceed 0.85 Bq $\cdot m^{-3}$. This can be a result of low vertical mixing height as observed from the LIDAR and ECMWF data, but also to a high fraction of air masses coming from the marine sectors (hence, naturally containing lower levels of ^{222}Rn within the BL).

In order to proceed with the identification of AL/FT air masses based on ^{222}Rn measurements, we followed the methodology introduced by Herrmann et al., (2015) for the JFJ site, which is based on the relationship between the ^{222}Rn levels and the number concentration of particles larger than 90 nm (N_{90}). As illustrated in Figure 4.1.5a, in a similar way as was done by Herrmann et al., (2015), we first investigated the variations of N_{90} as a function of the air mass residence time in the FT since last BL contact. As previously reported for the JFJ, we observed decreasing exponential trend of N_{90} with time since the last BL contact, but the parameters of the fit are, however, different from those obtained for the JFJ. Specifically, the threshold value below which N_{90} does not further decrease, that is, indicating FT background concentrations, is around 151 cm^{-3} at PUY, being almost 4 times higher than at JFJ (40 cm^{-3}). This is likely to be explained by a higher proximity to the BL/FT inversion when the PUY station is in the FT, compared to when the JFJ is in the FT. Indeed, (Chauvigné et al., 2016) pointed out that the aerosol concentrations are not homogeneously distributed over the vertical column within the FT, with a negative aerosol concentration gradient with altitude also within the FT. Plotting N_{90} as a function of the ^{222}Rn level (Figure 4.1.5b) also shows a clear decreasing exponential trend that indicates that ^{222}Rn is also a good indicator of the BL influence on the PUY station. Using a threshold of N_{90} = 151 cm^{-3} on Figure 4.1.5b leads to a threshold of ^{222}Rn = 0.5 Bq $\cdot m^{-3}$. This translates on Figure 4.1.2d to the PUY station being in the AL all the time during spring, summer, and autumn. For winter, the site would be in the FT before 10 am and after 8 pm.

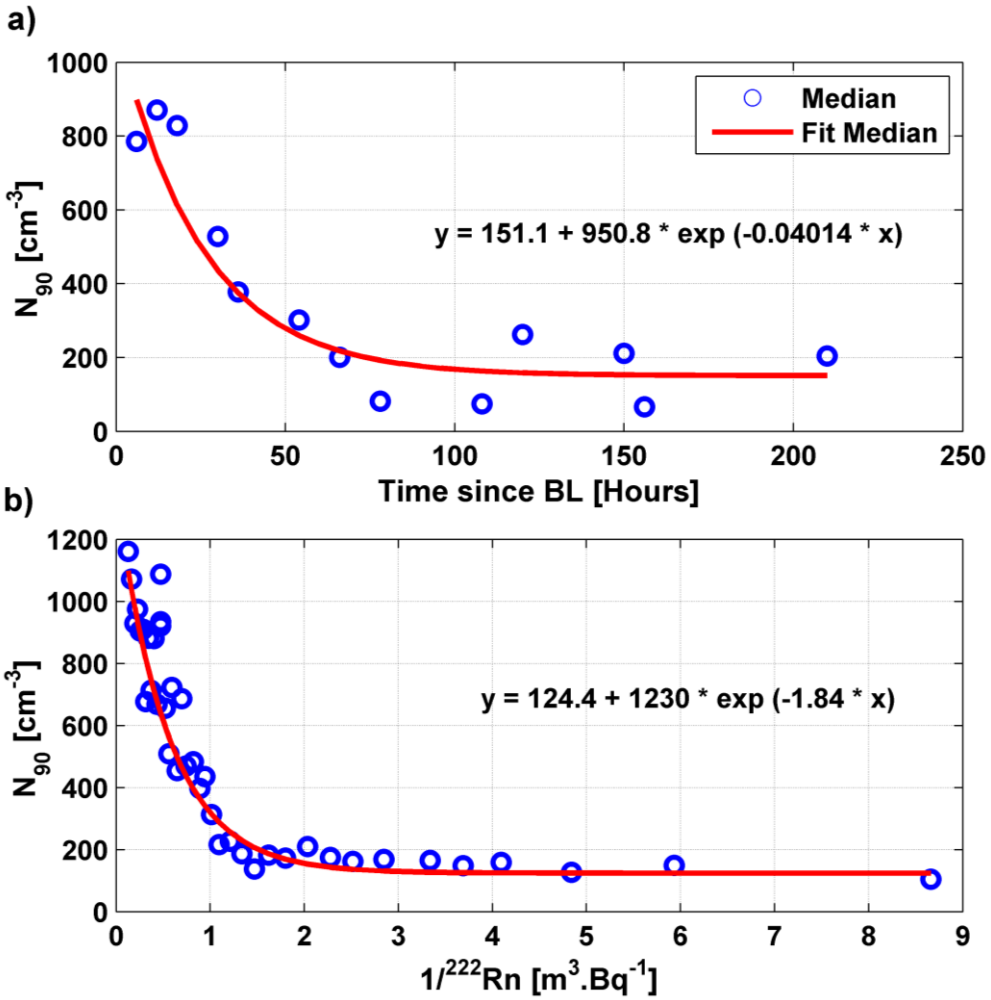

Figure 4.1. 5. The N_{90} (a) as a function of time since BL and (b) as a function of $1/^{222}Rn$ with fitted lines for the median.

4.1.1.4. Comparison of the Four Criteria

Each of the four methods used to segregate whether the PUY station lies within the BL/AL or in the FT has specific criteria, based on the vertical profile of aerosols retrieved from LIDAR, on the "global method of Richardson" from the ECMWF model, the "photochemical age" of an air mass from NO_x/CO and the estimation of local to regional surface emissions of trace gases from ^{222}Rn.

During daytime, the prediction of the BLH_{ECMWF} agrees relatively well with the ALH_{LIDAR}, but it should be noted that some uncertainties can be associated with these simulations due to forced convection and their horizontal distance from the site, as is discussed in Section 3.1.1 and shown in Figure 4.1.3 above. The NO_x/CO tracer would agree best with the prediction of the ECMWF in the sense that the diurnal variations of this indicator are clear between night and day, even though the seasonal variation

is not very evident. It may be that these two criteria agree because NO_x/CO values are decreased in the residual layer compared to the daytime BL. The ^{222}Rn tracer predicts that the site is in the BL with a similar trend than the ALH_{LIDAR}: the site is measured to be influenced by the BL most of the time except during winter and at night. Hence, ^{222}Rn would be more sensitive to the presence of the residual layer at night than the NO_x/CO indicator. However, using a single set of measurements such as NO_x/CO, WCT from LIDAR, ECMWF, or ^{222}Rn was not sufficient to classify air masses in the FT/(BL/AL) at the PUY station.

As all four criteria may have their own bias, a combined classification of these four criteria is proposed in order to increase the robustness of our methodology to determine if the PUY station is in the FT/(BL/AL).

4.1.1.5. Classification of Air Masses by Combining Four Criteria

Venzac et al., (2009) previously used temperature, relative humidity and the ECMWF model to separate BL and free tropospheric air masses at the PUY station. In this work, we present a more robust classification of air masses using a combination of four criteria (Figure 4.1.6a).

As mentioned above, WCT from LIDAR, NO_x/CO, and ^{222}Rn retrieve the ALH while the ECMWF retrieves the BLH. However, AL corresponds to the BL during the daytime and RL during nighttime. For the simplicity of this work, we use the terminology BL/RL for BL, AL, and RL altogether. Thus, this section aims at using all available criteria to classify air masses sampled at the PUY station as those from the FT/(BL/RL).

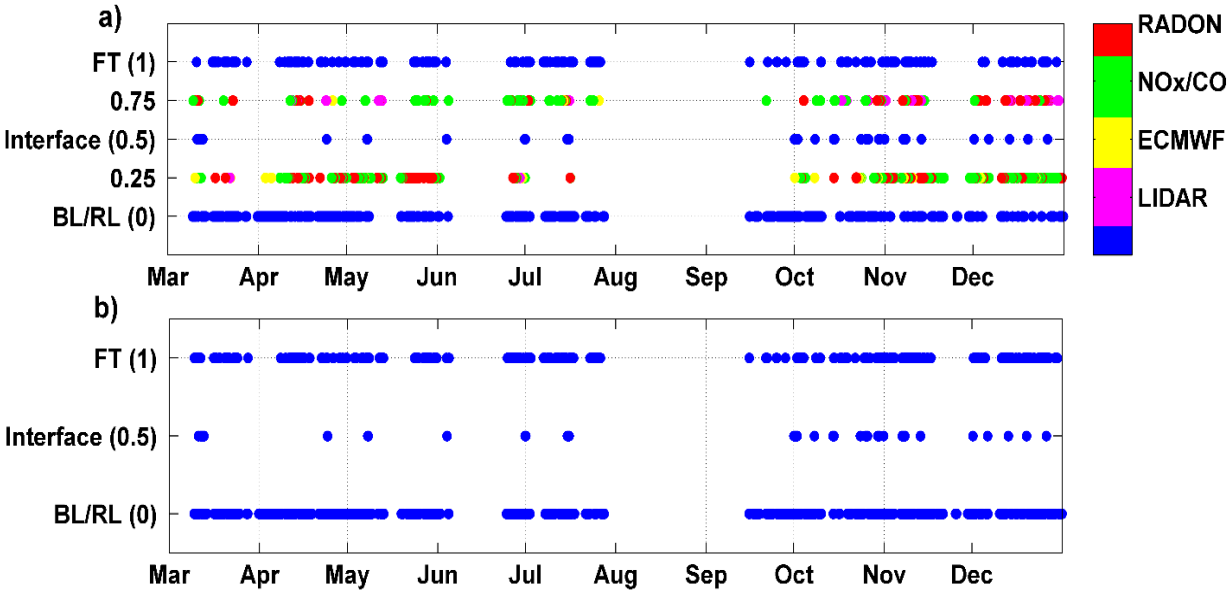

Figure 4.1. 6. The combined classification of the four methods for the year 2015. a) 1: All four methods classified the air mass to be within the FT, 0.75: three out of four methods classified the air mass as being within the FT, 0.5: only two out of four methods classified the air mass as being in the FT, 0.25: Three out of four methods classified the air mass as being within the BL/RL and 0: all four methods considered that the air mass was within the BL/RL. Color bar indicates where the method failed in calculating the FT(1)/(BL/RL)(0) conditions. Violet: LIDAR, yellow: ECMWF, Green: NO_x/CO, Red: Radon-222 and Blue: successful or equality in the calculation of the FT/(BL/RL) conditions. b) Same as (a) with 0.25 and 0.75 combined with 0 and 1, respectively.

Figure 4.1.6a shows the average classification of the measured air masses as FT/(BL/RL) at the PUY station. In order to average the four classification criteria, we use a specific labeling. When a measurement criterion classifies the air mass at the PUY station as FT, the corresponding date is labeled "1", when it is classified as BL/RL air mass, the corresponding date is labeled "0". Hence, when all four criteria give the air mass as FT, the average classification is "1", while only three criteria out of four classify the air mass as FT, the average classification is "0.75". Similarly, when all four criteria give the air mass as BL/RL, the average classification is "0". Additionally, when two criteria of four go wrong for classifying the air mass as FT or BL/RL, the average classification is "0.5" which corresponds to the interface mode, while only one criteria out of four are classifying the air mass as BL/RL, the average classification is "0.25". Colors in the figure correspond to the one criteria that differs from the other three. We observe that the WCT criteria did not identify FT air masses in the winter (violet color in 0.75). For classifications of BL/RL conditions, disagreements between the four methods were largely related to either NO_x/CO or ^{222}Rn (green and red color, respectively in 0.25 (Figure 4.1.6)). For the tracer NO_x/CO, it is possible that this tracer is more representative of aged regional emissions as reported by Freney et al., (2011).

^{222}Rn levels can also be influenced by the changes in air mass at PUY station. Indeed, for a given BLH, an oceanic air mass will have lower levels than a terrestrial air mass. Hence, we believe that ^{222}Rn is the less reliable tracer of FT air masses for our site. This analysis also highlights that at the PUY station, radon and NO_x/CO overestimate when the PUY station is in the BL/AL than the other methods. ECMWF is also not adequate for the estimation of FT/BL conditions at night time, retrieving the stable nocturnal BL and not considering the residual nocturnal layer. By combining four criteria for the determination of FT or BL/RL conditions, we provide a more robust method. As a consequence, we chose to classify the station in FT air masses when 3 of the 4 criteria identify FT air masses (0.75) and classify the station in BL/RL air masses when the majority of methods identified BL/RL air masses (0.25). When only two out of four methods disagree with the others (0.5), the air mass is classified at the interface (Figure 4.1.6b).

At the PUY station, using a combination of these four criteria for assessing if the site is in free tropospheric conditions, we determine that the site is in the FT for 20% of the time as a yearly average, over 25% during winter and below 17% during summer. At the JFJ, Herrmann et al., (2015) compared three criteria for assessing if the site lies in free tropospheric condition, and found FT prevalence for 39% of the time as a yearly average, with over 60% during winter and below 20% during summer. Chauvigné et al., (2018), also reports time spent in the FT for the Chacaltaya (CHC) (5240 m a.s.l, Bolivia) site, and found FT prevalence for 45% of the time as a yearly average, with no marked seasonal variations. The difference between the PUY and these sites is probably that the PUY is at a lower altitude, but also because the configuration of the topography is different (North-South orientated single mountain chain) (Collaud Coen et al., 2017).

For the four seasons, the percentage of time that the site is in the BL/RL (red) increases during the day (between 9 and 18 UTC) to reach a maximum at 18 UTC, and decrease during the night (after 18 UTC) to reach a minimum at 00 h for winter, at 3 UTC for spring and summer, and at 6 UTC for autumn (Figure 4.1.7). On the contrary, this percentage in FT (blue) decreases during the day (between 9 and 18 UTC) to reach a minimum at 18 UTC for winter spring and summer, and at 15 UTC for autumn. During the night the percentage of FT air masses at the site reaches a maximum at 00 h for winter, at 3 UTC for spring, and at 6 UTC for summer and autumn.

Air masses are classified at the interface between the BL/RL and the FT (black), at a higher frequency at night/early morning than during the late evening, and higher

during winter than during summer. Between 3 and 12 UTC, this percentage reaches a maximum of 15.5% and 10% at 6 UTC respectively for winter and spring. The high percentage at the interface is related to the diurnal variation of the BLH which reaches the PUY station at around 6 UTC.

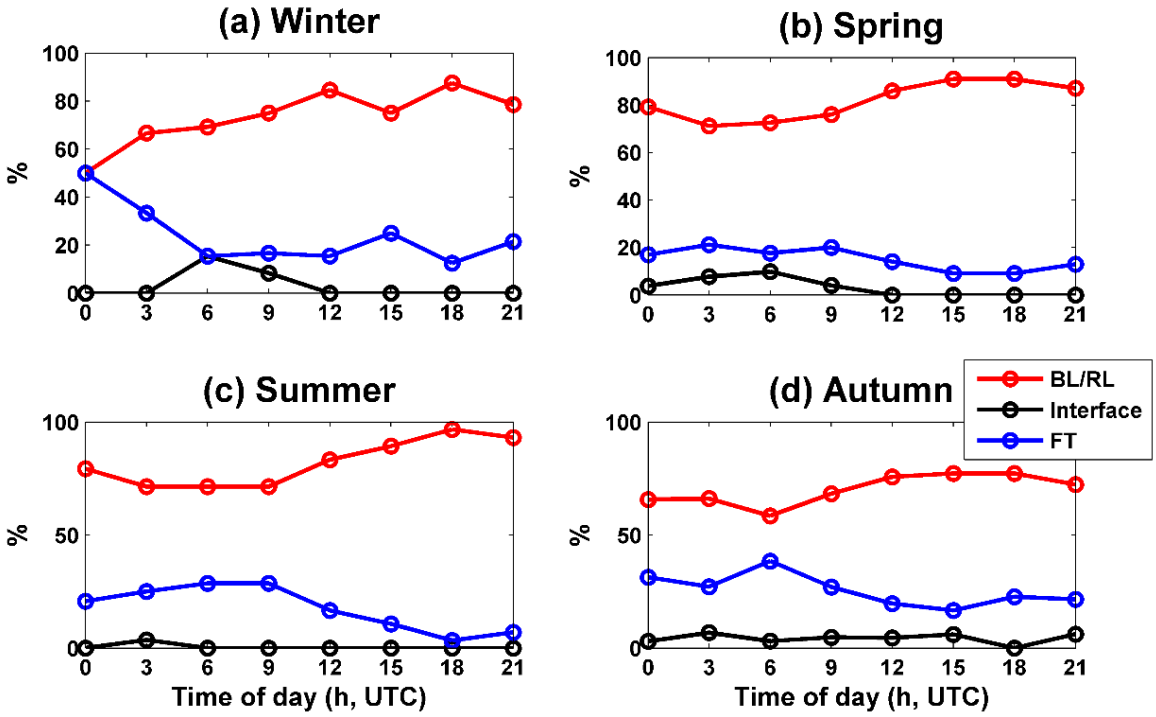

Figure 4.1. 7. The diurnal variation of percentage that the PUY station is in FT/Interface/(BL/RL) conditions for the four seasons: (a) Winter; (b) Spring; (c) Summer; (d) Autumn. red: Boundary Layer (BL) (daytime)/Residual Layer (RL) (nighttime), black: Interface, blue: Free Troposphere (FT).

4.1.2. Comparisons of the Free Troposphere and Boundary Layer Aerosol Properties

In this section, we use the classification proposed by the combination of the four criteria of FT/(BL/RL) segregation in order to investigate the differences of thermodynamical variables and aerosol properties when sampled in the BL/RL or in the FT at the PUY station. The values obtained for all criteria when the PUY station is at the interface between both layers represent a smaller database that is not statistically relevant and will not be discussed here (Table 4.1.2).

Table 4.1. 2. Number of data sets of several atmospheric parameters for each season.

	Winter			Spring			Summer			Autumn		
	FT	Inter	BL/RL	FT	Inter	BL/RL	FT	Inter	BL/RL	FT	Inter	BL/RL
EBC	26	3	81	38	11	317	5	0	86	132	21	357
T	26	3	81	64	13	350	40	1	189	132	22	363
P	26	3	81	64	13	350	40	1	189	132	22	363
RH	26	3	81	64	13	350	40	1	189	132	22	363
Nuc	26	3	79	47	13	278	40	1	189	132	22	363
Ait	26	3	79	47	13	278	40	1	189	132	22	363
Acc	26	3	79	47	13	278	40	1	189	132	22	363
Coa	X	X	X	40	9	195	39	1	157	X	X	X

In order to assess whether the different parameters show statistically significant differences in FT/(BL/RL), the Wilcoxon–Mann–Whitney test (DePuy et al., 2005) was applied to the median values (Temperature (T), Relative Humidity (RH), Pressure (P), equivalent Black Carbon (EBC), and for the nucleation (Nuc), Aitken (Ait), accumulation (Acc) and coarse (Coa) aerosol particles size mode concentrations) (Figure 4.1.8). This nonparametric test evaluates the difference in medians between two similarly shaped populations. This test showed that the FT/(BL/RL) difference was significant for some parameters (for example, T, RH, and P), however, for certain parameters during certain seasons (for example, the E BC and Acc mode particles in summer and for Nuc mode particles during all seasons) no differences between BL/RL and FT properties were detected.

At first, the meteorological parameters (T, RH, and P) were characterized in the FT and in BL/RL air masses (Figure 4.1.9a–c). As expected higher median RH concentrations were found in BL/RL conditions for all seasons compared to FT conditions, this difference is shown to be significant by the Wilcoxon–Mann–Whitney test (Figure 4.1.8). The higher RH in BL/RL conditions at the PUY station is the result of sources of humidity from the surface in the BL/RL. Higher median T and P were measured in FT conditions compared to BL/RL conditions for all seasons (except in winter for P), the significance being confirmed by the Wilcoxon–Mann–Whitney test (Figure 4.1.8). Higher pressures in the FT than in the BL/RL could be related to anticyclone conditions, which decrease the BLH (Salzano et al., 2016). Higher

temperatures in the FT than in the BL/RL may be explained by the fact that the PUY station is situated in the lower part of the FT in which the temperature increases over a limited altitude range (temperature inversion starting at the very lower part of the FT) (Tennekes, 1973).

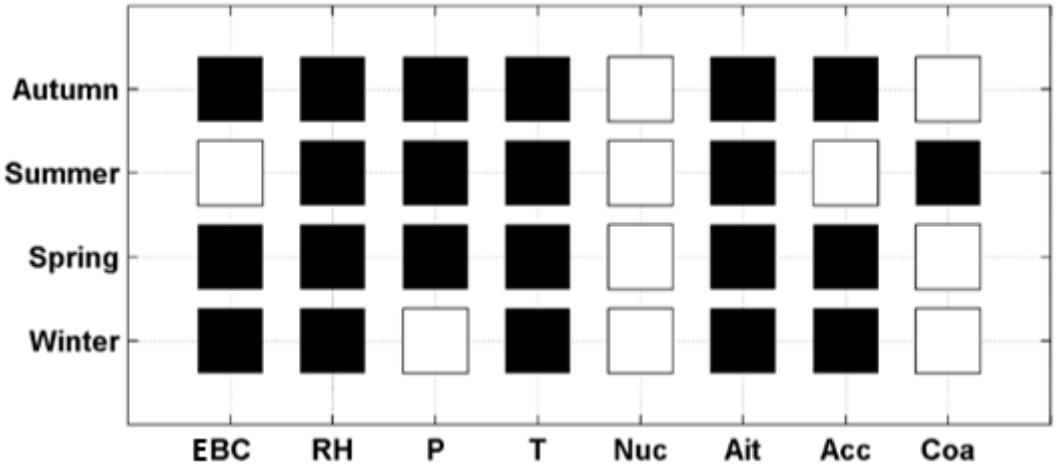

Figure 4.1. 8. The Wilcoxon–Mann–Whitney test applied on Equivalent Black Carbon (EBC), Relative Humidity (RH), Pressure (P), Temperature (T), Nucleation (Nuc), Aitken (Ait), Accumulation (Acc) and Coarse (Coa) concentrations measured for each season. The squares are black (white) when the medians are significantly different (equal) with a threshold of 5%. Black Crosses are for missing data.

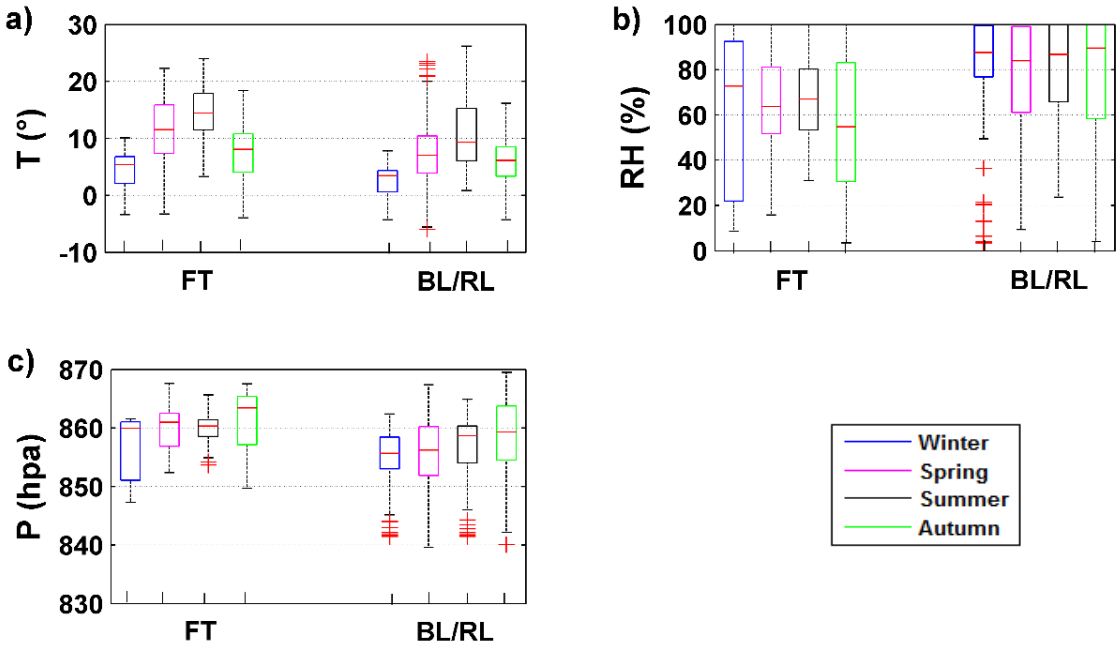

Figure 4.1. 9. The FT/(BL/RL) variation of (**a**) Temperature (T); (**b**) Relative Humidity (RH), and (**c**) pressure (P), for the four seasons at the PUY station. Red lines represent the median value, bottom and top sides of the boxes symbolize the 25th and 75th percentile respectively

and the extremities of the black lines are the 10th and 90th percentile. Red Crosses represent the outliers.

Figure 4.1.10a shows, for different seasons, the equivalent Black Carbon (EBC) concentration when the PUY is in the FT or BL/RL. The Wilcoxon–Mann–Whitney test presented in Figure 4.1.8, shows that for winter, spring and autumn seasons, the null hypothesis that the two sets have equal medians was dismissed with a threshold of 5% (black square), while in summer the null hypothesis cannot be dismissed (transparent square). Hence it appears that in summer, there is no marked distinction between the median EBC concentration in the FT and the median EBC concentration in the BL/RL. However, we observe a stronger variability in the EBC in the BL/RL than in the FT. This variation is likely due to the diurnal cycle of sources in this layer. In winter and autumn, the median EBC concentration is significantly higher in the BL/RL compared to the FT. This is expected as sources of EBC are mainly from surface emissions. In spring, we observe an unusual trend with EBC concentrations significantly higher in the FT than in the BL/RL.

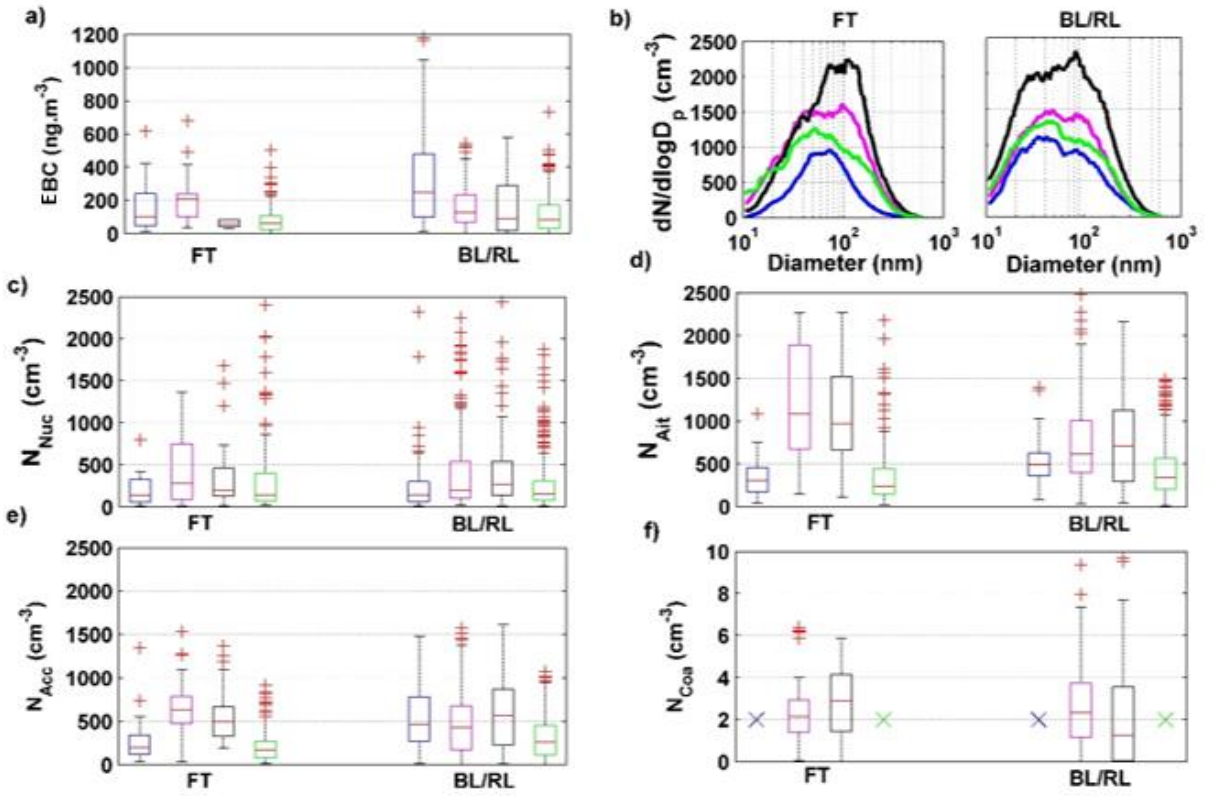

Figure 4.1. 10. The FT/(BL/RL) variation of: (**a**) EBC; (**b**) Full aerosol size distributions (10–650 nm); (**c**) Nucleation (Nuc) (10–20 nm); (**d**) Aitken (Ait) (40–80 nm); (**e**) Accumulation (Acc) (100–300 nm); (**f**) Coarse (Coa) (>1 μm), concentrations for the four seasons. Red lines

represent the median value, bottom and top sides of the boxes symbolize the 25th and 75th percentile respectively and the extremities of the black lines are the 10th and 90th percentile. Red Crosses represent the outliers.

The high concentrations of EBC in the BL/RL for winter and autumn are thought to be a result of higher contributions of local sources of combustion linked to conventional heating devices often observed during this time of the year (Barbet et al., 2016). This combined with lower BL heights results in an accumulation of these particle concentrations during the cold seasons. In spring and summer, transport of the materials from BL/RL to FT efficiently occurs by active convection, and the FT air masses are more impacted by intrusions of BL/RL air. The stronger EBC concentration in the FT during spring can be linked to EBC originating from biomass burning occurring frequently during this season during the burning of vegetation in gardens, that is likely injecting biomass burning particles directly into the FT from strong heat convection transport from BL/RL to FT.

In addition, Figure 4.1.10b represents median aerosol size distributions (10–650 nm) for the four seasons, in the BL/RL and FT, and highlights the various shapes observed in the different conditions. In order to further investigate the seasonal variation of the aerosol spectrum properties in both layers, we used four aerosol modes: nucleation (10 nm to 20 nm), Aitken (40 nm to 80 nm), accumulation (100 nm to 300 nm), and coarse (1 μm to 18 μm) modes (Figure 4.1.10c–f). During the winter and autumn months, the median Aitken and accumulation mode aerosol concentrations are significantly higher in the BL/RL, compared to the FT (Figure 4.1.10d,e). In spring (for the accumulation mode) and spring and summer (for the Aitken mode), we observe the opposite, with higher concentrations in the FT than in the BL/RL. In summer, the median accumulation mode particle concentration is comparable in the FT and in the BL/RL.

For nucleation mode particles (10–20 nm) (Figure 4.1.10c), there are no significant differences in median values in the FT and in the BL/RL for all seasons. The lack of difference between nucleation mode particles in the BL/RL and in the FT would suggest that there is an additional source of nucleation mode particles in the FT compared to the primary emissions traced by the accumulation mode particles during winter and autumn. This was already observed by Tröstl et al., (2016) at the JFJ site who reports that the nucleation mode particles occur within air masses that have been transported over long-range distances into the FT.

Additionally, these particles show the highest concentrations during summer ($N_{nuc, FT}$ = 489 cm^{-3}; $N_{nuc, BL/RL}$ = 512 cm^{-3}) (Table 4.1.3). This is in agreement with Venzac et al., (2009) at the same site, who reports highest concentrations of nucleation mode particles during summer (Venzac et al., 2009)). Boulon et al., (2011) reports the highest new particle formation frequency during spring and autumn, but the intensity of the new particle formation events (in term of nucleation rate and further growth) is the highest during summer.

The accumulation mode particle concentrations have a similar behavior to the EBC concentrations previously discussed, and we assume that they have similar sources for winter and autumn. Higher concentrations of the Aitken mode particles during springtime may be partly due to the growth of nucleation mode particles that were observed to occur more frequently during spring (Rose et al., 2015a; Venzac et al., 2007) and preferentially at higher altitudes (Boulon et al., 2011), as also witnessed by higher concentrations during the spring season for the present dataset, and partly due to a contribution from biomass burning aerosols due to the active convection transport from BL/RL to FT. During summer, the difference between concentrations in the FT and in the BL/RL is less marked than in Spring, which may be due to the less frequent nucleation frequency (Boulon et al., 2011; Rose et al., 2015b) and the less biomass burning events than in spring.

Table 4.1. 3. The mean concentration of the Nucleation, Aitken, and Accumulation mode particles for the four seasons.

Particle mode	Season	N (cm^{-3})	
		FT	BL/RL
Nucleation	Winter	190	254
	Spring	490	504
	Summer	489	512
	Autumn	374	312
Aitken	Winter	346	514
	Spring	1211	714
	Summer	1119	823
	Autumn	367	419

Accumulation	Winter	290	530
	Spring	630	470
	Summer	560	570
	Autumn	220	385

For both accumulation and Aitken mode concentrations, we clearly see that spring and summer ($N_{accumulation,\ spring,\ FT}$ = 630 cm^{-3}; $N_{accumulation,\ spring,\ BL/RL}$ = 470 cm^{-3}; $N_{aitken,\ spring,\ FT}$ = 1211 cm^{-3}; $N_{aitken,\ spring,\ BL/RL}$ = 714 cm^{-3} and $N_{accumulation,\ summer,\ FT}$ = 560 cm^{-3}; $N_{accumulation,\ summer,\ BL/RL}$ = 570 cm^{-3}; $N_{aitken,\ summer,\ FT}$ = 1119 cm^{-3}; $N_{aitken,\ summer,\ BL/RL}$ = 823 cm^{-3}) show the highest mean particle concentrations in both the FT and the BL/RL (Table 4.1.3). This is in agreement with that of Venzac et al., (2009) and Herrmann et al., (2015) during the summer season.

In our study, the observed concentrations are slightly higher then what was found by Venzac et al., (2009). This would confirm the tendency observed by Venzac et al., (2009) of the aerosol concentration increasing over the 6 years of data but would need a careful trend analysis which is beyond the scope of the present study.

For coarse mode particles, no data is available for winter and autumn, and the Wilcoxon–Mann–Whitney test is not significant for spring (medians are equal for FT and BL/RL) (Figure 4.1.10f). However, for summer, high median concentrations of the coarse mode particles were measured in FT conditions, compared to the BL/RL conditions. This difference is likely due to a more efficient long-range transport of dust and marine aerosols at high altitudes than at lower altitudes. Bourcier et al., (2012) reported higher concentrations of Cesium (Cs) associated to dust particles at PUY, than at the lower altitude of CZ, but the difference was mostly found during winter. The authors hypothesized that during winter, large particles are transported with a higher efficiency at high altitudes due to stronger winds. The variability of the coarse mode particle concentration is higher during the BL/RL conditions compared to FT conditions presumably due to the sporadic character of sources of large primary particles in the BL/RL.

The next step of our analysis is to investigate the variability of aerosol properties within the lower FT and the possible causes for this variability.

4.1.3. Aerosol Properties in the Lower Free Troposphere as a Function of Air Mass Type and Age

Our analysis of the air mass back-trajectory history relative to the latest contact with the BL over the 204 h prior sampling showed that air masses aerosol properties (for example, N_{90}) do not change for BL-contact-free times larger than 75 h (Figure 4.1.5a). In the following section, we investigate the change of aerosol particles within the lower free troposphere during the last 75 h prior to sampling.

Figure 4.1.11 presents the segregation of FT air masses as a function of the time they spent in the FT since their last contact with the BL/RL before reaching the PUY station. The BLH parameter of ERA-Interim ECMWF is interpolated spatially and temporally and compared with the altitude of each path point to determine the last contact with the BL. This analysis was done using LACYTRAJ, for the four seasons. Most noticeably, the vast majority (over 80%) of winter and autumn air masses did not have any contact with the BL/RL for at least the last 75 h before being sampled at PUY. This explains why certain aerosol concentrations are low in the FT during these seasons. For summer and spring, the large majority (60%) of air masses were in contact with the BL/RL in the last 15 h prior to measurement (Figure 4.1.11). Therefore, certain aerosol concentrations are high in the FT during these seasons. We hence assume that aerosol properties measured in these air masses during summer and spring are more representative of BL/RL than the unperturbed FT. Using this information, we focus the remaining discussion on aerosol properties measured during winter and autumn assuming that they are representative of the unperturbed FT and we can, therefore, study their characteristics as a function of the air mass origin.

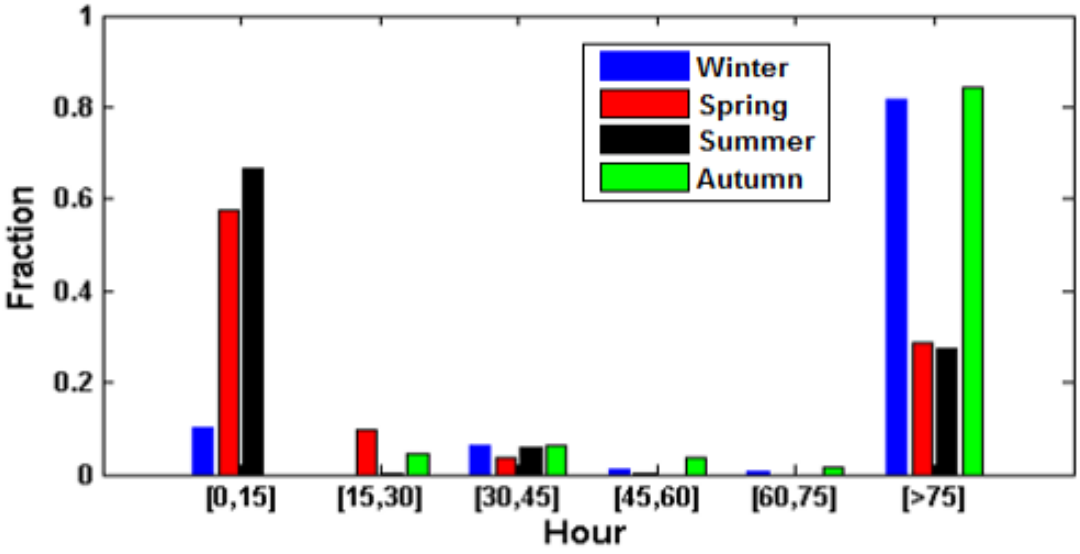

Figure 4.1. 11. The fraction of time since the last BL/RL contact of >75-h back trajectories of air masses reaching the Puy de Dôme for the four seasons.

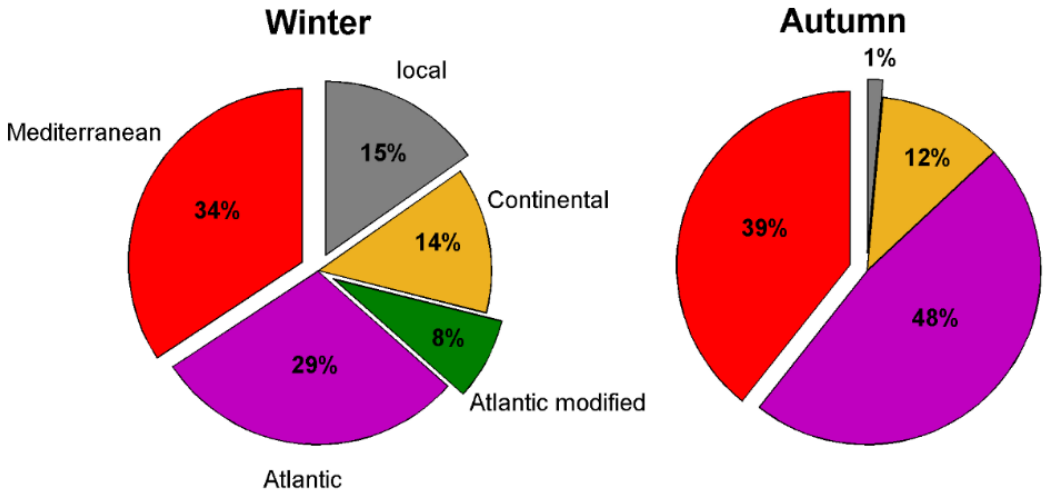

Figure 4.1. 12. The air masses classification in the FT for winter and autumn seasons: Violet: Atlantic, Green: Atlantic modified, Brown: Continental, Grey: Local, Red: Mediterranean.

LACYTRAJ has also been used to provide a classification of five possible sources, from Oceanic, Mediterranean, continental, northerly, or local (Figure 4.1.12), similar to Asmi et al., (2012) and Rose et al., (2015a) (details of the classification are shown in Figure 4.1.13). This classification is based on the location of the last interaction between the air mass and the BL. Therefore, the locations of the last contact with BL are essential. During the winter season, air masses are mainly of Mediterranean (34%) and Atlantic (29%) origins, and a smaller fraction of them are either local (15%), continental

(14%), or Atlantic modified (8%) (Figure 4.1.12). In autumn, air masses are mostly of Mediterranean (39%) and Atlantic (48%) origins, and a small fraction is of a continental origin (12%) (Figure 4.1.12).

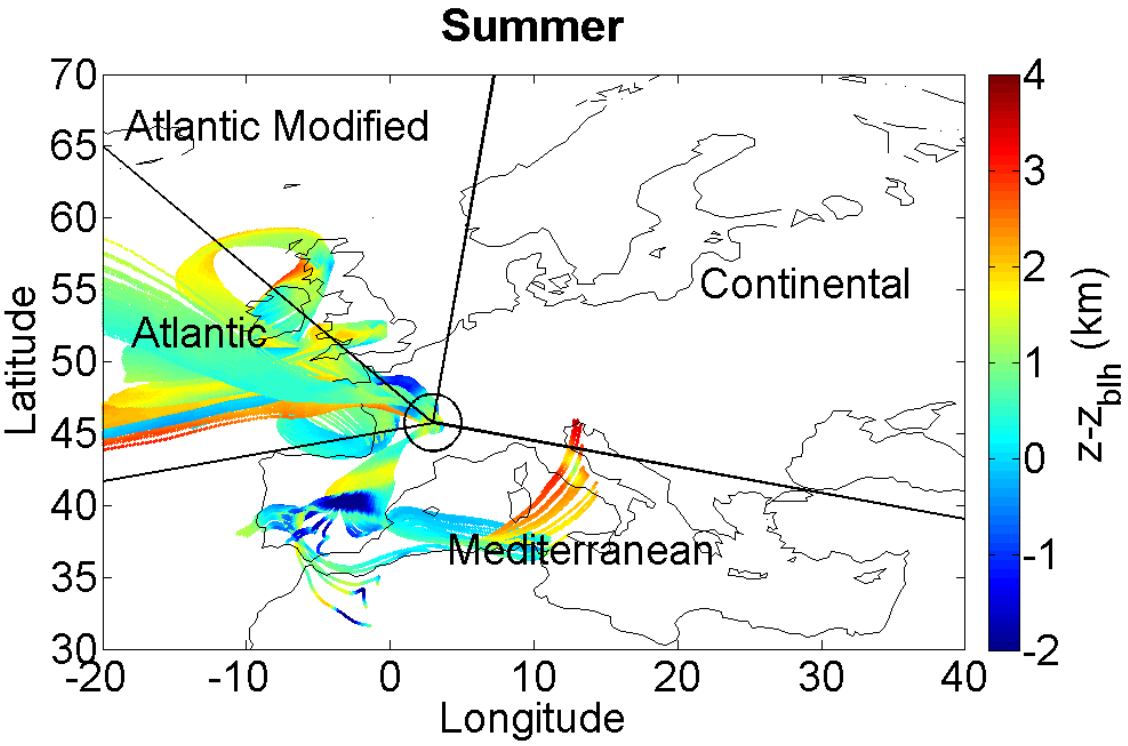

Figure 4.1. 13. 204-hours ECMWF backward trajectories for air masses arriving at the PUY site during FT sampling periods. The color scale represents the difference between the calculated height (z) of the air mass trajectory and the calculated height of the BL/RL height ($Z-Z_{blh}$ (km)).

In the following section we compare aerosol properties in the three types of air masses (Atlantic, Mediterranean, and Continental) observed during both seasons (winter and autumn) (Figure 4.1.14).

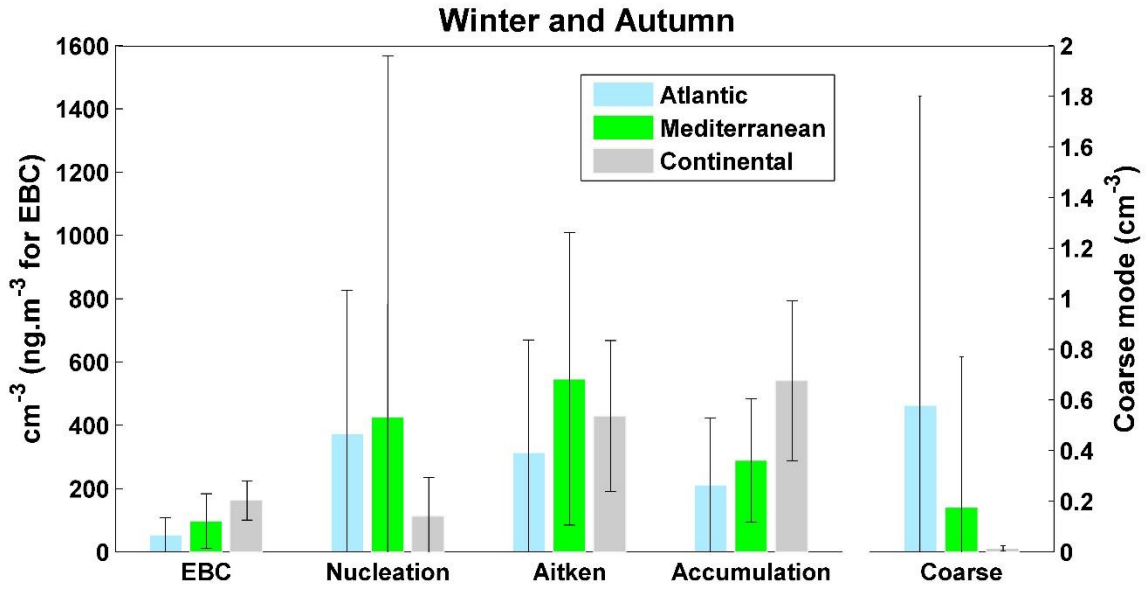

Figure 4.1. 14. The EBC, Nucleation, Aitken, Accumulation, and Coarse mode particles concentrations for >75 h in the FT for Atlantic, Mediterranean, and continental air masses for both winter and autumn.

Higher nucleation mode concentrations are measured when the PUY station is exposed to aged (>75 h) Atlantic and Mediterranean air masses than when exposed to continental air masses (Figure 4.1.14). We can hypothesize that these high concentrations of nucleation mode aerosols are formed at the PUY from marine precursor sources that have been transported from the Mediterranean sea and from the Atlantic ocean (Rose et al., 2015a; Schröder and Ström, 1997), or that the condensational sink associated to the Atlantic and Mediterranean air mass types are lower compared to continental air masses containing larger concentrations of accumulation mode particles. Bianchi et al., (2016) and Tröstl et al., (2016) show also that nucleation in the FT is favored after a certain time lapse has passed after the last contact with the BL/RL.

In aged air masses, the high concentrations of the Aitken and accumulation mode particles coincide with the high concentrations of EBC, originated from continental air masses. These high EBC, Aitken, and accumulation concentrations can, thus, partly be due to biomass burning emissions. Another source of these high concentrations of Aitken mode particles is the growth of nucleation mode particles originated from the Atlantic and Mediterranean air masses. Within aged air masses, coarse mode aerosol concentrations are also higher in Mediterranean and Atlantic air masses compared to continental air masses, likely a result of transported sea salt and dust particles.

Overall, we observe that even after more than 75 h with no contact with the BL/RL, FT aerosols preserve properties that are specific to their source region. To the author's knowledge, this is the first report of these observations from in situ measurements.

4.1.4. Conclusions

A one-year dataset of multiple measurements acquired at the PUY station has been used in this work to determine the specific physical characteristics of FT aerosols and hence of their sources and transport pathways from the BL.

In order to achieve this goal, a combination of four criteria was used to identify whether the PUY station lies within the FT or within the BL. BLH was determined using two independent methods, firstly the ECMWF model, using the "global method of Richardson" to calculate the $BLH_{ECMWF,}$ and secondly, the WCT method to calculate the ALH_{WCT} from LIDAR measurements. In addition, NO_x/CO and radon-222 tracers were used to determine the degree of influence from the $AL_{NOx/CO}$ and AL_{Rn}, respectively. Using these tracers, we observe that the PUY station is considered to be in the FT up to 50% during the winter months.

For most of the time and aerosol property, higher concentrations are found in the BL compared to FT, as expected from larger sources originating from the surface. However, higher EBC, accumulation, and Aitken modes median concentrations are observed in FT conditions compared to BL during spring. This might be linked to biomass burning from vegetation in gardens that inject aerosols directly to the FT from active convection transport. Another source of these high concentrations of Aitken mode particles is the growth of nucleation mode particles. In general, for these nucleation mode particles, there is no significant difference in the median values measured in the FT and in the BL/RL for all seasons. This suggests that there is an additional source of precursors to the formation of new particles at the PUY station. These additional sources likely originate from aged Atlantic or Mediterranean air masses. Higher median concentrations and higher variability of the coarse mode particles are also found in FT conditions during summer is a result of increased contribution from Mediterranean and Atlantic air masses, bringing dust and marine aerosol at higher altitudes. Finally, even after more than 75 h without any contact with the BL/RL, FT aerosols preserve properties specific to their air mass type/origin. However, as expected, these differences are less distinct in aged FT air masses (>75 h) than in recent FT air masses (>15 h).

4.2. One year of on-line chemistry measurements of the non-refractory submicron aerosol at the Puy-de-Dôme with an emphasis on air mass transport and free troposphere / boundary layer conditions (Farah et al., (2018) in prep.)

Aerosol chemical composition is essential to our understanding of the formation and transformation of aerosol particles in the atmosphere, notably since aerosol chemical properties can govern their reactivity in the atmosphere as well as their impact on health and climate. Having online rapid acquisition of aerosol chemical properties allows us to study temporel variations on short time scales and to observe the evolution of aerosol particles as a function of airmass source as well as during different seasons of the year. Thanks to the recent developments of aerosol mass spectrometry, notably with the Aerosol Chemical Speciation Monitor (ACSM, (Ng et al., 2011)), this information can be acquired over long periods of time with minimal intervention from the user. The ACSM is a robust tool that measures aerosol chemical properties of the aerosol with time resolutions of 10 to 30 minutes. Long-term ACSM data sets have recently been presented in the literature almost all over the world such as: 2 years near Paris (France) (Petit et al., 2015), 1.5 years in central Oklahoma (Parworth et al., 2015), 1 year in Zurich (Switzerland) (Canonaco et al., 2013¸ 2015), near Johannesburg (South Africa) (Tiitta et al., 2014; Vakkari et al., 2014), near Barcelona (Spain) (Minguillón et al., 2015; Ripoll et al., 2015), 1.2 years in Jungfraujoch (JFJ, Switzerland) (Fröhlich et al., 2015), and in the Southeastern United States (Budisulistiorini et al., 2016). These measurements are mostly being performed within the framework of the ACTRIS infrastructure (Aerosols, Clouds, and Trace gases Research InfraStructure). This infrastructureis a European wide initiative that aims to combine resources and knowledge of all European partners.. This network currently hosts 24 ACSMs to study long-term data sets of PM1 chemical composition across the continent. A large database of long-term ACSM data (including the data presented in this study) are available in the framework of ACTRIS via the EBAS database (http://ebas.nilu.no/).

Recent studies have investigated AMS databases almost all over the world (J L Jimenez et al., 2009; Zhang et al., 2007). Zhang et al., (2007) show that organic aerosols (OA) comprise more than 40% of the submicron fraction for almost all sites, largely independent of the region and type of environment. The OA mass concentrations is in many locations measured as secondary organic aerosol (SOA) which is dependent of the region and type of environment (Jimenez et al., 2009). However, in these studies the knowledge of the OA formation, sources and processes is still not very clear, especially for SOA formation. Ciarelli et al., (2017), using the CAMx (Comprehensive

Air Quality Model with extensions) model, compare the simulated chemical composition of aerosols against those of AMS measurements performed at 11 sites in Europe, showing that both model and observations suggest that OA was mainly composed of SOA. However, the model still under predicts the SOA formation suggesting a more detailed characterization is needed. For these reasons, OA measurements and analysis are required to better understand its chemical evolution in the atmosphere.

Similar to worldwide measurements at low altitude sites, organic species also dominate the PM1 mass concentrations at high altitude sites. Fröhlich et al., (2015) at JFJ (3580 m asl), show that organics were the dominant species, comprising 73 to 81% of the submicron fraction over all seasons and all air mass sources. As expected, the organic fraction was mainly secondary organic aerosol (SOA) that can partly be linked to long range transport air masses and partly to the vertical mixing of air masses up to JFJ. Ripoll et al., (2015) at montsec (MSC, 1570 m asl), show also a dominance of organic species all over the year 2011-2012 (50%). Their results also highlight the importance of the SOA formation processes at a remote site. Minguillón et al., (2015) at Montseny (MSY, 720 m a.s.l), show that the OA was the major component of submicron aerosol (53% of PM1) over all seasons, with a higher contribution in summer (58%) than in winter (45%). They show that all the chemical compositions were affected by the general breeze regime (as typical for mountain sites), leading to an increase during the day and decrease during the night. This leads us to the question of whether the same chemical features are true for the different lower atmospheric layers (i.e. BL, FT) of background environments. In order to contribute answering to this question, we focus in the present study on a yearlong data base of on-line ACSM chemistry measurements of the non-refractory submicron aerosol data collected at a high altitude PUY site (1465 m a.s.l) located in central France, allowing the investigation of both the lower free troposphere (FT) conditions at night and of boundrary layer (BL) conditions during the day (Farah et al., 2018; Venzac et al., 2009). The aim of this study is to identify specific signatures of aerosol chemical properties in the FT and to investigate the dependance of these properties on airmass sources.

The previous chapter made it possible to segregate between BL and FT air masses using a combination of four different parameters: Wavelet covariance transform (WCT) (Baars et al., 2008; Brooks, 2003; Cohn and Angevine, 2000) as an algorithm from LIDAR measurements, 2) radon-222 (^{222}Rn) concentrations as tracer (Chevillard et al., 2002; Griffiths et al., 2014; Herrmann et al., 2015), 3) the ratio NOy/CO as tracer (Herrmann et al., 2015; Pandey Deolal et al., 2013; Zanis et al., 2007; Zellweger et al.,

2003) and 4) ECMWF model (Venzac et al., 2009; von Engeln and Teixeira, 2013). In this chapter, this segregation is used on 1 year of on-line chemistry measurements of the non-refractory submicron aerosol data from the first long-term deployment of a time-of-flight aerosol chemical speciation monitor (ToF-ACSM, (Fröhlich et al., 2013, 2015) at the PUY site. The focus of this study was to characterize both seasonal and diurnal variability with the influence of air mass sources on the chemical composition. Also, OA source apportionment was performed using the Source Finder (SoFi) interface for the multilinear engine (ME-2). Furthermore, detailed discussion of chemical properties in the FT and BL is presented.

4.2.1. Time series and mass concentrations

The ToF-ACSM instrument was operating continuously from 01 April 2015 to 29 February 2016, providing measurements of the non refractory component of the PM1 aerosol, including nitrate, ammonium, sulphate, and organic mass concentrations (Figure 4.2.1). In order to best represent the submicron mass concentrations, these measurements are combined with black carbon concentrations. Averaged over the entire year, the most abundant component was organic 57% (2 $\mu g/m^3$), followed by sulphate 16% (0.4 $\mu g/m^3$), nitrate 12% (0.3 $\mu g/m^3$), ammonium 10% (0.24 $\mu g/m^3$) and EBC 5% (0.13 $\mu g/m^3$). Relative and/ or absolute mass concentrations agree well with previous long-term ACSM studies performed at the Montsec (Ripoll et al., 2015) and at Montseny stations in Spain (Minguillón et al., 2015), as well as those made at the Jungfraujoch station in Switzerland (Fröhlich et al., 2015).

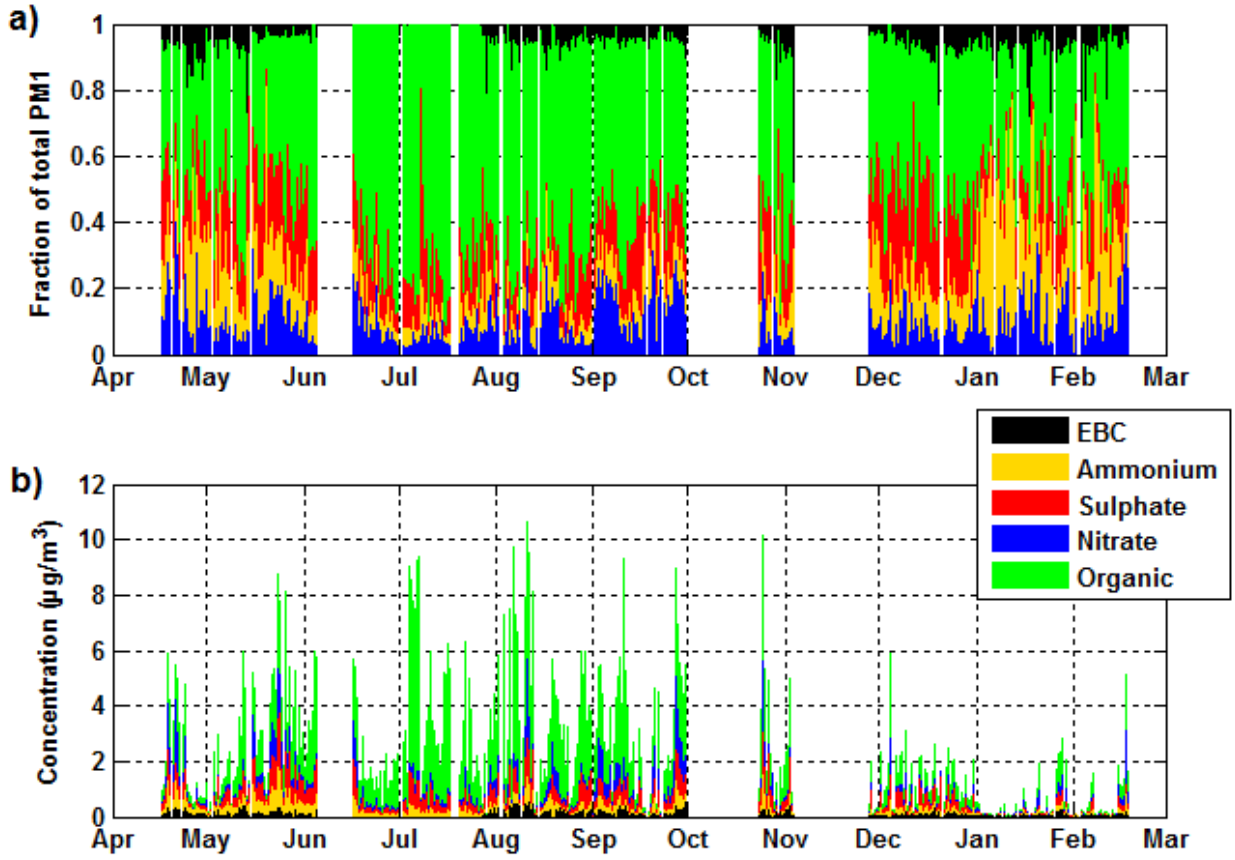

Figure 4.2. 1. **(a)** Time series of relative organic (green), sulphate (red), nitrate (blue), and ammonium (orange) contributions to the total PM1 aerosol measured by the ToF-ACSM and the EBC (Equivalent Black Carbon) concentration time series measured by the MAAP from April 2015 to February 2016. **(b)** Same as **(a)** in absolute concentrations ($\mu g/m^3$).

The acidity of the aerosols can be considered as an indicator of the age of the particles, as their neutralization takes place throughout their stay in the atmosphere. In order to estimate the degree of neutralization of the inorganic species measured by the ToF-ACSM, the measured NH_4 concentrations ($NH_{4,meas}$) are compared with the NH_4 concentrations predicted ($NH_{4,pred}$) if neutralization of sulphate, nitrate and chloride anions were complete. The necessary NH_4 for complete neutralization is calculated using the following equation:

$$NH_{4,pred} = 2*\left(\frac{18}{48}\right)*SO_4^{2-} + \left(\frac{18}{63}\right)*NO_3^- + \left(\frac{18}{35}\right)*CL^- \qquad \text{(Eq. 4.2.1)}$$

where SO_4^{2-}, NO_3^- and CL^- are the mass concentrations (in µg/m^3) of the corresponding inorganic species.

When plotting $NH_{4,meas}$ vs $NH_{4,pred}$, we obtained a slope of 0.93 (Figure 4.2.2), which emphasizes that the majority of the inorganic species are neutralized at the PUY site, in the form of ammonium sulphate $(NH_4)_2SO_4$, ammonium nitrate $(NH_4)(NO_3)$ or ammonium chloride (NH_4Cl).

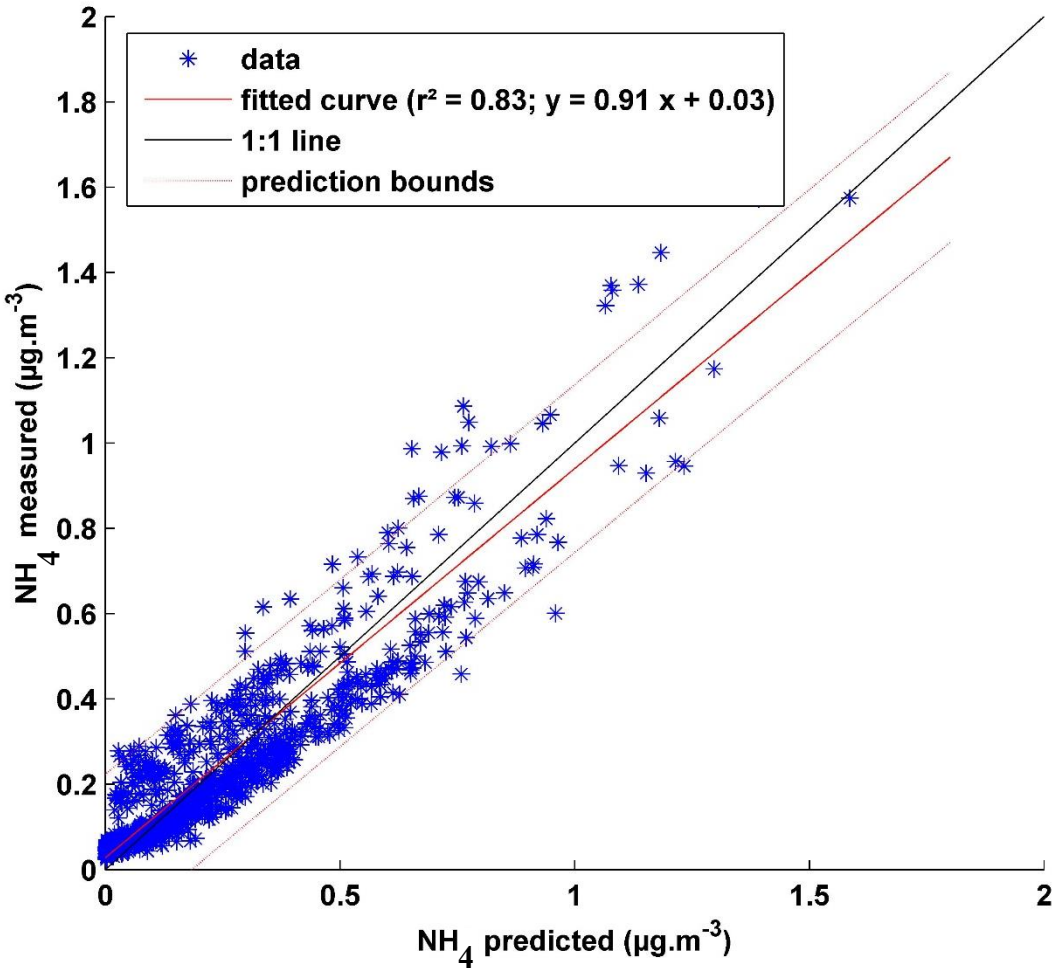

Figure 4.2. 2. Scatter plot between measured and predicted NH_4.

4.2.2 Seasonal variations

Average absolute concentrations of all species were around 4 µg/m^3 ±2.5 µg/m^3 during summer. In spring, autumn and winter they only amounted to 2.1 µg/m^3 ±1.3 µg/m^3, 1 µg/m^{-3} ±0.8 µg/m^3 and 0.8 µg/m^3 ±0.7 µg/m^3, respectively. Absolute mass concentrations agree well with previous short-term AMS studies performed at the JFJ

station which reported average non-refractory submicron aerosols (NR-PM1) concentrations of 2.5 μg/m^3 in summer (Cozic et al., 2008; Fröhlich et al., 2015), 1.6 μg/m^3 in spring (Lanz et al., 2010) and 0.4 μg/m^3 in winter (Fröhlich et al., 2015). The higher summer concentrations are likely due to a combination of increased vertical transport in this season, as well as secondary aerosol formation favored by increased photochemistry. This aspect will be further investigated by studying the relative contributions of the different primary / secondary compounds.

Although, the organic aerosol (OA) dominated the PM1 chemical components, its contribution varied from 48% in the autumn up to 73% in the summer (Figure 4.2.3). Sulphate particles contributed 19% (0.38 μg/m^3), 13% (0.42 μg/m^3), 23% (0.27 μg/m^3) and 13% (0.04 μg/m^3) to the total mass concentrations, respectively for spring, summer, autumn and winter. Sulphate concentrations are a factor 10 higher during summer than during winter. Nitrate contributed 14% (0.2 μg/m^3), 11% (0.3 μg/m^3), 12% (0.07 μg/m^3) and 17% (0.03 μg/m^3) for spring, summer, autumn and winter. Summer NO_3 concentrations are higher than those during winter by a factor 10. Ammonium contributed 14% (0.3 μg/m^3), 6% (0.2 μg/m^3), 11% (0.11 μg/m^3) and 14% (0.07 μg/m^3) for spring, summer, autumn and winter, respectively. Ammonia concentrations increased by a factor 3 during summer compared to winter. The last contributor to the PM1 aerosol mass was EBC, having similar contributions during all seasons; 6% (0.14 μg/m^3), 5% (0.17 μg/m^3), 6% (0.08 μg/m^3) and 7% (0.05 μg/m^3) during spring, summer, autumn and winter respectively. The dominance of organic species in the total PM1 mass was already reported in the literature (Zhang et al., 2007), especially during the warm months (Fröhlich et al., 2015; Lanz et al., 2010). Lanz et al., (2010) show highest OA in summer at JFJ related to charbroiling and a minor source, potentially representing food cooking.

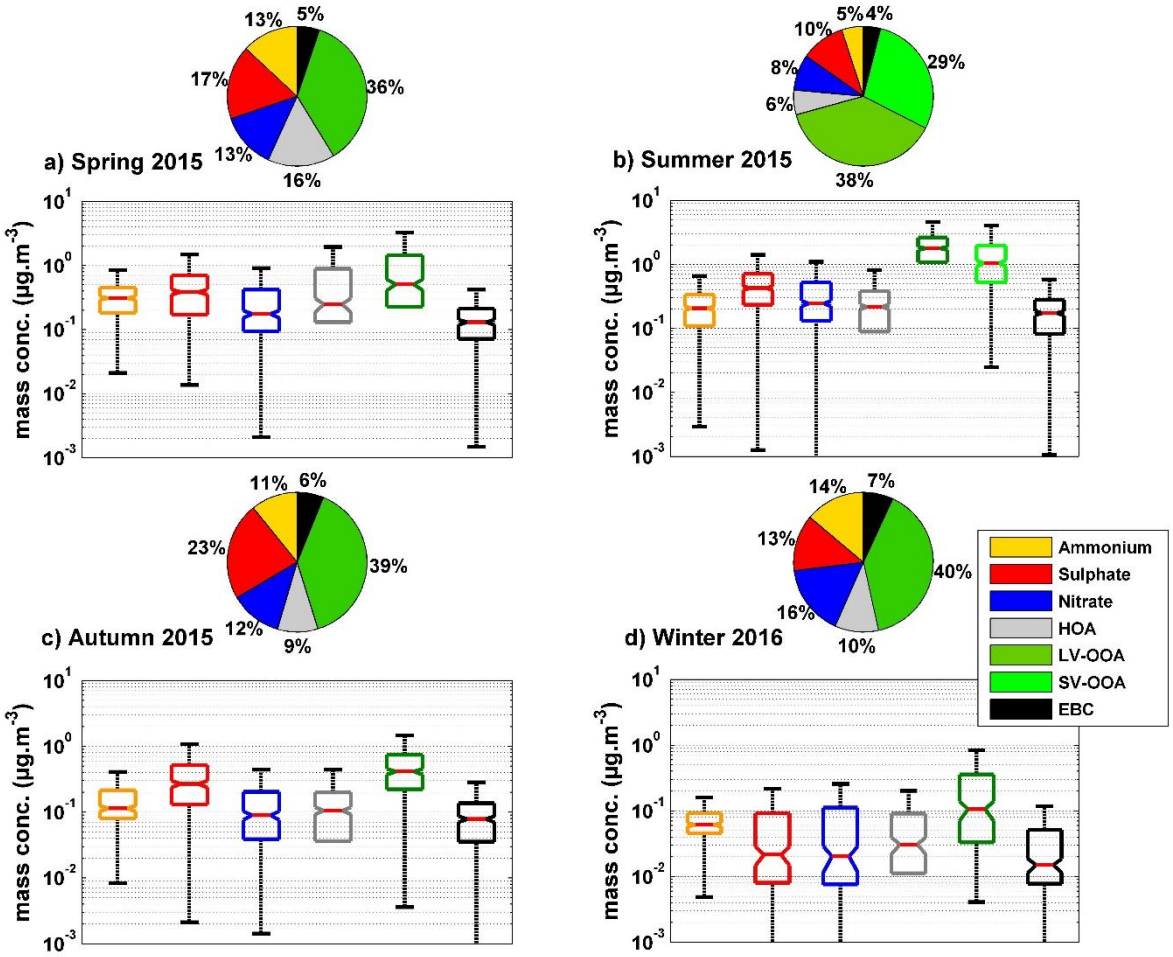

Figure 4.2. 3. Pie charts and boxplots (in µg/m³; line: median; box: interquartile range; whiskers: 10–90th percentile range) separated by seasons: a) spring (2015), b) summer (2015), c) autumn (2015) and d) winter (2016), for species measured with the ACSM (ammonium: orange; sulfate: red; nitrate: blue; HOA: grey; LV-OOA: dark green; and SV-OOA: light green) and EBC: Equivalent black derived from MAAP.

The dominance of organics for all seasons suggests contributions from multiple sources and formation mechanisms. For this, more detail analysis of these organic aerosols sources is needed.

Using the fractions of two major mass spectral peaks, m/z 44 (CO_2^+) and m/z 43 (mostly $C_2H_3O^+$) a triangular space was created in which organic aerosol particles are progressively more aged when one moves towards the highest point of the triangle (Ng et al.,2010). Previous studies of SOA formation also show that the right side of the Ng triangle indicate a biogenic influence (Jimenez et al., 2009; Ng et al., 2010), whereas those from biomass burning emissions tend to be situated on the upper left side of the triangle (Heringa et al., 2011), and finally those of traffic emissions are probably

situated on the lower left to middle side of the triangle (Ng et al., 2010). The frequent injection of OA from the BL which is less aged than the OA in the FT poses an additional important factor resulting in a wide range of f_{44}/f_{43} values at the PUY station compared to altitude stations (Figure 4.2.4).

The f44/f43 values lies principally inside the usual triangle boundaries. The reason for the situation of the f44; f43 values outside of the triangle during the summer is unsure, but could be linked to the uncertainties of these species in ACSM systems (Fröhlich et al., 2015). Those species of more biogenic origin are often reported to lie on the right hand side of the triangle (Asmi et al., 2011; Freney et al., 2011). Fröhlich et al., (2015) also reports that, depending on the season, JFJ aerosol lies inside and outside the usual triangle boundaries. OA sampled during autumn and winter are situated on the left and middle side of the triangle indicating a highest contribution from anthropogenic compared to spring and summer. OA appear to have a similar degree of ageing during autumn and winter.

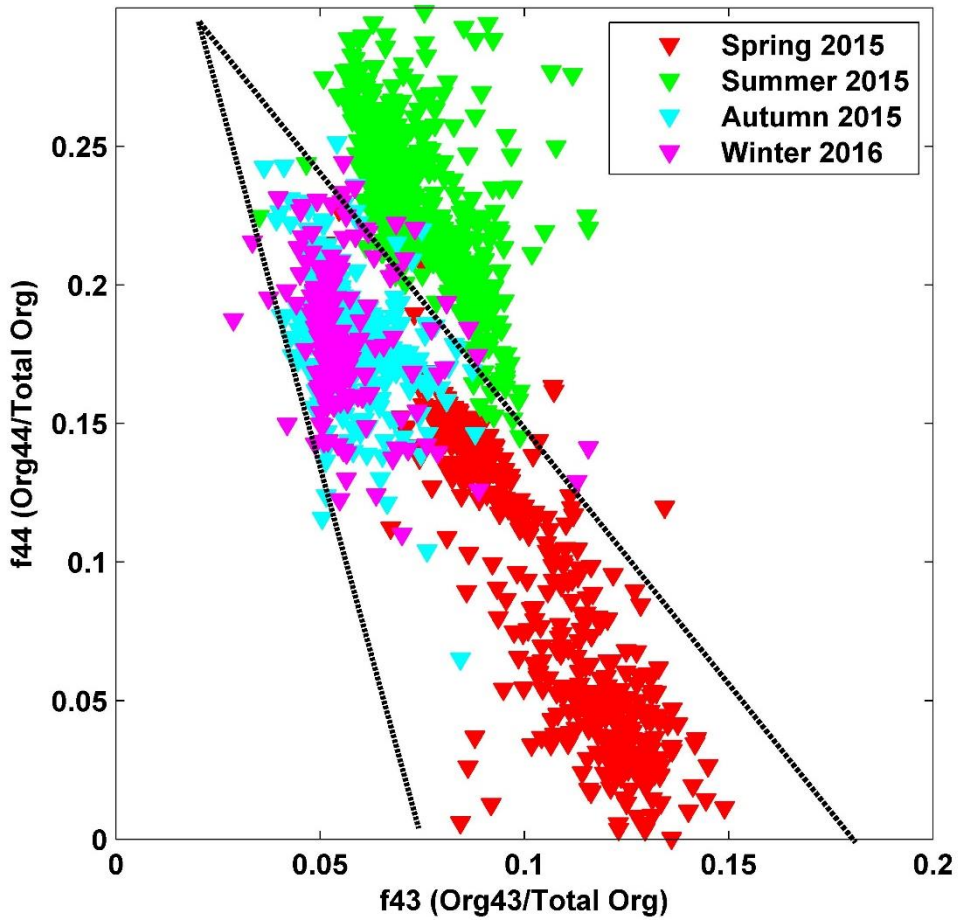

Figure 4.2. 4. Plot of the fraction of Org44 to total Organics (f44) against the fraction of Org43 to the total organics (f43) for each season. Each triangular point represents data averaged over a 180-min period. The different star shaped points show f44 and f43 of each of the different organic species extracted from the total organic signal using PMF. The black dotted lines show the boundaries set by Ng et al., (2010).

ME-2 results

In order to characterize the organic aerosol fraction collected at PUY, and to describe how the sources vary with the season, a ME-2 analysis was performed separately for all seasons. Seasonal PMF was previously performed in the literature and provides more accurate results than PMF over a full year period (Fröhlich et al., 2015; Minguillón et al., 2015; Tiitta et al., 2014). ME-2 input matrices with an m/z range of 12–100 were prepared. Higher m/z channels were removed due to low signal to noise ratios.

ME-2 was first applied without constraints (Figure 4.2.5), with solutions for 2 to 4 factors being evaluated. Two factors identified as hydrocarbon-like organic aerosol (HOA) and secondary oxygenated OA (OOA) were retrieved for all datasets. When

the number of factors is increased, another HOA factor appears, and remains in the unconstrained runs from 3 to 4 (Figure 4.2.5). Since a fraction of HOA was identified by the ME-2 without constraints at the PUY station, a high resolution mass spectra for HOA profile from Crippa et al., (2013) was used to constrain the PMF solution.

A priori information of organic aerosol source spectra is introduced into the model using the 'a value' technique available in ME-2. In the absence of distinct criteria for the determination of ideal a values a large range of a values was taken into account for the final result.

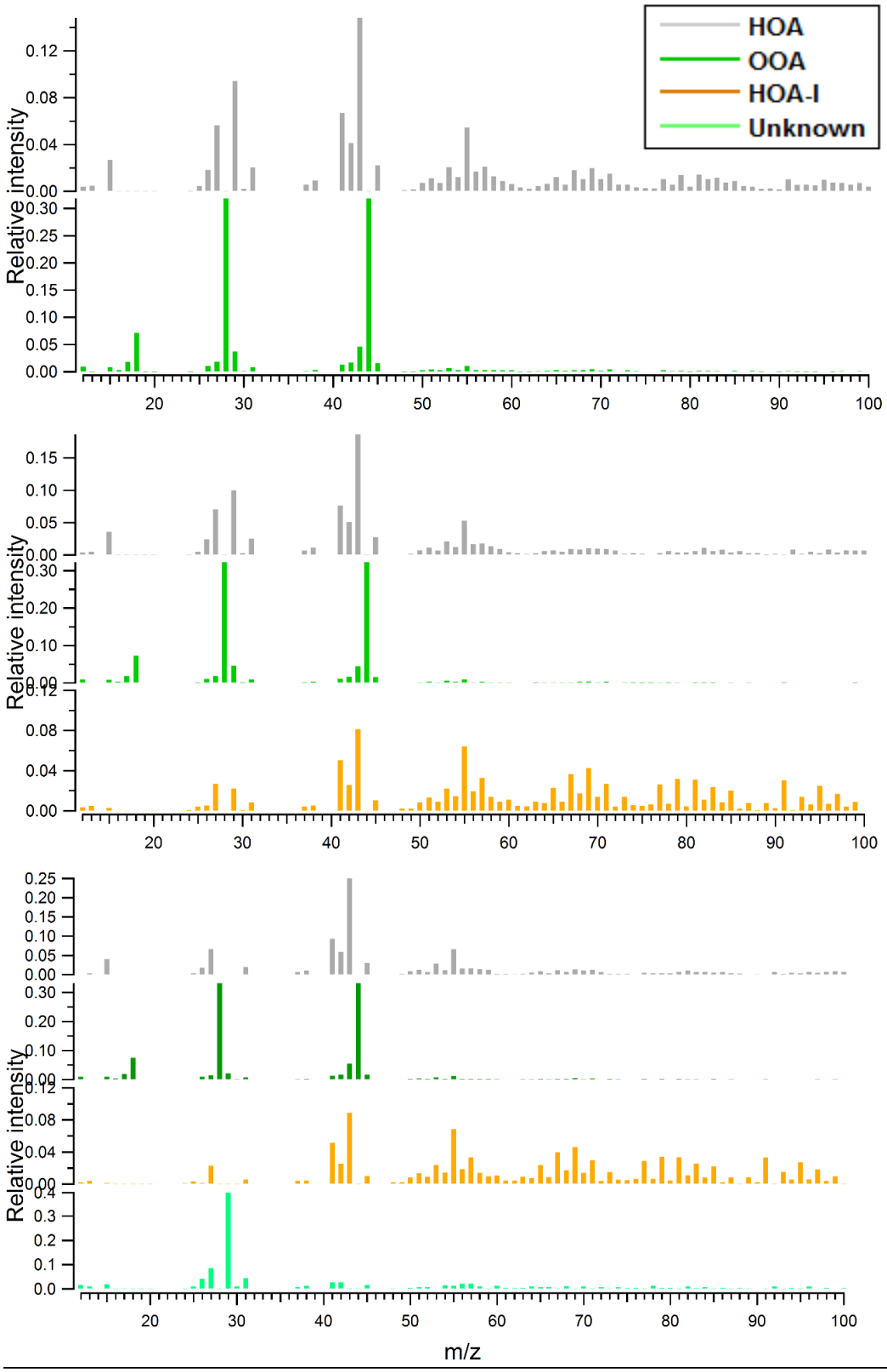

Figure 4.2. 5. Factor profiles of two, three and four factors without any constraints applied to the ME-2.

PMF/ME-2 analysis of the total organic matrix resulted in a two or three factor solution depending on the season. During all seasons, a primary and secondary organic aerosol was identified, having mass spectral profiles similar to those of Hydrocarbon organic aerosol (HOA) and oxidized organic aerosol (OOA) was identified. During the summer an addition oxidized OA factor was identified (OOA1 and OOA2) (Figure 4.2.6 and 4.2.7). Increasing the number of factors from a two to a three factor solution for spring, autumn and winter, and from three to four factor solution for summer, did not result in a significant improvement in residuals or in the correlations with external species (Figure 4.2.8). HOA mass spectra were used to constrain the PMF solution with 'a values' ranging from 0 to 0.6 (with Δa step of 0.1). For 'a values' above 0.6, HOA and OOA factors were mixed and they were therefore removed from this analysis. No other constrained were applied to this dataset.

In summer season, the first type of organic aerosol (OOA1) had a similar mass spectral signature to the OOA averaged profile reported by Ng et al., (2011). The mass spectral properties of this OOA are defined by having a dominant peak at m/z 18, 28 and 44, which underlined the low volatility and high level of oxidation characteristic of aged particles. They are therefore termed a low-volatility oxidised organic aerosol particle (LV-OOA). Furthermore, the second type of organic aerosol (OOA2) closely resembled a less aged oxidized organic aerosol. The less oxidized organic aerosol particle measured had dominant mass spectral peaks at m/z 43 and 44, and was similar to the mass spectra of semi volatile oxidized organic aerosol (SV-OOA) (Ng et al., 2011).

In agreement with the f44:f43 plots the HOA contributions to OA are lower in summer and autumn (14 ± 1%) than in spring and winter (23 ± 3%). In summer, autumn and winter, the time series of HOA showed good correlation with that of EBC (r^2 = 0.49, 0.65 and 0.44, respectively), whereas the correlation is not so good during spring (Table 4.2.1). Another source of HOA than combustion process is to be considered during spring. These results are in agreement with those of Minguillón et al., (2015) and Ripoll et al., (2015) who found an HOA contribution of 12±2% during the warmer period. Furthermore, the HOA contributions at the PUY are higher than those measured at the JFJ, where HOA contributions varied from 3% in the summer to 9% in winter (Fröhlich et al., 2015), which is expected give the higher altitude of the JFJ station. Crippa et al., (2014) and Lanz et al., (2010) found HOA contributions of 6% and 7% respectively in May 2008.

OOA contributed 86% (45% + 41% respectively for LV-OOA and SV-OOA) in summer and 80 ± 5% in spring, autumn and winter to the total OA. In summer and autumn, the time series of LV-OOA showed strongest correlations with that of EBC (r^2 = 0.6 and 0.57, respectively) (Table 4.2.1). Furthermore, weak correlations between the organic and inorganic species throughout the summer and autumn are suggesting different sources or sinks of the organics compared to the inorganic species. Fröhlich et al., (2015) at JFJ, identified a LV-OOA factor in summer; which represents the background of OOA and correlated with sulphate. Ripoll et al., (2015) at Montsec and Minguillón et al., (2015) at the Montseny, identified a LV-OOA factor in summer which also represents the background of OOA. During spring at PUY, the LV-OOA correlated with sulphate (r^2=0.46). During winter the LV-OOA component showed good correlations with sulphate, ammonium and nitrate suggesting similar sources (r^2 = 0.45, 0.52 and 0.56, respectively).

SVOOA was only identified in summer, but it contributed to 41% of OA. The time series of SV-OOA showed a good correlation with EBC (r^2=0.52) and nitrate (r^2=0.36). Fröhlich et al., (2015) also identified a less oxidised LV-OOA II and correlated better with nitrate. Ripoll et al., (2015) and Minguillón et al., (2015) also identified an SV-OOA factor only in summer. This factor is mostly attributed to fresher SOA formation and shows a low correlation with nitrate (r^2=0.16).

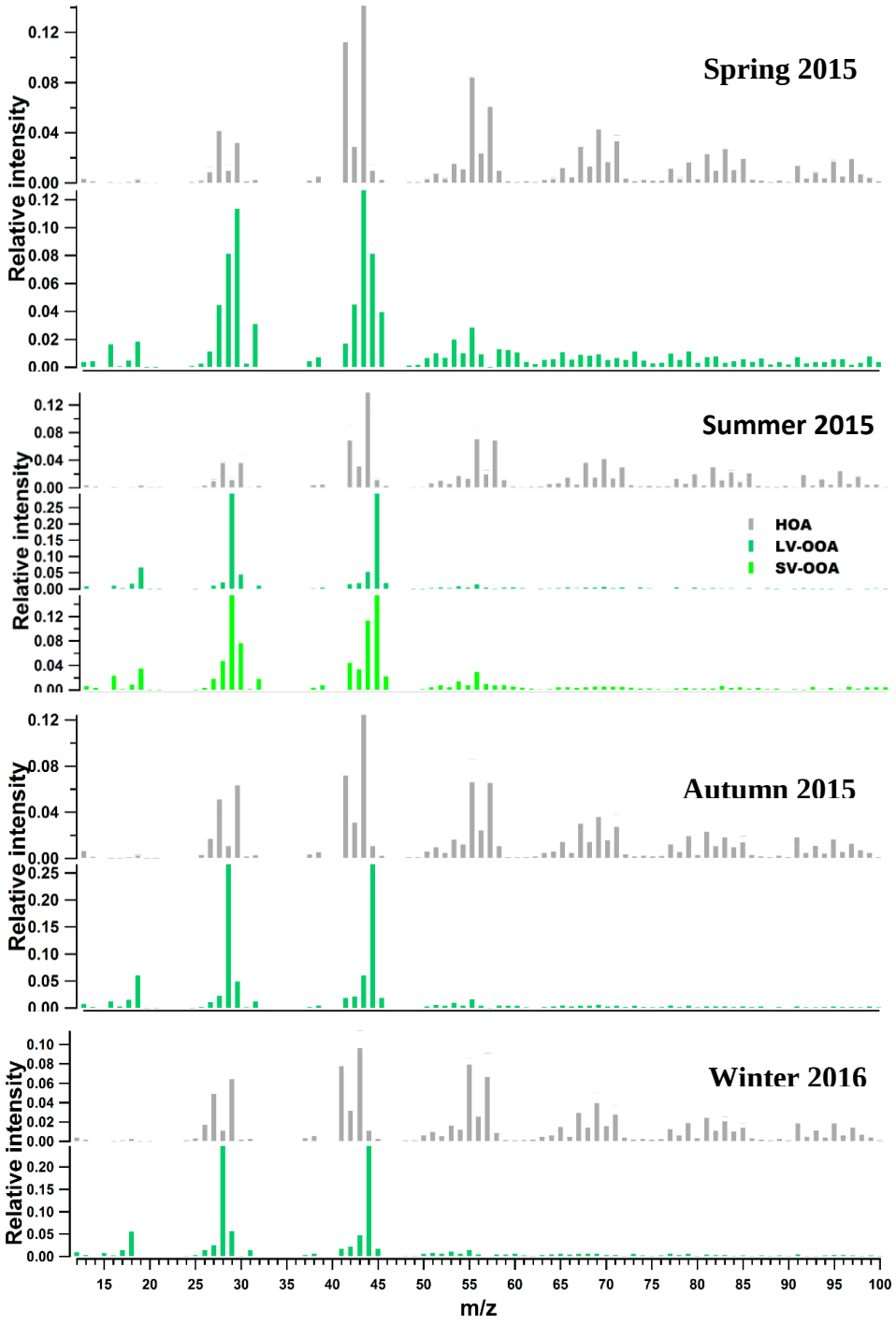

Figure 4.2. 6. Mass spectral profile of HOA (Grey), LV-OOA (Dark green) and SV-OOA (Light green) for spring, summer, autumn and winter extracted by ME-2.

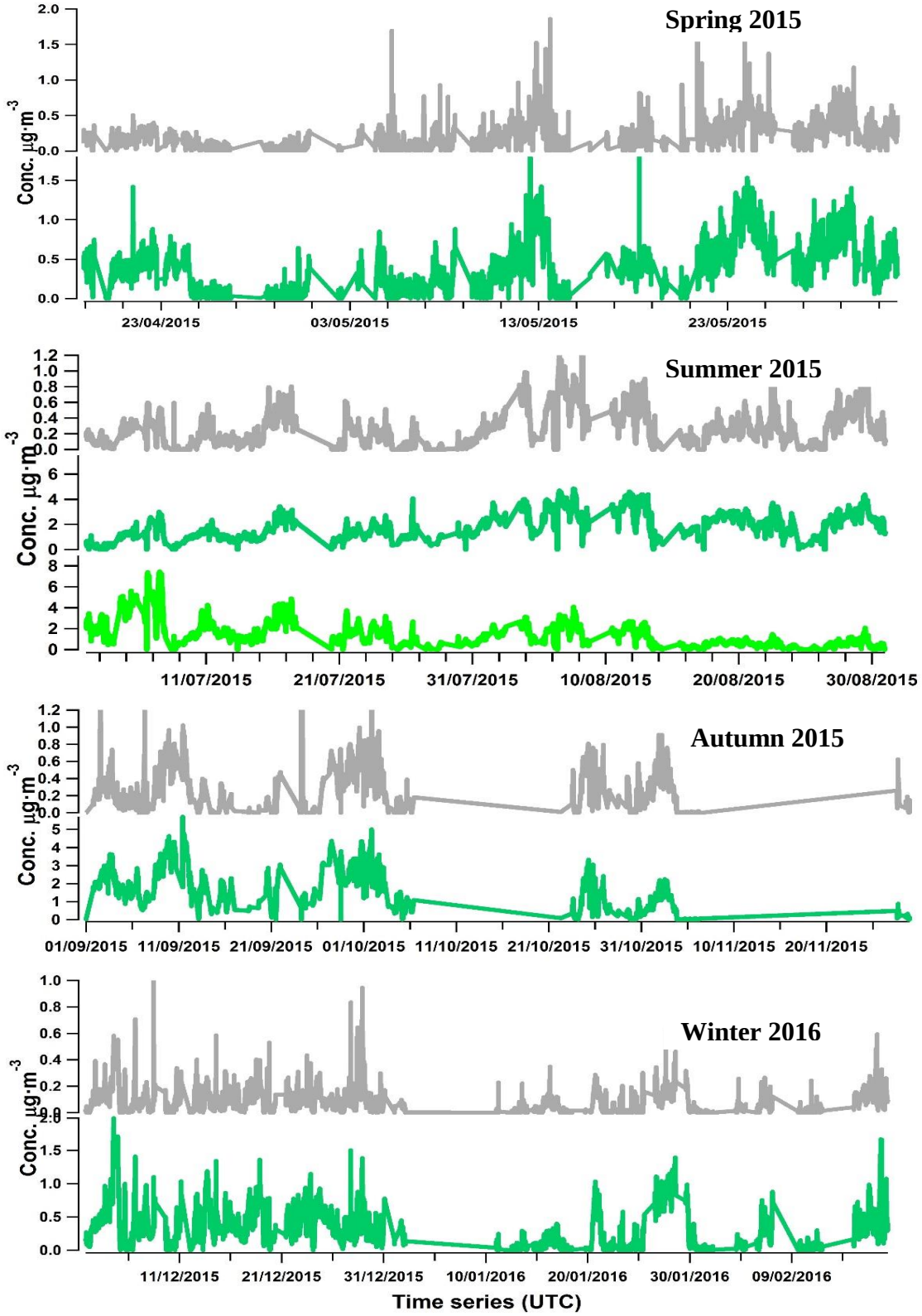

Figure 4.2. 7. Time series of ME-2 factors HOA (grey), LV-OOA (Dark green) and SV-OOA (Light green) for spring, summer, autumn and winter.

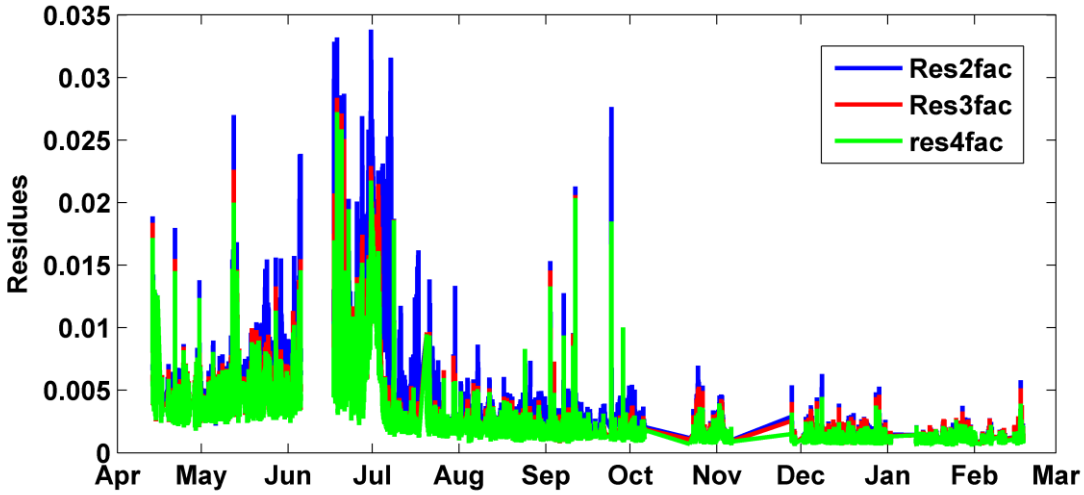

Figure 4.2. 8. Residues for: 2-, 3- and 4- factorial ME-2.

Table 4.2. 1. r^2 correlations of ME-2 components with time series of gas and particle phase species.

	Spring 2015		Summer 2015			Autumn 2015		Winter 2016	
	HOA	LVOOA	HOA	LVOOA	SVOOA	HOA	LVOOA	HOA	LVOOA
Temperature	0.11	0.09	0.01	0.05	0.13	0	0.01	0.02	0.04
Pressure	0.06	0.1	0.06	0	0.13	0.03	0	0.02	0.05
SO_2	0.1	0.07	0.17	0.11	0.21	0.26	0.33	0.06	0.06
O_3	0.02	0.01	0.06	0.07	0.04	0.15	0.02	0	0
NOx	0	0	0.05	0.01	0.04	0.21	0.06	0.1	0.03
Nitrate	0.09	0.2	0.01	0.16	0	0.18	0.37	0.32	**0.56**
Sulphate	0.26	**0.46**	0.04	0.18	0	0.19	0.23	0.18	**0.45**
EBC	0.26	0.32	**0.49**	**0.6**	**0.52**	**0.65**	**0.57**	**0.44**	**0.7**
Ammonium	0.13	0.26	0.03	0.2	0	0.2	0.29	0.25	**0.52**

4.2.3 Diurnal variations

The strongest diurnal variability in particle mass concentrations are observed in autumn and winter (Figure 4.2.9 (e, f, g and h)), which is consistent with the fact that the PUY site is expected to spend the majority of the time in the free troposphere (FT) or the residual layer during nighttime and only be affected by BL air masses during the day (Farah et al., 2018; Venzac et al., 2009). For these two seasons, we observe increases in the mass concentration of all species during the day and decreases at night, according to an increase of vertical transport from the boundary layer. For spring and summer however, the diurnal variations are weak and concentrations of nitrate even

decrease during the day compared to night (Figure 4.2.9 (a and c)). A particulate nitrate formation during nighttime and depletion during daytime could be due to temperature effects on nitrate phase partitioning. On the other hand, spring night time increases in nitrate are likely related to the lower mass concentrations of sulphate at night, allowing excess ammonia to react with nitrate (John H. Seinfeld and Pandis, 2006). Ammonia, sulphate and HOA also show no diurnal variability during spring and summer. While OOA showed daytime increases during spring (Figure 4.2.9(b)) and both for LV-OOA and SV-OOA during summer (Figure 4.2.9(d)). LV-OOA however exhibited a much less pronounced diurnal trend then SVOOA confirming its background nature. Nevertheless, the midday increase in the concentration of SV-OOA is also larger than that of EBC (Figure 4.2.10), and therefore it cannot simply be explained by the transport of pollutants, but is attributed to the secondary OA (SOA) formation during these hours in PUY.

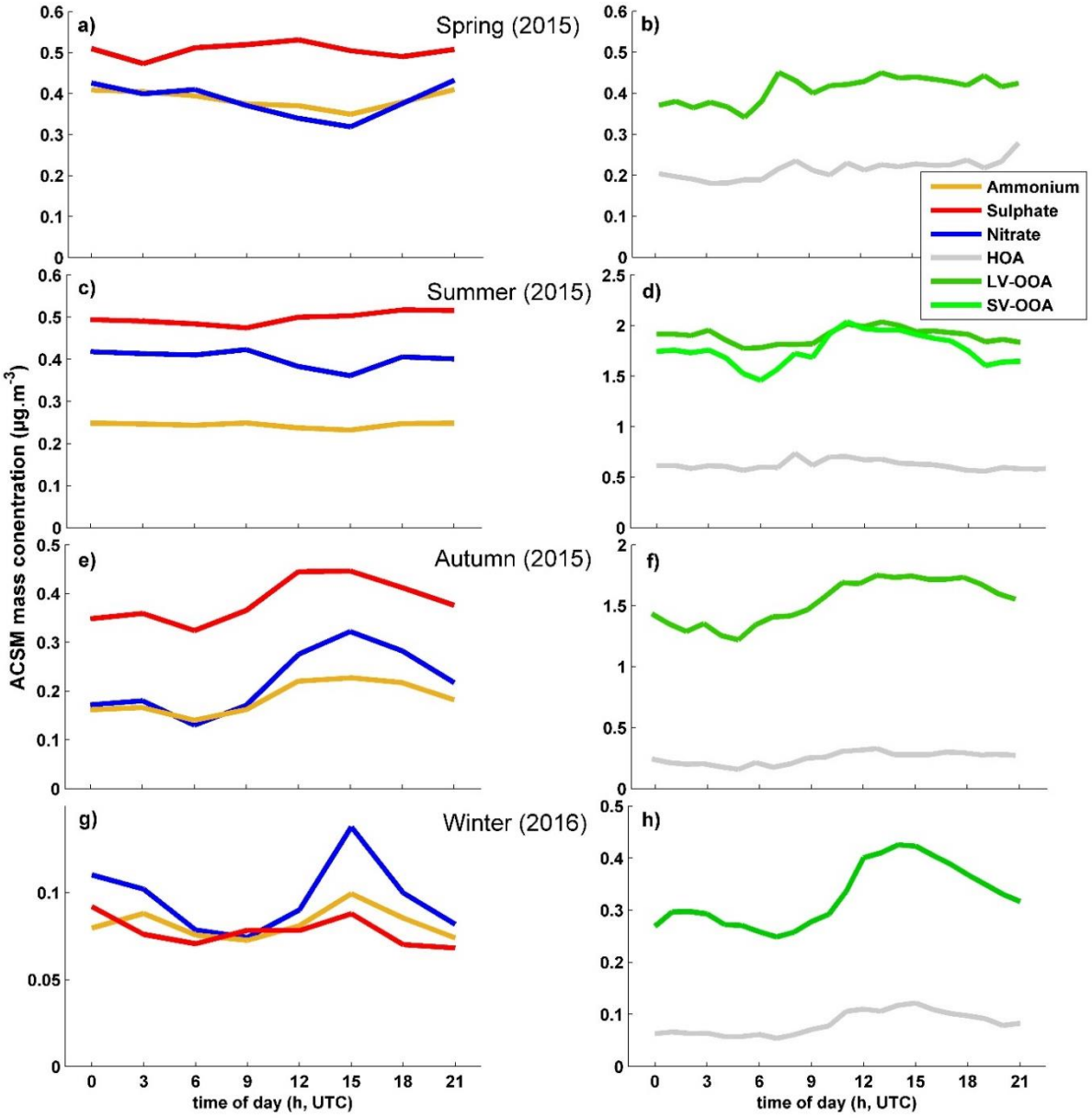

Figure 4.2. 9. Diurnal variation of mass concentration of inorganic and organic particles for Spring, (a) and (b), Summer, (c) and (d), Autumn, (e) and (f), and Winter, (g) and (h).

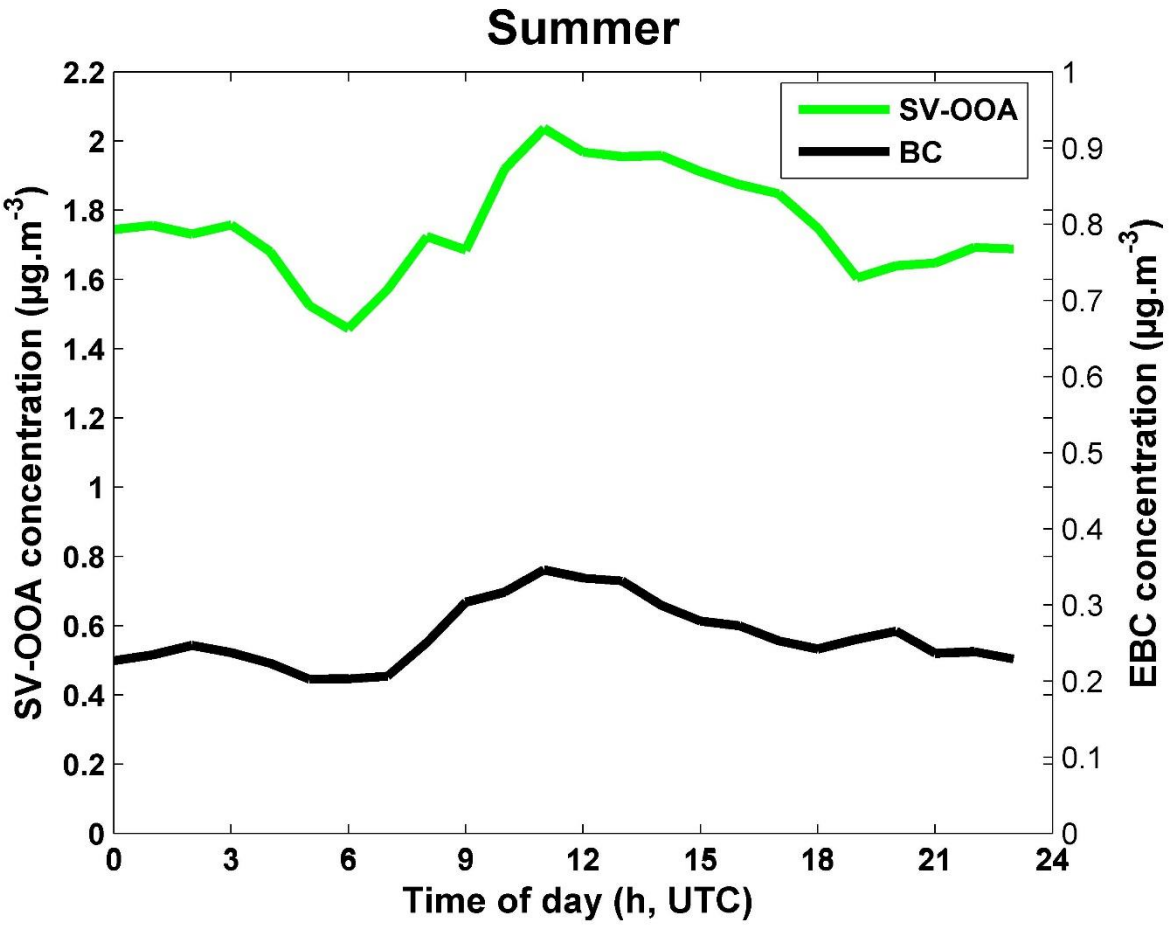

Figure 4.2. 10. Diurnal plots of SV-OOA: green and EBC: black, concentrations for summer.

4.2.4 Air mass speciation

Its central location in France makes the PUY station a good receptor site for atmospheric compounds from different source regions. The NR-PM1 and EBC aerosol particles composition is shown as a function of season and backward trajectory calculation of air mass origin into five sectors in Figure 4.2.11. Total contributions and mean concentrations for each sector are listed in Table 4.2.2 and Table 4.2.3, respectively. The sector type segregation analysis shows that air mass types contributed differently for each season. Globally, during autumn, air masses arrived mainly from the Mediterranean sector (63%) while during the other seasons, air masses arrived predominantly from the oceanic sector (46%, 43% and 54%, in spring, summer and winter, respectively). In comparison, the continental and local air masses occur less than 10% of the time independent of season (Table 4.2.2). This uneven repartition of air masses types among the seasons influences strongly the seasonal variations of the different components observed in the above section. In order to investigate this

point, it is necessary to determine how air-mass-type dependent is the chemical composition of aerosol.

The highest mean total concentrations were measured within continental air masses (4.67 $\mu.gm^{-3}$ and 4.32 $\mu.gm^{-3}$) respectively in spring and summer, while lowest concentrations are measured in oceanic modified air masses (1.16 $\mu.gm^{-3}$ and 1.13 $\mu.gm^{-3}$) respectively in autumn and winter. These observations are in agreement with Bourcier et al., (2012) and Freney et al., (2011). In terms of absolute yearly concentrations of different species (Table 4.2.3), organic concentrations are highest in continental and local air masses (6.2 $\mu.gm^{-3}$ and 5.98 $\mu.gm^{-3}$, respectively) and lowest in the marine modified sector (3.81 $\mu.gm^{-3}$). Sulphate concentrations are highest in the continental air masses as well (2.36 $\mu.gm^{-3}$) but also high in the oceanic (1.94 $\mu.gm^{-3}$) and Mediterranean air masses (2.09 $\mu.gm^{-3}$). This could indicate a marine source of sulphate in these air masses. Nitrate and ammonium are as expected highest in the continental air masses (2.1 $\mu.gm^{-3}$ and 1.80 $\mu.gm^{-3}$ respectively), but lowest in the local air masses (1.10 $\mu.gm^{-3}$ and 1.31 $\mu.gm^{-3}$ respectively). The contribution of each species to the total aerosol mass load is quite air-mass type dependent (Figure 4.2.11). In particular there is a rather strong variability of the aerosol composition on the air mass type, for a given season, as already mentioned in Freney et al., (2011) at PUY site. For example during summer, the contribution of OA to the total mass is highest in the local sector (79%), and lowest for the Oceanic modified sector (64%). This indicates that despite the low organic concentrations for the Oceanic modified sector, they contribute to a large fraction of the total PM1 aerosol mass in these air masses during summer. This feature was already pointed out in the Bourcier et al., (2012) study, where it was illustrated through offline analysis that the organic fraction of the submicron aerosol is highest for the Oceanic modified and Oceanic air mass sector. Here we show that this high OA contribution is mainly of secondary origin, the HOA contribution being the lowest in these oceanic modified air masses compared to the other air masses (LV-OOA 39%, SV-OOA 21% and HOA 4%). The highest HOA contributions were from the local sector (25% and 24%) in autumn and winter, respectively, which is coherent with fresher OA sources contributing the most in air masses that have spent a large amount of time in the vicinity of the station. SV-OOA was only identified in summer, with highest contribution from continental sector (29%) and lowest from continental and oceanic modified sectors (21% for both).

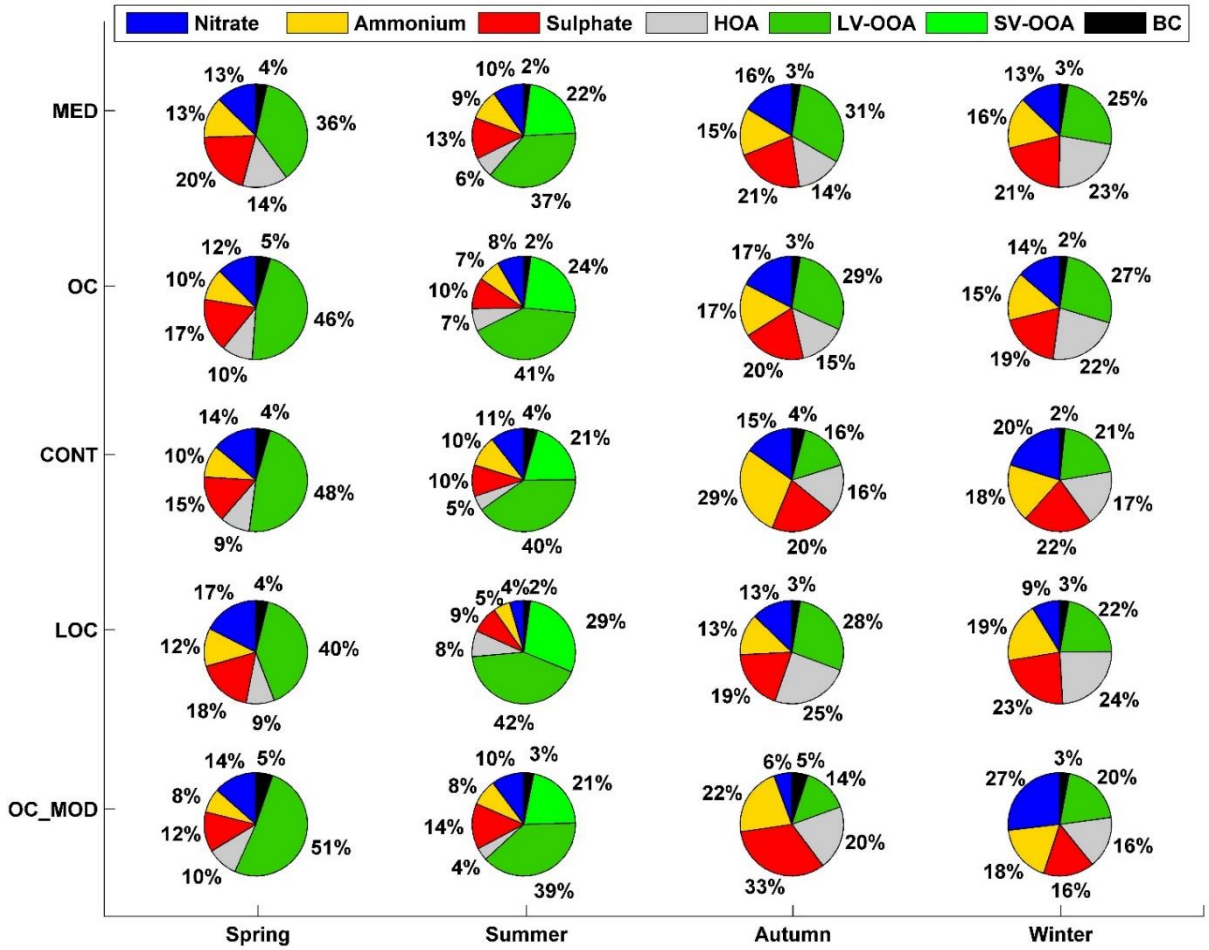

Figure 4.2. 11. Particle composition averaged over season and airmass type.

Table 4.2. 2. Total contribution of each air mass type frequency of occurrence during each season.

Contribution (%)	Spring (2015)	Summer (2015)	Autumn (2015)	Winter (2016)
Mediterranean	22%	25%	63%	23%
Oceanic	46%	43%	26%	54%
Continental	10%	10%	6%	10%
Local	7%	6%	4%	7%
Oceanic Modified	15%	16%	1%	6%

Table 4.2. 3. Mean concentrations of nitrate, ammonium, sulfate and organic as a function of air mass origin and seasons.

Mean	(µg.m^{-3})	Spring (2015)	Summer (2015)	Autumn (2015)	Winter (2016)	Total 2015/2016
Mediterranean	**Nitrate**	0.17	0.40	0.53	0.35	1.45
	Ammonium	0.29	0.36	0.53	0.40	1.58
	Sulfate	0.35	0.54	0.68	0.52	2.09
	Organic	0.95	1.80	1.37	1.35	5.47
	BC	0.05	0.05	0.05	0.05	0.20
	PM1	1.81	3.15	3.16	2.67	10.79
Oceanic	**Nitrate**	0.26	0.30	0.26	0.61	1.43
	Ammonium	0.32	0.33	0.32	0.55	1.52
	Sulfate	0.45	0.48	0.36	0.65	1.94
	Organic	1.15	1.79	0.82	1.23	4.99
	BC	0.04	0.05	0.04	0.06	0.19
	PM1	2.22	2.95	1.80	3.10	10.07
Continental	**Nitrate**	1.09	0.59	0.21	0.20	2.10
	Ammonium	0.72	0.49	0.23	0.34	1.80
	Sulfate	0.85	0.73	0.19	0.57	2.36
	Organic	1.92	2.43	0.55	1.29	6.20
	BC	0.09	0.08	0.03	0.04	0.26
	PM1	4.67	4.32	1.20	1.44	12.72
Local	**Nitrate**	0.16	0.29	0.55	0.10	1.10
	Ammonium	0.20	0.36	0.47	0.28	1.31
	Sulfate	0.31	0.56	0.59	0.32	1.78
	Organic	1.89	1.96	1.53	0.60	5.98
	BC	0.06	0.04	0.07	0.03	0.20
	PM1	2.62	3.21	3.21	1.33	10.37
Oceanic Modified	**Nitrate**	0.71	0.27	0.11	0.14	1.23
	Ammonium	0.60	0.27	0.26	0.27	1.40
	Sulfate	0.78	0.41	0.28	0.22	1.69
	Organic	1.47	1.40	0.46	0.48	3.81
	BC	0.05	0.06	0.05	0.02	0.18
	PM1	3.61	2.41	1.16	1.13	8.21

We clearly see that the aerosol composition is clearly dependent on the air mass type for a given season, but also that for all air mass types, the same seasonal variation is observed with a sharp increase of organic matter and percentage during summer compared to the other seasons. At the PUY site, these variations in season and with air mass source can sometimes be influenced by the boundary layer dynamics. In the next section, we will segregate between BL and FT conditions, in order to better assess the seasonal variability of the aerosol composition in a given layer of the atmosphere.

4.2.5 FT/BL conditions

In this section, we apply the method described in Farah et al., (2018) classification air masses as being FT or BL using a combination of the four indicators of FT/BL. The Wilcoxon–Mann–Whitney test (DePuy et al., 2005) was applied to medians of each aerosol chemical component (Ammonium, nitrate and sulphate) and organic sources (HOA, SV-OOA and LV-OOA), in order to assess whether these measurements show statistically significant differences between their BL or FT concentrations (Figure 4.2.12).

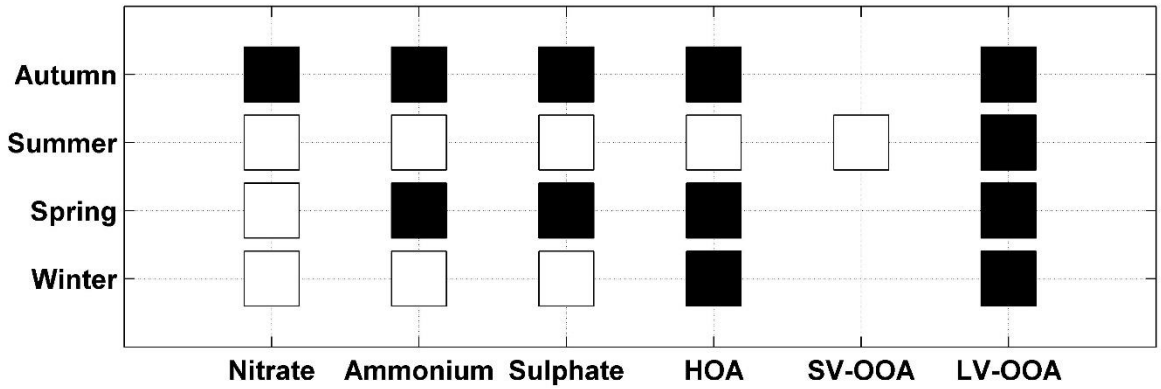

Figure 4.2. 12. Wilcoxon–Mann–Whitney test applied on nitrate, ammonium, sulphate and organic: HOA, SV-OOA and LV-OOA concentrations measured for each season. The squares are black (white) when the medians are significantly different (equal) with a threshold of 5%.

Figure 4.2.12 shows that the chemical composition of the non-refractory PM1 aerosol in the FT differs from the one of the BL during autumn and spring for most compounds (except nitrate in spring which is the same in the BL and in the FT). When concentrations are different between BL and FT, they are higher in the BL compared to the FT for inorganic species (Figure 4.2.13). This is expected, as the particulate mass source of these compounds is believed to be located in the BL, and eventually reaches the FT under favorable conditions. Higher concentrations of nitrate in the BL than in the FT are in agreement with Fröhlich et al., (2015) at the JFJ site, who reports highest concentrations of nitrate in BL during autumn.

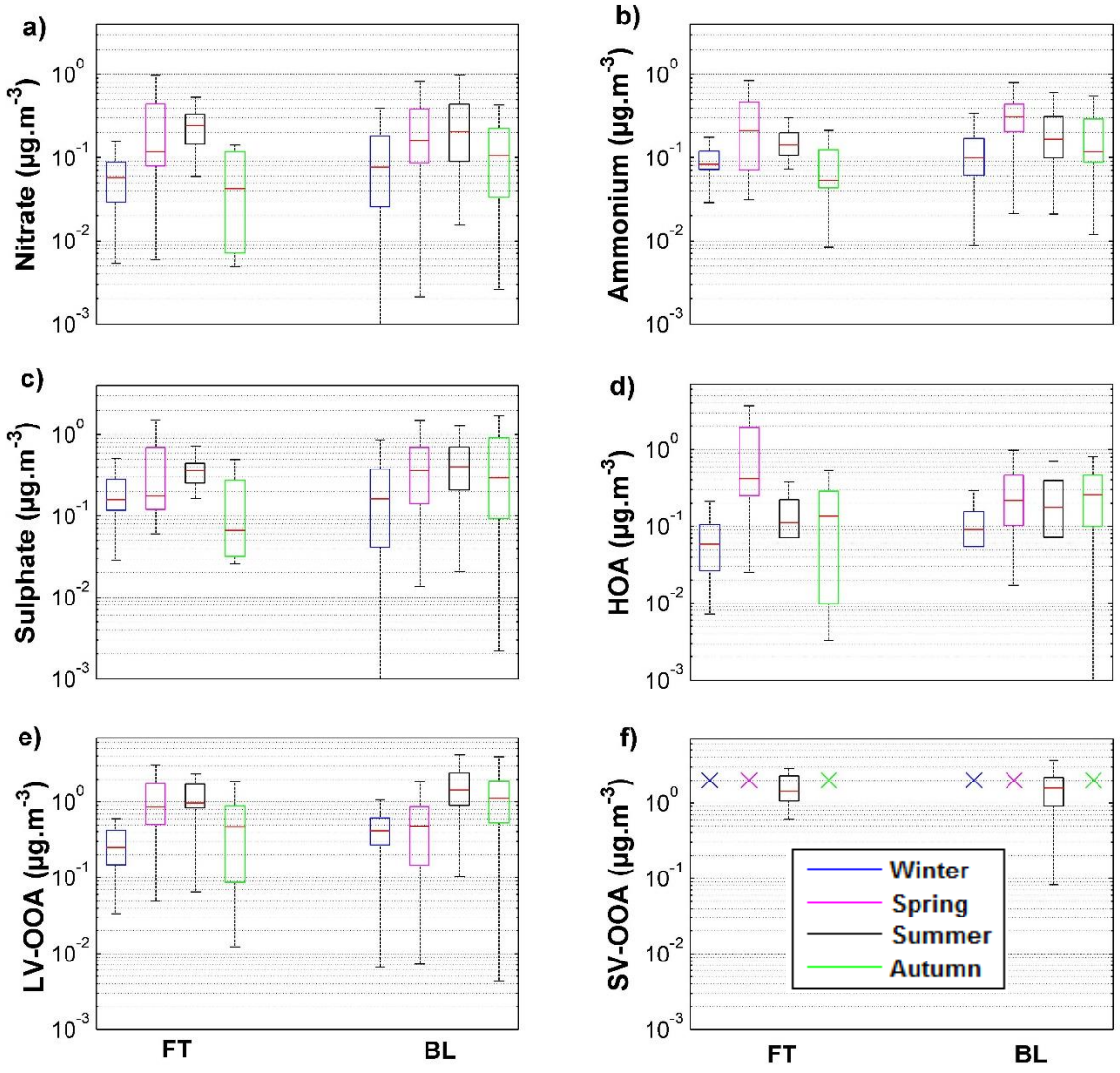

Figure 4.2. 13. FT/BL variation of: a) Nitrate, b) Ammonium, c) Sulphate and d) HOA, e) LV-OOA, f) SV-OOA, concentrations for the four seasons at the PUY site. Red line represents the median value, bottom and top sides of the boxes symbolize the 25th and 75th percentile respectively and the extremities of the black lines are the 10th and 90th percentile.

For organic species, we also observe that concentrations were higher in the BL than in the FT for HOA and LV-OOA during winter and autumn, but a more surprising feature is that during spring, the median concentrations of HOA and LV-OOA are higher in the FT (0.41 µg/m^{-3} and 0.86 µg/m^{-3}, respectively) than in the BL (0.22 µg/m^{-3} and 0.48 µg/m^{-3}, respectively). These observations are in agreement with what have been found by Crumeyrolle et al., (2013) during airborne measurements over central Europe and the north sea in May 2008. The latter study showed an enhancement of the total mass concentration (mainly organic) in the altitude range

between 1 and 3 km in air masses originating from south and east Europe. Farah et al., (2018) reported that at the same site, higher EBC, Aitken and accumulation mode particle concentrations were observed in the FT compared to the BL during spring, while for the other seasons concentrations were higher than or equal to the FT concentrations. Higher concentrations in the FT during spring were attributed to the active transport by heat convection of particles from BL to the FT originating from open biomass burning events occurring during this season. This would be in agreement with the higher concentrations of HOA in the FT compared to BL during this season. LV-OOA could be a contributor to the observed nucleation and growth of particles in the FT that might be due to photochemical processes of organic vapors (Boulon et al., 2011). Farah et al., (2018) also investigated the air mass back-trajectory relative to the latest contact with the BL over the last 204 hours. They show that during spring and summer, around 60% of air masses sampled in the FT were in the BL 15 hours before sampling which indicates that aerosol properties measured in the FT during these seasons are more influenced by the BL than during the other seasons. While, for autumn and winter, over 80% of air masses did not have any contact with BL for at least 75h before being sampled at PUY. In this study, the NR-PM1 chemical properties during these periods need to be treated with caution due to the limited statistics in the aged (>75h) FT air masses. Organic was the most abundant component 58%, followed by sulphate 18%, nitrate 10%, ammonium 9% and EBC 5% (Figure 4.2.14).

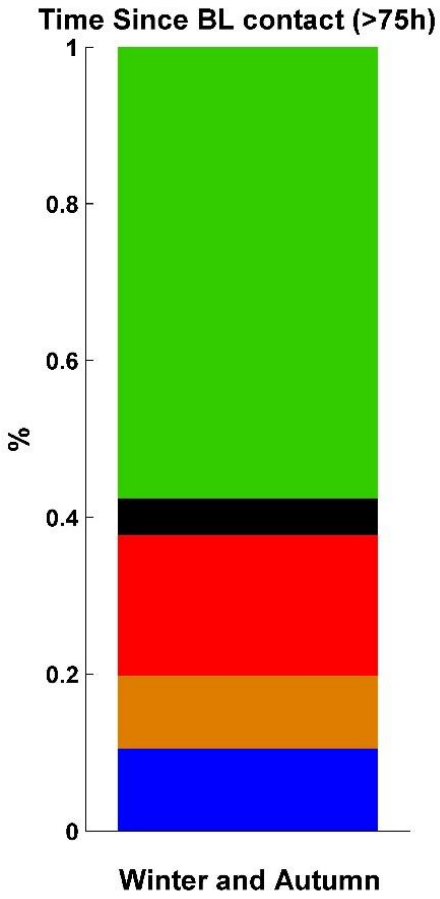

Figure 4.2. 14. Bar plot of average relative concentrations of non-refractory submicron aerosol as measured by ACSM as a function of >75h in the FT before the last BL contact for winter and autumn seasons.

Additionally, the chemical composition of the FT is not significantly different in the FT than in the BL for all inorganic components and SV-OOA in summer and winter. This result is in agreement with similar accumulation mode concentrations found in both layers during summer (Farah et al., 2018), presumably as a result of a better mixing between BL and FT than during the other seasons for summer. The lack of differences in the composition of the BL and FT aerosols during winter for inorganic species is however not well understood and would call for further investigations, for instance with modeling tools.

The mass ratio of submicron sulphate to organics (SO_4/org) is a useful marker to describe the acidity of aerosols. In this study, this ratio showed higher values (0.5) in the FT air masses than those in the BL layer (0.35), in agreement with previous studies from high altitude sites or airborne measurement, in North America; Western Europe and Asia, where reports higher values (0.72 to 1.1) in the FT air masses than those in

the boundary layer (0.13 – 0.7) (Zhou et al., 2018). However the values in this study are low, indicating that the majority of the species are neutralized at the PUY site.

4.2.6. Conclusions

The present study investigates one year of aerosol chemical properties using a ToF-ACSM from April 2015 to February 2016 at PUY site, providing an opportunity to study the temporal variability of aerosol chemistry in relation with boundary layer dynamics/vertical transport and air mass sources. OA represents a substantial part of the PM1 concentration during all seasons and within all air mass types. Depending on the season, organics comprised from 48 to 73 % of the total mass. A detailed analysis of the seasonal source apportionment of organic species, using the ME-2 technique showed that the HOA contributes between 14% and 23% of the OA mass. The prevailing OA source was the OOA (74-85%) that could be segregated into a background LV-OOA and SV-OOA during the summer months.

OA has the highest contribution to total mass during summer, while in winter and during the transient months comparably high fractions of sulphate were measured. Nitrate and ammonium contributed lower amounts. The high contribution of OA during the summer months was identified to be the result of not only vertical transport, but also the result of a larger secondary organic formation during the warmer months. Highest mean total concentrations were measured within continental air masses, while lowest concentrations are measured in local and oceanic modified air masses.

The PUY site is sampling in the FT approximately 20% of the time, providing us with a chance to compare aerosol properties in both the FT and the BL. Higher median concentrations of ammonium and sulphate in autumn and spring, and nitrate in autumn were measured during BL conditions compared to FT conditions, coherent with the contribution of surface-related sources of these species to these aerosol composition. Higher organic particle concentrations (HOA and LVOOA) were observed in the FT compared to the BL in spring corresponding to higher Aitken and accumulation mode particle concentrations in this layer and season reported by Farah et al., (2018).

This combination of in-situ measurements, back-trajectory analysis and segregation between FT and BL contribute to better understanding of aerosol particles sources, properties and their dynamics in the atmosphere. In particular, we have illustrated that the aerosol chemical properties at lower atmospheric layers (i.e. BL, FT)

are similar to what have been found using the in situ measurements at other European ground sites, despite variable sources. These measurements can be used to evaluate and compare with atmospheric transport models.

4.3. Understanding sources of aerosol particles and their exchanges between the high altitude PUY and its surrounds.

In order to study the exchanges between atmospheric layers, we deployed a number of instruments at a low altitude site to run in parallel with the measurements performed at the PUY station. In this chapter, we will firstly present an overview of meteorological parameters and chemical composition observed at the PUY station and at the AtmoAura's station during the intensive campaign (winter 2018). In the second part, a comparison will be carried out between the two sites in terms of chemical composition and sources of organic aerosols influencing these sites as a function of free troposphere/boundary layer segregation.

4.3.1 Overview

This intensive sampling period took place in winter 2018, from December to March 2018 when a ToF-ACSM instrument, owned and operated by INERIS was installed at a low altitude sampling site simultaneously to the ToF-ACSM running at the PUY station. The low altitude sampling site, the regional air quality network AtmoAura's, station, is situated near the Clermont-Ferrand city center and can be considered as an urban background station (Figure 4.3.1 (a)). The winter season was chosen due to the higher frequency of occurrence of FT conditions at the Puy de Dome and to the occurrence of high aerosol concentrations in the city of Clermont-Ferrand. Our sampling strategy provided us with the opportunity to analyze, at high temporal resolution, the chemistry of fine particles simultaneously in both urban and regional sites, in order to evaluate the influence of boundary layer dynamics on the vertical mixing of aerosol properties and local aerosol sources in an urban environment. In addition to the chemical measurements, additional measurements of meteorological properties and black carbon (AE33) were performed at both sites. PM_1, $PM_{2.5}$ mass concentration measurement were also performed at AtmoAura station, while PM_{10} mass concentrations were performed at the PUY station. We used statistical (ie. correlation) and receiver source (ie. PMF) tools to establish the origin of aerosol organic particles at both sites. HYSPLIT backward trajectories were used to better understand the impacts of air masses on the chemical composition and overall concentrations measured by the ACSM.

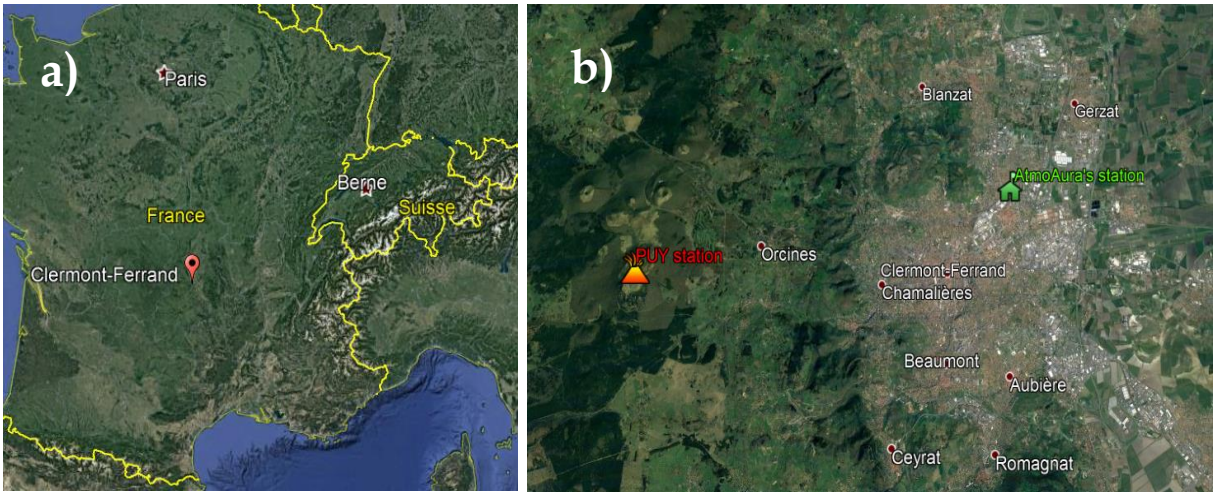

Figure 4.3. 1. **a)** Regional map of Clermont-Ferrand, **b)** Zoom on Clermont-Ferrand city. The green house represents the AtmoAura's station (Montferrand) in downtown Clermont, and the orange volcano represents the PUY station.

An overview of meteorological parameters and PM_1 chemical composition is presented in the next section.

4.3.2 Characterization of meteorology, back-trajectories

In this study we focused on the period started on the 1th of February and continued until the 28th of February, 2018, in which the ACSM operated continuously at both stations. For the first two weeks of February, oceanic air masses arrived at the stations (Figure 4.3.2). Average temperatures and wind speed were (0°C ± 5°C and 10 m/s ± 6 m/s) and (7°C ± 5°C and 2.5 m/s ± 2 m/s), for PUY and AtmoAura's stations, respectively and there were several cloud periods. From the 20th of February onwards, cold and dry air masses arrived from the continent. During the cold event, the temperature were as low as -17°C and -10°C and the wind speed were around 4 m/s ± 2 m/s and 3 m/s ± 1.4 m/s, respectively for PUY and AtmoAura's stations. According to Météo-France, the cold weather was a result of the "Moscow-Paris" cold front resulting in exceptionally cold temperatures over a large area in Europe.

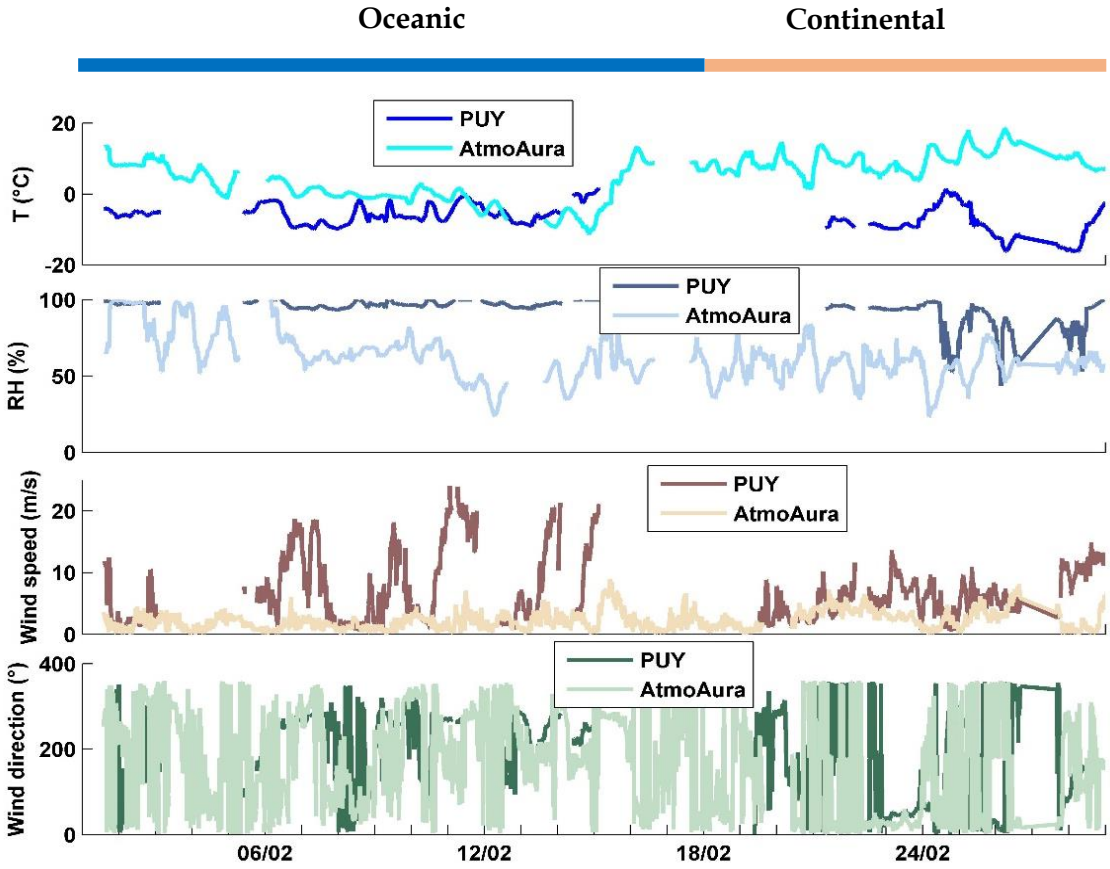

Figure 4.3. 2. Comparison of time series of meteorological parameters measured at the PUY and AtmoAura's, stations. Colored bars at the top of each graph indicate the source of the air mass.

In section 4.1, we described a method to segregate FT/BL air masses using a combination of four parameters (WCT, ^{222}Rn, NOy/CO and ECMWF) measured at the PUY station. In the present chapter, WCT, ^{222}Rn and NOy/CO were not available, and therefore only the ECMWF model was applied to segregate between BL and FT air masses. The resulting classification as a function of time is shown as horizontal bars on the upper part of Figure 4.3.4. During the first period when the site was mainly under oceanic influence, the station was sampling FT air, while during the second period when the site was mainly under continental influence, the station was sampling BL air.

4.3.3 Bulk PM1 chemical composition

The aerosol chemical measurements at the Puy de Dome averaged over the entire campaign, consisted of 0.2 µg/m^3 organics (dominant species), 0.04 µg/m^3 sulphate, 0.08 µg/m^3 nitrate, 0.06 µg/m^3 ammonium and 0.08 µg/m^3 EBC (Figure 4.3.3 bottom). These concentrations are very similar to the ones reported in chapter 4.2 for the whole

winter 2016, with 0.1 µg/m^{-3} organics, 0.05 µg/m^{-3} sulphate, 0.04 µg/m^{-3} nitrate, 0.07 µg/m^{-3} ammonium and 0.05 µg/m^{-3} EBC, although they appear to be slightly higher and more variable in February 2018 than in winter 2016 (Figure 4.3.3).

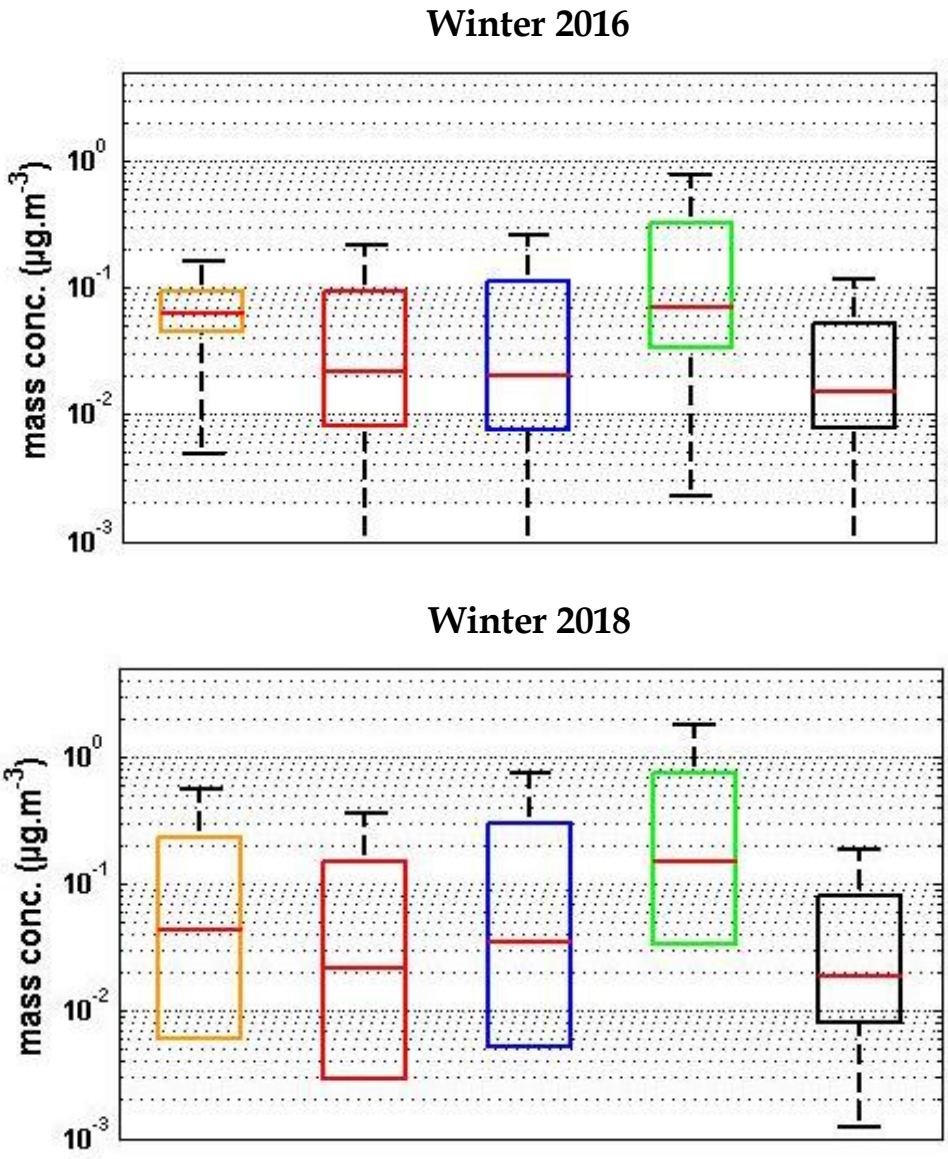

Figure 4.3. 3. Comparison of boxplots (in µg/m-3; line: median; box: interquartile range; whiskers: 10–90th percentile range) for species measured with the ACSM (ammonium: orange; sulphate: red; nitrate: blue; organic: light green) and EBC: Equivalent black derived from AE33 at PUY for winter 2016 and winter 2018.

While at AtmoAura station, the average concentrations over the entire campaign consisted of 2.2 µg/m^3 organics, 1.3 µg/m^3 nitrate, 0.5 µg/m^3 ammonium, 0.36 µg/m^3 sulphate, 0.04 µg/m^3 chloride and 1 µg/m^3 EBC; they appear to be always higher at AtmoAura compared to those at PUY (Figure 4.3.4). During this sampling period two

very distinct periods are identified, illustrated by a strong contrast on the meteorological conditions, with different air mass origins. These contrasting periods are also reflected in the PM_1 and the origin of air masses. The first period is identified from 2nd to 13th of February, while the second period is from 21th to 28th of February (excluding the 24th). We will discuss separately these two periods.

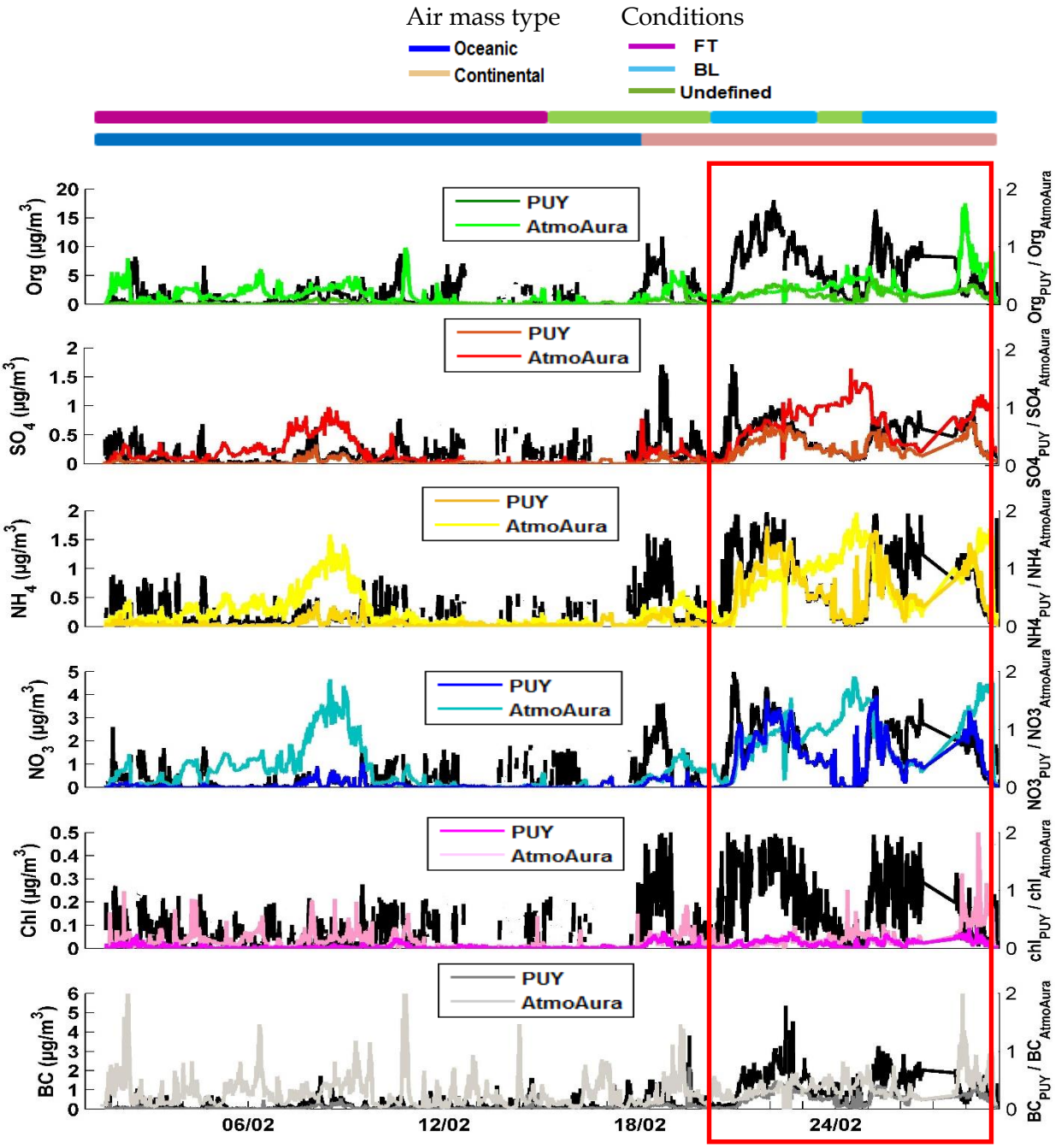

Figure 4.3. 4. Left axis: Comparison of PM1 chemical composition from ACSM (organics (Org), sulphates (SO_4), nitrates (NO_3), ammonium (NH_4), chloride (Chl)) and equivalent black carbon (EBC)

measurements at PUY and AtmoAura's stations. Right axis: Ratio of PUY over AtmoAura concentrations (Black). Colored bars at the top of each graph indicate the source of the air mass and FT/BL conditions. Red box: time series plot of the BL region for the PUY and AtmoAura's stations.

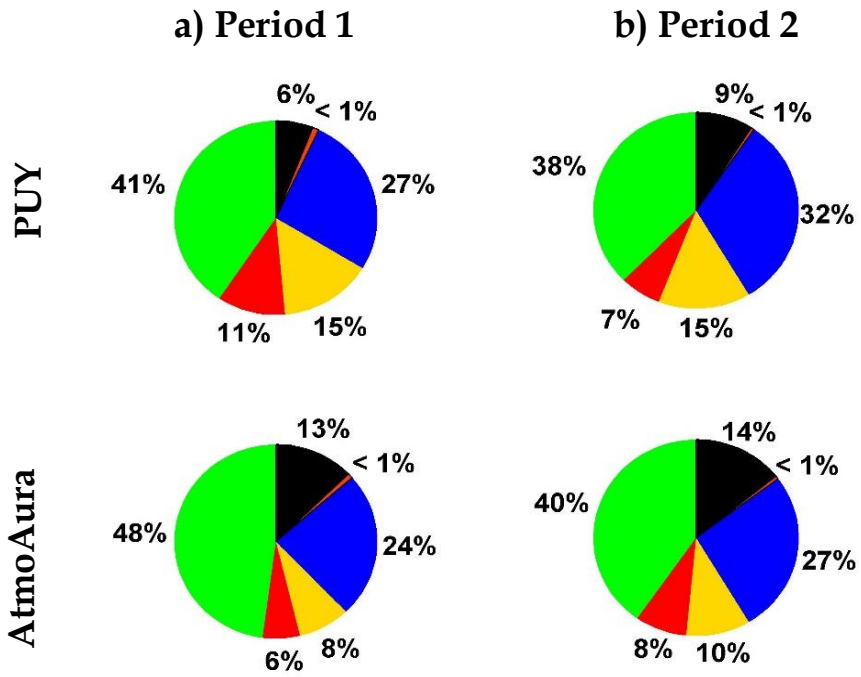

Figure 4.3. 5. Comparison of relative species concentration (SO4 (red), NH4 (orange), NO3 (blue), organics (green) and EBC (equivalent black carbon)) for **a)** period 1 and **b)** period 2 at PUY and AtmoAura's stations.

4.3.3.1 PUY Free Tropospheric (FT) conditions

4.3.3.1.1 Time series and concentrations

During the first period, the PUY station was influenced by warm and wet FT oceanic air masses (Figure 4.3.4 (violet bar)). The average chemical composition are different between the PUY and AtmoAura stations (Figure 4.3.5 (a)). Organic and EBC have higher relative concentrations at AtmoAura (48% and 13%, respectively) compared to PUY (41% and 6%, respectively), while SO_4, NH_4 and NO_3 have lower relative concentrations at AtmoAura (6%, 8% and 24%, respectively) compared to PUY (11%, 15% and 27%, respectively). In terms of absolute concentrations, PM_1 concentrations are low at PUY (0.13 µg/m^3, 0.035 µg/m^3, 0.07 µg/m^3 and 0.02 µg/m^3, respectively for Org, NH_4, NO_3 and SO_4), while at AtmoAura's station, the PM1 mass concentrations are high (1.6 µg/m^3, 0.27 µg/m^3, 0.78 µg/m^3 and 0.2 µg/m^3, respectively for Org, NH_4, NO_3 and SO_4), (Figure 4.3.4). The concentrations at the Puy

de Dome are only 30% of those measured at the AtmoAura for all species, except for sporadic episodes of BL air intrusions to the level of the PUY station, at the very beginning of the period (from 2nd to 4th) and during the 10-12th of February (Figure 4.3.4 black).The different levels of concentrations detected at the two sites suggests that the boundary layer (or aerosol layer) is not well mixed to the altitude of the PUY, and confirms the ECMWF model predictions to classify air masses at PUY as FT air masses.

4.3.3.1.2 Diurnal variations

Different diurnal patterns are also observed for the PM1 at both stations (Figure 4.3.6 (a and b)). A weak daily pattern is seen for ammonium and sulphate at both sites. The organic species peak during the morning and evening rush hours at AtmoAura's station, corresponding to peaks in road traffic, while at the PUY station, higher values are recorded between 9 UTC and 19 UTC. The same diurnal variation is observed for nitrate, ammonia and sulphate at the PUY station. For EBC, the morning and evening peaks at the AtmoAura station are the same than for the organic aerosol, showing the influence of traffic-originating aerosol. The EBC at the PUY site is a good tracer for the transport of BL air masses, and at the station, but does not show any strong diurnal variation, unlike the secondary species (organics, nitrate, sulphate, ammonia), which illustrate increases during the day. These observations might suggest that the daytime increase of the secondary species (nitrate, ammonia, sulphate) are not due to vertical transport from the BL but due to secondary aerosol formation linked to photochemistry within the FT (Figure 4.3.6 (c)).

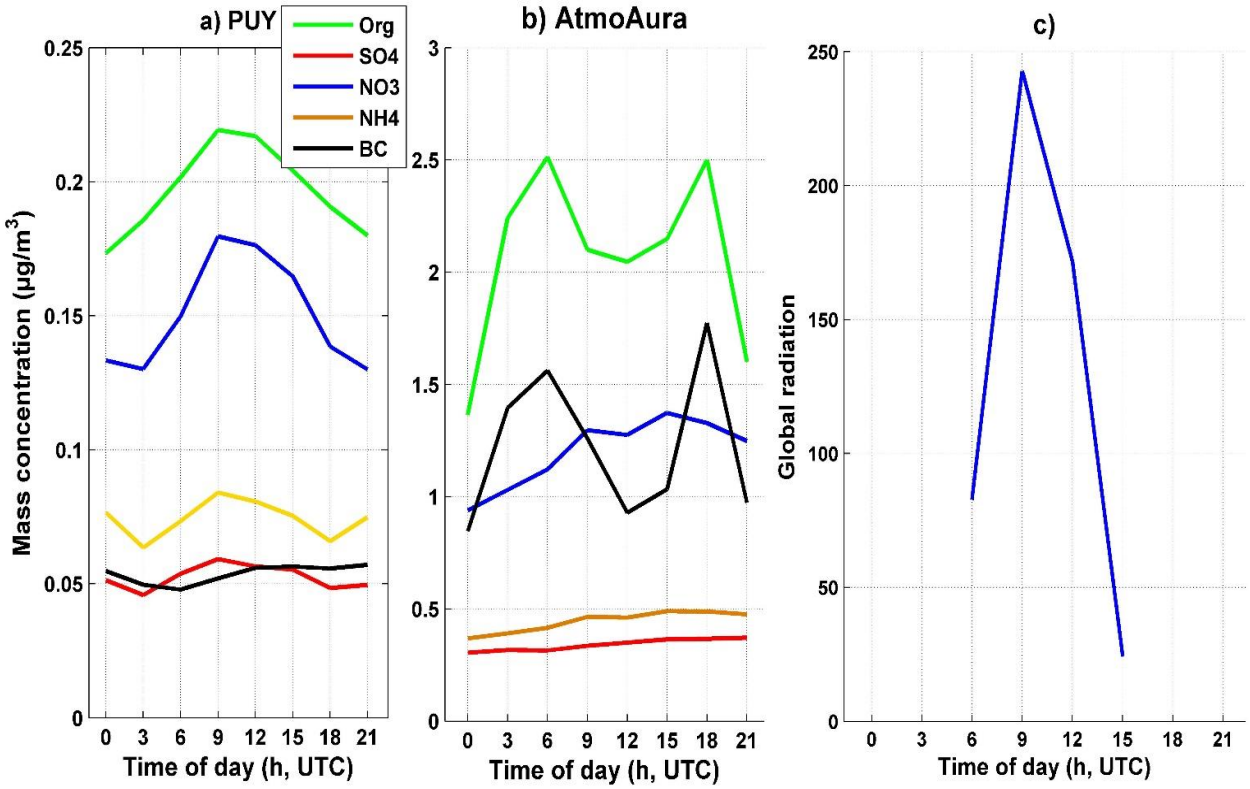

Figure 4.3. 6. Diurnal cycles of organic, inorganics and black carbon throughout the FT period at: **a)** PUY and **b)** AtmoAura. **c)** represents the diurnal cycle of global radiation at PUY station.

4.3.3.2 PUY Boundary Layer (BL) conditions

4.3.3.2.1 Time series and concentrations

From Figure 4.3.7, we observe that while the ECMWF model classified air masses arriving at the PUY station as BL air masses, the ratio of the PUY/AtmoAura concentrations for most species is significantly lower than 1 during some short periods. During these short periods we hypothesis that the ECMWF model overpredicts the BLH over the PUY station and further classified air masses into mixed layer periods and transition zone periods (Figure 4.3.7)). In the following we only use mixed layer periods for comparing the PUY and AtmoAura stations concentrations.

For the second period of February, the PUY and the AtmoAura stations were influenced by a cold and dry BL continental air masses (figure 4.3.4 (blue bar)) and the ECMWF model predicts that the PUY station lays within the BL. Coherent with model estimations, the average composition and time series are similar among the sites for

both organic and inorganic fractions (2.3 µg/m^3 ± 0.05 µg/m^3, 0.82 µg/m^3 ± 0.05 µg/m^3, 1.97 µg/m^3 ± 0.01 µg/m^3 and 0.5 µg/m^3 ± 0.1 µg/m^3 respectively for Org, NH_4, NO_3 and SO_4). The observed homogeneity in terms of chemical composition, mass concentration and sources among the two sites indicates that the background regional level, observed at PUY contributes to a high proportion of the concentrations observed in the city of Clermont-Ferrand. This is also shown by the ratio of concentrations measured at PUY over concentrations measured at AtmoAura, which often reach 1 for most species when the model predicts that the PUY station lays within the BL (Black line in Figure 4.3.4).

Furthermore, It can be noted that the distribution of species is very similar between the sites for period 2 (BL) and between period 1 and 2 for the AtmoAura site.

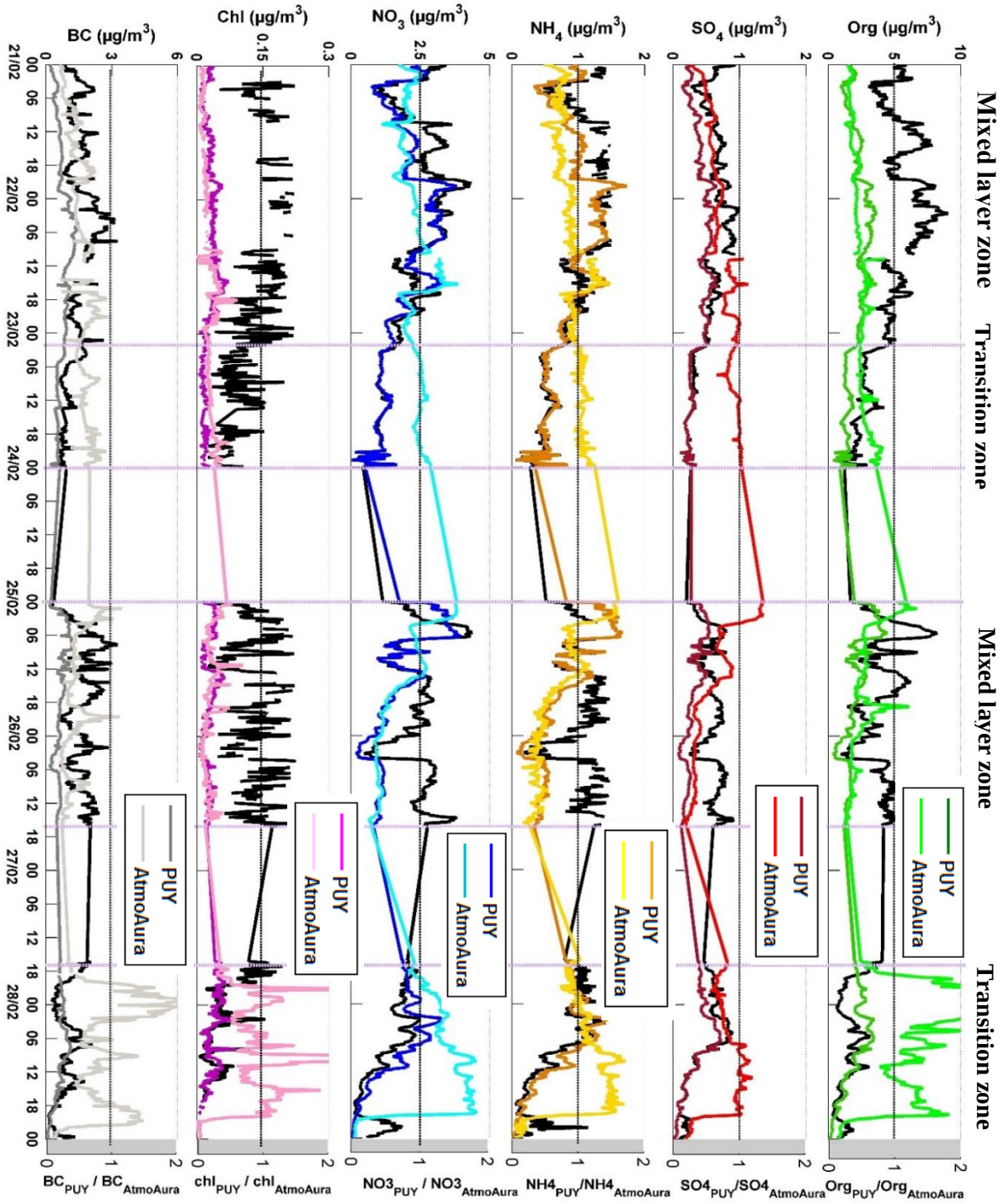

Figure 4.3. 7. Zoom of the BL region indicated in red (about one week) in the time series plot in figure 4.3.4 for the PUY and AtmoAura stations both predicted to be in the BL by the model ECMWF. We further segregated the BL classification into mixed layer period and transition layer period.

4.3.3.2.2 Diurnal variation

Similar diurnal patterns are also observed for the ACSM at both sites (Figure 4.3.8). However, clearer patterns are identified at the AtmoAura's station due to its proximity to local emission sources.

In comparison with period 1 at AtmoAura station, organic compounds and EBC concentrations show higher diurnal variations with the same peaks during the morning and evening rush hours but a large increase from late afternoon to late evening. These features are also observed for both species at PUY station in period 2.

Nitrate also has higher diurnal pattern in period 2 compared to period 1, which is due to the lower temperature in period 2. However, for both periods, higher concentrations are observed during nighttime which are likely related to temperature regulated gas/ particle partitioning. These features are also shown for nitrate at PUY station in period 2. These are in agreement with what have been previously found in Paris (Crippa et al., 2013). Total mass concentrations of ammonium and sulphate are lower and show a weak diurnal variations with small increases during mid-day at both sites, suggesting a similar source between the two compounds at the two sites.

In order to quantify the contribution of local pollution at the AtmoAura station, we calculated the ratio of the PUY concentrations over the AtmoAura concentrations. For organic, nitrate, and ammonium this ratio is around 1 indicating, as already mentioned above, that the concentrations measured at both the PUY and the city of Clermont-Ferrand arrive from regionally transported aerosols (Figure 4.3.8 (c)). However, the complex features in the organics daily pattern suggest contribution from multiple sources, formation mechanisms and/or influence of meteorological conditions, which will be addressed in a following section. For sulphate and EBC, the ratio PUY/AtmoAura is around 0.6 indicating that around 40% of these species are locally emitted. The ratio for EBC and sulphate are lower during the night and mid-day, indicating stronger contributions of local sources at these periods of the day. Hence, at night, the local contribution of EBC is of around 60% of the total EBC concentration measured in the city of Clermont-Ferrand.

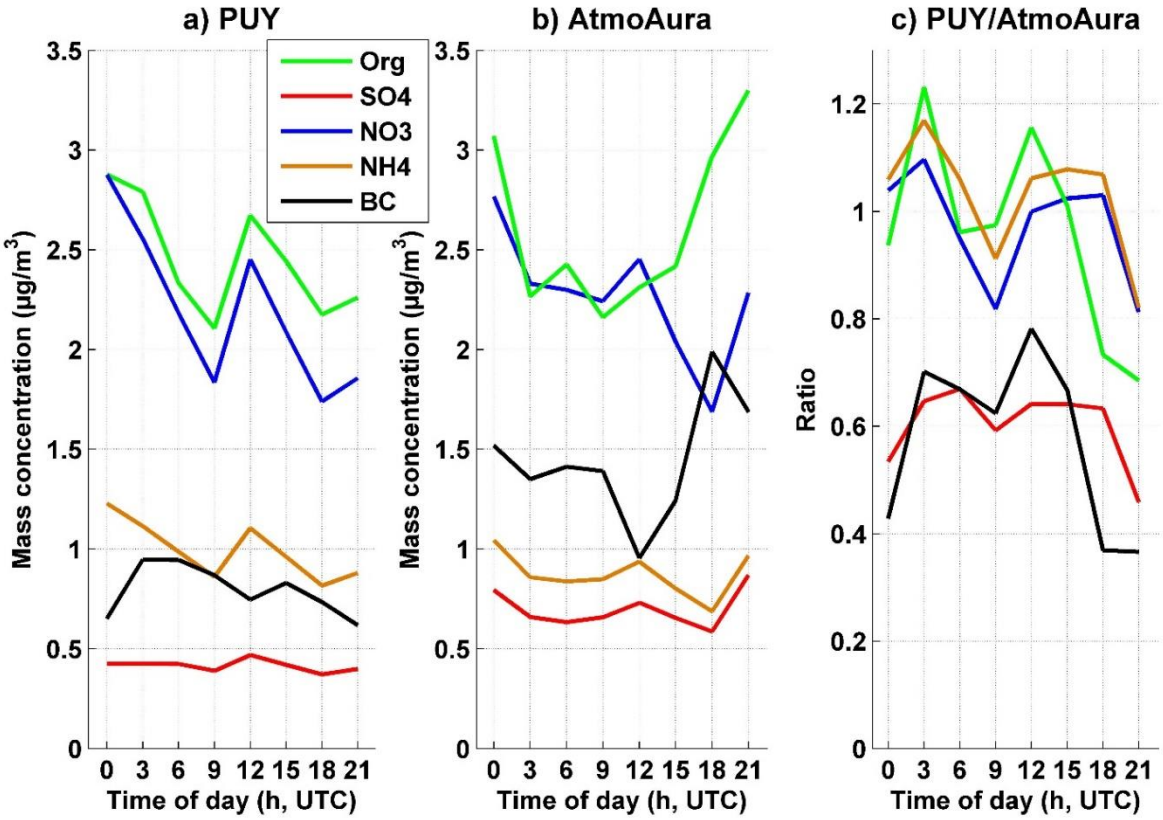

Figure 4.3. 8. Diurnal cycles of organic, inorganics and black carbon throughout the BL period at: **a)** PUY, **b)** AtmoAura and **c)** Puy/AtmoAura ratio.

4.3.3.2.2 Statistical study for the separation of sources

4.3.3.2.2.1 ME-2 results

In order to determine the sources of the organic aerosol, we applied the positive matrix factorization (PMF) method separately at the two sites. The PMF could only be applied at the two sites separately during the BL conditions, the concentrations measured at the PUY station during FT conditions being too low. This method allows us to deconvolute the mass spectra of organic aerosol measured by the ACSM, and is explained in detail in section 3.2.1.4. This approach helps to identify groups of organic aerosol (Jimenez et al., 2009), by detecting organic aerosols families differentiated by their level of oxidation (eg, Oxidised Organic Aerosols (OOA) vs Hydrogenated Organic Aerosols (HOA), Ng et al., (2010)) and / or their probable sources (eg, Biomass Burning Organic Aerosols (BBOA)). As mentioned in section 4.2.5, In order to get information of organic aerosol source spectra the "a value" technique was used within the SoFi program (Canonaco et al., 2013) available in ME-2 engine.

In this study three and four factors could be identified depending on site location (Figure 4.3.9). For both sites, a HOA, BBOA and OOA factor was identified. At the AtmoAura site, the OOA could be further divided into a low-volatility oxidized organic aerosols (LV-OOA) and a semi-volatile oxidized organic aerosol, mixed with BBOA (SVOOA-BBOA) mass spectra signatures m/z 60 and m/z 73. The HOA profile is dominated by peaks characteristic of aliphatic hydrocarbons, including m/z 27 ($C_2H_3^+$), 41 ($C_3H_5^+$), 43 ($C_3H_7^+$), 55 ($C_4H_7^+$), 57 ($C_4H_9^+$), 69 ($C_5H_9^+$), 71 ($C_5H_{11}^+$) (Aiken et al., 2010; Canagaratna et al., 2004). The BBOA was identified when the signal of its most specific fragment peak at m/z 29 (CHO^+), 60 ($C_2H_4O_2^+$) and 73 ($C_3H_5O_2^+$) was above the background level. This factor was extracted directly from the data set by a separate unconstraint PMF. Besides, the important photochemistry observed on-site coupled with mass spectra signals for levoglucosan (m/z 60, 73) fast reactivity under photo-oxidative conditions (Hennigan et al., 2010) might lead to a fast transformation of BBOA into SOA which would appear as an SVOOA-BBOA factor in our PMF solution at AtmoAura station. The SVOOA-BBOA profile is characterized by both the masses typical of biomass burning and literature spectra of SVOOA spectra (m/z 29 (CHO^+), m/z 43 ($C_2H_3O^+$), m/z 44 (CO_2^+), m/z 60 ($C_2H_4O_2^+$)) (Alfarra et al., 2007). The last component identified at both stations was the LVOOA. This component is highly oxygenated, as evidenced by the large contribution from m/z 44 (CO_2^+). Mean HOA and BBOA reference spectra taken from Crippa et al., (2013) and Ng et al., (2011), respectively, were used as constraining factors in the ME-2.

For both stations, BBOA always remained tightly constrained (a = 0.1), while for HOA many solutions with an 'a values' ranging from 0 to 0.7 (with Δa step of 0.1) were averaged. For 'a values' above 0.7, no good separation of OOA's factors and they were therefore removed from this analysis. The OOAs were always completely unconstrained (no a priori mass spectrum).

A final constrained solution of three and four factors is presented in Figure 4.3.9 (a) and (b), respectively, for PUY and AtmoAura's stations through their time series and mass spectra.

HOA contributed to 13% of the total organic aerosol (OA) at the PUY station, and 16% of OA at the AtmoAura station during the BL conditions. This contribution of HOA at the PUY station is similar to what we observed at the PUY station during the winter 2016 period (section 4.2), as well as concentrations measured at other altitude sites (8% ± 2% at the JFJ (Crippa et al., 2014; Fröhlich et al., 2015; Lanz et al., 2010). Similar temporal evolution of HOA and inorganic (r^2 = 0.7, 0.7 and 0.65, respectively

for NH4, NO3 and SO4), suggests that these aerosol components arrived from similar sources at the altitude (background) station. On the Contrary, correlations of the HOA factor with traffic related tracers such as EBC and Chl are not very high (r^2= 0.4 and r^2= 0.4 with EBC and r^2= 0.54, r^2= 0.35 with Chl, for PUY and AtmoAura stations respectively).

The BBOA concentrations contributed to 11% of the OA concentration at the PUY station, and 12% at the AtmoAura station. Similar to our study, Stavroulas et al., (2018), in the city of Athens reported that BBOA contributed 10% to OA. BBOA was found to be well correlated to the EBC concentrations.

OOA concentrations contributed to 76% of OA at the PUY station and 72% (42%+30% respectively for LVOOA and SVOOA-BBOA) at the AtmoAura station. For PUY stations, the LV-OOA component showed good correlations with sulphate, ammonium and nitrate (r^2 >/= 0.85). Correlations between the organic and the inorganic species during the cold month suggest that these species have similar sources as already shown in the past (Freney et al., 2011; Farah et al. 2018 in prep). Furthermore, the LV-OOA showed a good correlation with EBC (r^2 = 0.55), suggesting that some of the LV-OOA may be related to anthropogenic sources (Freney et al., 2011). Similar to the present study, Farah et al. (2018 in prep) and Freney et al., (2011) at PUY, found LV-OOA contributions of 78% and 65% in winter, respectively. For AtmoAura station, the LV-OOA component showed also good correlations with sulphate, ammonium and nitrate (r^2 >/= 0.85) suggesting that these species have similar sources. In Athens, Stavroulas et al., (2018) found LV-OOA contributions of 35% which is close to the 42% found at the AtmoAura station. The authors attributed the LV-OOA component to the extensive oxidation of the local primary combustion sources.

SVOOA-BBOA was only identified at AtmoAura's station, where it comprised 30% of OA. The SVOOA-BBOA mass spectra is similar to the reference mass spectra of SVOOA and BBOA (Ng et al., 2011). Also, the SVOOA-BBOA showed a good correlation with Chl (r^2 =0.36), suggesting that this factor is majorly related to biomass burning emission sources. The time series of SVOOA-BBOA showed a good correlation with EBC (r^2 =0.4) suggesting that particles arrived from an anthropogenic source. Stavroulas et al., (2018) found SV-OOA contributions of 31% which is close to the 30% found at AtmoAura station. The authors showed a good correlation with wood burning "fingerprint" fragments of m/z 60 and 73 demonstrating the direct link between SV-OOA and primary combustion sources (mainly biomass burning).

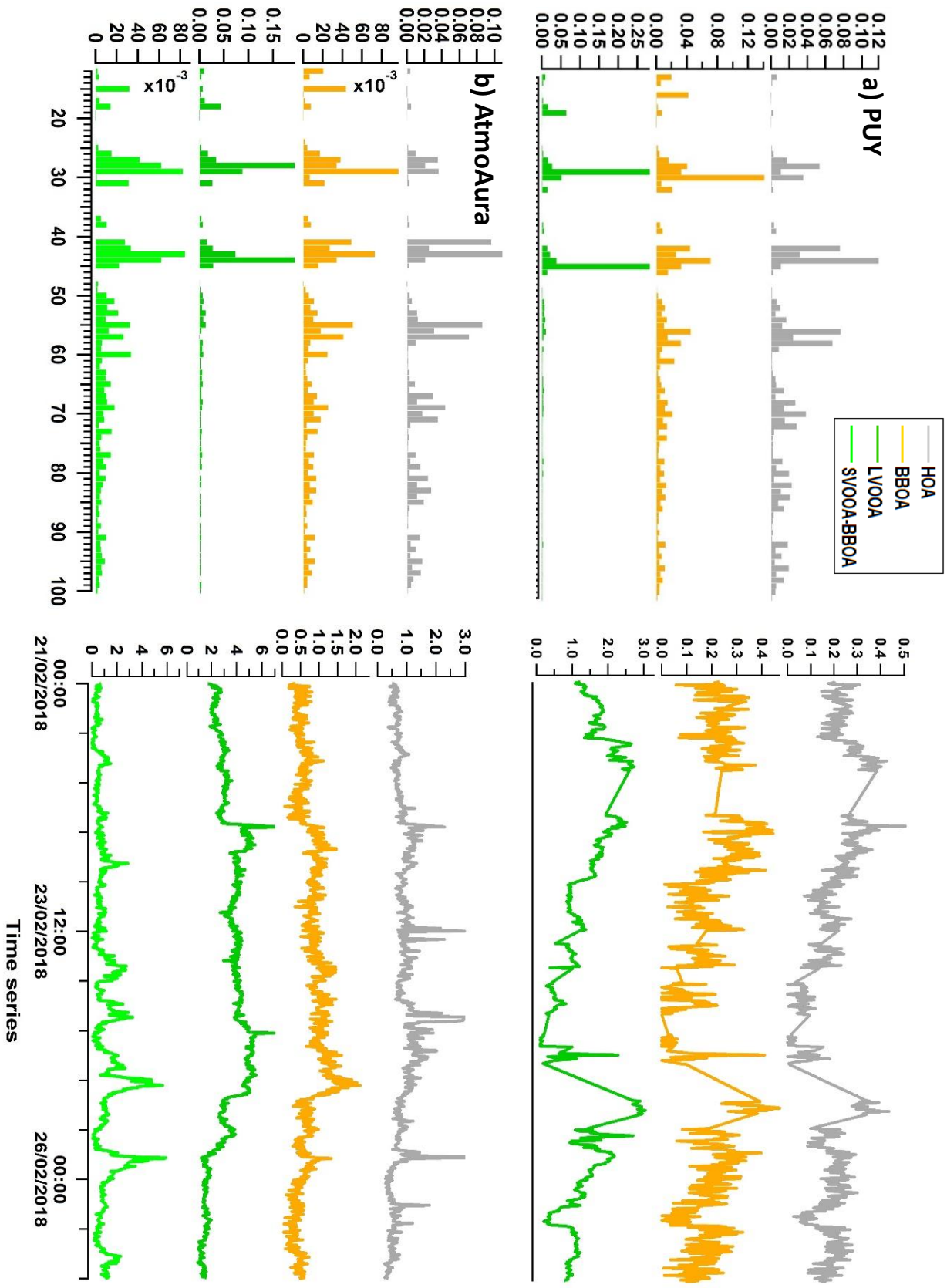

Figure 4.3. 9. ME-2 example solution for: a) PUY and b) AtmoAura for BL conditions.

Table 4.3. 1. r^2 correlations of ME-2 components with time series of particle phase species.

	PUY			AtmoAura			
	HOA	BBOA	LVOOA	HOA	BBOA	LVOOA	SVOOA-BBOA
SO_4	**0.65**	**0.56**	**0.88**	0.22	0.08	**0.85**	**0.39**
NO_3	**0.7**	**0.55**	**0.95**	0.29	0.16	**0.8**	**0.45**
NH_4	**0.7**	**0.6**	**0.96**	0.26	0.12	**0.83**	**0.4**
Chl	**0.54**	0.3	**0.54**	**0.35**	**0.36**	0.2	**0.36**
BC	**0.4**	**0.4**	**0.55**	**0.4**	**0.4**	0.09	**0.4**

4.3.3.2.2.2 ME-2 factors diurnal variations

The absolute concentrations from the ME-2 factors vary with the time of the day, as shown in Figure 4.3.10. For AtmoAura station, the diurnal cycle of HOA presented in grey, clearly shows peaks in the morning (8 UTC) and evening (19 UTC), corresponding to peaks of road traffic. Rivellini et al., (2017) at a coastal site in Senegal, measured a HOA factor that correlated with EBC, and having a diurnal variation with peaks during morning and evening corresponding to anthropogenic activities. Also, Stavroulas et al., (2018) in the city of Athens, reported strong diurnal variations of HOA as a result of combustion from central heating and traffic emissions. On the other hand, PUY diurnal HOA concentrations were always stable and low.

At AtmoAura station, BBOA diurnal were affected by emissions related to biomass burning that increase in the morning along with traffic emissions, but at night the concentrations are highest one to two hours later than vehicular emissions and remain high all night long (Fig. 4.3.9 in orange). Similar to our study, Stavroulas et al., (2018) found a pronounced BBOA diurnal cycle with peaking values during night from combustion for heating purposes. While at PUY, BBOA diurnal variations were always stable and low, suggesting a contribution from regional transport. The SVOOA-BBOA diurnal variation increase in the morning (8 UTC) and evening (19 UTC), and similar to BBOA remain high all night long.

The LV-OOA diurnals show an increase in the mass concentration during the day and decrease at night for both stations (Fig. 4.3.9 in dark green). These changes can be a result of extensive oxidation of the local primary combustion sources, but considering that both sites have similar variations we can also estimate a regional influence of this aged OA.

Regarding the ratio of concentrations measured at PUY over concentrations measured at AtmoAura, POA (HOA and BBOA) ratio varies between 0.3 at night (minimum of 0.15 at 8 UTC) and up to 0.6 during the day (maximum of 0.65 at 15 UTC). This indicates that 70% of the primary organic aerosols measured at the PUY during the nighttime are from local emissions, whereas there is only a 35% contribution during the daytime (Figure 4.3.11 (c) magenta). The level of contribution of local POA to the total POA measured at AtmoAura, as well as its diurnal variation, are very similar to the one measured for EBC (between 40% daytime and 60% nighttime locally produced). The ratio of OOA species (SVOOA and LVOOA) is around 0.7 indicating that at AtmoAura, only 30% of these species are locally emitted and the rest being of a regional origin. Furthermore, the POA and sulphate ratios time series have an r^2 correlation of 0.36 and 0.32 with that of EBC ratio, respectively, while the OOA, nitrate and ammonium ratios time series show a low correlation with that of EBC ratio (r^2=0.05, r^2=0.04 and r^2=0.07, respectively). POA local contributions being higher than the secondary ones is in agreement with our understanding of the origin of organic aerosols, and gives confidence in our results.

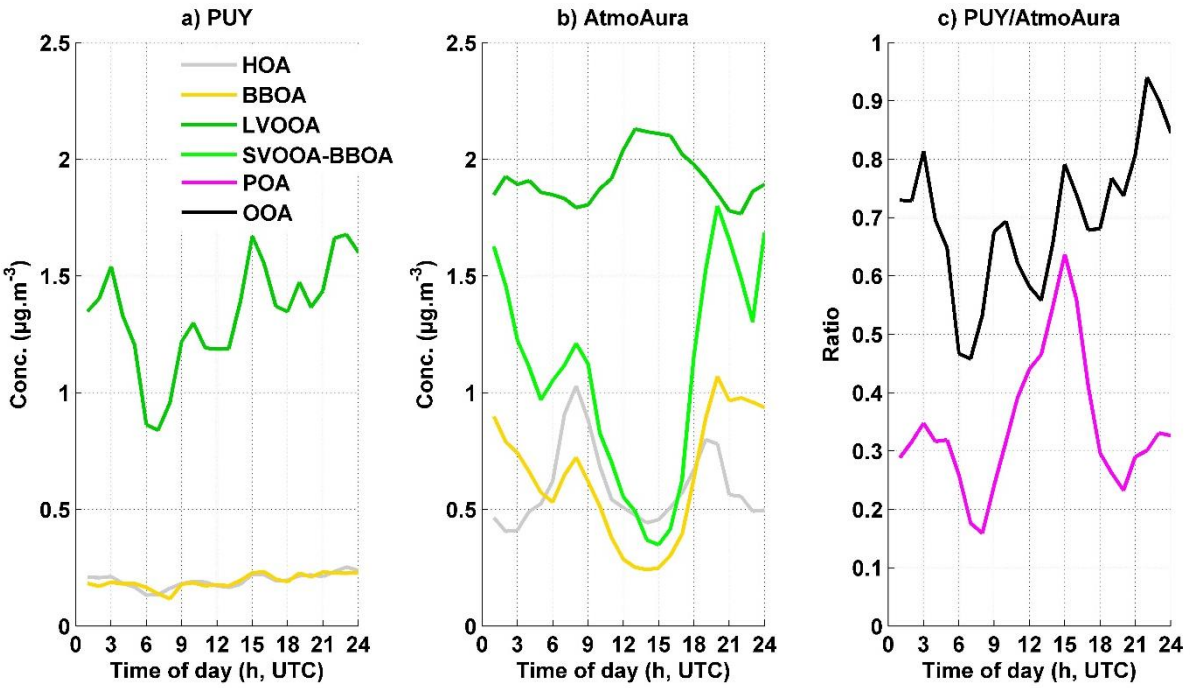

Figure 4.3. 10. Diurnal cycles of different organic sources throughout the BL period at: a) PUY, b) AtmoAura and c) Puy/AtmoAura ratio.

4.3.4 Conclusions

An intensive field campaign took place at the agglomeration of Clermont-Ferrand (AtmoAura's station) and at PUY station, during the month of February 2018. The measurement sites were equipped with an extensive range of measurements including meteorological parameters, particle phase chemistry, aerosol concentrations, and aerosol optical properties. During this campaign, two case studies are analyzed.

In the first case study, the PUY station was affected by a warm and wet FT oceanic air masses. In agreement with this, the average composition and time series are different among the stations, with low PM1 mass concentrations at the PUY station and high PM1 mass concentrations at AtmoAura station. The relatively heterogeneous chemical composition throughout the two stations confirm that particle composition at the PUY station is dominated by regional factors with little boundary layer influence. This period when the PUY station was in the FT in the majority of the time allows to conclude, that the daytime increase of the inorganic species (nitrate, sulphate, ammonia), are not due to vertical transport from the BL but likely due to secondary aerosol formation linked to photochemistry within the FT. In the second case study period, the PUY station was influenced by cold and dry BL continental air masses. Coherent with this observation, the average composition, mass concentrations, and temporal variation are similar among the sites for both organic and inorganic fractions. The observed homogeneity in terms of chemical composition and mass concentration among the two sites suggest that the source of these high PM1 concentrations were from regional air masses rather than locally from the city of Clermont-Ferrand. However, the sharp increases in PM1 mass concentrations during low wind speed, might be a result of local emissions, which are (between 40% daytime and 60% nighttime) of EBC and sulphate.

For BL conditions, a more detailed source apportionment using ME-2 (SoFi) allowed for a separation of three and four sources, respectively, at the PUY and AtmoAura stations. The contribution of primary organic compounds is around 24% (HOA (13%) + BBOA (11%) at PUY and 28% (HOA (16%) + BBOA (12%)) at AtmoAura. This fraction of HOA can be linked to local traffic activities at AtmoAura, and PUY station as a result vertical transport containing higher amounts of HOA. While BBOA fraction can be linked to local traffic emissions during daytime and local sources of combustion linked to conventional heating devices during nighttime. The local emissions of POA are between 35% daytime and 70% nighttime.

Furthermore, the prevailing OA source was oxygenated OA (OOA) splitting up into a long-distance transport LV-OOA (42% (AtmoAura) and 76% (PUY)) and a photo-oxidative SVOOA-BBOA (30% (AtmoAura)). LVOOA fraction is typically representative of regional aged OA. While SVOOA-BBOA represents an atmospheric mixture of primary BBOA and SVOOA. The local emissions of OOA are around 30%.

Finally, this combination of in-situ measurements and meteorological model analysis contributes to a better understanding of the connection between the two stations in terms of aerosol composition and mass concentration. The connection between the two stations in terms of chemical compositions, should be further investigated on a larger temporal scale (e.g. 1 year), in order to compare the short time and seasonal variabilities, and to better evaluate the vertical distribution of aerosol physical and chemical properties.

Chapter 5: Synthesis and perspectives

5.1 Synthesis

In this work, long-term and short-term datasets of numerous aerosol properties acquired at the Puy de Dome (PUY), and low altitude sites Cézeaux (CZ) and AtmoAura stations have been used to determine the specific physical and chemical characteristics of free tropospheric (FT) aerosols and their sources and transport pathways from the boundary layer (BL).

The first part of the study incorporated the use of four independent criteria to identify whether the PUY station lies within the FT or the BL. These criteria are based on LIDAR measurements using the WCT method, BLH simulations from the ECMWF model, and in situ measurements of BL tracers (NOx/CO and ^{222}Rn). This methodology was applied to a year-long dataset to determine the specific physical characteristics (size distributions) of FT aerosols and their sources and transport pathways from the BL. Using these tracers, we observe that the PUY station is considered to be in the FT up to 20% during the year 2015. Based on this segregation, we observed higher concentrations in the BL compared to FT for EBC, Aitken and accumulation mode particle concentrations for most seasons, as expected from larger sources originating from the surface. The nucleation mode particles however showed no significant difference between the BL and FT aerosol, suggesting an additional FT source of precursors to the formation of new particles at the PUY station. Using air mass segregation, we observe highest nucleation mode aerosols in marine aerosols (Atlantic and Mediterranean) suggesting that these air masses are rich in precursor species favoring new particle formation. Also, we found that the spring season had specific characteristics: higher EBC, accumulation and Aitken modes median concentrations in spring FT conditions compared to BL, which might be linked to biomass burning from vegetation in gardens that inject aerosols directly to the FT from active convection transport. During spring periods the PUY station is often advected by long range transported continental aerosol, often carrying polluted aerosols. Another source of these high concentrations of Aitken mode particles is the growth of nucleation mode particles.

Using ECMWF analysis we were able to determine the time since last BL contact. This provided us with a means to separate BL air masses into two different classes, those that were recently in contact with the BL (<15h) and those that spent more than 75 hrs in the FT. This helped us reduce the variability in air mass properties observed

within FT air masses and permitted us to obtain a specific aerosol characteristics associated with FT air masses. We found that an air-mass signature was preserved in the FT even for air masses that had passed more than 75 hours without any contact with the BL.

Using this same methodology, the analysis was applied to one year (April 2015 to February 2016) of aerosol chemistry measurements using a ToF-ACSM at PUY site. Up until now aerosol chemistry measurements at the site were made on weekly filter analysis. Short-term events and diurnal variations are difficult /impossible to interpret from offline filter analysis, and therefore having the ability of long-term on-line measurements at the site provides us with a unique ability to assess how aerosol chemical properties daily variations evolve over a year long period. Averaged over the entire year, OA was the most abundant component during all seasons and within all air mass types. Depending on the season, organics comprised from 48 to 73% of the total mass with a minimum in winter and maximum in summer. The high contribution of OA during the summer months was identified to be the result of not only vertical transport, but also the result of a larger secondary organic formation during the warmer months. Highest mean total concentrations were measured within continental air masses, while lowest concentrations are measured in oceanic modified air masses.

The PMF/ME-2 statistical analysis was used to deconvolve aerosol organic sources. This analysis was performed separately for all seasons to account for seasonal changes in factor profiles (especially OOA) which resulted in a two and three factor solution depending on the season. During all seasons, HOA contributes between 14% and 23% of the OA mass. The prevailing OA source was the OOA (74-85%) that could be segregated into a background LV-OOA and SV-OOA during the summer months. Furthermore, using the method to separate between BL and FT at the PUY station, we observed that higher organic particle concentrations (HOA and LVOOA) were observed in the FT compared to the BL in spring corresponding to higher Aitken and accumulation mode particle concentrations in this layer and season as reported in the first part of the study. LV-OOA could also be resulting from the growth of nucleation mode particles in the FT. However, it should be noted that LV-OOA aerosols is generally representative of aged organic aerosol. This combination of in-situ measurements, back-trajectory analysis and segregation between FT and BL contribute to better understanding of aerosol particles sources, properties and their dynamics in the atmosphere. In particular, we have illustrated that the aerosol chemical properties at lower atmospheric layers (i.e. BL, FT) are similar to what have been found using the in situ measurements at other European high and medium altitude sites.

To assess the mixing between atmospheric layers, measurements of submicron aerosol composition were performed during the month of February 2018 at a low altitude site (AtmoAura) and a high altitude site (PUY). The aerosol non-refractory composition and black carbon content were determined by ToF-ACSM and aethalometer measurements, respectively, at both sites simultaneously. Again, the ECMWF model was applied to segregate between BL and FT air masses resulting in two case studies. During the first part of this field exercise, the PUY station was affected by a warm and wet FT oceanic air masses. The relatively heterogeneous chemical composition throughout the two stations (AtmoAura/Puy) confirm that particle composition at the PUY station is dominated by regional factors with little boundary layer influence. This period when the PUY station was in the FT in the majority of the time allows to conclude, that the daytime increase of the inorganic species (nitrate, sulphate, ammonia), are not due to vertical transport from the BL but likely due to secondary aerosol formation linked to photochemistry within the FT. In the second case study period, the PUY station was influenced by cold and dry BL continental air masses. Coherent with this observation, the aerosol composition was similar at both sites. The homogeneity of the particle composition and highly correlated time series among the two sites suggest a dominating influence of regional air masses on Clermont-Ferrand air quality. However, the sharp increases in some species related to others has allowed to evaluate the contribution of local sources to the composition of the aerosol composition at the urban site.

For the second case study, organic source apportionment using PMF technique indicates a dominant contribution from secondary organic aerosol (72-76%, depending on the site) with the major primary emissions sources consisting of traffic and biomass burning. While lower on average than the secondary sources, these primary emissions exhibit strong diurnal cycles and can become significant aerosol sources during peak hours.

Finally, the results obtained from the ACSM data allow a better understanding of the synergy between sources, chemical composition and meteorological parameters responsible for particulate pollution at PUY and AtmoAura's stations.

5.2 Perspectives

As we have seen throughout the manuscript, the various results obtained during this thesis contribute to the improvement of the knowledge on the physical and chemical properties of aerosols within the different atmospheric layers (Boundary

layer (BL) and free troposphere (FT)). However, several questions remain open and need deeper investigations in future studies.

First, there is the question of whether we observe similar physical properties in the FT at other altitude sites and how are they influenced by air mass history. In order to partially answer this question, the method of differentiating between BL and FT used in this work could be applied to other stations of higher altitude within the CLimate relevant Aerosol Properties from near surface observations (CLAP) such as: Observatoire de Physique de l'Atmosphere de la Reunion (OPAR) (la Réunion, 2200 m a.s.l) or Chacaltaya (CHC) (Bolivia, 5240 m asl); and later: Pic du Midi (PdM) (France, 2877 m asl).

Furthermore, we have shown throughout the manuscript that aerosol chemical composition is dominated by organic aerosol during all seasons. This leads us to the question on how to provide a seasonal perspective of specific organic aerosol source properties. In order to answer this question, additional information on the gas-phase precursors responsible for new particle formation is necessary to provide information not only on the sources of organic aerosols but also on the photochemical age of the air mass.

Finally, Using ECMWF model, we found that during autumn and winter 2015-2016 over 80% of air masses did not have any contact with BL for at least 75h before being sampled at PUY station. During these periods, the NR-PM1 chemical properties are treated with caution due to the limited statistics in the aged (>75h) FT air masses. This leads us to the question on how to increase the statistics on these properties in the aged FT air masses. For this, the ECMWF model can be applied to a pluri-annual datasets at the PUY station, in order to be able to statistically identify the robust signatures of the chemical properties in these aged FT air masses.

References

Aiken, A.C., De Foy, B., Wiedinmyer, C., Decarlo, P.F., Ulbrich, I.M., Wehrli, M.N., Szidat, S., Prevot, A.S.H., Noda, J., Wacker, L., Volkamer, R., Fortner, E., Wang, J., Laskin, A., Shutthanandan, V., Zheng, J., Zhang, R., Paredes-Miranda, G., Arnott, W.P., Molina, L.T., Sosa, G., Querol, X., Jimenez, J.L., 2010. Mexico city aerosol analysis during MILAGRO using high resolution aerosol mass spectrometry at the urban supersite (T0)-Part 2: Analysis of the biomass burning contribution and the non-fossil carbon fraction. Atmos. Chem. Phys 10, 5315–5341. doi:10.5194/acp-10-5315-2010

Albrecht, B.A., 1989. Aerosols, Cloud Microphysics, and Fractional Cloudiness. Science (80-.). 245, 1227–1230. doi:10.1126/science.245.4923.1227

Allan, J.D., Delia, A.E., Coe, H., Bower, K.N., Alfarra, M.R., Jimenez, J.L., Middlebrook, A.M., Drewnick, F., Onasch, T.B., Canagaratna, M.R., Jayne, J.T., Worsnop, D.R., 2004. A generalised method for the extraction of chemically resolved mass spectra from Aerodyne aerosol mass spectrometer data. J. Aerosol Sci. 35, 909–922. doi:10.1016/j.jaerosci.2004.02.007

Asmi, A., Wiedensohler, A., Laj, P., Fjaeraa, A.-M., Sellegri, K., Birmili, W., Weingartner, E., Baltensperger, U., Zdimal, V., Zikova, N., 2011. Number size distributions and seasonality of submicron particles in Europe 2008–2009. Atmos. Chem. Phys. 11, 5505–5538.

Asmi, E., Freney, E., Hervo, M., Picard, D., Rose, C., Colomb, A., Sellegri, K., 2012. Aerosol cloud activation in summer and winter at puy-de-Dôme high altitude site in France. Atmos. Chem. Phys. 12, 11589–11607. doi:10.5194/acp-12-11589-2012

Baars, H., Ansmann, A., Engelmann, R., Althausen, D., 2008. Continuous monitoring of the boundary-layer top with LIDAR. Atmos. Chem. Phys. 8, 7281–7296.

Barbet, C., Deguillaume, L., Chaumerliac, N., Leriche, M., Freney, E., Colomb, A., Sellegri, K., Patryl, L., Armand, P., 2016. Evaluation of Aerosol Chemical Composition Simulations by the WRF-Chem Model at the Puy de Dôme Station (France). Aerosol Air Qual. Res. 16, 909–917. doi:10.4209/aaqr.2015.05.0342

Beddows, D.C.S., Dall'Osto, M., Harrison, R.M., Kulmala, M., Asmi, A., Wiedensohler, A., Laj, P., Fjaeraa, A.M., Sellegri, K., Birmili, W., Bukowiecki, N., Weingartner, E., Baltensperger, U., Zdimal, V., Zikova, N., Putaud, J.-P., Marinoni, A., Tunved, P., Hansson, H.-C., Fiebig, M., Kivekäs, N., Swietlicki, E., Lihavainen, H., Asmi, E., Ulevicius, V., Aalto, P.P., Mihalopoulos, N., Kalivitis, N., Kalapov, I., Kiss, G., de Leeuw, G., Henzing, B., O'Dowd, C., Jennings, S.G., Flentje, H., Meinhardt, F.,

Ries, L., Denier van der Gon, H.A.C., Visschedijk, A.J.H., 2014. Variations in tropospheric submicron particle size distributions across the European continent 2008–2009. Atmos. Chem. Phys. 14, 4327–4348. doi:10.5194/acp-14-4327-2014

Bianchi, F., Tröstl, J., Junninen, H., Frege, C., Henne, S., Hoyle, C.R., Molteni, U., Herrmann, E., Adamov, A., Bukowiecki, N., Chen, X., Duplissy, J., Gysel, M., Hutterli, M., Kangasluoma, J., Kontkanen, J., Kürten, A., Manninen, H.E., Münch, S., Peräkylä, O., Petäjä, T., Rondo, L., Williamson, C., Weingartner, E., Curtius, J., Worsnop, D.R., Kulmala, M., Dommen, J., Baltensperger, U., 2016. New particle formation in the free troposphere: A question of chemistry and timing. Science (80-.). 352, 1109–1112. doi:10.1126/science.aad5456

Biraud, S., Ciais, P., Ramonet, M., Simmonds, P., Kazan, V., Monfray, P., O'Doherty, S., Spain, T.G., Jennings, S.G., 2000. European greenhouse gas emissions estimated from continuous atmospheric measurements and radon 222 at Mace Head, Ireland. J. Geophys. Res. Atmos. 105, 1351–1366.

Boucher, O., 2015. Atmospheric Aerosols, in: Atmospheric Aerosols. Springer Netherlands, Dordrecht, pp. 9–24. doi:10.1007/978-94-017-9649-1_2

Boulon, J., Sellegri, K., Hervo, M., Picard, D., Pichon, J.-M., Fréville, P., Laj, P., 2011. Investigation of nucleation events vertical extent: a long term study at two different altitude sites. Atmos. Chem. Phys. 11, 5625–5639. doi:10.5194/acp-11-5625-2011

Bourcier, L., Sellegri, K., Chausse, P., Pichon, J.M., Laj, P., 2012. Seasonal variation of water-soluble inorganic components in aerosol size-segregated at the puy de Dôme station (1,465 m a.s.l.), France. J. Atmos. Chem. 69, 47–66. doi:10.1007/s10874-012-9229-2

Bressi, M., Cavalli, F., Putaud, J.P., Prevot, A.S.H., Aas, W., Äijälä, M., Alastuey, A., Allan, J.D., Aurela, M., Berico, M., Bougiatioti, A., Bukowiecki, N., Canonaco, F., Crenn, V., Dusanter, S., Ehn, M., Eller, M., Elsasser, M., Favez, O., Fröhlich, R., Graf, P., Green, D.C., Heikkinen, L., Holzinger, R., Hueglin, C., Kiendler-Scharr, A., Kubelová, L., Lunder, C., Maasikmets, M., Makeš, O., Malaguti, A., Mihalopoulos, N., Minguillón, M.C., Nicolas, J.B., O'Dowd, C.D., Ovadnevaite, J., Petit, J.-E., Petralia, E., Poulain, L., Priestman, M., Riffault, V., Ripoll, A., Schlag, P., Schwarz, J., Sciare, J., Slowik, J.G., Sosedova, Y., Stavroulas, I., Teinemaa, E., Vodička, P., Williams, P.I., Young, D.E., Zhang, S., 2018. A European aerosol phenomenology - 6: high-time resolution chemical characteristics of submicron particulate matter across Europe.

Brooks, I.M., 2003. Finding boundary layer top: Application of a wavelet covariance transform to LIDAR backscatter profiles. J. Atmos. Ocean. Technol. 20, 1092–1105.

Budisulistiorini, S.H., Baumann, K., Edgerton, E.S., Bairai, S.T., Mueller, S., Shaw, S.L., Knipping, E.M., Gold, A., Surratt, J.D., 2016. Seasonal characterization of submicron aerosol chemical composition and organic aerosol sources in the southeastern United States: Atlanta, Georgia, and Look Rock, Tennessee. Atmos. Chem. Phys. 16, 5171–5189.

Burkart, J., Steiner, G., Reischl, G., Moshammer, H., Neuberger, M., Hitzenberger, R., 2010. Characterizing the performance of two optical particle counters (Grimm OPC1.108 and OPC1.109) under urban aerosol conditions. J. Aerosol Sci. 41, 953–962. doi:10.1016/j.jaerosci.2010.07.007

Canagaratna, M.R., Jayne, J.T., Ghertner, D.A., Herndon, S., Shi, Q., Jimenez, J.L., Silva, P.J., Williams, P., Lanni, T., Drewnick, F., Demerjian, K.L., Kolb, C.E., Worsnop, D.R., 2004. Chase Studies of Particulate Emissions from in-use New York City Vehicles. Aerosol Sci. Technol. 38, 555–573. doi:10.1080/02786820490465504

Canagaratna, M.R., Jayne, J.T., Jimenez, J.L., Allan, J.D., Alfarra, M.R., Zhang, Q., Onasch, T.B., Drewnick, F., Coe, H., Middlebrook, A., Delia, A., Williams, L.R., Trimborn, A.M., Northway, M.J., DeCarlo, P.F., Kolb, C.E., Davidovits, P., Worsnop, D.R., 2007. Chemical and microphysical characterization of ambient aerosols with the aerodyne aerosol mass spectrometer. Mass Spectrom. Rev. 26, 185–222. doi:10.1002/mas.20115

Canonaco, F., Crippa, M., Slowik, J.G., Baltensperger, U., Prévôt, A.S.H., 2013. SoFi, an IGOR-based interface for the efficient use of the generalized multilinear engine (ME-2) for the source apportionment: ME-2 application to aerosol mass spectrometer data. Atmos. Meas. Tech. 6, 3649–3661.

Canonaco, F., Slowik, J.G., Baltensperger, U., Prévôt, A.S.H., 2015. Seasonal differences in oxygenated organic aerosol composition: implications for emissions sources and factor analysis. Atmos. Chem. Phys. 15, 6993–7002.

Chambers, S.D., Williams, A.G., Conen, F., Griffiths, A.D., Reimann, S., Steinbacher, M., Krummel, P.B., Steele, L.P., van der Schoot, M. V., Galbally, I.E., 2016. Towards a universal "baseline" characterisation of air masses for high-and low-altitude observing stations using Radon-222. Aerosol Air Qual. Res 16, 885–899.

Charlson, R.J., Langner, J., Rodhe, H., Leovy, C.B., Warren, S.G., 1991. Perturbation of the northern hemisphere radiative balance by backscattering from anthropogenic sulfate aerosols*. Tellus A 43, 152–163. doi:10.1034/j.1600-0870.1991.00013.x

Charlson, R.J., Schwartz, S.E., Hales, J.M., Cess, R.D., Coakley, J.A., Hansen, J.E., Hofmann, D.J., 1992. Climate Forcing by Anthropogenic Aerosols. Science (80-.). 255, 423–430. doi:10.1126/science.255.5043.423

Chauvigné, A., Aliaga, D., Karine, S., Nadège, M., Fernando, V., Isabel, M., Marcos, A., Paolo, L., 2018. Aerosol Optical Properties and Radiative forcing in the Andes Cordilliera based on measurements at the Chacaltaya observatory, Bolivia (5240 m a.s.l.). To be Submitt.

Chauvigné, A., Sellegri, K., Hervo, M., Montoux, N., Freville, P., Goloub, P., 2016. Comparison of the aerosol optical properties and size distribution retrieved by sun photometer with in situ measurements at midlatitude. Atmos. Meas. Tech. 9, 4569.

Chevillard, A., Ciais, P., Karstens, U., Heimann, M., Schmidt, M., Levin, I., Jacob, D., Podzun, R., Kazan, V., Sartorius, H., Weingartner, E., 2002. Transport of 222Rn using the regional model REMO: a detailed comparison with measurements over Europe. Tellus B 54, 850–871. doi:10.1034/j.1600-0889.2002.01339.x

Ciarelli, G., Aksoyoglu, S., Haddad, I. El, Bruns, E.A., Crippa, M., Poulain, L., Äijälä, M., Carbone, S., Freney, E., O 'dowd, C., Baltensperger, U., Prévôt, A.S.H., 2017. Modelling winter organic aerosol at the European scale with CAMx: evaluation and source apportionment with a VBS parameterization based on novel wood burning smog chamber experiments. Atmos. Chem. Phys 17, 7653–7669. doi:10.5194/acp-17-7653-2017

Clain, G., Baray, J.L., Delmas, R., Keckhut, P., Cammas, J.P., 2010. A lagrangian approach to analyse the tropospheric ozone climatology in the tropics: Climatology of stratosphere-troposphere exchange at Reunion Island. Atmos. Environ. 44, 968–975. doi:10.1016/j.atmosenv.2009.08.048

Coakley, J.A., Cess, R.D., Yurevich, F.B., Jr., J.A.C., Cess, R.D., Yurevich, F.B., 1983. The Effect of Tropospheric Aerosols on the Earth's Radiation Budget: A Parameterization for Climate Models. J. Atmos. Sci. 40, 116–138. doi:10.1175/1520-0469(1983)040<0116:TEOTAO>2.0.CO;2

Cohen, A.J., Ross Anderson, H., Ostro, B., Pandey, K.D., Krzyzanowski, M., Künzli, N., Gutschmidt, K., Pope, A., Romieu, I., Samet, J.M., 2005. The global burden of disease due to outdoor air pollution. J. Toxicol. Environ. Heal. Part A 68, 1301–1307.

Cohn, S.A., Angevine, W.M., 2000. Boundary Layer Height and Entrainment Zone Thickness Measured by LIDARs and Wind-Profiling Radars. J. Appl. Meteorol. 39, 1233–1247. doi:10.1175/1520-0450(2000)039<1233:BLHAEZ>2.0.CO;2

Collaud Coen, M., Andrews, E., Aliaga, D., Andrade, M., Angelov, H., Bukowiecki, N., Ealo, M., Fialho, P., Flentje, H., Hallar, A.G., Hooda, R., Kalapov, I., Krejci, R., Lin, N.-H., Marinoni, A., Ming, J., Nguyen, N.A., Pandolfi, M., Pont, V., Ries, L., Rodríguez, S., Schauer, G., Sellegri, K., Sharma, S., Sun, J., Tunved, P., Velasquez,

P., Ruffieux, D., 2017. The topography contribution to the influence of the atmospheric boundary layer at high altitude stations. Atmos. Chem. Phys. Discuss. 1–44. doi:10.5194/acp-2017-692

Collaud Coen, M., Weingartner, E., Schaub, D., Hueglin, C., Corrigan, C., Henning, S., Schwikowski, M., Baltensperger, U., 2004. Saharan dust events at the Jungfraujoch: detection by wavelength dependence of the single scattering albedo and first climatology analysis. Atmos. Chem. Phys. 4, 2465–2480. doi:10.5194/acp-4-2465-2004

Cozic, J., Verheggen, B., Weingartner, E., Crosier, J., Bower, K.N., Flynn, M., Coe, H., Henning, S., Steinbacher, M., Henne, S., 2008. Chemical composition of free tropospheric aerosol for PM1 and coarse mode at the high alpine site Jungfraujoch. Atmos. Chem. Phys. 8, 407–423.

Crippa, M., Canonaco, F., Lanz, V.A., Äijälä, M., Allan, J.D., Carbone, S., Capes, G., Ceburnis, D., Dall'Osto, M., Day, D.A., DeCarlo, P.F., Ehn, M., Eriksson, A., Freney, E., Ruiz, L.H., Hillamo, R., Jimenez, J.L., Junninen, H., Kiendler-Scharr, A., Kortelainen, A.M., Kulmala, M., Laaksonen, A., Mensah, A.A., Mohr, C., Nemitz, E., O'Dowd, C., Ovadnevaite, J., Pandis, S.N., Petäjä, T., Poulain, L., Saarikoski, S., Sellegri, K., Swietlicki, E., Tiitta, P., Worsnop, D.R., Baltensperger, U., Prévôt, A.S.H., 2014. Organic aerosol components derived from 25 AMS data sets across Europe using a consistent ME-2 based source apportionment approach. Atmos. Chem. Phys. 14, 6159–6176. doi:10.5194/acp-14-6159-2014

Crippa, M., DeCarlo, P.F., Slowik, J.G., Mohr, C., Heringa, M.F., Chirico, R., Poulain, L., Freutel, F., Sciare, J., Cozic, J., Di Marco, C.F., Elsasser, M., Nicolas, J.B., Marchand, N., Abidi, E., Wiedensohler, A., Drewnick, F., Schneider, J., Borrmann, S., Nemitz, E., Zimmermann, R., Jaffrezo, J.-L., Prévôt, A.S.H., Baltensperger, U., 2013. Wintertime aerosol chemical composition and source apportionment of the organic fraction in the metropolitan area of Paris. Atmos. Chem. Phys. 13, 961–981. doi:10.5194/acp-13-961-2013

Crippa, M., El Haddad, I., Slowik, J.G., DeCarlo, P.F., Mohr, C., Heringa, M.F., Chirico, R., Marchand, N., Sciare, J., Baltensperger, U., 2013. Identification of marine and continental aerosol sources in Paris using high resolution aerosol mass spectrometry. J. Geophys. Res. Atmos. 118, 1950–1963.

Cross, E.S., Onasch, T.B., Canagaratna, M., Jayne, J.T., Kimmel, J., Yu, X.-Y., Alexander, M.L., Worsnop, D.R., Davidovits, P., 2009. Single particle characterization using a light scattering module coupled to a time-of-flight aerosol mass spectrometer. Atmos. Chem. Phys. 9, 7769–7793. doi:10.5194/acp-9-7769-2009

Crumeyrolle, S., Schwarzenboeck, A., Roger, J.C., Sellegri, K., Burkhart, J.F., Stohl, A.,

Gomes, L., Quennehen, B., Roberts, G., Weigel, R., Villani, P., Pichon, J.M., Bourrianne, T., Laj, P., 2013. Overview of aerosol properties associated with air masses sampled by the ATR-42 during the EUCAARI campaign (2008). Atmos. Chem. Phys 13, 4877–4893. doi:10.5194/acp-13-4877-2013

Crumeyrolle, S., Schwarzenboeck, A., Sellegri, K., Burkhart, J.F., Stohl, A., Gomes, L., Quennehen, B., Roberts, G., Weigel, R., Roger, J.C., 2012. Overview of aerosol properties associated with air masses sampled by the ATR-42 during the EUCAARI campaign (2008). Atmos. Chem. Phys. Discuss. 12, 9451–9490.

Curtis, S., Adler, R.F., Huffman, G.J., Gu, G., Bolvin, D.T., Nelkin, E.J., 2006. El Niño: Catastrophe or Opportunity "

De Wekker, S.F.J., Kossmann, M., 2015. Convective Boundary Layer Heights Over Mountainous Terrain—A Review of Concepts. Front. Earth Sci. 3, 1–22. doi:10.3389/feart.2015.00077

Delmas, R., Mégie, G., Peuch, V.-H., 2005. Physique et chimie de l'atmosphère, Belin.

DePuy, V., Berger, V.W., Zhou, Y., 2005. Wilcoxon–Mann–Whitney test. Encycl. Stat. Behav. Sci.

Draxler, R.R., Rolph, G.D., 2003. HYSPLIT (HYbrid Single-Particle Lagrangian Integrated Trajectory) model access via NOAA ARL READY website (http://www. arl. noaa. gov/ready/hysplit4. html). NOAA Air Resources Laboratory, Silver Spring. Md.

Drinovec, L., Močnik, G., Zotter, P., Prévôt, A.S.H., Ruckstuhl, C., Coz, E., Rupakheti, M., Sciare, J., Müller, T., Wiedensohler, A., Hansen, A.D.A., 2015. The " dual-spot " Aethalometer: an improved measurement of aerosol black carbon with real-time loading compensation. Atmos. Meas. Tech 8, 1965–1979. doi:10.5194/amt-8-1965-2015

Emeis, S., Münkel, C., Vogt, S., Müller, W.J., Schäfer, K., 2004. Atmospheric boundary-layer structure from simultaneous SODAR, RASS, and ceilometer measurements. Atmos. Environ. 38, 273–286. doi:10.1016/j.atmosenv.2003.09.054

Etling, D., 1988. On atmospheric vortex streets in the wake of large islands. Meteorol. Atmos. Phys. 41, 157–164. doi:10.1007/BF01043134

Farah, A., Freney, E., Chauvigné, A., Baray, J.-L., Rose, C., Picard, D., Colomb, A., Hadad, D., Abboud, M., Farah, W., Sellegri, K., 2018. Seasonal Variation of Aerosol Size Distribution Data at the Puy de Dôme Station with Emphasis on the Boundary Layer/Free Troposphere Segregation. Atmos. 2018, Vol. 9, Page 244 9, 244. doi:10.3390/ATMOS9070244

FLAMANT, C., PELON, J., FLAMANT, P.H., DURAND, P., 1997. LIDAR DETERMINATION OF THE ENTRAINMENT ZONE THICKNESS AT THE TOP OF THE UNSTABLE MARINE ATMOSPHERIC BOUNDARY LAYER. Boundary-Layer Meteorol. 83, 247–284. doi:10.1023/A:1000258318944

Freney, E., Sellegri, K., Asmi, E., Rose, C., Chauvigne, A., Baray, J.-L., Colomb, A., Hervo, M., Montoux, N., Bouvier, L., Picard, D., 2016. Experimental Evidence of the Feeding of the Free Troposphere with Aerosol Particles from the Mixing Layer. Aerosol Air Qual. Res. 16, 702–716. doi:10.4209/aaqr.2015.03.0164

Freney, E.J., Sellegri, K., Canonaco, F., Boulon, J., Hervo, M., Weigel, R., Pichon, J.M., Colomb, A., Prévôt, A.S.H., Laj, P., 2011. Seasonal variations in aerosol particle composition at the puy-de-Dôme research station in France. Atmos. Chem. Phys. 11, 13047–13059.

Freville, P., Montoux, N., Baray, J.-L., Chauvigné, A., Réveret, F., Hervo, M., Dionisi, D., Payen, G., Sellegri, K., 2015. LIDAR Developments at Clermont-Ferrand—France for Atmospheric Observation. Sensors 15, 3041–3069. doi:10.3390/s150203041

Fröhlich, R., Cubison, M.J., Slowik, J.G., Bukowiecki, N., Canonaco, F., Croteau, P.L., Gysel, M., Henne, S., Herrmann, E., Jayne, J.T., Steinbacher, M., Worsnop, D.R., Baltensperger, U., Prévôt, A.S.H., 2015. Fourteen months of on-line measurements of the non-refractory submicron aerosol at the Jungfraujoch (3580 m a.s.l.) – chemical composition, origins and organic aerosol sources. Atmos. Chem. Phys. 15, 11373–11398. doi:10.5194/acp-15-11373-2015

Fröhlich, R., Cubison, M.J., Slowik, J.G., Bukowiecki, N., Prévôt, A.S.H., Baltensperger, U., Schneider, J., Kimmel, J.R., Gonin, M., Rohner, U., Worsnop, D.R., Jayne, J.T., 2013. The ToF-ACSM: a portable aerosol chemical speciation monitor with TOFMS detection. Atmos. Meas. Tech. 6, 3225–3241. doi:10.5194/amt-6-3225-2013

Ginoux, P., Chin, M., Tegen, I., Prospero, J.M., Holben, B., Dubovik, O., Lin, S.-J., 2001. Sources and distributions of dust aerosols simulated with the GOCART model. J. Geophys. Res. Atmos. 106, 20255–20273. doi:10.1029/2000JD000053

Griffiths, A.D., Conen, F., Weingartner, E., Zimmermann, L., Chambers, S.D., Williams, A.G., Steinbacher, M., 2014. Surface-to-mountaintop transport characterised by radon observations at the Jungfraujoch. Atmos. Chem. Phys. 14, 12763–12779. doi:10.5194/acp-14-12763-2014

Guedalia, D., Lopez, A., Fontan, J., Birot, A., 1972. Aircraft Measurements of Rn-222, Aitken Nuclei and Small Ions up to 6 km. J. Appl. Meteorol. 11, 357–365. doi:10.1175/1520-0450(1972)011<0357:AMORAN>2.0.CO;2

Guyot, G., Gourbeyre, C., Febvre, G., Shcherbakov, V., Burnet, F., Dupont, J.-C., Sellegri, K., Jourdan, O., 2015. Quantitative evaluation of seven optical sensors for cloud microphysical measurements at the Puy-de-Dôme Observatory, France. Atmos. Meas. Tech. 8, 4347–4367. doi:10.5194/amt-8-4347-2015

Henne, S., Brunner, D., Folini, D., Solberg, S., Klausen, J., Buchmann, B., 2010. Assessment of parameters describing representativeness of air quality in-situ measurement sites. Atmos. Chem. Phys. 10, 3561–3581.

Hennigan, C.J., Sullivan, A.P., Collett, J.L., Robinson, A.L., 2010. Levoglucosan stability in biomass burning particles exposed to hydroxyl radicals. Geophys. Res. Lett. 37. doi:10.1029/2010GL043088

Heringa, M.F., Decarlo, P.F., Chirico, R., Tritscher, T., Dommen, J., Weingartner, E., Richter, R., Wehrle, G., Prévôt, A.S.H., Baltensperger, U., 2011. Investigations of primary and secondary particulate matter of different wood combustion appliances with a high-resolution time-of-flight aerosol mass spectrometer. Atmos. Chem. Phys. Atmos. Chem. Phys. 11, 5945–5957. doi:10.5194/acp-11-5945-2011

Herrmann, E., Weingartner, E., Henne, S., Vuilleumier, L., Bukowiecki, N., Steinbacher, M., Conen, F., Collaud Coen, M., Hammer, E., Jurányi, Z., Baltensperger, U., Gysel, M., 2015. Analysis of long-term aerosol size distribution data from Jungfraujoch with emphasis on free tropospheric conditions, cloud influence, and air mass transport. J. Geophys. Res. Atmos. 120, 2015JD023660. doi:10.1002/2015JD023660

Holtslag, a. a. M., De Bruijn, E.I.F., Pan, H.-L., 1990. A High Resolution Air Mass Transformation Model for Short-Range Weather Forecasting. Mon. Weather Rev. doi:10.1175/1520-0493(1990)118<1561:AHRAMT>2.0.CO;2

Holzworth, G.C., 1964. Estimates of Mean Maximum Mixing Depths in the Contiguous United States. Mon. Weather Rev. 92, 235–242. doi:10.1175/1520-0493(1964)092<0235:EOMMMD>2.3.CO;2

Hopke, P.K., 2003. Recent developments in receptor modeling. J. Chemom. 17, 255–265. doi:10.1002/cem.796

Hov, Ø., Flatøy, F., 1997. Convective Redistribution of Ozone and Oxides of Nitrogen in the Troposphere over Europe in Summer and Fall. J. Atmos. Chem. 28, 319–337. doi:10.1023/A:1005780730600

Huang, S., Rahn, K.A., Arimoto, R., 1999. Testing and optimizing two factor-analysis techniques on aerosol at Narragansett, Rhode Island. Atmos. Environ. 33, 2169–2185. doi:10.1016/S1352-2310(98)00324-0

IPCC, 2007. IPCC(AR4):Climate change 2007: Impacts, Adaptation and Vulnerability. Contribution of working group II to the Fourth Assessment Report of the Intergovernmental Panel on Climate Change, edited by: Parry, M.L., Canziani, O.F., Palutikof, J.P., van der Linden, P.J., and Hanson, C.E. Cambridge Univ. Press. Cambridge,.

Jacobson, M.Z., 2005. Fundamentals of Atmospheric Modeling, Cambridge University Press.

Jaenicke, R., Mathias-Maser, S., 1992. Natural source of atmospheric aerosol particles, S.E. Schwartz, W.G.N. Slinn (Eds.), Precipitation Scavenging and Atmosphere-Surface Exchange, Hemisphere, Washington DC, pp. 1617-1639.

Jimenez, J.L., Canagaratna, M.R., Donahue, N.M., Prevot, A.S.H., Zhang, Q., Kroll, J.H., DeCarlo, P.F., Allan, J.D., Coe, H., Ng, N.L., 2009. Evolution of organic aerosols in the atmosphere. Science (80-.). 326, 1525–1529.

Jimenez, J.L., Canagaratna, M.R., Donahue, N.M., Prevot, A.S.H., Zhang, Q., Kroll, J.H., DeCarlo, P.F., Allan, J.D., Coe, H., Ng, N.L., Aiken, A.C., Docherty, K.S., Ulbrich, I.M., Grieshop, A.P., Robinson, A.L., Duplissy, J., Smith, J.D., Wilson, K.R., Lanz, V.A., Hueglin, C., Sun, Y.L., Tian, J., Laaksonen, A., Raatikainen, T., Rautiainen, J., Vaattovaara, P., Ehn, M., Kulmala, M., Tomlinson, J.M., Collins, D.R., Cubison, M.J., Dunlea, E.J., Huffman, J.A., Onasch, T.B., Alfarra, M.R., Williams, P.I., Bower, K., Kondo, Y., Schneider, J., Drewnick, F., Borrmann, S., Weimer, S., Demerjian, K., Salcedo, D., Cottrell, L., Griffin, R., Takami, A., Miyoshi, T., Hatakeyama, S., Shimono, A., Sun, J.Y., Zhang, Y.M., Dzepina, K., Kimmel, J.R., Sueper, D., Jayne, J.T., Herndon, S.C., Trimborn, A.M., Williams, L.R., Wood, E.C., Middlebrook, A.M., Kolb, C.E., Baltensperger, U., Worsnop, D.R., Worsnop, D.R., 2009. Evolution of organic aerosols in the atmosphere. Science 326, 1525–9. doi:10.1126/science.1180353

Jokinen, V., Mäkelä, J.M., 1997. Closed-loop arrangement with critical orifice for DMA sheath/excess flow system. J. Aerosol Sci. 28, 643–648.

Kiendler-Scharr, A., Mensah, A.A., Friese, E., Topping, D., Nemitz, E., Prevot, A.S.H., Äijälä, M., Allan, J., Canonaco, F., Canagaratna, M., Carbone, S., Crippa, M., Dall Osto, M., Day, D.A., De Carlo, P., Di Marco, C.F., Elbern, H., Eriksson, A., Freney, E., Hao, L., Herrmann, H., Hildebrandt, L., Hillamo, R., Jimenez, J.L., Laaksonen, A., McFiggans, G., Mohr, C., O'Dowd, C., Otjes, R., Ovadnevaite, J., Pandis, S.N., Poulain, L., Schlag, P., Sellegri, K., Swietlicki, E., Tiitta, P., Vermeulen, A., Wahner, A., Worsnop, D., Wu, H.C., 2016. Ubiquity of organic nitrates from nighttime chemistry in the European submicron aerosol. Geophys. Res. Lett. 43, 7735–7744. doi:10.1002/2016GL069239

Knibbs, L.D., Cole-Hunter, T., Morawska, L., 2011. A review of commuter exposure to ultrafine particles and its health effects. Atmos. Environ. 45, 2611–2622. doi:10.1016/j.atmosenv.2011.02.065

Kompalli, S.K., Suresh Babu, S., Krishna Moorthy, K., Mukunda M Gogoi, Vijayakumar S Nair, Jai Prakash Chaubey, 2014. The formation and growth of ultrafine particles in two contrasting environments: a case study. Ann. Geophys. 32, 817–830. doi:10.5194/angeo-32-817-2014

Kulmala, M., Kerminen, V.-M., 2008. On the formation and growth of atmospheric nanoparticles. Atmos. Res. 90, 132–150. doi:10.1016/J.ATMOSRES.2008.01.005

Lagzi, I., Meszaros, R., Gelybo, G., Leelossy, A., 2014. Atmospheric Chemistry.

Lanz, V.A., Prévôt, A.S.H., Alfarra, M.R., Weimer, S., Mohr, C., DeCarlo, P.F., Gianini, M.F.D., Hueglin, C., Schneider, J., Favez, O., 2010. Characterization of aerosol chemical composition with aerosol mass spectrometry in Central Europe: an overview. Atmos. Chem. Phys. 10, 10453–10471.

Leck, C., Keith Bigg, E., 2008. Comparison of sources and nature of the tropical aerosol with the summer high Arctic aerosol. Tellus B Chem. Phys. Meteorol. 60, 118–126. doi:10.1111/j.1600-0889.2007.00315.x

Lee, H.N., Larsen, R.J., 1997. Vertical Diffusion in the Lower Atmosphere Using Aircraft Measurements of 222Rn. J. Appl. Meteorol. 36, 1262–1270. doi:10.1175/1520-0450(1997)036<1262:VDITLA>2.0.CO;2

Luo, C., Mahowald, N.M., Del Corral, J., 2003. Sensitivity study of meteorological parameters on mineral aerosol mobilization, transport, and distribution. J. Geophys. Res 108. doi:10.1029/2003JD003483

M. Rami Alfarra, *,†, Andre S. H. Prevot, *,†, Sönke Szidat, †,‡, Jisca Sandradewi, †, Silke Weimer, †,§, Valentin A. Lanz, §, Daniel Schreiber, §, Martin Mohr, § and, Baltensperger†, U., 2007. Identification of the Mass Spectral Signature of Organic Aerosols from Wood Burning Emissions. doi:10.1021/ES062289B

Manninen, H.E., Nieminen, T., Asmi, E., Gagné, S., Häkkinen, S., Lehtipalo, K., Aalto, P., Vana, M., Mirme, A., Mirme, S., Hõrrak, U., Plass-Dülmer, C., Stange, G., Kiss, G., Hoffer, A., Töro, N., Moerman, M., Henzing, B., De Leeuw, G., Brinkenberg, M., Kouvarakis, G.N., Bougiatioti, A., Mihalopoulos, N., O'Dowd, C., Ceburnis, D., Arneth, A., Svenningsson, B., Swietlicki, E., Tarozzi, L., Decesari, S., Facchini, M.C., Birmili, W., Sonntag, A., Wiedensohler, A., Boulon, J., Sellegri, K., Laj, P., Gysel, M., Bukowiecki, N., Weingartner, E., Wehrle, G., Laaksonen, A., Hamed, A., Joutsensaari, J., Petäjä, T., Kerminen, V.M., Kulmala, M., 2010. EUCAARI ion spectrometer measurements at 12 European sites-analysis of new particle

formation events. Atmos. Chem. Phys. 10, 7907–7927. doi:10.5194/acp-10-7907-2010

Maring, H., Savoie, D.L., Izaguirre, M.A., McCormick, C., Arimoto, R., Prospero, J.M., Pilinis, C., 2000. Aerosol physical and optical properties and their relationship to aerosol composition in the free troposphere at Izaña, Tenerife, Canary Islands, during July 1995. J. Geophys. Res. Atmos. 105, 14677–14700. doi:10.1029/2000JD900106

Martin, S.T., Hung, H.-M., Park, R.J., Jacob, D.J., Spurr, R.J.D., Chance, K. V., Chin, M., 2004. Effects of the physical state of tropospheric ammonium-sulfate-nitrate particles on global aerosol direct radiative forcing. Atmos. Chem. Phys. 4, 183–214.

Mckendry, I.G., Hacker, J.P., Stull, R., Sakiyama, S., Mignacca, D., Reid, K., 2001. Long-range transport of Asian dust to the Lower Fraser Valley, British Columbia, Canada : Quantifying the radiative impacts of mineral dust (DUST). J. Geophys. Res. 106, 18361–18370.

Menut, L., Flamant, C., Pelon, J., Flamant, P.H., 1999. Urban boundary-layer height determination from LIDAR measurements over the Paris area. Appl. Opt. 38, 945. doi:10.1364/AO.38.000945

Middlebrook, A.M., Bahreini, R., Jimenez, J.L., Canagaratna, M.R., 2012. Evaluation of Composition-Dependent Collection Efficiencies for the Aerodyne Aerosol Mass Spectrometer using Field Data. Aerosol Sci. Technol. 46, 258–271. doi:10.1080/02786826.2011.620041

Minguillón, M.C., Ripoll, A., Pérez, N., Prévôt, A.S.H., Canonaco, F., Querol, X., Alastuey, A., 2015. Chemical characterization of submicron regional background aerosols in the western Mediterranean using an Aerosol Chemical Speciation Monitor. Atmos. Chem. Phys. 15, 6379–6391.

Minguillón, M.C., Ripoll, A., Pérez, N., Prévôt, A.S.H., Canonaco, F., Querol, X., Alastuey, A., 2015. Chemical characterization of submicron regional background aerosols in the western Mediterranean using an Aerosol Chemical Speciation Monitor. Atmos. Chem. Phys 15, 6379–6391. doi:10.5194/acp-15-6379-2015

Mishra, A.K., Klingmueller, K., Fredj, E., Lelieveld, J., Rudich, Y., Koren, I., 2014. Radiative signature of absorbing aerosol Radiative signature of absorbing aerosol over the Eastern Mediterranean Basin Radiative signature of absorbing aerosol Radiative signature of absorbing aerosol. Atmos. Chem. Phys. Discuss 14, 2403–2447. doi:10.5194/acpd-14-2403-2014

Moorthy, K.K., Sreekanth, V., Prakash Chaubey, J., Gogoi, M.M., Suresh Babu, S.,

Kumar Kompalli, S., Bagare, S.P., Bhatt, B.C., Gaur, V.K., Prabhu, T.P., Singh, N.S., 2011. Fine and ultrafine particles at a near–free tropospheric environment over the high-altitude station Hanle in the Trans-Himalaya: New particle formation and size distribution. J. Geophys. Res. 116, D20212. doi:10.1029/2011JD016343

Müller, T., Henzing, J.S., de Leeuw, G., Wiedensohler, A., Alastuey, A., Angelov, H., Bizjak, M., Collaud Coen, M., Engström, J.E., Gruening, C., Hillamo, R., Hoffer, A., Imre, K., Ivanow, P., Jennings, G., Sun, J.Y., Kalivitis, N., Karlsson, H., Komppula, M., Laj, P., Li, S.-M., Lunder, C., Marinoni, A., Martins dos Santos, S., Moerman, M., Nowak, A., Ogren, J.A., Petzold, A., Pichon, J.M., Rodriquez, S., Sharma, S., Sheridan, P.J., Teinilä, K., Tuch, T., Viana, M., Virkkula, A., Weingartner, E., Wilhelm, R., Wang, Y.Q., 2011. Characterization and intercomparison of aerosol absorption photometers: result of two intercomparison workshops. Atmos. Meas. Tech. 4, 245–268. doi:10.5194/amt-4-245-2011

Nazaroff, W.W., 2004. Indoor particle dynamics. Indoor Air 14, 175–183. doi:10.1111/j.1600-0668.2004.00286.x

Ng, N., Canagaratna, M., Jimenez, J., Zhang, Q., Ulbrich, I., Worsnop, D., 2011. Real-Time Methods for Estimating Organic Component Mass Concentrations from Aerosol Mass Spectrometer Data. Environ. Sci. Technol. 45, 910–916. doi:10.1021/es102951k

Ng, N.L., Canagaratna, M.R., Zhang, Q., Jimenez, J.L., Tian, J., Ulbrich, I.M., Kroll, J.H., Docherty, K.S., Chhabra, P.S., Bahreini, R., Murphy, S.M., Seinfeld, J.H., Hildebrandt, L., Donahue, N.M., Decarlo, P.F., Lanz, V.A., Prévôt, A.S.H., Dinar, E., Rudich, Y., Worsnop, D.R., 2010. Organic aerosol components observed in Northern Hemispheric datasets from Aerosol Mass Spectrometry. Atmos. Chem. Phys. Atmos. Chem. Phys. 10, 4625–4641. doi:10.5194/acp-10-4625-2010

Ng, N.L., Herndon, S.C., Trimborn, A., Canagaratna, M.R., Croteau, P.L., Onasch, T.B., Sueper, D., Worsnop, D.R., Zhang, Q., Sun, Y.L., 2011. An Aerosol Chemical Speciation Monitor (ACSM) for routine monitoring of the composition and mass concentrations of ambient aerosol. Aerosol Sci. Technol. 45, 780–794.

Ng, N.L.A.R., Onasch, T.; ; onasch@aerodyne com, Trimborn, A.; trimborn@aerodyne com, Herndon, S.; herndon@aerodyne com, Canagaratna, M.; mrcana@aerodyne com, Sueper, D.; donna sueper@colorado edu, Worsnop, D.; worsnop@aerodyne com, Jayne, J.; jayne@aerodyne com, 2010. An Aerosol Chemical Speciation Monitor (ACSM) for Routine Monitoring of Atmospheric Aerosol Composition, in: AAAR 29th Annual Conference. American Association for Aerosol Research, Oregon Convention Center, Portland, Oregon, USA http://aaarabstracts.com/2010/.

O'Dowd, C.D., Smith, M.H., Consterdine, I.E., Lowe, J.A., 1997. Marine aerosol, sea-salt, and the marine sulphur cycle: A short review. Atmos. Environ. 31, 73–80. doi:10.1016/S1352-2310(96)00106-9

Oberdörster, G., Oberdörster, E., Oberdörster, J., 2005. Nanotoxicology: an emerging discipline evolving from studies of ultrafine particles. Environ. Health Perspect. 113, 823–39. doi:10.1289/EHP.7339

Onasch, T.B., Trimborn, A., Fortner, E.C., Jayne, J.T., Kok, G.L., Williams, L.R., Davidovits, P., Worsnop, D.R., 2012. Soot Particle Aerosol Mass Spectrometer: Development, Validation, and Initial Application. Aerosol Sci. Technol. 46, 804–817. doi:10.1080/02786826.2012.663948

Paatero, P., 2007. User's guide for positive matrix factorization programs PMF2 and PMF3, part 1-2: tutorial. Univ. Helsinki, Finl.

Paatero, P., 1999. The Multilinear Engine—A Table-Driven, Least Squares Program for Solving Multilinear Problems, Including the *n* -Way Parallel Factor Analysis Model. J. Comput. Graph. Stat. 8, 854–888. doi:10.1080/10618600.1999.10474853

Paatero, P., 1997. Least squares formulation of robust non-negative factor analysis. Chemom. Intell. Lab. Syst. 37, 23–35. doi:10.1016/S0169-7439(96)00044-5

Paatero, P., Tapper, U., 1994. Positive matrix factorization: A non-negative factor model with optimal utilization of error estimates of data values. Environmetrics 5, 111–126. doi:10.1002/env.3170050203

Pandey Deolal, S., Staehelin, J., Brunner, D., Cui, J., Steinbacher, M., Zellweger, C., Henne, S., Vollmer, M.K., 2013. Transport of PAN and NOy from different source regions to the Swiss high alpine site Jungfraujoch. Atmos. Environ. 64, 103–115. doi:10.1016/j.atmosenv.2012.08.021

Papayannis, A., Balis, D., Amiridis, V., Chourdakis, G., Tsaknakis, G., Zerefos, C., Castanho, A.D.A., Nickovic, S., Kazadzis, S., Grabowski, J., 2005. Measurements of Saharan dust aerosols over the Eastern Mediterranean using elastic backscatter-Raman LIDAR, spectrophotometric and satellite observations in the frame of the EARLINET project. Atmos. Chem. Phys 5, 2065–2079.

Parworth, C., Fast, J., Mei, F., Shippert, T., Sivaraman, C., Tilp, A., Watson, T., Zhang, Q., 2015. Long-term measurements of submicrometer aerosol chemistry at the Southern Great Plains (SGP) using an Aerosol Chemical Speciation Monitor (ACSM). Atmos. Environ. 106, 43–55.

Pay, M.T., Jiménez-Guerrero, P., Baldasano, J.M., 2012. Assessing sensitivity regimes of secondary inorganic aerosol formation in Europe with the CALIOPE-EU

modeling system. Atmos. Environ. 51, 146–164. doi:10.1016/J.ATMOSENV.2012.01.027

Penner, J.E., Dickinson, R.E., O'neill, C.A., 1992. Effects of aerosol from biomass burning on the global radiation budget. Science 256, 1432–4. doi:10.1126/science.256.5062.1432

Petit, J.-E., Amodeo, T., Meleux, F., Bessagnet, B., Menut, L., Grenier, D., Pellan, Y., Ockler, A., Rocq, B., Gros, V., 2017. Characterising an intense PM pollution episode in March 2015 in France from multi-site approach and near real time data: Climatology, variabilities, geographical origins and model evaluation. Atmos. Environ. 155, 68–84.

Petit, J.-E., Favez, O., Sciare, J., Crenn, V., Sarda-Estève, R., Bonnaire, N., Močnik, G., Dupont, J.-C., Haeffelin, M., Leoz-Garziandia, E., 2015. Two years of near real-time chemical composition of submicron aerosols in the region of Paris using an Aerosol Chemical Speciation Monitor (ACSM) and a multi-wavelength Aethalometer. Atmos. Chem. Phys. 15, 2985–3005.

Petzold, A., Schönlinner, M., 2004. Multi-angle absorption photometry—a new method for the measurement of aerosol light absorption and atmospheric black carbon. J. Aerosol Sci. 35, 421–441. doi:10.1016/j.jaerosci.2003.09.005

Philippin, S., Laj, P., Putaud, J.-P., Wiedensohler, A., de Leeuw, G., Fjaeraa, A., Platt, U., Baltensperger, U., Fiebig, M., 2009. EUSAAR An Unprecedented Network of Aerosol Observation in Europe. Earozoru Kenkyu 24, 78–83. doi:10.11203/jar.24.78

Piironen, A.K., Eloranta, E.W., 1995. Convective boundary layer mean depths and cloud geometrical properties obtained from volume imaging LIDAR data. J. Geophys. Res. 100, 25569. doi:10.1029/94JD02604

Pilinis, C., Pandis, S.N., Seinfeld, J.H., 1995. Sensitivity of direct climate forcing by atmospheric aerosols to aerosol size and composition. J. Geophys. Res. 100, 18739. doi:10.1029/95JD02119

Polian, G., Lambert, G., Ardouin, B., Jegou, A., 1986. Long-range transport of continental radon in subantarctic and antarctic areas. Tellus B 38, 178–189.

Putaud, J.P., Van Dingenen, R., Alastuey, A., Bauer, H., Birmili, W., Cyrys, J., Flentje, H., Fuzzi, S., Gehrig, R., Hansson, H.C., Harrison, R.M., Herrmann, H., Hitzenberger, R., Hüglin, C., Jones, A.M., Kasper-Giebl, A., Kiss, G., Kousa, A., Kuhlbusch, T.A.J., Löschau, G., Maenhaut, W., Molnar, A., Moreno, T., Pekkanen, J., Perrino, C., Pitz, M., Puxbaum, H., Querol, X., Rodriguez, S., Salma, I., Schwarz, J., Smolik, J., Schneider, J., Spindler, G., ten Brink, H., Tursic, J., Viana, M.,

Wiedensohler, A., Raes, F., 2010. A European aerosol phenomenology - 3: Physical and chemical characteristics of particulate matter from 60 rural, urban, and kerbside sites across Europe. Atmos. Environ. 44, 1308–1320. doi:10.1016/j.atmosenv.2009.12.011

Ramanathan, V., Crutzen, P.J., Lelieveld, J., Mitra, A.P., Althausen, D., Anderson, J., Andreae, M.O., Cantrell, W., Cass, G.R., Chung, C.E., Clarke, A.D., Coakley, J.A., Collins, W.D., Conant, W.C., Dulac, F., Heintzenberg, J., Heymsfield, A.J., Holben, B., Howell, S., Hudson, J., Jayaraman, A., Kiehl, J.T., Krishnamurti, T.N., Lubin, D., McFarquhar, G., Novakov, T., Ogren, J.A., Podgorny, I.A., Prather, K., Priestley, K., Prospero, J.M., Quinn, P.K., Rajeev, K., Rasch, P., Rupert, S., Sadourny, R., Satheesh, S.K., Shaw, G.E., Sheridan, P., Valero, F.P.J., 2001. Indian Ocean Experiment: An integrated analysis of the climate forcing and effects of the great Indo-Asian haze. J. Geophys. Res. Atmos. 106, 28371–28398. doi:10.1029/2001JD900133

Ripoll, A., Minguillón, M.C., Pey, J., Jimenez, J.L., Day, D.A., Sosedova, Y., Canonaco, F., Prévôt, A.S.H., Querol, X., Alastuey, A., 2015. Long-term real-time chemical characterization of submicron aerosols at Montsec (southern Pyrenees, 1570 m asl). Atmos. Chem. Phys. 15, 2935–2951.

Ripoll, A., Minguillón, M.C., Pey, J., Jimenez, J.L., Day, D.A., Sosedova, Y., Canonaco, F., Prévôt, A.S.H., Querol, X., Alastuey, A., 2015. Long-term real-time chemical characterization of submicron aerosols at Montsec (southern Pyrenees, 1570 m a.s.l.). Atmos. Chem. Phys 15, 2935–2951. doi:10.5194/acp-15-2935-2015

Rivellini, L.-H., Chiapello, I., Tison, E., Fourmentin, M., Féron, A., Diallo, A., Diaye, T.N.', Goloub, P., Canonaco, F., Stephan, A., Prévôt, H., Riffault, V., 2017. Chemical characterization and source apportionment of submicron aerosols measured in Senegal during the 2015 SHADOW campaign. Atmos. Chem. Phys 175194, 10291–10314. doi:10.5194/acp-17-10291-2017

Rose, C., Boulon, J., Hervo, M., Holmgren, H., Asmi, E., Ramonet, M., Laj, P., Sellegri, K., 2013. Long-term observations of cluster ion concentration, sources and sinks in clear sky conditions at the high-altitude site of the Puy de Dôme, France. Atmos. Chem. Phys. 13, 11573–11594. doi:10.5194/acp-13-11573-2013

Rose, C., Sellegri, K., Freney, E., Dupuy, R., Colomb, A., Pichon, J.-M., Ribeiro, M., Bourianne, T., Burnet, F., Schwarzenboeck, A., 2015a. Airborne measurements of new particle formation in the free troposphere above the Mediterranean Sea during the HYMEX campaign. Atmos. Chem. Phys. 15, 10203–10218. doi:10.5194/acp-15-10203-2015

Rose, C., Sellegri, K., Velarde, F., Moreno, I., Ramonet, M., Weinhold, K., Krejci, R.,

Ginot, P., Andrade, M., Wiedensohler, A., 2015b. Frequent nucleation events at the high altitude station of Chacaltaya (5240 m asl), Bolivia. Atmos. Environ. 102, 18–29.

Salzano, R., Pasini, A., Casasanta, G., Cacciani, M., Perrino, C., 2016. Quantitative Interpretation of Air Radon Progeny Fluctuations in Terms of Stability Conditions in the Atmospheric Boundary Layer. Boundary-Layer Meteorol. 160, 529–550.

Sandradewi, J., Prévôt, A.S.H., Szidat, S., Perron, N., Alfarra, M.R., Lanz, V.A., Weingartner, E., Baltensperger, U., 2008. Using Aerosol Light Absorption Measurements for the Quantitative Determination of Wood Burning and Traffic Emission Contributions to Particulate Matter. Environ. Sci. Technol. 42, 3316–3323. doi:10.1021/es702253m

Satheesh, S.K., Krishna Moorthy, K., 2005. Radiative effects of natural aerosols: A review. Atmos. Environ. 39, 2089–2110. doi:10.1016/J.ATMOSENV.2004.12.029

Schmidt, M., 1999. Measurement and balancing anthropogenic greenhouse gases in Germany. Univ. Heidelberg, Heidelberg, Ger.

Schröder, F., Ström, J., 1997. Aircraft measurements of sub micrometer aerosol particles (> 7 nm) in the midlatitude free troposphere and tropopause region. Atmos. Res. 44, 333–356. doi:10.1016/S0169-8095(96)00034-8

Seibert, P., Beyrich, F., Gryning, S.-E., Joffre, S., Rasmussen, A., Tercier, P., 2000. Review and intercomparison of operational methods for the determination of the mixing height. Atmos. Environ. 34, 1001–1027. doi:10.1016/S1352-2310(99)00349-0

Seinfeld, J.H., Pandis, S.N., 2006. Atmospheric Chemistry and Physics: From Air Pollution to Climate Change, Atmospheric Chemistry and Physics. doi:10.1063/1.882420

Seinfeld, J.H., Pandis, S.N., 2006. Atmospheric chemistry and physics: from air pollution to climate change, John Wiley & Sons., New York. [online] Available from: http://www.scirp.org/(S(351jmbntvnsjt1aadkposzje))/reference/ReferencesPapers.aspx?ReferenceID=1345321 (Accessed 9 October 2017. AIP.

Sellegri, K., Laj, P., Dupuy, R., Legrand, M., Preunkert, S., Putaud, J.-P., 2003. Size-dependent scavenging efficiencies of multicomponent atmospheric aerosols in clouds. J. Geophys. Res. 108, AAC3.1-AAC3.15.

Stavroulas, I., Bougiatioti, A., Paraskevopoulou, D., Grivas, G., Liakakou, E., Gerasopoulos, E., Mihalopoulos, N., 2018. Sources and processes that control the

submicron organic aerosol in an urban Mediterranean environment (Athens) using high temporal resolution chemical composition measurements. ACPD. doi:10.5194/acp-2018-356

Stein, A.F., Lamb, D., 2002. Chemical indicators of sulfate sensitivity to nitrogen oxides and volatile organic compounds. J. Geophys. Res. 107, 4449. doi:10.1029/2001JD001088

Stocker, T.F., Qin, D., Plattner, G.-K., Tignor, M., Allen, S.K., Boschung, J., Nauels, A., Xia, Y., Bex, V., Midgley, P.M., 2013. IPCC, 2013: Climate Change 2013: The Physical Science Basis. Contribution of Working Group I to the Fifth Assessment Report of the Intergovernmental Panel on Climate Change. Cambridge Univ. Press. Cambridge, United Kingdom New York, NY, USA 1535 pp.

Stull, R.B. (Ed.), 1988. An Introduction to Boundary Layer Meteorology. Springer Netherlands, Dordrecht.

Szegvary, T., Leuenberger, M.C., Conen, F., 2007. Predicting terrestrial 222Rn flux using gamma dose rate as a proxy. Atmos. Chem. Phys. 7, 2789–2795. doi:10.5194/acp-7-2789-2007

Tennekes, H., 1973. A Model for the Dynamics of the Inversion Above a Convective Boundary Layer. J. Atmos. Sci. 30, 558–567. doi:10.1175/1520-0469(1973)030<0558:AMFTDO>2.0.CO;2

Tiitta, P., Vakkari, V., Croteau, P., Beukes, J.P., Van Zyl, P.G., Josipovic, M., Venter, A.D., Jaars, K., Pienaar, J.J., Ng, N.L., 2014. Chemical composition, main sources and temporal variability of PM 1 aerosols in southern African grassland. Atmos. Chem. Phys. 14, 1909–1927.

Timonen, H., Wigder, N., Jaffe, D., 2013. Influence of background particulate matter (PM) on urban air quality in the Pacific Northwest. J. Environ. Manage. 129, 333–340.

Troen, I.B., Mahrt, L., 1986. A simple model of the atmospheric boundary layer; sensitivity to surface evaporation. Boundary-Layer Meteorol. 37, 129–148.

Tröstl, J., Herrmann, E., Frege, C., Bianchi, F., Molteni, U., Bukowiecki, N., Hoyle, C.R., Steinbacher, M., Weingartner, E., Dommen, J., Gysel, M., Baltensperger, U., 2016. Contribution of new particle formation to the total aerosol concentration at the high altitude site Jungfraujoch (3’580 m a.s.l., Switzerland). J. Geophys. Res. Atmos. 2015JD024637. doi:10.1002/2015JD024637

Twomey, S., 1977. The Influence of Pollution on the Shortwave Albedo of Clouds. J. Atmos. Sci. 34, 1149–1152. doi:10.1175/1520-

0469(1977)034<1149:TIOPOT>2.0.CO;2

Ulbrich, I.M., Canagaratna, M.R., Zhang, Q., Worsnop, D.R., Jimenez, J.L., 2009. Interpretation of organic components from Positive Matrix Factorization of aerosol mass spectrometric data. Atmos. Chem. Phys. 9, 2891–2918. doi:10.5194/acp-9-2891-2009

Vakkari, V., Kerminen, V.-M., Beukes, J.P., Tiitta, P., Zyl, P.G., Josipovic, M., Venter, A.D., Jaars, K., Worsnop, D.R., Kulmala, M., 2014. Rapid changes in biomass burning aerosols by atmospheric oxidation. Geophys. Res. Lett. 41, 2644–2651.

van der Laan, S., van der Laan-Luijkx, I.T., Zimmermann, L., Conen, F., Leuenberger, M., 2014. Net CO2 surface emissions at Bern, Switzerland inferred from ambient observations of CO2, δ(O2/N2), and 222Rn using a customized radon tracer inversion. J. Geophys. Res. Atmos. 119, 2013JD020307. doi:10.1002/2013JD020307

Venzac, H., Sellegri, K., Laj, P., 2007. Nucleation events detected at the high altitude site of the Puy de Dôme Research Station, France. Boreal Environ. Res. 12, 345–359.

Venzac, H., Sellegri, K., Villani, P., Picard, D., Laj, P., 2009. Seasonal variation of aerosol size distributions in the free troposphere and residual layer at the puy de Dôme station, France. Atmos. Chem. Phys. 9, 1465–1478. doi:10.5194/acp-9-1465-2009

Viana, M., Hammingh, P., Colette, A., Querol, X., Degraeuwe, B., Vlieger, I. de, van Aardenne, J., 2014. Impact of maritime transport emissions on coastal air quality in Europe. Atmos. Environ. 90, 96–105. doi:10.1016/J.ATMOSENV.2014.03.046

Villani, P., Picard, D., Marchand*, N., Laj, P., 2007. Design and Validation of a 6-Volatility Tandem Differential Mobility Analyzer (VTDMA). Aerosol Sci. Technol. 41, 898–906. doi:10.1080/02786820701534593

von der Weiden, S.-L., Drewnick, F., Borrmann, S., 2009. Particle Loss Calculator – a new software tool for the assessment of the performance of aerosol inlet systems. Atmos. Meas. Tech. 2, 479–494. doi:10.5194/amt-2-479-2009

von Engeln, A., Teixeira, J., 2013. A Planetary Boundary Layer Height Climatology Derived from ECMWF Reanalysis Data. J. Clim. 26, 6575–6590. doi:10.1175/JCLI-D-12-00385.1

Weingartner, E., Saathoo, H., Schnaiter, M., Streit, N., Bitnar, B., Baltensperger, U., 2003. Absorption of light by soot particles: determination of the absorption coeecient by means of aethalometers. Aerosol Sci. 34, 1445–1463. doi:10.1016/S0021-8502(03)00359-8

Whitby, K.T., Cantrell, B.K., Kittelson, D.B., 1978. Nuclei formation rates in a coal-fired power plant plume. Atmos. Environ. 12, 313–321. doi:10.1016/0004-6981(78)90213-5

Wiedensohler, A., Birmili, W., Nowak, A., Sonntag, A., Weinhold, K., Merkel, M., Wehner, B., Tuch, T., Pfeifer, S., Fiebig, M., Fjäraa, A.M., Asmi, E., Sellegri, K., Depuy, R., Venzac, H., Villani, P., Laj, P., Aalto, P., Ogren, J.A., Swietlicki, E., Williams, P., Roldin, P., Quincey, P., Hüglin, C., Fierz-Schmidhauser, R., Gysel, M., Weingartner, E., Riccobono, F., Santos, S., Grüning, C., Faloon, K., Beddows, D., Harrison, R., Monahan, C., Jennings, S.G., O'Dowd, C.D., Marinoni, A., Horn, H.-G., Keck, L., Jiang, J., Scheckman, J., McMurry, P.H., Deng, Z., Zhao, C.S., Moerman, M., Henzing, B., de Leeuw, G., Löschau, G., Bastian, S., 2012. Mobility particle size spectrometers: harmonization of technical standards and data structure to facilitate high quality long-term observations of atmospheric particle number size distributions. Atmos. Meas. Tech. 5, 657–685. doi:10.5194/amt-5-657-2012

Wiegner, M., Emeis, S., Freudenthaler, V., Heese, B., Junkermann, W., Münkel, C., Schäfer, K., Seefeldner, M., Vogt, S., 2006. Mixing layer height over Munich, Germany: Variability and comparisons of different methodologies. J. Geophys. Res. Atmos. 111, D13201. doi:10.1029/2005JD006593

Williams, A.G., Zahorowski, W., Chambers, S., Griffiths, A., Hacker, J.M., Element, A., Werczynski, S., 2010. The Vertical Distribution of Radon in Clear and Cloudy Daytime Terrestrial Boundary Layers. J. Atmos. Sci. 68, 155–174. doi:10.1175/2010JAS3576.1

Woodcock, A.H., Kientzler, C.F., Arons, A.B., Blanchard, D.C., 1953. Giant condensation nuclei from bursting bubbles. Nature 172, 1144–1145. doi:10.1038/1721144a0

Zanis, P., Ganser, A., Zellweger, C., Henne, S., Steinbacher, M., Staehelin, J., 2007. Seasonal variability of measured ozone production efficiencies in the lower free troposphere of Central Europe. Atmos. Chem. Phys. 7, 223–236. doi:10.5194/acp-7-223-2007

Zellweger, C., Forrer, J., Hofer, P., Nyeki, S., Schwarzenbach, B., Weingartner, E., Ammann, M., Baltensperger, U., 2003. Partitioning of reactive nitrogen (NOy) and dependence on meteorological conditions in the lower free troposphere. Atmos. Chem. Phys. 3, 779–796. doi:10.5194/acp-3-779-2003

Zender, C.S., Miller, R.L.R.L., Tegen, I., 2004. Quantifying mineral dust mass budgets:Terminology, constraints, and current estimates. Eos, Trans. Am. Geophys. Union 85, 509. doi:10.1029/2004EO480002

Zhang, K., Feichter, J., Kazil, J., Wan, H., Zhuo, W., Griffiths, A.D., Sartorius, H., Zahorowski, W., Ramonet, M., Schmidt, M., Yver, C., Neubert, R.E.M., Brunke, E.-G., 2011. Radon activity in the lower troposphere and its impact on ionization rate: a global estimate using different radon emissions. Atmos. Chem. Phys. 11, 7817–7838. doi:10.5194/acp-11-7817-2011

Zhang, Q., Alfarra, M.R., Worsnop, D.R., Allan, J.D., Coe, H., Canagaratna, M.R., Jimenez, J.L., 2005. Deconvolution and quantification of hydrocarbon-like and oxygenated organic aerosols based on aerosol mass spectrometry. Environ. Sci. Technol. 39, 4938–4952.

Zhang, Q., Jimenez, J.L., Canagaratna, M.R., Allan, J.D., Coe, H., Ulbrich, I., Alfarra, M.R., Takami, A., Middlebrook, A.M., Sun, Y.L., Dzepina, K., Dunlea, E., Docherty, K., DeCarlo, P.F., Salcedo, D., Onasch, T., Jayne, J.T., Miyoshi, T., Shimono, A., Hatakeyama, S., Takegawa, N., Kondo, Y., Schneider, J., Drewnick, F., Borrmann, S., Weimer, S., Demerjian, K., Williams, P., Bower, K., Bahreini, R., Cottrell, L., Griffin, R.J., Rautiainen, J., Sun, J.Y., Zhang, Y.M., Worsnop, D.R., 2007. Ubiquity and dominance of oxygenated species in organic aerosols in anthropogenically-influenced Northern Hemisphere midlatitudes. Geophys. Res. Lett. 34, 1–6. doi:10.1029/2007GL029979

Zhou, S., Collier, S., Jaffe, D.A., Zhang, Q., 2018. Free Tropospheric Aerosols at the Mt. Bachelor Observatory: More Oxidized and Higher Sulfate Content Compared to Boundary Layer Aerosols. Atmos. Chem. Phys. Discuss. 1–25. doi:10.5194/acp-2018-821

Summary of Figures and Tables

Figures

Tables

Appendix

Farah et al., 2018

Farah, A., Freney, E., Chauvigné, A., Baray, J.-L., Rose, C., Picard, D., Colomb, A., Hadad, D., Abboud, M., Farah, W., Sellegri, K., 2018. Seasonal Variation of Aerosol Size Distribution Data at the Puy de Dôme Station with Emphasis on the Boundary Layer/Free Troposphere Segregation. Atmos. 2018, Vol. 9, Page 244 9, 244. doi:10.3390/ATMOS9070244

atmosphere

MDPI

Article

Seasonal Variation of Aerosol Size Distribution Data at the Puy de Dôme Station with Emphasis on the Boundary Layer/Free Troposphere Segregation

Antoine Farah [1,*], Evelyn Freney [1], Aurélien Chauvigné [2], Jean-Luc Baray [1,3], Clémence Rose [1], David Picard [1], Aurélie Colomb [1,3], Dani Hadad [1], Maher Abboud [4], Wehbeh Farah [4] and Karine Sellegri [1,*]

1 Laboratoire de Météorologie Physique, UMR6016, Université Clermont Auvergne-CNRS, 4 avenue Blaise Pascal, 63178 Aubière, France; e.freney@opgc.univ-bpclermont.fr (E.F.); J.L.Baray@opgc.fr (J.-L.B.); C.Rose@opgc.univ-bpclermont.fr (C.R.); d.picard@opgc.univ-bpclermont.fr (D.P.); A.Colomb@opgc.univ-bpclermont.fr (A.C.); d.hadad@opgc.univ-bpclermont.fr (D.H.)

2 Laboratoire d'Optique Atmosphérique, UMR 8518, Université de Lille, 59000 Lille, France; chauvigneaurelien@gmail.com

3 Observatoire de Physique du Globe de Clermont Ferrand, UMS 833, Université Clermont Auvergne-CNRS, 4 avenue Blaise Pascal, 63178 Aubière, France

4 Unité de Recherche EGFEM, Faculté des Sciences, Université Saint Joseph, BP 17-5208-Mar Mikhaël, Beyrouth-1104 2020, Liban; maher.abboud@usj.edu.lb (M.A.); wehbeh.farah@usj.edu.lb (W.F.)

* Correspondence: a.farah@opgc.univ-bpclermont.fr (A.F.); K.Sellegri@opgc.univ-bpclermont.fr (K.S.); Tel.: +33-473-407-678 (A.F.); +33-473-407-394 (K.S.)

Received: 26 April 2018; Accepted: 22 June 2018; Published: 26 June 2018

check for updates

Abstract: Aerosol particles are important due to their direct and indirect impacts on climate. Within the planetary boundary layer (BL), these particles have a relatively short lifetime due to their frequent removal process by wet deposition. When aerosols are transported into the free troposphere (FT), their atmospheric lifetime increases significantly, making them representative of large spatial areas. In this work, we use a combination of in situ measurements performed at the high altitude PUY (Puy de Dôme, 45°46′ N, 2°57′ E, 1465 m a.s.l) station, together with LIDAR profiles at Clermont-Ferrand for characterizing FT conditions, and further characterize the physical properties of aerosol in this poorly documented area of the atmosphere. First, a combination of four criteria was used to identify whether the PUY station lies within the FT or within the BL. Results show that the PUY station is located in BL with frequencies ranging from 50% during the winter, up to 97% during the summer. Then, the classification is applied to a year-long dataset (2015) of particle size distribution data to study the differences in particle physical characteristics (size distribution) and black carbon (BC) concentrations between the FT and the BL. Although BC, Aitken, and the accumulation mode particles concentrations were higher in the BL than in the FT in winter and autumn, they were measured to be higher in the FT compared to BL in spring. No significant difference between the BL and the FT concentrations was observed for the nucleation mode particles for all seasons, suggesting a continuous additional source of nucleation mode particles in the FT during winter and autumn. Coarse mode particle concentrations were found higher in the FT than in the BL for all seasons and especially during summer. This indicates an efficient long-range transport of large particles in the FT from distant sources (marine and desert) due to higher wind speeds in the FT compared to BL. For FT air masses, we used 204-h air mass back-trajectories combined with boundary layer height estimations from ECMWF ERA-Interim to assess the time they spent in the FT since their last contact with the BL and to evaluate the impact of this parameter on the aerosol properties. We observed that even after 75 h without any contact with the BL, FT aerosols preserve specific properties of their air mass type.

Keywords: aerosol size distribution; high altitude site; long-range transport; boundary layer/lower free troposphere

1. Introduction

Aerosol particles affect climate through both direct and indirect effects, as well as being an important factor in public health [1]. These aerosol particles are mostly concentrated in the atmospheric boundary layer (BL) (Table A1). The BL is defined as the first atmospheric layer which is directly influenced by the Earth's surface, and responds to surface forcing within a timescale of an hour or less [2]. The BL develops during daytime in response to convection, and is therefore usually referred to as a convective mixed layer. Slightly before sunset, when turbulence decreases, the formerly mixed layer is replaced by the so-called residual layer (RL), which initial properties (in terms of both mean state variables and concentrations) are similar to those of the mixed layer. As the night advances, the lower part of the residual layer which is in contact with the ground is progressively transformed into a stable BL.

The BL height (BLH) varies daily and seasonally according to surface energy balance, and the top of the BL is usually found between 500 m over the sea and 2 km above land. However, as illustrated by Herrmann et al. (2015) [3], the determination of the BLH is complex due to the lack of a commonly accepted technique to measure it. This evaluation is even more challenging over complex mountainous terrain, above which the atmospheric structure becomes more complicated [4]. In addition to pioneer methods based on vertical temperature profiles [5,6], several techniques have been developed to determine the BLH. Those include radio sounding system [7], active remote sensing such as ceilometer, SODAR and LIDAR [8,9], in situ measurements of trace gases, aerosol particles concentrations, and wind direction from high altitude sites [3,10–12] as well as atmospheric models [13,14]. However, the majority of the abovementioned methods retrieve the height of the so-called aerosol layer (AL, also referred to as aerosol mixing layer in the literature) that can occasionally differ from the BL ([4] and references therein). Mostly during the daytime, the AL can be assimilated to the BL when aerosol particles are homogeneously mixed within the BL. Herrmann et al. (2015) [3] compared three criteria for selecting free tropospheric conditions at the Jungfraujoch (JFJ) research station (Swiss Alps, 3580 m a.s.l.) and found that FT conditions prevail for 39% of the time (over 60% during winter and below 20% during summer). However, it was highlighted that one of the major difficulties in these studies is providing a robust selection of FT air masses.

BL aerosols can be transported into the FT when they cross the temperature inversion at the top of the BL, either due to turbulence in the inversion layer, strong thermal convection or cold fronts over polluted areas [15]. Other sources of particles in the FT can be nucleation of low-volatility gas-phase components into new particle clusters and their growth to larger sizes. As evidenced in earlier studies [16–18] new particle formation (NPF) may have specific characteristics at high altitudes. Once in the FT, aerosol particles have a longer residence time due to the lower frequency at which they are scavenged by clouds and precipitation, allowing them to be transported in the atmosphere for several days [19] increasing their impact on the climate. Additionally, aerosol particles transported into the FT or formed in the FT can be re-injected again into BL, affecting the air quality far from the source region [20,21]. For these reasons, it is important to characterize the properties of FT aerosols. Additionally, these measurements are needed to validate and improve numerical mesoscale or global scale transport models [22]. A number of studies focused on FT conditions from ground-based high altitude sites [3,14,19] or from airborne measurement campaigns [23,24], providing information on aerosol physical and chemical properties in this part of the atmosphere. Fröhlich et al. (2015) [25] and Freney et al. (2016) [19] showed that the FT air masses are strongly influenced by injections from BL, however, the number of studies comparing the transport from the BL to the FT over long periods of time are rare.

In this work, we compare four criteria for determining the BLH relatively to the high altitude Puy de Dôme station (PUY) during the year 2015. These criteria are based on LIDAR measurements using the wavelet covariance transform (WCT) method, BLH simulations from the ERA-Interim reanalysis of the European Center for Medium-Range Weather Forecasts (ECMWF) model, and in situ measurements of BL tracers (NO_x/CO and radon-222 (^{222}Rn)). Then, the four criteria are combined to reliably segregate the BL and FT air masses sampled at the PUY station. The segregation between BL and FT air masses is then used to investigate the differences in aerosol properties belonging to each of these atmospheric layers over the 12-month period.

2. Site and Instrumentations

For this study, we used data collected at Puy de Dôme and Cézeaux stations (Figure A1). These stations are part of the CO-PDD measurement site located in central France, in the vicinity of Clermont-Ferrand (300,000 inhabitants). The Puy de Dôme station, hereafter referred to as PUY, is part of GAW (Global Atmospheric Watch) and ACTRIS (Aerosol Cloud and Trace gases Research Infra Structure) networks and is located at the top of Puy de Dôme (45°46′ N, 2°57′ E, 1465 m a.s.l.), in a mountain chain orientated North-South and exposed to dominantly westerly winds. The station hosts a wide variety of instruments to characterize the aerosols, gas, and cloud properties. For instance, the long-term variation of the particle size distribution has been studied by Venzac et al. (2009) [14], and the occurrence of the new particle formation (NPF) process was specifically investigated in several dedicated studies [24,26–28]. Filter measurements, as well as online mass spectrometry analysis, have been used to document the particles chemical composition [19,29,30] and aerosol-cloud interactions were also investigated from this station which offers favorable conditions for such analysis [28,31,32]. The second site, Cézeaux, hereafter referred to as CZ, is located on the University campus in Clermont-Ferrand (420 m a.s.l.), 16 km west from PUY. Continuous measurement of routine meteorological parameters and a Rayleigh-Mie-Raman Raymetrics LIDAR system are operated at CZ.

In this study, we focus on the physical characteristics of aerosol particles measured at the PUY station using a Scanning Mobility Particle Sizer (SMPS) and a GRIMM optical particle counter (OPC) [33] for particle size distribution measurements and a Multi-Angle Absorption Photometer (MAAP) for absorption properties and aerosol black carbon (BC) content. Additionally, the LIDAR system at CZ station is used to determine the vertical aerosol layer height (ALH).

2.1. Investigation of the Vertical Aerosol Distribution Based on LIDAR Measurements

The Rayleigh-Mie-Raman LIDAR is an active remote sensing instrument capable of characterizing the vertical structure of the atmosphere based on the interaction between a laser and particles as well as gas molecules [34–36]. The instrument used in the present work includes a laser type Quantel CFR-400 emitting at 355 nm and a 400 mm Cassegrain telescope. An optical box is dedicated to the splitting of the receiving laser light in 4 different channels (2 elastic channels in parallel and cross polarization, and 2 inelastic channels for nitrogen and water vapor Raman scattering). Vertical profiles of volume backscatter coefficients, extinction coefficients, and the depolarization ratio are retrieved with a time resolution of 10 min. The system is in operation in the framework of the EARLINET network (European Aerosol Research Lidar Network).

The altitude of the particles and molecules interfering with the emitted laser pulses is calculated from the time lapse between the emission of a pulse and the reception of the backscattered light. In this study, LIDAR profiles are specifically targeted to evaluate the ALH. The estimation of ALH is based on the gradient in aerosol concentrations observed at the top of the AL, which coincides with a sharp change in the return signal from LIDAR. Following earlier work by Baars et al. (2008) [13], we applied the Wavelet Covariance Technique (WCT) method, reported as a robust technique that can handle very different aerosol situations during all seasons of the year.

The WCT uses the covariance transform of the Haar function [37] as follows:

$$WCT\ (a,b) = \frac{1}{a}\int_{z_b}^{z_t} f(z) * h\left(\frac{z-b}{a}\right)dz \quad (1)$$

with

$$h\left(\frac{z-b}{a}\right) = \begin{cases} +1, & b-\frac{a}{2} \le z \le b \\ -1 & b \le z \le b+\frac{a}{2} \\ 0, & elsewhere \end{cases} \quad (2)$$

where $f(z)$ is the LIDAR signal corrected with z^2, with z being the altitude, z_b and z_t are the lower and upper limits of the LIDAR signal, respectively, a is the extent of the step function. a was set to 12 Δz in the present work, as recommended by Baars et al. (2008) [13], where Δz = 7.5 m is the spatial resolution of the LIDAR. ALH was determined in clear sky conditions for each LIDAR profile as the maximum of the WCT function.

2.2. In Situ Aerosol Properties at the Puy Station

2.2.1. Particle Number Size Distribution

Particle number size distributions in the range from 10 nm to 650 nm were measured using a custom-made scanning mobility particle sizer (SMPS), with a time resolution of 130 s. This instrument consists of a differential mobility analyzer (DMA) as described by Villani et al. (2007) [38], a condensation particle counter (CPC, TSI model 3010) for particle detection downstream of the DMA and a ^{63}Ni aerosol neutralizer, 95 MBq source. The DMA sheath flow rate is controlled using a blower in a closed-loop arrangement [39]. The SMPS has been inter-compared with other European SMPS and DMPS systems in the framework of the European structure ACTRIS (Aerosols, Clouds, and Trace gases Research Infrastructure Network), and satisfies all requirements for providing a reliable aerosol size distribution. In specific, uncertainties of the measurements conducted in the frame of ACTRIS were reported to be lower than 10% for particle number size distributions in the 20 to 200 nm size range, while below and above this size range the discrepancies increase [40].

Three particle size distribution modes were previously identified by Venzac et al. (2009) [14] using SMPS data at the PUY station. Hence, based on the aforementioned study, we define the nucleation mode concentration as the integrated concentrations of particles ranging from 10 nm to 20 nm, the Aitken mode concentration as the integrated concentrations of particles ranging from 40 nm to 80 nm and accumulation mode (100–300 nm) for aged particles. Particles having diameters from 20–40 nm and 80–100 nm are not included as they can either be nucleation or Aitken modes and Aitken or accumulation modes, respectively.

In addition, particle number size distributions from 350 nm to 18 µm were measured using an optical particle counter (OPC, GRIMM 1.108). Combining OPC measurements with those obtained from the SMPS allowed us to cover diameters ranging from 10 nm up to 18 µm [36], and therefore characterizing 4 particle size distribution modes (Nucleation, Aitken, Accumulation, and Coarse).

Aerosol particles are sampled through a whole air inlet (WAI) in which the 50% cut-off diameter is 30 µm. This allows the whole aerosol size distribution to be sampled, even in the presence of a cloud. Although cloud events were excluded from our study, these inlets ensure that cloud droplets are evaporated in the WAI so that both interstitial and residual cloud residues are sampled (as if they had not been activated into cloud droplets) [28].

2.2.2. Black Carbon (BC) Concentrations

BC concentrations were derived from particle absorption measurements conducted with a Multi-Angle Absorption Photometer (MAAP 5012, central wavelength at 637 nm). The instrument measures the transmitted and backscattered radiation impacted by the particles on a filter and

transforms the absorption into an equivalent black carbon mass concentration. Since the wavelength of the laser beam given by the manufacturer is not exactly that emitted (637 nm instead of 670 nm), absorption coefficients were corrected according to Müller et al. (2011) [41]. Uncertainties in the measurements were around 12% [42].

2.3. Gas-Phase Measurements

2.3.1. Carbon Monoxide (CO)

Carbon monoxide (CO) has been measured at PUY station using the Thermo Scientific™ Model 48i-TLE CO analyzer, which is based on the principle that CO absorbs infrared radiation at a wavelength of 4.6 microns.

2.3.2. Nitrogen Oxides (NO_x)

The concentration of nitrogen oxides (NOx) was measured using the ozone chemiluminescence technology with the Thermo Scientific™ Model 42i-TL TRACE Level NO_x Analyzer.

2.3.3. Radon (^{222}Rn)

Radon-222 (^{222}Rn) has been measured at the PUY station with the active deposit method [43]. The method is based on the measurement of ^{222}Rn short-lived daughters (^{218}Po, ^{214}Bi, ^{214}Po) [44] which are quickly absorbed onto aerosol particles. The accumulated aerosol particles are collected on a cellulose filter for one hour. Then the filter is automatically moved under an alpha detector coupled to a photomultiplier. Total α radioactive decay is measured every 10 min over the span of one hour. Uncertainties in the measurements can reach 10 to 20% [44]. A disequilibrium factor of 1.15, like the one estimated by Schmidt, (1999) [45] for a similar mountain station at Shauinsland, Germany, was used for correcting the data.

2.4. ECMWF-ERA-Interim and LACYTRAJ

The BLH_{ECMWF} was extracted from the reanalysis ERA-Interim of the European Center for Medium-Range Weather Forecasts (ECMWF) model [14,46]. This technique is based on the "global method of Richardson" which includes the influences of mixing generated by wind shear and surface heating [47]. To estimate BLH_{ECMWF} at the location of the PUY, we extracted the nearest grid point (45°75′ N, 3°25′ E) in a resolution of 0.25° × 0.25° grid.

However, it should be noted that the ECMWF model provides a BLH above sea level, but does not take into account the surface elevation field, therefore it is necessary to add a surface layer height to estimate a true BLH. Using the ERA-interim model (https://software.ecmwf.int/wiki/display/CKB/ERA-Interim%3A+elevation+and+orography), this surface layer height of the relevant grid square (45°75′ N, 3°25′ E) was calculated to be 620 ± 10 m.

Back-trajectories have been computed using LACYTRAJ, a three-dimensional kinematic trajectory code [48]. We use 3D wind fields produced by the ERA-Interim reanalyses with a horizontal resolution of 1° in latitude and longitude, and 37 vertical levels for the trajectory calculations. Each grid point is advected using a bilinear interpolation for horizontal wind fields and time and a log-linear interpolation on pressure level for the vertical wind field. A cluster of 100 trajectories starting from a box between 45.6 and 46° N and 2.7 and 3.1° E near 1465 m a.s.l is calculated, with a time resolution of 15 min, during 204 h.

The altitude of each trajectory is compared with the calculated height of the BL, interpolated in time and space from ECMWF ERA-Interim, along all trajectory points, in order to estimate the interaction of the air mass with the BL, that is, the time spent of the sampled air mass in the FT since last contact with the BL.

3. Results and Discussion

3.1. Segregating between Boundary Layer (BL)/Aerosol Layer (AL) and FT Air Masses

Four different criteria were investigated in the present work to determine when the PUY station is sampling in the BL/AL or in the FT, including the analysis of LIDAR profiles, radon concentration, the ratio of NO_x to CO concentrations and ECMWF outputs. In the present paper, as in previous studies (example: De Wekker et al. (2015) [4]), we assimilate the ALH to the convective BLH during the daytime, and to the RLH during nighttime. In order to harmonize the different datasets over the same time resolution, data were averaged over a time step of 3 h. The dataset was further harmonized by only selecting data when all methods are available simultaneously; resulting in 1429 values (Figure 1). Specifically, this implies that only clear sky conditions will be discussed hereafter since the presence of clouds prevents the estimation of the ALH from LIDAR.

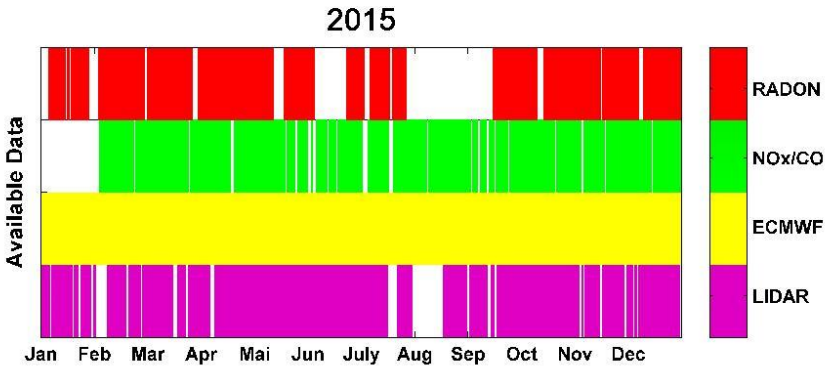

Figure 1. The available data from the main instruments used in the determination of the boundary layer height. Red: Radon-222, Green: NO_x/CO, Yellow: ECMWF, and Violet: LIDAR.

In the following sections, we will compare these four different criteria in order to segregate FT from "BL/AL" air masses.

3.1.1. Comparison between the Aerosol Layer Height from LIDAR Profiles and Boundary Layer Height Simulated with ECMWF

Figure 2a shows the 3-h average diurnal variation of the ALH retrieved from the LIDAR profiles (ALH_{LIDAR}) for the four seasons separately (Winter: 1 January to 19 March, Spring: 20 March to 19 June, Summer: 20 June to 21 September, and Autumn: 22 September to 21 December) using data from 2015. The ALH_{LIDAR} does not show strong variations with the time of the day. The maximum of the ALH_{LIDAR} is reached during summer and spring (average 2000 m a.s.l., green and black) while in winter and autumn (red and blue), the average ALH_{LIDAR} never exceeds 1600 m. Lowest ALH_{LIDAR} are observed during night time, before 9 UTC, when the WCT most likely retrieves the height of the RL. These typical ALH diurnal and seasonal variations are similar to the ones previously reported for the PUY station (Figure 2 in Chauvigné et al. (2016) [36]) and for the Leipzig station (Figures 7, 9 and 17 in Baars et al. (2008) [13]). The LIDAR is located approximately 16 km to the east of the PUY station, that is, downwind of the North-South mountain chain for the western prevailing winds. It is likely that there is a deformation of the upwind atmospheric structure due to the obstacle that the mountain chain represents and, hence, we expect that the ALH retrieved by the LIDAR is slightly increased compared to the surrounding flat and low altitude areas.

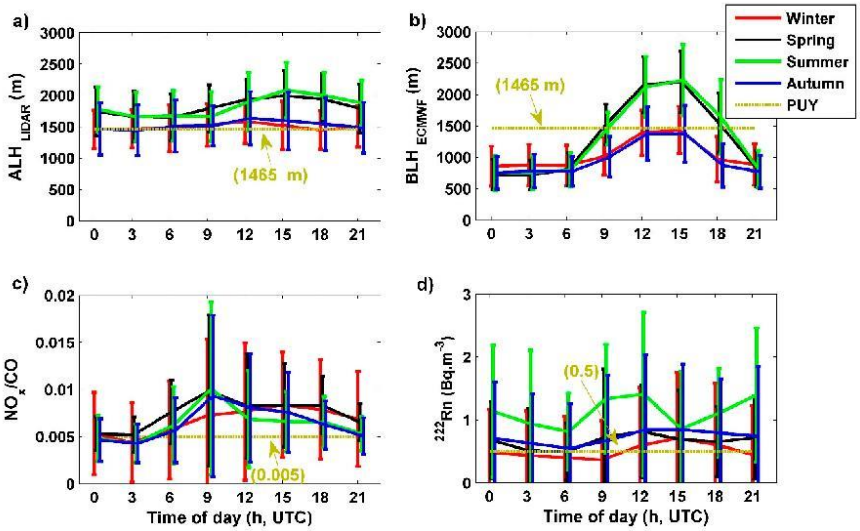

Figure 2. The diurnal variation of the 3-h averaged parameters used to segregate between BL/AL and FT air masses as a function of the season: (**a**) ALH_{LIDAR}; (**b**) BLH_{ECMWF}; (**c**) NO_x/CO, and (**d**) ^{222}Rn. Variability within each season indicates the standard deviation.

BLH_{ECMWF} varies between 700 m a.s.l. at night in winter and 2200 m a.s.l. during the day in summer (Figure 2b). The model predicts that the PUY station is in the BL during the day (between 9 and 18 UTC) in summer and spring, with 3-h averaged BLH_{ECMWF} reaching a maximum of 2200 m a.s.l. In contrast, the model shows that the site is generally above the BL at all times during winter and autumn, and therefore considered to be in the FT. These results are in agreement with the study performed by Venzac et al. (2009) [14] who reported that the PUY station was in the BL during the daytime during the warm seasons (spring and summer) and in the FT during nighttime during the cold seasons (autumn and winter). The ECMWF model is not taking into account the forced convection on the mountain chain. Hence, we expect that the model underpredicts the BLH above the grid square.

Significant differences are observed between ALH_{LIDAR} and BLH_{ECMWF} during nighttime (Figure 2a,b). This is related to the fact that the LIDAR retrieves RLH, while BLH_{ECMWF} instead corresponds to the height of the shallower stable nocturnal BL. On the contrary, ALH_{LIDAR} can be compared to the BLH_{ECMWF} over the daytime period (9 UTC-18 UTC), when the AL can be assimilated to the convective BL. As evidenced in Figure 3, the ALH_{LIDAR} and BLH_{ECMWF} correlate and agree well with each other (correlation coefficient Pr = 0.6 and linear regression slope 0.78). The value of the slope below 1 either indicates an overestimation of the ALH_{LIDAR} or an underestimation of the BLH_{ECMWF}. As mentioned above, the overestimation of the ALH_{LIDAR} could be due to the deformation of the upwind atmospheric structure between CZ and PUY stations. Indeed, the ECMWF model spatial resolution does not take into account local scale dynamical processes around the PUY mountain chain (due to a flattening effect over the surface mode grid).

In order to assess if the PUY station is within the BL/AL or in the FT, the real forced convection from the local topography needs to be taken into account. We calculate the splitting height (SH) for both WCT and ECMWF methods, which corresponds to the height below which an air mass encountering an obstacle is going around it, and above which the air mass is overpassing it. Details of the method for calculating SH is described in Etling, (1989) [49], (Equation (3)).

$$SH = H\,(1 - Fr) \tag{3}$$

H is the height difference between the PUY station and the foot of the mountain and *Fr* is the Froude number [14,49]. When ALH/BLH are higher than the altitude of PUY, the station is always considered to be in the BL/AL. This is especially the case for unstable conditions ($Fr > 1$) when the BLH always reaches the PUY station after the air mass encounters the obstacle. For stable conditions ($Fr < 1$), two different situations are identified depending on SH. If the BLH/ALH is lower than SH, the stream will drift away from the obstacle, and the station will be in free tropospheric conditions. In contrast, for a BLH/ALH higher than SH, the air mass will be uplifted along the mountain slope, and the station will, hence, lay in the BL/AL (Table 1). SH data was calculated every three hours for 2015.

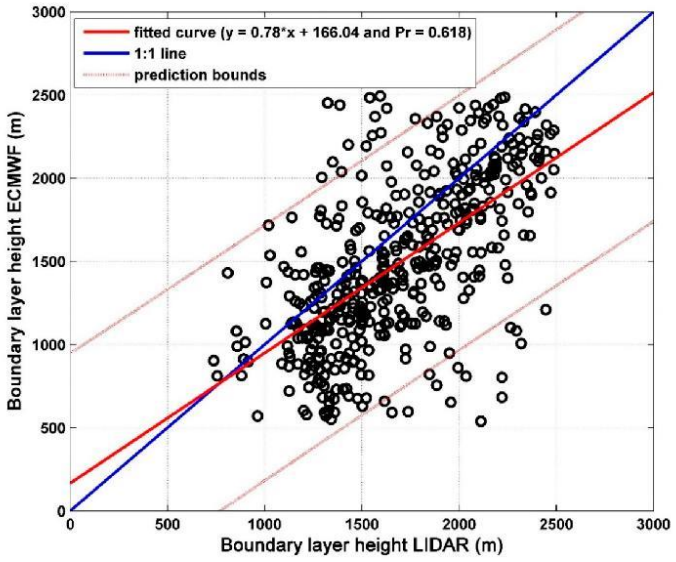

Figure 3. The BLH from ECMWF versus LIDAR on the site 'CZ' between 9 and 18 UTC. Blue, red line, red dashed line, and Pr represent the first bisecting, the linear regression, the prediction bounds and the correlation coefficient, respectively.

Table 1. The classification of the air mass type (BL/AL or FT) sampled at the PUY station as a function of BLH/ALH, and Splitting Height (SH).

	Comparison of PUY Altitude, ALH/BLH and SH	PUY Conditions
Unstable Conditions	BLH/ALH > PUY	BL/AL
Stable Conditions	BLH/ALH > PUY	BL/AL
	BLH/ALH < PUY and BLH/ALH > SH	BL/AL
	BLH/ALH < PUY and BLH/ALH < SH	FT

3.1.2. NO_x/CO

NO_y/CO is an indicator of the "photochemical age" of an air mass that can be used to identify fresh pollution transported to high altitude sites from lower atmospheric layers [3,10]. Higher values of NO_y/CO represent fresh pollution, while lower values correspond to regional air masses. Hence, this ratio usually shows lower values in the FT than in the AL [3]. NO_y is defined as the sum of NO_x and its atmospheric oxidation products (that is, NO_z). In absence of NO_y measurements at PUY in 2015, we used NO_x data, since a good agreement between NO_y and NO_x is observed at this site based

on measurements conducted in 2012 (Pr = 0.93 and slope = 1.11, Figure A2). We, therefore, consider that at the PUY, the NO_x measurements are a relatively good indicator of aged air masses. However, we are aware that NO_x measurements can often be influenced by more local emissions than NO_y, and care should be taken when interpreting these measurements.

For all seasons, we observe a clear diurnal variation with low values at night and high values during the day (Figure 2c). During daytime, an average NO_x/CO maximum of 0.01 was observed for spring, summer, and autumn, at 9 UTC. For winter, a maximum of 0.08 was reported at 18 UTC.

In order to determine whether NO_x/CO is a good indicator for segregating between AL and FT conditions, we investigated the linear regression between NO_x/CO and the BLH_{ECMWF}. We found that both criteria are correlated at the 95% significance level (Pr = 0.54) with the following equation determined over the one-year dataset:

$$BLH_{ECMWF} = 1204 + 1.3 \times \left(\frac{1}{NO_x/CO}\right) \quad (4)$$

This equation allowed us to determine a threshold value of NO_x/CO = 0.005 above which the PUY station is considered to be in the FT (that is, for BLH_{ECMWF} > 1465 m).

However, we observe that the diurnal amplitude of the NO_x/CO ratio varies according to the season (Figure 2c). As a consequence, using a yearly threshold, the site is considered to be in the AL during the day (between 6 and 21 UTC) and in the FT in the night (from 21 to 6 UTC) for all seasons.

3.1.3. Radon-222 (^{222}Rn)

The last technique to evaluate AL/FT conditions is based on the level of ^{222}Rn measured at the PUY station. ^{222}Rn is naturally emitted from the land surface at a relatively constant rate [50,51]. Since ^{222}Rn is naturally emitted from land surfaces, it is often used as a mean to determine the level of contact of the air mass to the land surface. Hence, the lower the value of ^{222}Rn, the less contact the air mass has had with the AL. This criterion was recently used by Griffiths et al. (2014) [11] and Herrmann et al. (2015) [3] to study vertical mixing, based on sites at different altitudes [52] or on vertical profiles from aircraft [53–55]. It has also been used for the estimation of local to regional surface emissions of trace gases [56].

As shown in Figure 2d, the ^{222}Rn concentration does not show strong seasonal variations at PUY, with the exception for summer. As expected, the maximum values of the ^{222}Rn concentration are reached during summer (average 1.41 $Bq \cdot m^{-3}$), especially during daytime. This is likely caused by the increased vertical mixing of air masses during the summer transported to the PUY site. In winter, spring, and autumn, the average ^{222}Rn concentrations never exceed 0.85 $Bq \cdot m^{-3}$. This can be a result of low vertical mixing height as observed from the LIDAR and ECMWF data, but also to a high fraction of air masses coming from the marine sectors (hence, naturally containing lower levels of ^{222}Rn within the BL).

In order to proceed with the identification of AL/FT air masses based on ^{222}Rn measurements, we followed the methodology introduced by Herrmann et al. (2015) [3] for the JFJ site, which is based on the relationship between the ^{222}Rn levels and the number concentration of particles larger than 90 nm (N_{90}). As illustrated in Figure 4a, in a similar way as was done by Herrmann et al. (2015) [3], we first investigated the variations of N_{90} as a function of the air mass residence time in the FT since last BL contact. As previously reported for the JFJ, we observed decreasing exponential trend of N_{90} with time since the last BL contact, but the parameters of the fit are, however, different from those obtained for the JFJ. Specifically, the threshold value below which N_{90} does not further decrease, that is, indicating FT background concentrations, is around 151 cm^{-3} at PUY, being almost 4 times higher than at JFJ (40 cm^{-3}). This is likely to be explained by a higher proximity to the BL/FT inversion when the PUY station is in the FT, compared to when the JFJ is in the FT. Indeed, Chauvigné et al. (2016) [36] pointed out that the aerosol concentrations are not homogeneously distributed over the vertical column within the FT, with a negative aerosol concentration gradient with altitude also within the FT. Plotting

N_{90} as a function of the ^{222}Rn level (Figure 4b) also shows a clear decreasing exponential trend that indicates that ^{222}Rn is also a good indicator of the BL influence on the PUY station. Using a threshold of N_{90} = 151 cm^{-3} on Figure 4b leads to a threshold of ^{222}Rn = 0.5 Bq·m^{-3}. This translates on Figure 2d to the PUY station being in the AL all the time during spring, summer, and autumn. For winter, the site would be in the FT before 10 am and after 8 pm.

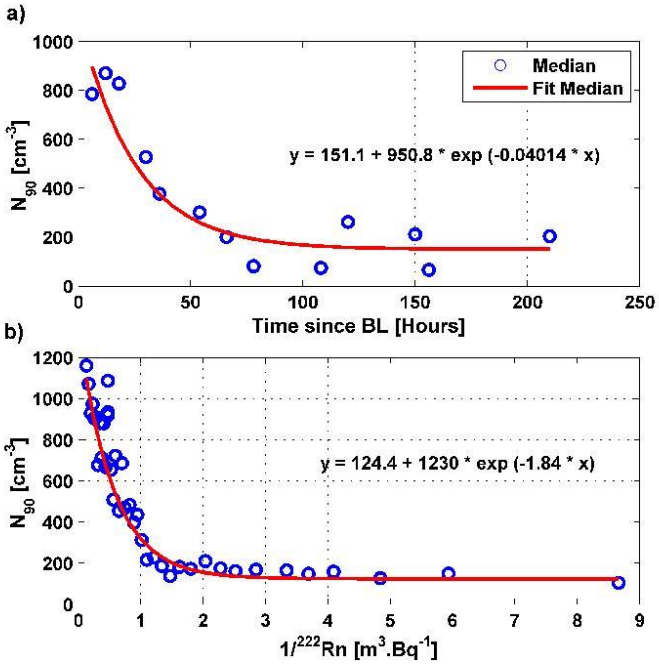

Figure 4. The N_{90} (**a**) as a function of time since BL and (**b**) as a function of $1/^{222}$Rn with fitted lines for the median.

3.1.4. Comparison of the Four Criteria

Each of the four methods used to segregate whether the PUY station lies within the BL/AL or in the FT has specific criteria, based on the vertical profile of aerosols retrieved from LIDAR, on the "global method of Richardson" from the ECMWF model, the "photochemical age" of an air mass from NO_x/CO and the estimation of local to regional surface emissions of trace gases from ^{222}Rn.

During daytime, the prediction of the BLH_{ECMWF} agrees relatively well with the ALH_{LIDAR}, but it should be noted that some uncertainties can be associated with these simulations due to forced convection and their horizontal distance from the site, as is discussed in Section 3.1.1 and shown in Figure 3 above. The NO_x/CO tracer would agree best with the prediction of the ECMWF in the sense that the diurnal variations of this indicator are clear between night and day, even though the seasonal variation is not very evident. It may be that these two criteria agree because NO_x/CO values are decreased in the residual layer compared to the daytime BL. The ^{222}Rn tracer predicts that the site is in the BL with a similar trend than the ALH_{LIDAR}: the site is measured to be influenced by the BL most of the time except during winter and at night. Hence, ^{222}Rn would be more sensitive to the presence of the residual layer at night than the NO_x/CO indicator. However, using a single set of measurements such as NO_x/CO, WCT from LIDAR, ECMWF, or ^{222}Rn was not sufficient to classify air masses in the FT/(BL/AL) at the PUY station.

As all four criteria may have their own bias, a combined classification of these four criteria is proposed in order to increase the robustness of our methodology to determine if the PUY station is in the FT/(BL/AL).

3.1.5. Classification of Air Masses by Combining Four Criteria

Venzac et al. (2009) [14] previously used temperature, relative humidity and the ECMWF model to separate BL and free tropospheric air masses at the PUY station. In this work, we present a more robust classification of air masses using a combination of four criteria (Figure 5a).

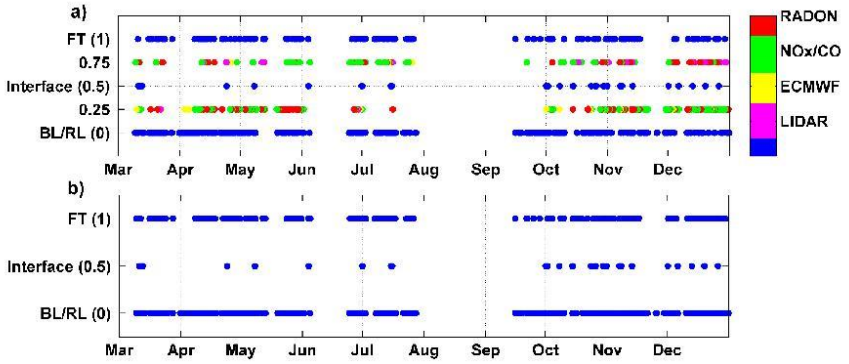

Figure 5. The combined classification of the four methods for the year 2015. (**a**) 1: All four methods classified the air mass to be within the FT, 0.75: three out of four methods classified the air mass as being within the FT, 0.5: only two out of four methods classified the air mass as being in the FT, 0.25: Three out of four methods classified the air mass as being within the BL/RL and 0: all four methods considered that the air mass was within the BL/RL. Color bar indicates where the method failed in calculating the FT(1)/(BL/RL)(0) conditions. Violet: LIDAR, yellow: ECMWF, Green: NO_x/CO, Red: Radon-222 and Blue: successful or equality in the calculation of the FT/(BL/RL) conditions. (**b**) Same as (**a**) with 0.25 and 0.75 combined with 0 and 1, respectively.

As mentioned above, WCT from LIDAR, NO_x/CO, and ^{222}Rn retrieve the ALH while the ECMWF retrieves the BLH. However, AL corresponds to the BL during the daytime and RL during nighttime. For the simplicity of this work, we use the terminology BL/RL for BL, AL, and RL altogether. Thus, this section aims at using all available criteria to classify air masses sampled at the PUY station as those from the FT/(BL/RL).

Figure 5a shows the average classification of the measured air masses as FT/(BL/RL) at the PUY station. In order to average the four classification criteria, we use a specific labeling. When a measurement criterion classifies the air mass at the PUY station as FT, the corresponding date is labeled "1", when it is classified as BL/RL air mass, the corresponding date is labeled "0". Hence, when all four criteria give the air mass as FT, the average classification is "1", while only three criteria out of four classify the air mass as FT, the average classification is "0.75". Similarly, when all four criteria give the air mass as BL/RL, the average classification is "0". Additionally, when two criteria of four go wrong for classifying the air mass as FT or BL/RL, the average classification is "0.5" which corresponds to the interface mode, while only one criteria out of four are classifying the air mass as BL/RL, the average classification is "0.25". Colors in the figure correspond to the one criteria that differs from the other three. We observe that the WCT criteria did not identify FT air masses in the winter (violet color in 0.75). For classifications of BL/RL conditions, disagreements between the four methods were largely related to either NO_x/CO or ^{222}Rn (green and red color, respectively in 0.25 (Figure 5)). For the tracer NO_x/CO, it is possible that this tracer is more representative of aged regional emissions as reported by

Freney et al. (2011) [29]. ^{222}Rn levels can also be influenced by the changes in air mass at PUY station. Indeed, for a given BLH, an oceanic air mass will have lower levels than a terrestrial air mass. Hence, we believe that ^{222}Rn is the less reliable tracer of FT air masses for our site. This analysis also highlights that at the PUY station, radon and NO_x/CO overestimate when the PUY station is in the BL/AL than the other methods. ECMWF is also not adequate for the estimation of FT/BL conditions at night time, retrieving the stable nocturnal BL and not considering the residual nocturnal layer. By combining four criteria for the determination of FT or BL/RL conditions, we provide a more robust method. As a consequence, we chose to classify the station in FT air masses when 3 of the 4 criteria identify FT air masses (0.75) and classify the station in BL/RL air masses when the majority of methods identified BL/RL air masses (0.25). When only two out of four methods disagree with the others (0.5), the air mass is classified at the interface (Figure 5b).

At the PUY station, using a combination of these four criteria for assessing if the site is in free tropospheric conditions, we determine that the site is in the FT for 20% of the time as a yearly average, over 25% during winter and below 17% during summer. At the JFJ, Herrmann et al. (2015) [3] compared three criteria for assessing if the site lies in free tropospheric condition, and found FT prevalence for 39% of the time as a yearly average, with over 60% during winter and below 20% during summer. Chauvigné et al. (2018) [57], also reports time spent in the FT for the Chacaltaya (CHC) (5240 m a.s.l, Bolivia) site, and found FT prevalence for 45% of the time as a yearly average, with no marked seasonal variations. The difference between the PUY and these sites is probably that the PUY is at a lower altitude, but also because the configuration of the topography is different (North-South orientated single mountain chain) [58].

For the four seasons, the percentage of time that the site is in the BL/RL (red) increases during the day (between 9 and 18 UTC) to reach a maximum at 18 UTC, and decrease during the night (after 18 UTC) to reach a minimum at 00 h for winter, at 3 UTC for spring and summer, and at 6 UTC for autumn (Figure 6). On the contrary, this percentage in FT (blue) decreases during the day (between 9 and 18 UTC) to reach a minimum at 18 UTC for winter spring and summer, and at 15 UTC for autumn. During the night the percentage of FT air masses at the site reaches a maximum at 00 h for winter, at 3 UTC for spring, and at 6 UTC for summer and autumn.

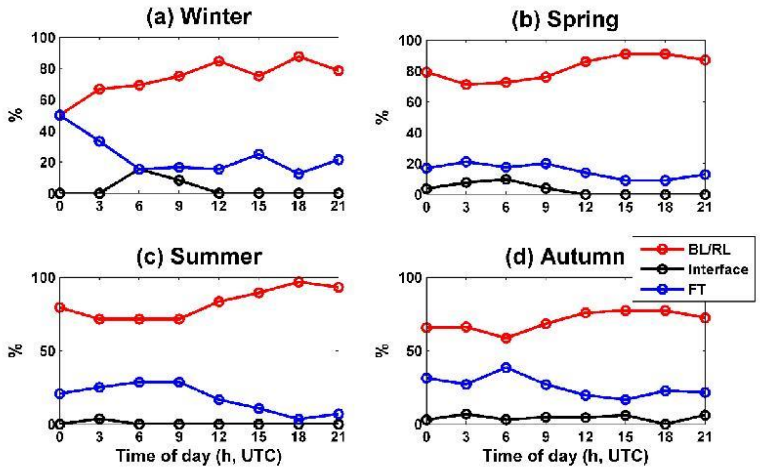

Figure 6. The diurnal variation of percentage that the PUY station is in FT/Interface/(BL/RL) conditions for the four seasons: (**a**) Winter; (**b**) Spring; (**c**) Summer; (**d**) Autumn. **red**: Boundary Layer (BL) (daytime)/Residual Layer (RL) (nighttime), **black**: Interface, **blue**: Free Troposphere (FT).

Air masses are classified at the interface between the BL/RL and the FT (black), at a higher frequency at night/early morning than during the late evening, and higher during winter than during summer. Between 3 and 12 UTC, this percentage reaches a maximum of 15.5% and 10% at 6 UTC respectively for winter and spring. The high percentage at the interface is related to the diurnal variation of the BLH which reaches the PUY station at around 6 UTC.

3.2. Comparisons of the Free Troposphere and Boundary Layer Aerosol Properties

In this section, we use the classification proposed by the combination of the four criteria of FT/(BL/RL) segregation in order to investigate the differences of thermodynamical variables and aerosol properties when sampled in the BL/RL or in the FT at the PUY station. The values obtained for all criteria when the PUY station is at the interface between both layers represent a smaller database that is not statistically relevant and will not be discussed here (Table A1).

In order to assess whether the different parameters show statistically significant differences in FT/(BL/RL), the Wilcoxon–Mann–Whitney test [59] was applied to the median values (Temperature (T), Relative Humidity (RH), Pressure (P), Black Carbon (BC), and for the nucleation (Nuc), Aitken (Ait), accumulation (Acc) and coarse (Coa) aerosol particles size mode concentrations) (Figure 7). This nonparametric test evaluates the difference in medians between two similarly shaped populations. This test showed that the FT/(BL/RL) difference was significant for some parameters (for example, T, RH, and P), however, for certain parameters during certain seasons (for example, the BC and Acc mode particles in summer and for Nuc mode particles during all seasons) no differences between BL/RL and FT properties were detected.

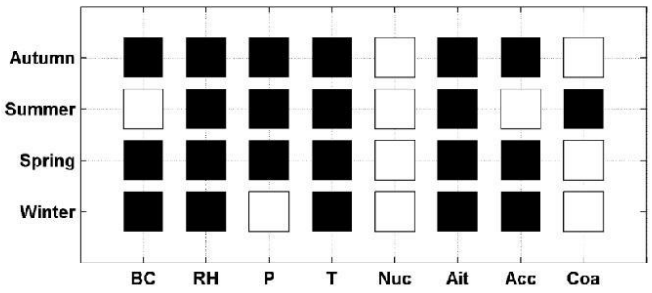

Figure 7. The Wilcoxon–Mann–Whitney test applied on Black Carbon (BC), Relative Humidity (RH), Pressure (P), Temperature (T), Nucleation (Nuc), Aitken (Ait), Accumulation (Acc) and Coarse (Coa) concentrations measured for each season. The squares are black (white) when the medians are significantly different (equal) with a threshold of 5%. Black Crosses are for missing data.

At first, the meteorological parameters (T, RH, and P) were characterized in the FT and in BL/RL air masses (Figure 8a–c). As expected higher median RH concentrations were found in BL/RL conditions for all seasons compared to FT conditions, this difference is shown to be significant by the Wilcoxon–Mann–Whitney test (Figure 7). The higher RH in BL/RL conditions at the PUY station is the result of sources of humidity from the surface in the BL/RL. Higher median T and P were measured in FT conditions compared to BL/RL conditions for all seasons (except in winter for P), the significance being confirmed by the Wilcoxon–Mann–Whitney test (Figure 7). Higher pressures in the FT than in the BL/RL could be related to anticyclone conditions, which decrease the BLH [60]. Higher temperatures in the FT than in the BL/RL may be explained by the fact that the PUY station is situated in the lower part of the FT in which the temperature increases over a limited altitude range (temperature inversion starting at the very lower part of the FT) [61].

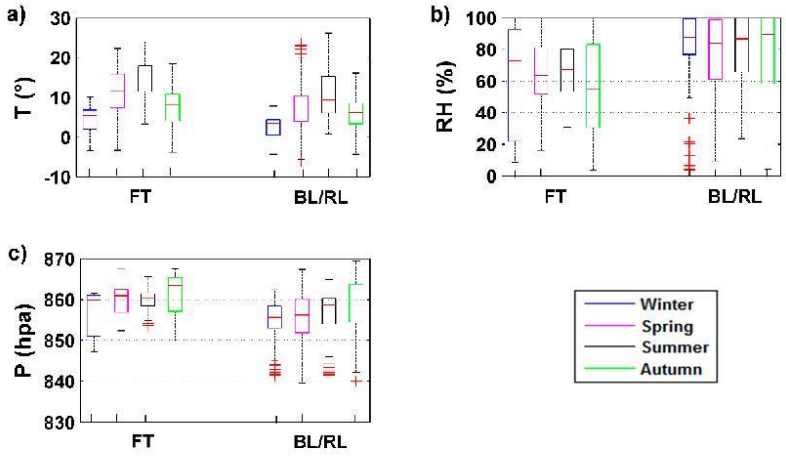

Figure 8. The FT/(BL/RL) variation of (**a**) Temperature (T); (**b**) Relative Humidity (RH), and (**c**) pressure (P), for the four seasons at the PUY station. Red lines represent the median value, bottom and top sides of the boxes symbolize the 25th and 75th percentile respectively and the extremities of the black lines are the 10th and 90th percentile. Red Crosses represent the outliers.

Figure 9a shows, for different seasons, the Black Carbon (BC) concentration when the PUY is in the FT or BL/RL. The Wilcoxon–Mann–Whitney test presented in Figure 7, shows that for winter, spring and autumn seasons, the null hypothesis that the two sets have equal medians was dismissed with a threshold of 5% (black square), while in summer the null hypothesis cannot be dismissed (transparent square). Hence it appears that in summer, there is no marked distinction between the median BC concentration in the FT and the median BC concentration in the BL/RL. However, we observe a stronger variability in the BC in the BL/RL than in the FT. This variation is likely due to the diurnal cycle of sources in this layer. In winter and autumn, the median BC concentration is significantly higher in the BL/RL compared to the FT. This is expected as sources of BC are mainly from surface emissions. In spring, we observe an unusual trend with BC concentrations significantly higher in the FT than in the BL/RL.

The high concentrations of BC in the BL/RL for winter and autumn are thought to be a result of higher contributions of local sources of combustion linked to conventional heating devices often observed during this time of the year [62]. This combined with lower BL heights results in an accumulation of these particle concentrations during the cold seasons. In spring and summer, transport of the materials from BL/RL to FT efficiently occurs by active convection, and the FT air masses are more impacted by intrusions of BL/RL air. The stronger BC concentration in the FT during spring can be linked to BC originating from biomass burning occurring frequently during this season during the burning of vegetation in gardens, that is likely injecting biomass burning particles directly into the FT from strong heat convection transport from BL/RL to FT.

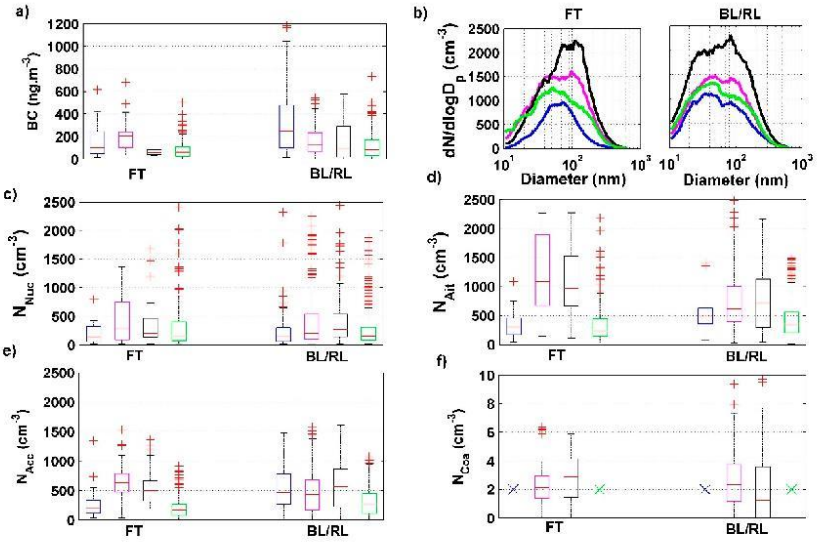

Figure 9. The FT/(BL/RL) variation of: (**a**) BC; (**b**) Full aerosol size distributions (10–650 nm); (**c**) Nucleation (Nuc) (10–20 nm); (**d**) Aitken (Ait) (40–80 nm); (**e**) Accumulation (Acc) (100–300 nm); (**f**) Coarse (Coa) (>1 µm), concentrations for the four seasons. Red lines represent the median value, bottom and top sides of the boxes symbolize the 25th and 75th percentile respectively and the extremities of the black lines are the 10th and 90th percentile. Red Crosses represent the outliers.

In addition, Figure 9b represents median aerosol size distributions (10–650 nm) for the four seasons, in the BL/RL and FT, and highlights the various shapes observed in the different conditions. In order to further investigate the seasonal variation of the aerosol spectrum properties in both layers, we used four aerosol modes: nucleation (10 nm to 20 nm), Aitken (40 nm to 80 nm), accumulation (100 nm to 300 nm), and coarse (1 µm to 18 µm) modes (Figure 9c–f). During the winter and autumn months, the median Aitken and accumulation mode aerosol concentrations are significantly higher in the BL/RL, compared to the FT (Figure 9d,e). In spring (for the accumulation mode) and spring and summer (for the Aitken mode), we observe the opposite, with higher concentrations in the FT than in the BL/RL. In summer, the median accumulation mode particle concentration is comparable in the FT and in the BL/RL.

For nucleation mode particles (10–20 nm) (Figure 9c), there are no significant differences in median values in the FT and in the BL/RL for all seasons. The lack of difference between nucleation mode particles in the BL/RL and in the FT would suggest that there is an additional source of nucleation mode particles in the FT compared to the primary emissions traced by the accumulation mode particles during winter and autumn. This was already observed by Tröstl et al. (2016) [63] at the JFJ site who reports that the nucleation mode particles occur within air masses that have been transported over long-range distances into the FT.

Additionally, these particles show the highest concentrations during summer ($N_{nuc,\,FT}$ = 489 cm^{-3}; $N_{nuc,\,BL/RL}$ = 512 cm^{-3}) (Table 2). This is in agreement with Venzac et al. (2009) [14] at the same site, who reports highest concentrations of nucleation mode particles during summer [14]). Boulon et al. (2011) [27] reports the highest new particle formation frequency during spring and autumn, but the intensity of the new particle formation events (in term of nucleation rate and further growth) is the highest during summer.

Table 2. The mean concentration of the Nucleation, Aitken, and Accumulation mode particles for the four seasons.

Particle Mode	Season	N (cm^{-3})	
		FT	BL/RL
Nucleation	Winter	190	254
	Spring	490	504
	Summer	489	512
	Autumn	374	312
Aitken	Winter	346	514
	Spring	1211	714
	Summer	1119	823
	Autumn	367	419
Accumulation	Winter	290	530
	Spring	630	470
	Summer	560	570
	Autumn	220	385

The accumulation mode particle concentrations have a similar behavior to the BC concentrations previously discussed, and we assume that they have similar sources for winter and autumn. Higher concentrations of the Aitken mode particles during springtime may be partly due to the growth of nucleation mode particles that were observed to occur more frequently during spring [24,26] and preferentially at higher altitudes [27], as also witnessed by higher concentrations during the spring season for the present dataset, and partly due to a contribution from biomass burning aerosols due to the active convection transport from BL/RL to FT. During summer, the difference between concentrations in the FT and in the BL/RL is less marked than in Spring, which may be due to the less frequent nucleation frequency [27,64] and the less biomass burning events than in spring.

For both accumulation and Aitken mode concentrations, we clearly see that spring and summer ($N_{accumulation,\ spring,\ FT}$ = 630 cm^{-3}; $N_{accumulation,\ spring,\ BL/RL}$ = 470 cm^{-3}; $N_{aitken,\ spring,\ FT}$ = 1211 cm^{-3}; $N_{aitken,\ spring,\ BL/RL}$ = 714 cm^{-3} and $N_{accumulation,\ summer,\ FT}$ = 560 cm^{-3}; $N_{accumulation,\ summer,\ BL/RL}$ = 570 cm^{-3}; $N_{aitken,\ summer,\ FT}$ = 1119 cm^{-3}; $N_{aitken,\ summer,\ BL/RL}$ = 823 cm^{-3}) show the highest mean particle concentrations in both the FT and the BL/RL (Table 2). This is in agreement with that of Venzac et al. (2009) [14] and Herrmann et al. (2015) [3] during the summer season.

In our study, the observed concentrations are slightly higher then what was found by Venzac et al. (2009) [14]. This would confirm the tendency observed by Venzac et al. (2009) [14] of the aerosol concentration increasing over the 6 years of data but would need a careful trend analysis which is beyond the scope of the present study.

For coarse mode particles, no data is available for winter and autumn, and the Wilcoxon–Mann–Whitney test is not significant for spring (medians are equal for FT and BL/RL) (Figure 9f). However, for summer, high median concentrations of the coarse mode particles were measured in FT conditions, compared to the BL/RL conditions. This difference is likely due to a more efficient long-range transport of dust and marine aerosols at high altitudes than at lower altitudes. Bourcier et al. (2012) [30] reported higher concentrations of Cesium (Cs) associated to dust particles at PUY, than at the lower altitude of CZ, but the difference was mostly found during winter. The authors hypothesized that during winter, large particles are transported with a higher efficiency at high altitudes due to stronger winds. The variability of the coarse mode particle concentration is higher during the BL/RL conditions compared to FT conditions presumably due to the sporadic character of sources of large primary particles in the BL/RL.

The next step of our analysis is to investigate the variability of aerosol properties within the lower FT and the possible causes for this variability.

3.3. Aerosol Properties in the Lower Free Troposphere as a Function of Air Mass Type and Age

Our analysis of the air mass back-trajectory history relative to the latest contact with the BL over the 204-h prior sampling showed that air masses aerosol properties (for example, N_{90}) do not change

for BL-contact-free times larger than 75 h (Figure 4a). In the following section, we investigate the change of aerosol particles within the lower free troposphere during the last 75 h prior to sampling.

Figure 10 presents the segregation of FT air masses as a function of the time they spent in the FT since their last contact with the BL/RL before reaching the PUY station. The BLH parameter of ERA-Interim ECMWF is interpolated spatially and temporally and compared with the altitude of each path point to determine the last contact with the BL. This analysis was done using LACYTRAJ, for the four seasons. Most noticeably, the vast majority (over 80%) of winter and autumn air masses did not have any contact with the BL/RL for at least the last 75 h before being sampled at PUY. This explains why certain aerosol concentrations are low in the FT during these seasons. For summer and spring, the large majority (60%) of air masses were in contact with the BL/RL in the last 15 h prior to measurement (Figure 10). Therefore, certain aerosol concentrations are high in the FT during these seasons. We hence assume that aerosol properties measured in these air masses during summer and spring are more representative of BL/RL than the unperturbed FT. Using this information, we focus the remaining discussion on aerosol properties measured during winter and autumn assuming that they are representative of the unperturbed FT and we can, therefore, study their characteristics as a function of the air mass origin.

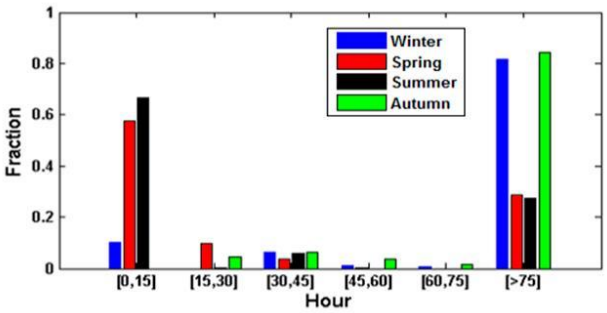

Figure 10. The fraction of time since the last BL/RL contact of >75-h back trajectories of air masses reaching the Puy de Dôme for the four seasons.

LACYTRAJ has also been used to provide a classification of five possible sources, from Oceanic, Mediterranean, continental, northerly, or local (Figure 11), similar to Asmi et al. (2012) [28] and Rose et al. (2015a) [24] (details of the classification are shown in Figure A3). This classification is based on the location of the last interaction between the air mass and the BL. Therefore, the locations of the last contact with BL are essential. During the winter season, air masses are mainly of Mediterranean (34%) and Atlantic (29%) origins, and a smaller fraction of them are either local (15%), continental (14%), or Atlantic modified (8%) (Figure 11). In autumn, air masses are mostly of Mediterranean (39%) and Atlantic (48%) origins, and a small fraction is of a continental origin (12%) (Figure 11).

In the following section we compare aerosol properties in the three types of air masses (Atlantic, Mediterranean, and Continental) observed during both seasons (winter and autumn) (Figure 12).

Higher nucleation mode concentrations are measured when the PUY station is exposed to aged (>75 h) Atlantic and Mediterranean air masses than when exposed to continental air masses (Figure 12). We can hypothesize that these high concentrations of nucleation mode aerosols are formed at the PUY from marine precursor sources that have been transported from the Mediterranean sea and from the Atlantic ocean [24,65], or that the condensational sink associated to the Atlantic and Mediterranean air mass types are lower compared to continental air masses containing larger concentrations of accumulation mode particles. Bianchi et al. (2016) [66] and Tröstl et al. (2016) [63] show also that nucleation in the FT is favored after a certain time lapse has passed after the last contact with the BL/RL.

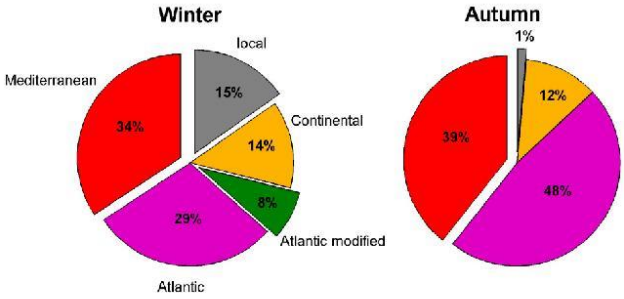

Figure 11. The air masses classification in the FT for winter and autumn seasons: Violet: Atlantic, Green: Atlantic modified, Brown: Continental, Grey: Local, Red: Mediterranean.

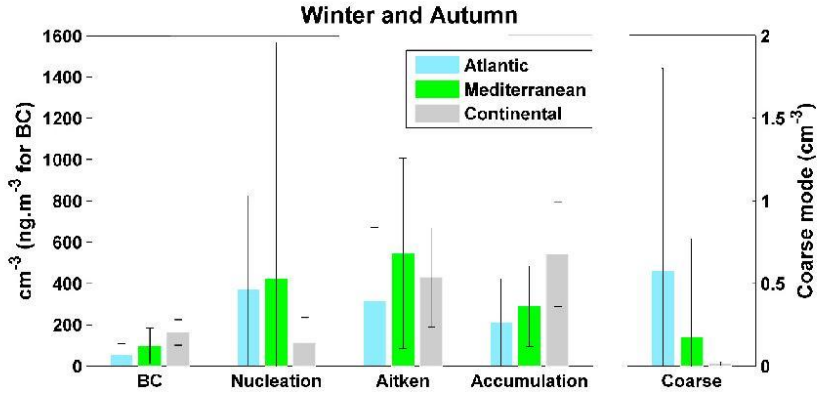

Figure 12. The BC, Nucleation, Aitken, Accumulation, and Coarse mode particles concentrations for >75 h in the FT for Atlantic, Mediterranean, and continental air masses for both winter and autumn.

In aged air masses, the high concentrations of the Aitken and accumulation mode particles coincide with the high concentrations of BC, originated from continental air masses. These high BC, Aitken, and accumulation concentrations can, thus, partly be due to biomass burning emissions. Another source of these high concentrations of Aitken mode particles is the growth of nucleation mode particles originated from the Atlantic and Mediterranean air masses. Within aged air masses, coarse mode aerosol concentrations are also higher in Mediterranean and Atlantic air masses compared to continental air masses, likely a result of transported sea salt and dust particles.

Overall, we observe that even after more than 75 h with no contact with the BL/RL, FT aerosols preserve properties that are specific to their source region. To the author's knowledge, this is the first report of these observations from in situ measurements.

4. Conclusions

A one-year dataset of multiple measurements acquired at the PUY station has been used in this work to determine the specific physical characteristics of FT aerosols and hence of their sources and transport pathways from the BL.

In order to achieve this goal, a combination of four criteria was used to identify whether the PUY station lies within the FT or within the BL. BLH was determined using two independent methods, firstly the ECMWF model, using the "global method of Richardson" to calculate the $BLH_{ECMWF,}$

and secondly, the WCT method to calculate the ALH_{WCT} from LIDAR measurements. In addition, NO_x/CO and radon-222 tracers were used to determine the degree of influence from the $AL_{NOx/CO}$ and AL_{Rn}, respectively. Using these tracers, we observe that the PUY station is considered to be in the FT up to 50% during the winter months.

For most of the time and aerosol property, higher concentrations are found in the BL compared to FT, as expected from larger sources originating from the surface. However, higher BC, accumulation, and Aitken modes median concentrations are observed in FT conditions compared to BL during spring. This might be linked to biomass burning from vegetation in gardens that inject aerosols directly to the FT from active convection transport. Another source of these high concentrations of Aitken mode particles is the growth of nucleation mode particles. In general, for these nucleation mode particles, there is no significant difference in the median values measured in the FT and in the BL/RL for all seasons. This suggests that there is an additional source of precursors to the formation of new particles at the PUY station. These additional sources likely originate from aged Atlantic or Mediterranean air masses. Higher median concentrations and higher variability of the coarse mode particles are also found in FT conditions during summer is a result of increased contribution from Mediterranean and Atlantic air masses, bringing dust and marine aerosol at higher altitudes. Finally, even after more than 75 h without any contact with the BL/RL, FT aerosols preserve properties specific to their air mass type/origin. However, as expected, these differences are less distinct in aged FT air masses (>75 h) than in recent FT air masses (>15 h).

This work introduces a robust method to establish when a site is in the FT or in the BL/RL. Using this method, we were able to identify typical physical properties of different air mass sources in both the BL/RL and in the FT. This method has been applied to the PUY site, which is at the frontier of the BL and the FT, where the majority of exchanges and interactions occur, making it a unique area to study these exchanges. The method of differentiating between BL/RL and FT used in this work can be applied to future studies at altitude sites, providing a real-time estimate of FT air mass sampling. These aerosol properties (size, number concentration, and so forth) can subsequently be used for comparison with different aerosol transport models outputs.

Author Contributions: Conceptualization, A.F., E.F. and K.S.; Data curation, A.F., A.C. (Aurélien Chauvigné), C.R. and A.C. (Aurélie Colomb); Formal analysis, A.F.; Funding acquisition, K.S.; Investigation, A.F.; Methodology, A.F., J.-L.B. and D.H.; Project administration, K.S.; Software, A.F., A.C. (Aurélien Chauvigné), C.R. and D.P.; Supervision, E.F., M.A., W.F. and K.S.; Validation, A.F.; Visualization, A.F.; Writing–original draft, A.F.; Writing–review & editing, A.F., E.F., J.-L.B., C.R., M.A., W.F. and K.S.

Funding: This project has received funding from the European Union's Horizon 2020 research and innovation program under grant agreement No 654109 (ACTRIS-2), and from the French program SNO-CLAP and the research council of the Saint Joseph University.

Acknowledgments: The authors would like to acknowledge the staff of OPGC and LaMP for their work on the instrumentation. INSU-CNRS, CNES and the University Clermont Auvergne are also acknowledged for their support to the PUY station, and the operation of the LIDAR instrument at the Cezeaux site.

Conflicts of Interest: The authors declare no conflicts of interest.

Appendix A

Table A1. Acronyms.

Acronym	Explication
BL	Boundary Layer
BLH	Boundary Layer Height
FT	Free Troposphere
RL	Residual Layer
AL	Aerosol Layer
ALH	Aerosol Layer Height
PUY	Puy de Dôme
CZ	Cézeaux
JFJ	Jungfraujoch

Table A1. *Cont.*

Acronym	Explication
WCT	Wavelet Covariance Transform
ECMWF	European Center for Medium-Range Weather Forecasts
NO_x	Nitrogen oxides
CO	Carbon monoxide
^{222}Rn	Radon-222
BC	Black Carbon
GAW	Global Atmospheric Watch
ACTRIS	Aerosol Cloud and Trace gases Research Infra Structure
EARLINET	European Aerosol Research Lidar Network
NPF	New Particle Formation
SMPS	Scanning Mobility Particle Sizer
DMA	Differential Mobility Analyser
CPC	Condensation Particle Counter
OPC	Optical Particle Counter
MAAP	Multi-Angle Absorption Photometer
WAI	Whole air inlet
T	Temperature
RH	Relative Humidity
P	Pressure
Nuc	Nucleation
Ait	Aitken
Acc	Accumulation
Coa	Coarse

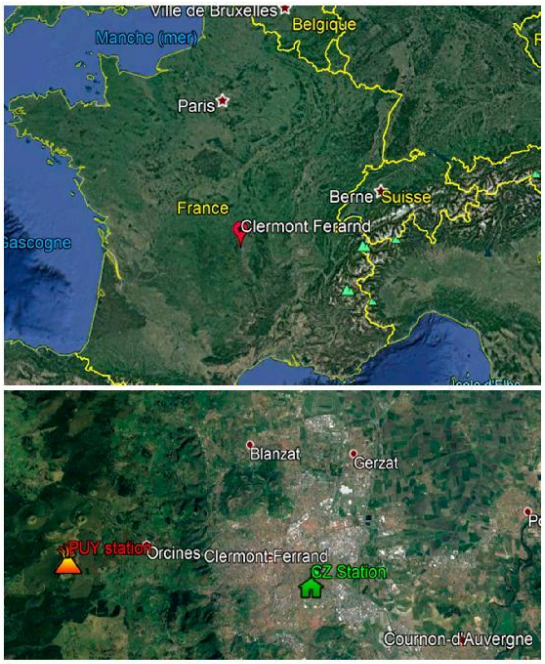

Figure A1. (**Top**) The regional map of Clermont-Ferrand; (**bottom**) Zoom on Clermont-Ferrand city. The green house represents the CZ station, and the orange volcano represents the PUY station. (Adapted from Google Earth).

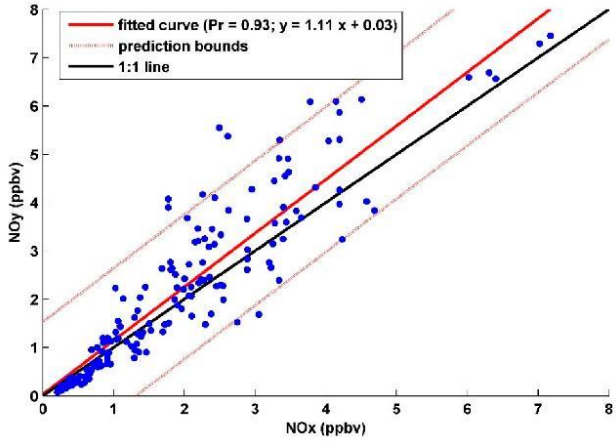

Figure A2. The scatter plot between NO_x and NO_y concentrations.

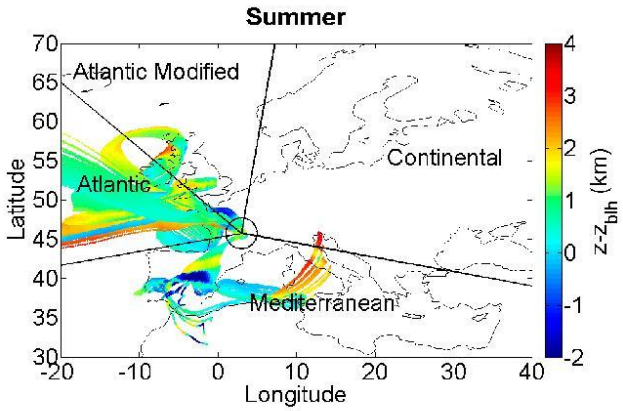

Figure A3. The 204-h ECMWF backward trajectories for air masses arriving at the PUY site during FT sampling periods. The color scale represents the difference between the calculated height (z) of the air mass trajectory and the calculated height of the BL/RL height (Z-Z_{blh} (km)).

References

1. Stocker, T.F.; Qin, D.; Plattner, G.-K.; Tignor, M.; Allen, S.K.; Boschung, J.; Nauels, A.; Xia, Y.; Bex, V.; Midgley, P.M. *IPCC, 2013: Climate Change 2013: The Physical Science Basis*; Contribution of Working Group I to the Fifth Assessment Report of the Intergovernmental Panel on Climate Change; Cambridge University Press: Cambridge, UK; New York, NY, USA, 2013; p. 1535.
2. Stull, R.B. *An Introduction to Boundary Layer Meteorology*; Springer: Dordrecht, The Netherlands, 1988.
3. Herrmann, E.; Weingartner, E.; Henne, S.; Vuilleumier, L.; Bukowiecki, N.; Steinbacher, M.; Conen, F.; Collaud Coen, M.; Hammer, E.; Jurányi, Z.; et al. Analysis of long-term aerosol size distribution data from Jungfraujoch with emphasis on free tropospheric conditions, cloud influence, and air mass transport. *J. Geophys. Res. Atmos.* **2015**, *120*, 9459–9480. [CrossRef]
4. De Wekker, S.F.J.; Kossmann, M. Convective Boundary Layer Heights over Mountainous Terrain—A Review of Concepts. *Front. Earth Sci.* **2015**, *3*, 1–22. [CrossRef]

5. Holzworth, G.C. Estimates of Mean Maximum Mixing Depths in the Contiguous United States. *Mon. Weather Rev.* **1964**, *92*, 235–242. [CrossRef]
6. Holtslag, A.A.M.; De Bruijn, E.I.F.; Pan, H.-L. A High Resolution Air Mass Transformation Model for Short-Range Weather Forecasting. *Mon. Weather Rev.* **1990**, *118*, 1561–1575. [CrossRef]
7. Seibert, P.; Beyrich, F.; Gryning, S.-E.; Joffre, S.; Rasmussen, A.; Tercier, P. Review and intercomparison of operational methods for the determination of the mixing height. *Atmos. Environ.* **2000**, *34*, 1001–1027. [CrossRef]
8. Emeis, S.; Münkel, C.; Vogt, S.; Müller, W.J.; Schäfer, K. Atmospheric boundary-layer structure from simultaneous SODAR, RASS, and ceilometer measurements. *Atmos. Environ.* **2004**, *38*, 273–286. [CrossRef]
9. Wiegner, M.; Emeis, S.; Freudenthaler, V.; Heese, B.; Junkermann, W.; Münkel, C.; Schäfer, K.; Seefeldner, M.; Vogt, S. Mixing layer height over Munich, Germany: Variability and comparisons of different methodologies. *J. Geophys. Res. Atmos.* **2006**, *111*, D13201. [CrossRef]
10. Zellweger, C.; Forrer, J.; Hofer, P.; Nyeki, S.; Schwarzenbach, B.; Weingartner, E.; Ammann, M.; Baltensperger, U. Partitioning of reactive nitrogen (NO_y) and dependence on meteorological conditions in the lower free troposphere. *Atmos. Chem. Phys.* **2003**, *3*, 779–796. [CrossRef]
11. Griffiths, A.D.; Conen, F.; Weingartner, E.; Zimmermann, L.; Chambers, S.D.; Williams, A.G. Surface-to-mountaintop transport characterised by radon observations at the Jungfraujoch. *Atmos. Chem. Phys.* **2014**, *14*, 12763–12779. [CrossRef]
12. Chambers, S.D.; Williams, A.G.; Conen, F.; Griffiths, A.D.; Reimann, S.; Steinbacher, M.; Krummel, P.B.; Steele, L.P.; van der Schoot, M.V. Towards a universal "baseline" characterisation of air masses for high-and low-altitude observing stations using Radon-222. *Aerosol Air Qual. Res.* **2016**, *16*, 885–899. [CrossRef]
13. Baars, H.; Ansmann, A.; Engelmann, R.; Althausen, D. Continuous monitoring of the boundary-layer top with lidar. *Atmos. Chem. Phys.* **2008**, *8*, 7281–7296. [CrossRef]
14. Venzac, H.; Sellegri, K.; Villani, P.; Picard, D.; Laj, P. Seasonal variation of aerosol size distributions in the free troposphere and residual layer at the puy de Dôme station, France. *Atmos. Chem. Phys.* **2009**, *9*, 1465–1478. [CrossRef]
15. Hov, Ø.; Flatøy, F. Convective Redistribution of Ozone and Oxides of Nitrogen in the Troposphere over Europe in Summer and Fall. *J. Atmos. Chem.* **1997**, *28*, 319–337. [CrossRef]
16. Moorthy, K.K.; Sreekanth, V.; Prakash Chaubey, J.; Gogoi, M.M.; Suresh Babu, S.; Kumar Kompalli, S.; Bagare, S.P.; Bhatt, B.C.; Gaur, V.K.; Prabhu, T.P.; et al. Fine and ultrafine particles at a near–free tropospheric environment over the high-altitude station Hanle in the Trans-Himalaya: New particle formation and size distribution. *J. Geophys. Res.* **2011**, *116*, D20212. [CrossRef]
17. Rose, C.; Boulon, J.; Hervo, M.; Holmgren, H.; Asmi, E.; Ramonet, M.; Laj, P.; Sellegri, K. Long-term observations of cluster ion concentration, sources and sinks in clear sky conditions at the high-altitude site of the Puy de Dôme, France. *Atmos. Chem. Phys.* **2013**, *13*, 11573–11594. [CrossRef]
18. Kompalli, S.K.; Babu, S.S.; Krishna Moorthy, K.; Gogoi, M.M.; Nair, V.S.; Chaubey, J.P. The formation and growth of ultrafine particles in two contrasting environments: A case study. *Ann. Geophys.* **2014**, *32*, 817–830. [CrossRef]
19. Freney, E.; Sellegri Karine, S.K.; Eija, A.; Clemence, R.; Aurelien, C.; Jean-Luc, B.; Aurelie, C.; Hervo Maxime, H.M.; Nadege, M.; Laeticia, B.; et al. Experimental Evidence of the Feeding of the Free Troposphere with Aerosol Particles from the Mixing Layer. *Aerosol Air Qual. Res.* **2016**, *16*, 702–716. [CrossRef]
20. Mckendry, I.G.; Hacker, J.P.; Stull, R.; Sakiyama, S.; Mignacca, D.; Reid, K. Long-range transport of Asian dust to the Lower Fraser Valley, British Columbia, Canada: Quantifying the radiative impacts of mineral dust (DUST). *J. Geophys. Res.* **2001**, *106*, 18361–18370. [CrossRef]
21. Timonen, H.; Wigder, N.; Jaffe, D. Influence of background particulate matter (PM) on urban air quality in the Pacific Northwest. *J. Environ. Manag.* **2013**, *129*, 333–340. [CrossRef] [PubMed]
22. Martin, S.T.; Hung, H.-M.; Park, R.J.; Jacob, D.J.; Spurr, R.J.D.; Chance, K.V.; Chin, V. Effects of the physical state of tropospheric ammonium-sulfate-nitrate particles on global aerosol direct radiative forcing. *Atmos. Chem. Phys.* **2004**, *4*, 183–214. [CrossRef]
23. Crumeyrolle, S.; Schwarzenboeck, A.; Sellegri, K.; Burkhart, J.F.; Stohl, A.; Gomes, L.; Quennehen, B.; Roberts, G.; Weigel, R.; Roger, J.C.; et al. Overview of aerosol properties associated with air masses sampled by the ATR-42 during the EUCAARI campaign (2008). *Atmos. Chem. Phys.* **2012**, *12*, 9451–9490. [CrossRef]

24. Rose, C.; Sellegri, K.; Freney, E.; Dupuy, R.; Colomb, A.; Pichon, J.-M.; Ribeiro, M.; Bourianne, T.; Burnet, F.; Schwarzenboeck, A. Airborne measurements of new particle formation in the free troposphere above the Mediterranean Sea during the HYMEX campaign. *Atmos. Chem. Phys.* **2015**, *15*, 10203–10218. [CrossRef]
25. Fröhlich, R.; Cubison, M.J.; Slowik, J.G.; Bukowiecki, N.; Canonaco, F.; Henne, S.; Herrmann, E.; Gysel, M.; Steinbacher, M.; Baltensperger, U.; et al. Fourteen months of on-line measurements of the non-refractory submicron aerosol at the Jungfraujoch (3580 m a.s.l.)—Chemical composition, origins and organic aerosol sources. *Atmos. Chem. Phys.* **2015**, *15*, 11373–11398. [CrossRef]
26. Venzac, H.; Sellegri, K.; Laj, P. Nucleation events detected at the high altitude site of the Puy de Dôme Research Station, France. *Boreal Environ. Res.* **2007**, *12*, 345–359.
27. Sellegri, K.; Hervo, M.; Picard, D.; Pichon, J.-M.; Fréville, P.; Laj, P. Investigation of nucleation events vertical extent: A long term study at two different altitude sites. *Atmos. Chem. Phys.* **2011**, *11*, 5625–5639.
28. Asmi, E.; Freney, E.; Hervo, M.; Picard, D.; Rose, C.; Colomb, A.; Sellegri, K. Aerosol cloud activation in summer and winter at puy-de-Dôme high altitude site in France. *Atmos. Chem. Phys.* **2012**, *12*, 11589–11607. [CrossRef]
29. Freney, E.J.; Sellegri, K.; Canonaco, F.; Boulon, J.; Hervo, M.; Weigel, R.; Pichon, J.M.; Colomb, A.; Prévôt, A.S.H.; Laj, P. Seasonal variations in aerosol particle composition at the puy-de-Dôme research station in France. *Atmos. Chem. Phys.* **2011**, *11*, 13047–13059. [CrossRef]
30. Bourcier, L.; Sellegri, K.; Chausse, P.; Pichon, J.M.; Laj, P. Seasonal variation of water-soluble inorganic components in aerosol size-segregated at the puy de Dôme station (1465 m a.s.l.), France. *J. Atmos. Chem.* **2012**, *69*, 47–66. [CrossRef]
31. Sellegri, K.; Laj, P.; Dupuy, R.; Legrand, M.; Preunkert, S.; Putaud, J.-P. Size-dependent scavenging efficiencies of multicomponent atmospheric aerosols in clouds. *J. Geophys. Res.* **2003**, *108*, AAC3.1–AAC3.15. [CrossRef]
32. Guyot, G.; Gourbeyre, C.; Febvre, G.; Shcherbakov, V.; Burnet, F.; Dupont, J.-C.; Sellegri, K.; Jourdan, O. Quantitative evaluation of seven optical sensors for cloud microphysical measurements at the Puy-de-Dôme Observatory, France. *Atmos. Meas. Tech.* **2015**, *8*, 4347–4367. [CrossRef]
33. Burkart, J.; Steiner, G.; Reischl, G.; Moshammer, H.; Neuberger, M.; Hitzenberger, R. Characterizing the performance of two optical particle counters (Grimm OPC1.108 and OPC1.109) under urban aerosol conditions. *J. Aerosol Sci.* **2010**, *41*, 953–962. [CrossRef] [PubMed]
34. Hervo, M.; Quennehen, B.; Kristiansen, N.I.; Boulon, J.; Stohl, A.; Fréville, P.; Pichon, J.-M.; Picard, D.; Labazuy, P.; Gouhier, M.; et al. Physical and optical properties of 2010 Eyjafjallajökull volcanic eruption aerosol: Ground-based, Lidar and airborne measurements in France. *Atmos. Chem. Phys.* **2012**, *12*, 1721–1736. [CrossRef]
35. Freville, P.; Montoux, N.; Baray, J.-L.; Chauvigné, A.; Réveret, F.; Hervo, M.; Dionisi, D.; Payen, G.; Sellegri, K. LIDAR Developments at Clermont-Ferrand—France for Atmospheric Observation. *Sensors* **2015**, *15*, 3041–3069. [CrossRef] [PubMed]
36. Chauvigné, A.; Sellegri, K.; Hervo, M.; Montoux, N.; Freville, P.; Goloub, P. Comparison of the aerosol optical properties and size distribution retrieved by sun photometer with in situ measurements at midlatitude. *Atmos. Meas. Tech.* **2016**, *9*, 4569–4585. [CrossRef]
37. Brooks, I.M. Finding boundary layer top: Application of a wavelet covariance transform to lidar backscatter profiles. *J. Atmos. Ocean. Technol.* **2003**, *20*, 1092–1105. [CrossRef]
38. Villani, P.; Picard, D.; Marchand, N.; Laj, P. Design and Validation of a 6-Volatility Tandem Differential Mobility Analyzer (VTDMA). *Aerosol Sci. Technol.* **2007**, *41*, 898–906. [CrossRef]
39. Jokinen, V.; Mäkelä, J.M. Closed-loop arrangement with critical orifice for DMA sheath/excess flow system. *J. Aerosol Sci.* **1997**, *28*, 643–648. [CrossRef]
40. Wiedensohler, A.; Birmili, W.; Nowak, A.; Sonntag, A.; Weinhold, K.; Merkel, M.; Wehner, B.; Tuch, T.; Pfeifer, S.; Fiebig, M.; et al. Mobility particle size spectrometers: Harmonization of technical standards and data structure to facilitate high quality long-term observations of atmospheric particle number size distributions. *Atmos. Meas. Tech.* **2012**, *5*, 657–685. [CrossRef]
41. Müller, T.; Henzing, J.S.; de Leeuw, G.; Wiedensohler, A.; Alastuey, A.; Angelov, H.; Bizjak, M.; Collaud Coen, M.; Engström, J.E.; Gruening, C.; et al. Characterization and intercomparison of aerosol absorption photometers: Result of two intercomparison workshops. *Atmos. Meas. Tech.* **2011**, *4*, 245–268. [CrossRef]
42. Petzold, A.; Schönlinner, M. Multi-angle absorption photometry—A new method for the measurement of aerosol light absorption and atmospheric black carbon. *J. Aerosol Sci.* **2004**, *35*, 421–441. [CrossRef]

43. Biraud, S.; Ciais, P.; Ramonet, M.; Simmonds, P.; Kazan, V.; Monfray, P.; O'Doherty, S.; Spain, T.G.; Jennings, S.G. European greenhouse gas emissions estimated from continuous atmospheric measurements and radon 222 at Mace Head, Ireland. *J. Geophys. Res. Atmos.* **2000**, *105*, 1351–1366. [CrossRef]
44. Polian, G.; Lambert, G.; Ardouin, B.; Jegou, A. Long-range transport of continental radon in subantarctic and antarctic areas. *Tellus B* **1986**, *38*, 178–189. [CrossRef]
45. Schmidt, M. Measurement and balancing anthropogenic greenhouse gases in Germany. Ph.D. Thesis, Univ. Heidelberg, Heidelberg, Germany, 1999.
46. Von Engeln, A.; Teixeira, J. A Planetary Boundary Layer Height Climatology Derived from ECMWF Reanalysis Data. *J. Clim.* **2013**, *26*, 6575–6590. [CrossRef]
47. Troen, I.B.; Mahrt, L. A simple model of the atmospheric boundary layer; sensitivity to surface evaporation. *Bound.-Layer Meteorol.* **1986**, *37*, 129–148. [CrossRef]
48. Clain, G.; Baray, J.L.; Delmas, R.; Keckhut, P.; Cammas, J.P. A lagrangian approach to analyse the tropospheric ozone climatology in the tropics: Climatology of stratosphere-troposphere exchange at Reunion Island. *Atmos. Environ.* **2010**, *44*, 968–975. [CrossRef]
49. Etling, D. On atmospheric vortex streets in the wake of large islands. *Meteorol. Atmos. Phys.* **1988**, *41*, 157–164. [CrossRef]
50. Szegvary, T.; Leuenberger, M.C.; Conen, F. Predicting terrestrial 222Rn flux using gamma dose rate as a proxy. *Atmos. Chem. Phys.* **2007**, *7*, 2789–2795. [CrossRef]
51. Zhang, K.; Feichter, J.; Kazil, J.; Wan, H.; Zhuo, W.; Griffiths, A.D.; Sartorius, H.; Zahorowski, W.; Ramonet, M.; Schmidt, M.; et al. Radon activity in the lower troposphere and its impact on ionization rate: A global estimate using different radon emissions. *Atmos. Chem. Phys.* **2011**, *11*, 7817–7838. [CrossRef]
52. Chevillard, A.; Ciais, P.; Karstens, U.; Heimann, M.; Schmidt, M.; Levin, I.; Jacob, D.; Podzun, R.; Kazan, V.; Sartorius, H.; et al. Transport of 222Rn using the regional model REMO: A detailed comparison with measurements over Europe. *Tellus B* **2002**, *54*, 850–871. [CrossRef]
53. Guedalia, D.; Lopez, A.; Fontan, J.; Birot, A. Aircraft Measurements of Rn-222, Aitken Nuclei and Small Ions up to 6 km. *J. Appl. Meteorol.* **1972**, *11*, 357–365. [CrossRef]
54. Lee, H.N.; Larsen, R.J. Vertical Diffusion in the Lower Atmosphere Using Aircraft Measurements of 222Rn. *J. Appl. Meteorol.* **1997**, *36*, 1262–1270. [CrossRef]
55. Williams, A.G.; Zahorowski, W.; Chambers, S.; Griffiths, A.; Hacker, J.M.; Element, A.; Werczynski, S. The Vertical Distribution of Radon in Clear and Cloudy Daytime Terrestrial Boundary Layers. *J. Atmos. Sci.* **2010**, *68*, 155–174. [CrossRef]
56. Van der Laan, S.; van der Laan-Luijkx, I.T.; Zimmermann, L.; Conen, F.; Leuenberger, M. Net CO_2 surface emissions at Bern, Switzerland inferred from ambient observations of CO_2, $\delta(O_2/N_2)$, and 222Rn using a customized radon tracer inversion. *J. Geophys. Res. Atmos.* **2014**, *119*, 2013JD020307. [CrossRef]
57. Chauvigné, A.; Marcos, A.; Aliaga, D.; Radovan, K.; Grisa, M.; Montoux, N.; Moreno, I.; Thomas, M.; Marco, P.; Sellegri, K.; et al. Aerosol Optical Properties and Radiative forcing in the Andes Cordilliera based on measurements at the Chacaltaya observatory, Bolivia (5240 m a.s.l.). To be Submitt. 2018.
58. Collaud Coen, M.; Andrews, E.; Aliaga, D.; Andrade, M.; Angelov, H.; Bukowiecki, N.; Ealo, M.; Fialho, P.; Flentje, H.; Hallar, A.G.; et al. The topography contribution to the influence of the atmospheric boundary layer at high altitude stations. *Atmos. Chem. Phys.* **2017**, 1–44. [CrossRef]
59. DePuy, V.; Berger, V.W.; Zhou, Y. Wilcoxon–Mann–Whitney Test. Available online: https://onlinelibrary.wiley.com/doi/full/10.1002/0470013192.bsa712 (accessed on 20 June 2018).
60. Salzano, R.; Pasini, A.; Casasanta, G.; Cacciani, M.; Perrino, C. Quantitative Interpretation of Air Radon Progeny Fluctuations in Terms of Stability Conditions in the Atmospheric Boundary Layer. *Bound.-Layer Meteorol.* **2016**, *160*, 529–550. [CrossRef]
61. Tennekes, H. A Model for the Dynamics of the Inversion above a Convective Boundary Layer. *J. Atmos. Sci.* **1973**, *30*, 558–567. [CrossRef]
62. Barbet, C.; Deguillaume, L.; Chaumerliac, N.; Leriche, M.; Freney, E.; Colomb, A.; Sellegri, K.; Patryl, L.; Armand, P. Evaluation of Aerosol Chemical Composition Simulations by the WRF-Chem Model at the Puy de Dôme Station (France). *Aerosol Air Qual. Res.* **2016**, *16*, 909–917. [CrossRef]
63. Tröstl, J.; Herrmann, E.; Frege, C.; Bianchi, F.; Molteni, U.; Bukowiecki, N.; Hoyle, C.R.; Steinbacher, M.; Weingartner, E.; Dommen, J.; et al. Contribution of new particle formation to the total aerosol concentration at the high altitude site Jungfraujoch (3580 m a.s.l., Switzerland). *J. Geophys. Res. Atmos.* **2016**. [CrossRef]

64. Rose, C.; Sellegri, K.; Velarde, F.; Moreno, I.; Ramonet, M.; Weinhold, K.; Krejci, R.; Ginot, P.; Andrade, M.; Wiedensohler, A.; et al. Frequent nucleation events at the high altitude station of Chacaltaya (5240 m a.s.l.), Bolivia. *Atmos. Environ.* **2015**, *102*, 18–29. [CrossRef]
65. Schröder, F.; Ström, J. Aircraft measurements of sub micrometer aerosol particles (>7 nm) in the midlatitude free troposphere and tropopause region. *Atmos. Res.* **1997**, *44*, 333–356. [CrossRef]
66. Bianchi, F.; Tröstl, J.; Junninen, H.; Frege, C.; Henne, S.; Hoyle, C.R.; Molteni, U.; Herrmann, E.; Adamov, A.; Bukowiecki, N.; et al. New particle formation in the free troposphere: A question of chemistry and timing. *Science* **2016**, *352*, 1109–1112. [CrossRef] [PubMed]

Abstract

Aerosol particles are important due to their direct and indirect impacts on climate. Within the planetary boundary layer (BL), these particles have a relatively short lifetime due to their frequent removal process by wet deposition. When aerosols are transported into the free troposphere (FT), their atmospheric lifetime increases significantly, making them representative of large spatial areas. In this work, we use a combination of in situ measurements performed at the high altitude PUY (Puy de Dôme, 45°46′ N, 2°57′E, 1465 m asl) station, together with LIDAR profiles at Clermont-Ferrand for characterizing FT conditions, and further characterize the physical and chemical properties of aerosol in this poorly documented area of the atmosphere. First, a combination of four criteria was used to identify whether the PUY station lies within the FT or within the BL. Results show that the PUY station is located in BL with frequencies ranging from 50% during the winter, up to 97% during the summer. Then, the classification is applied to a year-long dataset of particle size distribution and NR-PM1 data's to study the differences in particle physical and chemical characteristics and BC concentrations between the FT and the BL. Based on this segregation, we observed higher concentrations in the BL compared to FT for BC, Aitken and accumulation mode particle concentrations for most seasons, as expected from larger sources originating from the surface. However, BC, Aitken mode, accumulation mode and organic aerosols concentrations were higher in the FT compared to BL during spring. These organic aerosols were identified as aged/less aged, and were correlated with sulphate and BC and we suspect that the higher concentrations of particles observed in the FT compared to BL during spring originate from direct injection of BB aerosols in the FT through strong heat convection. No significant difference between the BL and the FT concentrations was observed for the nucleation mode particles for all seasons, suggesting a continuous additional source of nucleation mode particles in the FT during winter and autumn. Coarse mode particle concentrations were found higher in the FT than in the BL for all seasons and especially during summer. This indicates an efficient long-range transport of large particles in the FT from distant sources (marine and desert) due to higher wind speeds in the FT compared to BL. For FT air masses, we used 204-h air mass back-trajectories combined with boundary layer height estimations from ECMWF ERA-Interim to assess the time they spent in the FT since their last contact with the BL and to evaluate the impact of this parameter on the aerosol properties. We observed that even after 75 h without any contact with the BL, FT aerosols preserve specific properties of their air mass type. This manuscript is also presenting a study of simultaneous measurements at PUY and an urban low altitude station AtmoAura. Results show that when the PUY is influenced by FT air masses, the PM1 species are lower at the PUY compared to AtmoAura confirming our classification. When the PUY is predicted to lay within the BL, the aerosol composition was similar among the two sites for several species, which allowed for a quantification of the local urban pollution contribution for the species enhanced within the city of Clermont-Ferrand.

Keywords: aerosol size distribution; aerosol chemical speciation monitor; organic aerosol sources; high altitude site; long-range transport; boundary layer/free troposphere.